Non-equilibrium real time dynamics of quantum spin systems and the quantum critical dynamics of 'dirty' bosons

Non-equilibrium real time dynamics of quantum spin systems and the quantum critical dynamics of 'dirty' bosons

By

Ray Ng Yeh Yi, BSc.,MSc.

A Thesis Submitted to the School of Graduate Studies
in Partial Fulfilment of the Requirements for the Degree

Doctor of Philosophy

July 2015

DOCTOR OF PHILOSOPHY (2015) McMaster University
(Physics and Astronomy) Hamilton, Ontario

TITLE: Non-equilibrium real time dynamics of quantum spin systems and the quantum critical dynamics of 'dirty' bosons

AUTHOR: Ray Ng Yeh Yi, B.Sc. (Simon Fraser University), M.Sc. (McMaster University)

SUPERVISOR: Professor Erik Sørensen

NUMBER OF PAGES: xviii, 171

Dedicated to my mom and dad:
Christine Foo Siew Lan and Harold Ng Hung Chuan

"What you are will show in what you do."

- Thomas A. Edison

ABSTRACT

This thesis presents our work on two separate subfields and has for this reason been divided into two parts: (I) the development and implementation of a numerical technique for non-equilibrium dynamics and a (II) detailed investigation of the dirty-boson problem.

In part (I), we optimize and develop the quantum phase space method known as the positive-P representation (PPR) specifically for the simulations of the real time quench dynamics of quantum spin systems. The main benefit of this approach is that the dynamics of the density operator is mapped onto $\sim N$ stochastic variables (where N is the size of the system) that obey Langevin-type stochastic differential equations, thereby greatly reducing the complexity of the problem.

The first publication presents our initial use of the PPR on spin systems by using a Schwinger mapping for spin operators on to Bosonic operators since the underlying basis comprises of Bosonic coherent states. We simulate the quench dynamics of the generalized transverse-field spin-1/2 XXZ model in 1d showing that simulations of up to 100 spins are possible, albeit for relatively short simulation times. In our second publication, we reformulate the PPR using SU(2) spin coherent states and further optimize simulation lifetimes by implementing an extrapolation scheme, to achieve several-fold improvements over the results of our first publication. We focus solely on the transverse Ising model and simulate its quench dynamics in 1d and 2d using up to 10^4 spins, while significantly extending simulation lifetimes.

The second part of this thesis is a numerical study of the universality class of the Superfluid-Bose Glass transition of the dirty-boson system. Recently the longstanding exact result $z = d$, where z is the dynamic critical exponent and d is the dimensionality of the system, has been challenged by a series of numerical studies, suggesting the alternative scenario that z should be instead unconstrained. To address this controversy, we use large scale quantum Monte-Carlo simulations on two independent quantum models, and average over $5 \times 10^4 - 10^5$ disorder realizations to numerically determine the universality class of the dirty-boson transition, paying particular attention to the dynamic critical exponent, z and without any biasing assumptions.

ACKNOWLEDGEMENTS

I have spent the last four months looking forward to writing my acknowledgements as I had decided to leave it as the last thing to do. It is indeed a surreal experience to be writing it now. I can safely say that pursuing my doctoral studies has been an arduous and trying journey that I could not have completed without the support of my family, friends and colleagues. Through it all, I have always felt that they were all in their own way rooting for my success and it is this invisible force that has helped me overcome the toughest parts of this endeavor. As such, you all have lent a hand in getting me to this stage and all I can say is thank you from the bottom of my heart.

None of this would have been possible if my supervisor, Prof. Erik Sorensen had not taken a chance on me. Erik has always been encouraging and supportive of me regardless of how research was going. He has always taken my ideas seriously and never ceased to make time for me to talk them through. This unwavering confidence in me has been instrumental in honing my abilities as a physicist. I particularly enjoyed working together on the final project on dirty-bosons (despite the time difference!). His enthusiasm and profound insight certainly made it a joy to be working on the problem even if it was into the obscene hours of the night (or morning).

I would also like to thank Prof. Sung-Sik Lee and Prof. Duncan O'Dell for taking time out of their busy schedules to be part of my committee. I have found Sung-Sik to be a very inspirational person to be around. His silent confidence and clarity of thought are qualities that I strive to emulate. I have always found Duncan to be exceptionally personable and have always enjoyed our conversations. He is always enthusiastic and up for discussing new research ideas and I look forward to finally working on a project together. Thanks also goes to the external member of my committee, Prof. Anders Sandvik, for making the trek from Boston University to be here in person and for even agreeing to be a part of my thesis defense. Although, I had not met Anders before, I have always held a secret admiration for his work. He has been a major proponent for the progress in computational techniques, especially those rooted in quantum Monte-Carlo and the field owes him a great deal. The stochastic series expansion for example (which we use in part II of this thesis), is a staple of the modern day condensed matter computational toolbox.

Special thanks goes to my collaborator and friend, Prof. Piotr Deuar whom I honestly believe that

there is none other like him. Piotr and I became acquainted with each other only through an email I had sent as a pesky Master's student. To this day, I still do not understand what made him decide to entertain my endless barrages of questions but I am most grateful that he did. I have learned a great deal from Piotr, especially the importance of scrutinizing graphs, leaving no anomalous features unchecked (no matter how slight) and always asking the right questions as the main line of assault to any problem. Piotr has also graciously hosted me for several research collaboration visits at the Institute of Physics in Warsaw, Poland and has in turn generously visited Erik and I at McMaster. Before I met Piotr, I did not realize that road trips without a plan were possible.

To my parents, I am forever indebted to the both of you for your unconditional love and endless support for all my endeavors even if you did not fully comprehend my passion for them in the first place. My mom taught me that overcoming an obstacle is like attempting to get pass a brick wall and that it sometimes calls for sickening unrelenting effort. My dad however, taught me that sometimes you can simply just walk around it to get to the other side. I would also like to express appreciation and thanks to my older sister, Dawn, who I know loves me a great deal and would never hesitates to be there for me should I need it. As much as I would hate to admit it, I do enjoy answering your sporadic phone calls. To my older brother, Jed, I have admired his steadfast resolve and self-confidence and wish him nothing but success. Needless to say, I am also grateful for the support of my extended families all over the globe, especially the other 'Ng' family' at Anglesea drive: Uncle Harry, Aunty Lucy, Rachel and Darrell, who played a crucial role in my formative years while I was living in BC. I have also had the fortune of being cared for by the Forsyth family: Scott, Marylisa, Delaney, Zoe and Georgia, who I know I will always have a special place with. The three girls will always be my little sisters no matter what, and I, their older brother.

My love and gratitude goes out to Jessica Donat, who has had to put up the most with my bouts of crankiness especially throughout this writing process and my endless obsession with Monte-Carlo 'Worms'. Her unrelenting love and trust in me been a major source of emotional support for me to lean on. I am truly blessed to have her in my life. Her family has also been kind enough to open their home to me and I thank them for such unconditional welcome.

I am also blessed with close friends who have willingly (or unwillingly) volunteered to be my sounding boards in all matters ranging from physics to just life in general. In no order of importance, I would especially like to thank Dennis Ng, Andrew Louca, Gabriela Chang, Sedigh Ghamari, Andreas Deschna, Nick Miladinovic, Rory Woods, Rob D'ortenzio, Laura Toppozini, Shouvik Sur, Wen Huang, Allan Bayntun, Michelle Tan, Goldie Ng, Phil and Karen Day for always being ready to listen. Dr. Ranjan Bhaduri certainly deserves special mention for taking interest in my future career plans and Dr. Matthew Nobes (who was my TA at SFU) and still selflessly bestows invaluable career advice. Thank you both for looking out for me simply out of the generosity of your hearts.

Last but not least, I would like to thank the undergrads whom I have had the pleasure of teaching, met through the McMaster Dragonboat club or through the 'Pulse' community. Our interactions have always been a refreshing and positive experience that never failed to lift my spirits. Thank you all for your friendship.

I deeply apologize if I have forgotten to mention anyone who has contributed in any way, it is purely unintentional. You have my heartfelt thanks all the same.

List of Figures

List of Tables

Declaration of Academic achievement

In this 'Sandwich' thesis, I present the three publications listed below, along with my collaborators' and my personal contributions to them.

Paper 1

Exact Real-Time Dynamics of Quantum Spin Systems Using the Positive-P Representation
– *Ray Ng and Erik S. Sørensen*

J. Phys. A: Math. Theor. 44 065305

doi: 10.1088/1751-8113/44/6/065305

Calculations: I performed all the simulations and produced all the figures.

Manuscript: I wrote the bulk of the manuscript. Erik S. Sørensen helped to refine and edit the Introduction.

In this publication, we set out to answer the following questions:

- Is the PPR amenable to quantum spin systems in particular: the transverse field spin-1/2 XXZ and transverse-field Ising model?
- To what extent are we able to simulate the real time dynamics of spin system following a quantum quench?
- What are the largest system sizes that we can simulate?
- What are the largest time scales that can be achieved (without gauges)?
- What are the causes of the limitations (if any) of the PPR in the context of spin systems?

Paper 2

Simulation of the dynamics of many-body quantum spin systems using phase-space techniques
– *Ray Ng, Erik S. Sørensen, and Piotr Deuar*

Phys. Rev. B 88, 14430 (Editor's suggestion)

DOI: 10.1103/PhysRevB.88.144304

Calculations: I performed all stochastic simulations and produced half of the figures. Piotr Deuar carried out the extrapolation calculations and produced the figures that resulted from that numerical effort.

Manuscript: I wrote approximately 50% the manuscript and 50% of the figures. Erik S. Sørensen helped to refine and edit the paper.

In this publication, we set out to answer the following questions:

- Can the PP be reformulated using a spin coherent state basis?

Using the spin-1/2 transverse Ising model as a test system:

- What are the longest time scales, t_{life} that can be achieved (without gauges)?
- How does t_{life} depend on the parameters of the system?
- Can the extrapolation scheme further increase simulation lifetimes? And if so:
  - How much of an improvement can we achieve?

Paper 3

Quantum critical scaling of dirty bosons in two dimensions
– *Ray Ng and Erik S. Sørensen*

Phys. Rev. Lett. 114, 255701

DOI: 10.1103/PhysRevLett.114.255701

Calculations: I performed all simulations for the hardcore boson model and produced all the figures.

Manuscript: I wrote approximately 50% the manuscript and produced all the figures. The numerical simulations and results pertaining to the disordered quantum XY model were produced from an original SSE code that I had written myself. Erik S. Sørensen performed all simulations of the quantum rotor model. As such, we were each responsible for the portions of the manuscript addressing the results of our respective models.

In this publication, we set out to answer the following questions pertaining to the quantum rotor model and the hardcore boson model, in the presence of on-site disorder (without apriori assumptions on z in the simulations):

- Where are the exact locations of their critical points ?
- What values of z, ν and η do the models yield?
- Do both the critical exponents obtained from both models agree within errorbars?
- Do both independent models produce a value for ν that satisfies the (quantum) Harris criterion?
- Is Fisher's $z = d$ relation observed?

Contents

Thesis structure

This thesis aims to progress the field of condensed matter physics in vastly opposite areas, namely that of *non-equilibrium dynamics* and *equilibrium critical phenomena* using numerical means. As such, I saw it fitting to divide it into two parts. To optimize readability and coherence, I have also decided to write separate introductions for each area as opposed to writing a single comprehensive introduction section here. I would also like to state that this is a 'Sandwich' thesis and so the results can be found in the papers inserted *ad verbatim*.

The first part of this thesis is titled: ***Part I: Stochastic evolution equations for real time quantum spin quench dynamics*** and comprises of chapter 1 to chapter 3 and contains two publications. The premise of part I is the development and application of a real time simulation technique for spin systems, based on the positive-P representation (PPR). We use the paradigmatic transverse field Ising model as a test system in order to study the limits of the formalism and as a proof-of-concept.

In ***Chapter 1: An overview of non-equilibrium physics and its resurgence***, we first discuss the renewed interest in non-equilibrium phenomena by reviewing two key areas of the sub-field, namely the Kibble-Zurek mechanism and quantum thermalization. Although our research does not directly address these areas, I have nonetheless seen it fitting to include a brief review to convey the general research direction of both subfields. It provides the motivation for the timely development of a numerical tool for real time simulations, which is currently a very challenging problem.

In ***Chapter 2: The positive-P representation***, we introduce the PPR and provide explicit derivations of the formalism for both real and imaginary time evolution, and simulate the quench dynamics of 1D Bose-Hubbard model in the presence of harmonic confinement as an explicit example to elucidate the formalism. The details and results of our pioneering simulation of quantum spin dynamics however, can be found in the paper: ***'Exact real-time dynamics of quantum spin systems using the positive-P representation'*** in section 2.13 at the end of the chapter.

In ***Chapter 3: Spin coherent states***, we reformulate the PPR by switching the underlying basis to that of SU(2) spin coherent states. We further implement an extrapolation scheme (cf section 3.7) and an elaborate change of variables scheme (cf section 3.5) with the primary goal of extending simulation lifetimes. These overall results are showcased in our publication: ***'Simulation of the dynamics of many-body quantum spin systems using phase-space techniques'*** in section 3.8.

The second part of the thesis titled: ***Part II: Universality Class of the dirty-boson transition in 2d*** pertains to our numerical study of the Superfluid (SF)-Bose Glass (BG) transition in disordered bosonic models in 2d and covers our efforts to determine the highly debated value of the dynamical critical exponent: z.

In ***Chapter 4: The 'Dirty-Boson' problem***, we provide a review of the relevant results from scaling theory and discuss the existing controversy in the literature regarding value of z. We use large scale 2d QMC simulations on two independent disordered quantum models: (i) soft-core quantum rotors and (ii) hard-core bosons (HCB) to achieve this end. Because I was responsible for all results on the HCB, I decided to include the details of the Quantum Monte-Carlo technique used, i.e. the Stochastic Series Expansion (SSE) in ***Chapter 5: Quantum Monte-Carlo technique***. The SSE is discussed in the context of simulating HCB with disorder. Finally we present our results in

the article: ***'Quantum Critical Scaling of Dirty Bosons in Two Dimensions'*** included in section 5.7.

Having familiarised myself with the SSE and PPR, it only seemed natural to explore the possibilities of hybridizing the best features from each numerical techniques into a single algorithm. To this end, we document our ongoing research efforts in ***Chapter 6: QMC-SDE technique: a hybrid***.

This thesis is finally summarised in ***Chapter 6: Conclusion*** and a brief insight on its future direction is given.

Part I: Stochastic evolution equations for real time quench dynamics of quantum spin systems

CHAPTER 1

AN OVERVIEW OF NON-EQUILIBRIUM PHYSICS AND ITS RESURGENCE

1.1 A new numerical tool for non-equilibrium dynamics

The last decade has seen a renewed interest in the field of non-equilibrium physics owing to the feasibility of isolated non-equilibrium experiments afforded by ultra-cold atoms (Bloch, 2010). This has opened up the possibilities of testing long-standing theoretical phenomena, which heavily revolves around two areas (Dziarmaga, 2010, Polkovnikov et al., 2011). The first of these is the extension of the notion of universality, a concept that has its roots in equilibrium critical phenomena. In essence, this sets out to answer what is universal in regards to the non-equilibrium dynamics of a many-body system. Universality in this context is primarily addressed via the Kibble-Zurek Mechanism (KZM) (Kibble, 1976, Zurek, 1985) for defect generation. The second area deals with the thermalization of out-of-equilibrium isolated integrable and non-integrable quantum systems and the characterization of their long time asymptotic properties. The conditions under which a quantum mechanical system thermalizes are important areas of research. In particular, for certain non-integrable models, the conjecture known as the eigenstate thermalization hypothesis (ETH) (Srednicki, 1994) is the widely accepted mechanism behind quantum thermalization. Interestingly, integrable systems can also be shown to relax to the predictions of a generalized Gibbs ensemble (GGE) (Rigol et al., 2007a). While we have only briefly introduced these two areas an extended discussion can be found in the later parts of section 1.1.1 and section 1.1.2.

The investigation of non-equilibrium phenomena however requires a simulation technique that is capable of accurately producing the real time dynamics of a quantum system which is a notoriously

difficult problem since real time non-equilibrium simulations in general, require knowledge of the entire Hilbert space which grows exponentially with system size. In light of the rapid advances in this field, there is now more than ever a demand for such novel numerical techniques particularly in strongly-correlated quantum models. Several methods exist but each have their own limitations. Specifically for one-dimensional systems, the time-dependent density matrix renormalization group (tDMRG) (Daley et al., 2004, Schollwöck, 2005, White, 1992) and time-evolved block decimation (TEBD) methods (Zwolak and Vidal, 2004, Vidal, 2003, 2004) while highly efficient only last for relatively short simulation life times. In higher dimensions, the typical numerical methods used are exact diagonalization (ED) (Lin, 1990, Caffarel and Krauth, 1994) and numerical link-cluster expansions (NLCE) (Rigol, 2014), both of which are however limited to small system sizes. As a viable alternative, we turn our attention to the quantum phase space method known as the positive-P representation (PPR) (Drummond and Gardiner, 1980, Drummond, 2013).

The PPR is an **exact** quantum phase space method that was originally developed to simulate the real time dynamics of few-mode problems (McNeil and Craig, 1990, Smith and Gardiner, 1989, Plimak et al., 2001) in quantum optics. In essence, the quantum dynamics of the system is mapped on to $\sim N$ coupled classical fields obeying stochastic Langevin-type equations, where N is the size of the system. This vast improvement over the typical exponential scaling in CM problems is a very appealing feature of this technique. A brute-force approach by way of exact diagonalization (ED) for instance, while exact can only handle systems up to $N \sim 40$. Results thus obtained while capable of providing insight into strongly-correlated phenomena are not an ideal representation of the thermodynamic limit.

A major triumph of the PPR was achieved in 2007 through a pioneering work by Deuar et al (Deuar and Drummond, 2007) and has since shifted the focus of its application to many-body systems (Deuar et al., 2009, Midgley et al., 2009) particularly in dilute Bose-Einstein condensates (BECs). Deuar et al successfully simulated the 'Halo effect' in momentum space resulting from the collision of two weakly interacting three-dimesional BECs of nearly $\sim 150{,}000$ atoms. This 'Halo Effect' refers to the preferential scattering of particles into a spherical shell in momentum space of radius roughly equal to the colliding velocity. While this was observed much earlier on in experiments (Vogels et al., 2002) (see fig. 1.1), numerical treatments of BECs relied heavily on approximate schemes using the mean-field Gross-Pitaevskii Equation (GPE) (Dalfovo et al., 1999) and the semi-classical phase space method, Truncated Wigner Approximation (TWA) (Norrie et al., 2005). The GPE does not take quantum depletion into consideration and is therefore unable to simulate spontaneous scattering altogether. For the parameters of the simulation chosen, the TWA on the other hand produced clearly unphysical results, i.e. negative density of particles at larger velocities and a fictitious enhancement of particle density at the lower velocities. This is attributed to an artificial seeding of half a virtual particle per mode in the initial conditions to model quantum fluctuations as is typical in TWA simulations (Norrie et al., 2005, Sinatra et al., 2002). Surprisingly, the stochastic equations derived from the PPR bore a striking resemblance to the GPE, and only required the inclusion of independent white noise terms to reproduce the exact quantum dynamics of the colliding BECs. Fig 1.1 shows a comparison between experimental images (albeit for different parameters) and the simulation results using the PPR.

In addition to real time simulations, the versatility of the PPR was further demonstrated in simulating the imaginary-time dynamics as a possible alternative to conventional Monte-Carlo approaches. This

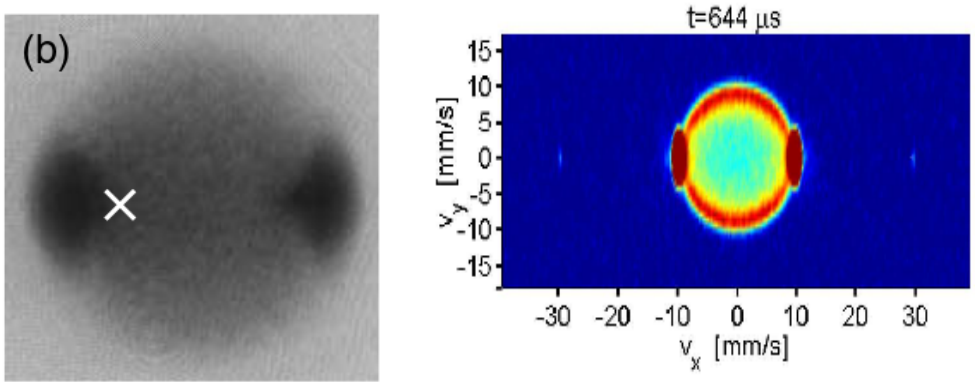

(a) Absorption imaging of velocity distribution taken from (Vogels et al., 2002)

(b) Full PP quantum dynamics taken from Deaur et al (Deuar and Drummond, 2007)

Figure 1.1: 'Halo effect' resulting from collision of two BECs.s

was carried out using the gauge-P representation (Deuar and Drummond, 2002), an extension of the PPR which entails the incorporation of an additional weight variable. Using the gauge-P, both the imaginary time evolution of the two point correlation functions in the 1D BH model (Ghanbari et al., 2010) and a 1D weakly interacting dilute bose-gas (Deuar et al., 2009) were simulated.

The PPR shows promise as a potential state-of-the-art numerical technique and leads one to wonder if it can be applied to strongly correlated quantum systems as well. In addition, it appears insensitive to the effects of frustration and unconstrained by the dimensionality of the system, both of which are afflictions of Quantum Monte Carlo (QMC) techniques (Henelius and Sandvik, 2000, Sandvik, 2010) and the DMRG (White, 1992) respectively. Surprisingly, its applicability to quantum simulations of spin systems had not been deeply explored. Given the resurgence of the field of non-equilibrium dynamics, it seemed timely to engage in a detailed study on the practical application of the PPR, details of which will comprise chapter 2. Before proceeding however, we shall survey the field of non-equilibrium dynamics by reviewing both the Kibble-Zurek Mechanism (KZM) and the notion of thermalization in quantum systems using select results in the literature to provide further insight on this exciting field. In order to not mislead the reader, I would like to highlight that the remainder of this chapter is purely pedagogical and the familiar reader can instead skip to chapter 2 for a direct introduction to the positive-P representation, which is the main numerical tool used in part I of this thesis.

1.1.1 Universality: Kibble-Zurek Mechanism

The Kibble-Zurek mechanism describes non-equilibrium dynamics and topological defect generation as a system passes through a continuous critical point at a finite rate. It was originally developed by Kibble (Kibble, 1976) to study domain structure formation in the early universe but later generalized to condensed matter systems by Zurek (Zurek, 1985).

Classical Kibble-Zurek mechanism

First let us derive the key result for the classical KZM (Kibble, 2007, Zurek, 1985). To this end, we consider a simple linear quench experiment, in which a system is swept through its finite temperature critical point, T_c with a quench velocity v. The temperature varies linearly as:

$$T = T_c - vt, \tag{1.1.1}$$

where $t \in (-\infty, \infty)$ represents real time and T is the instantaneous temperature of the system. In this experiment there exist two time scales, the time to reach the critical point: $t' = |T - T_c|/v$ and the relaxation time, which scales as: $t_{rel} \sim 1/|T - T_c|^{z\nu}$ where ν represents the critical exponents for the spatial correlation length and z the dynamic critical exponent. When $t' \gg t_{rel}$, the system is adiabatic and has sufficient time to equilibrate to the changes in the Hamiltonian. It therefore remains in equilibrium in this regime. On the other hand when $t' \ll t_{rel}$, the system is diabatic and the formation of topological defects or excitations can occur. In light of this, there exists a time scale, t^* at which a crossover from adiabatic to diabatic behaviour occurs. This can be obtained by equating t_{rel} and t' to yield the scaling relation:

$$t^* \sim v^{-\frac{z\nu}{z\nu+1}} \tag{1.1.2}$$

and in turn an expression for a corresponding length scale:

$$\xi^* \sim (t^*)^{1/z} \sim v^{-\frac{\nu}{z\nu+1}}. \tag{1.1.3}$$

This distance also represents the average separation between defects and as such immediately gives us the expression for the defect density:

$$n_{ex} = (\xi^*)^{-d} \sim v^{\frac{d\nu}{z\nu+1}}, \tag{1.1.4}$$

which is the celebrated expression characteristic of the KZM, that relates the defect density, n_{ex} in a linear quench to the quench velocity, v and the system's equilibrium critical exponents, ν and z that are associated with its spatial correlation length and characteristic energy gap.

Quantum Kibble-Zurek mechanism

Interestingly, this universal scaling carries over to the quantum regime as well, albeit using different arguments. Insight for the quantum case can be easily achieved by generalizing the results from a Landau-Zener (Zener, 1932, Majorana, 1932) analysis of a driven two-level quantum system, described by the Hamiltonian:

$$\hat{H} = g(t)\hat{\sigma}_z + \Delta\sigma_x, \tag{1.1.5}$$

where $g(t) = vt$ is a time-dependent splitting of the energy level and Δ is the excitation gap. The central result we will use is the expression for the excitation probability, i.e. the probability of a transition to the excited state at $t \to \infty$, starting from the ground state at $t \to -\infty$, which can be shown to be:

$$p_{ex} = e^{-\pi\gamma}, \tag{1.1.6}$$

where $\gamma = \Delta^2/v$ is called the Landau-Zener parameter. We see that when $\gamma \gg 1$, the system remains in it ground state, whereas when $\gamma \ll 1$, a transition to the excited state that is equivalent to defect generation occurs. We can again quantify the crossover from adiabatic to diabatic regimes as taking place when $\gamma \approx 1$. For a generic quantum phase transition, we can generalize this condition (using dimensional arguments) to:

$$\frac{d\tilde{\Delta}}{dt} \approx \tilde{\Delta}^2, \tag{1.1.7}$$

were $\tilde{\Delta}$ is a characteristic energy scale and $\frac{d\tilde{\Delta}}{dt}$ is the rate of change of this energy scale. Interestingly, this result has recently been reformulated using the adiabatic-impulse approximation (Damski, 2005) although this is not the route we have taken. In the event that the system crosses a QCP generically located at $\lambda = \lambda_c$ where λ is the tuning parameter, the characteristic energy scale is instead given by the energy gap which obeys the scaling relation:

$$\tilde{\Delta}(\lambda) \sim |\lambda - \lambda_c|^{-z\nu}. \tag{1.1.8}$$

Once again assuming a linear quench with velocity, v, such that $\lambda(t) = \lambda_c + vt$, we can write:

$$\tilde{\Delta}(t) \sim |vt|^{z\nu}, \tag{1.1.9}$$

which relates the gap via a scaling relation of its velocity and time. Via a simple substitution of eq. 1.1.9 into eq. 1.1.7, we can solve for the energy scale at which adiabaticity breaks down, i.e.

$$\tilde{\Delta}^* \sim |v|^{\frac{z\nu}{z\nu+1}} \tag{1.1.10}$$

and the corresponding length scale as well:

$$\xi^* \sim |v|^{-\frac{\nu}{z\nu+1}}. \tag{1.1.11}$$

Noting that the defect density scales as: $n_{ex} \sim (\xi^*)^{-d}$ we obtain the quantum KZM (Polkovnikov, 2005, Zurek et al., 2005) result:

$$n_{ex} \sim |v|^{\frac{d\nu}{z\nu+1}}, \tag{1.1.12}$$

which is identical to the classical result. It is important to note that in both cases, the KZM of eq. 1.1.12 and eq. 1.1.4 is not an exact equality but only an estimate of the order of magnitude. What is most intriguing about it is the appearance of power law exponents that are universal quantities.

Extensions of the KZM

The KZM is indeed a remarkable result where the controlled quench dynamics of the model can give insight to its equilibrium properties. We have thus far only covered the result of the bare KZM and other extensions do exist. It is possible for instance to take the effects of inhomogeneities in the system into consideration. This is of particular importance for an honest comparison with ultra-cold atoms (Lamporesi et al., 2013, Chen et al., 2011, Navon et al., 2015) and trapped ions (Ejtemaee and Haljan, 2013, Ulm et al., 2013, Pyka et al., 2013) experiments where the effects of inhomogeneous trap geometries (del Campo and Zurek, 2014, del Campo et al., 2013) have to be considered. For a linear temperature quench in a 2D BEC, the modifications to the generic KZM scaling for homoge-

neous, harmonic (del Campo et al., 2011) and toroidal confinement (Zurek, 2009) are summarized in table 1.1.

	Homogenous	Harmonic	Toroidal
Scaling (n)	$\frac{2\nu}{1+\nu z}$	$\frac{2(1+2\nu)}{1+\nu z}$	$\frac{1+3\nu}{1+\nu z}$

Table 1.1: KZM scaling for the density of vortices ascribing to different trap geometries for the cooling of a 2D BEC: $n_{ex} \sim v^n$, where n are the exponents detailed in the table.

For a more general, non-linear quench protocol that varies the tuning parameter as:

$$\lambda(t) \sim \lambda_c \pm v|t|^r, \tag{1.1.13}$$

Polkovnikov et al (De Grandi et al., 2010) were able to derive the following modifed KZM:

$$n_{ex} \sim |v|^{\frac{d\nu}{(z\nu r+1)}}, \tag{1.1.14}$$

by examining scaling relations for the adiabatic fidelity: $F(t) = |\langle\psi(t)|\psi_{gs}(t)\rangle|$, where $|\psi_{gs}(t)\rangle$ is the instantaneous ground state of the system and $|\psi(t)\rangle$ is the instantaneous wavefunction at time t. Note that the result for a linear quench is correctly reproduced upon setting $r = 1$. Interestingly, the heuristic arguments of section 1.1.1 can be used to derive the result of eq. 1.1.14 as well.

In general, the defect density can be a difficult quantity to measure. To this end, other analogous relations for more accessible physical quantities have also been derived, an obvious example of this is the energy of the system. More precisely, excess heat is guaranteed to be generated from a general quench as in eq. 1.1.13 as the QCP is crossed. For a quench that ends close to the critical point (De Grandi et al., 2010), this quantity has been shown to scale as:

$$Q \sim |v|^{\frac{(d+z)\nu}{z\nu r+1}} \tag{1.1.15}$$

Likewise, the entropy is also expected to increase when adiabaticity breaks down in the vicinity of the QCP. In the weakly interacting limit, the relation between the entropy and the energy is known and can just as easily be measured. While the Von-Neumann entropy: $S = -\mathrm{Tr}(\hat{\rho}\ln\hat{\rho})$ is conserved for unitary evolution, the diagonal entropy (Polkovnikov, 2005) which is defined by the relation:

$$S_d = -\sum_n \rho_{nn} \ln \rho_{nn}, \tag{1.1.16}$$

proliferates when adiabaticity breaks down. This quantity has been shown to obey the same scaling relation as the defect density in eq. 1.1.14.

Detection of the KZM

Several experiments have verified the KZM, mostly in classical phase transitions. Examples of which include the scaling of defect formation in multiferroics samples of rare earth compounds such as

$ErMnO_3$ (Chae et al., 2012), proliferation of solitons in thermal BECs (Damski and Zurek, 2010, Witkowska et al., 2011) and the formation of kinks in coulombic crystals (Dubin and O'Neil, 1999, Ejtemaee and Haljan, 2013, Pyka et al., 2013, Cormick and Morigi, 2012, del Campo et al., 2010) to name a few.

Testing the KZM in quantum systems however is more challenging due to complications of inhomogeneities and small system sizes (del Campo et al., 2013). Recently, a quench experiment has been performed on the generic transition in the SF-MI transition of the 1D BH model (Chen et al., 2011) using a gas of ^{87}Rb atoms trapped in an optical lattice. In this study, they use time-of-fight (TOF) imaging to retrieve the density profile of the expanding gas and calculated its deviation from a smooth Thomas-Fermi (TF) profile, as a measure of excitations, denoted by $\tilde{\chi}^2$. While they did indeed observe power law scaling with quench rate, they measured an exponent of $\alpha_{exp} = 0.31 \pm 0.03$ instead, contrary to the expected exponent: $\alpha_{MF} = 0.75$. The latter result is consistent with the universality class of the generic MI-SF crossing of the 1D BH model that has exponents $(\nu, z) = (\frac{1}{2}, 2)$. A possible explanation for this discrepancy among others is decoherence brought about by finite temperature effects, since the experimental condensate was noted to have a significant normal fraction of $\sim 10\%$ (del Campo et al., 2013).

In the presence of disorder, deriving a modified expression for the KZM, is not usually possible. Rare exceptions include disordered 1D spin chains where a logarithmic scaling is obtained instead (Dziarmaga, 2006, Caneva et al., 2007). To elucidate the KZM in a general disordered system, a recent quench experiment on the Superfluid (SF)- Bose Glass (BG) transition (Meldgin et al., 2015) of a 3D disordered Bose-Hubbard model (using ^{87}Rb atoms) was performed. A similar analysis as the experiments of del Campo et al showed a variation of $\tilde{\chi}^2$ with quench velocity that was too slight to detect and instead the excess heat was used. Indeed a power law scaling, indicative of a KZM was observed as opposed to a logarithmic one. The observed power scaling is a novel result that has yet to be reproduced numerically as well

1.1.2 Thermalization in integrable and non-integrable quantum systems

We now turn our attention to the thermalization of quantum system which is another focus of non-equilibrium dynamic research. As a definition, when an ***isolated*** system that is initially out-of-equilibrium relaxes to a state that can be described by a standard statistical ensemble, e.g. canonical, microcanonical, etc, we say that is has thermalized or that thermalization has occurred. We refer to a system as integrable if there exists additional constants of motion other than its energy. Typically, quantum integrable models can also be diagonalized using an appropriate basis choice and are therefore exactly solvable. Non-integrable systems however only conserve energy. In general, the conventional expectation is that thermalization only occurs in non-integrable systems and not in integrable ones.

1.1.3 Non-integrable models: the Eigenstate-thermalization hypothesis (ETH)

In classical systems, generic thermalization has its roots in dynamical chaos, which in turn implies ergodicity (Kardar, 2007); This can be neatly summarized by the expression (Polkovnikov et al.,

2011):

$$\overline{\delta(X - X(t))} \equiv \lim_{T\to\infty} \frac{1}{T}\int_0^T dt\delta(X - X(t)) = \rho_{mc}(E), \tag{1.1.17}$$

where X is a point in phase space and $\delta(.)$ is a dirac-delta function. Eq. 1.1.17 states that that the long time average of the set of phase space points, X, visited by dynamic trajectory of the system, $X(t)$, will uniformly cover the constant energy (E) hypersurface essentially mapping out a density of states that is reflective of the microcanonical ensemble, $\rho_{mc}(E)$. As a result, the long time averages of a generic observable, $\hat{A}$ will likewise match the ensemble averages of the microcanonical distribution, $\rho_{mc}(E)$ i.e.:

$$\bar{A}(t) = \langle A\rangle_{mc}. \tag{1.1.18}$$

The conventional wisdom is that non-integrable systems thermalize and while this generalization applies to quantum mechanical systems as well and has indeed been observed, the underlying mechanism necessarily differs. It is after all strange to attribute cause of thermalization to dynamical chaos given that quantum mechanical time evolution, governed by the Schrodinger equation, is linear. To address this paradox, a possible mechanism for quantum thermalization was conjectured by Schrednicki (Srednicki, 1994, Deutsch, 1991) known as the eigenstate thermalization hypothesis (ETH), which we will elucidate for a general quantum system. In (Srednicki, 1994), the ETH was used in tandem with Berry's conjecture (Berry and Keating, 1999)[1] to reproduce the Maxwell-Boltzmann distribution for a box of particles with hard-sphere constraints. Taking Bose and Fermi statistics into consideration, Srednicki was further able to reproduce the expected, Bose and Fermi distributions as well.

Formulation of the ETH

Let us consider a non-degenerate, isolated quantum system that is bounded and described by the Hamiltonian, $\hat{H}$, such that $\hat{H}|\alpha\rangle = E_\alpha|\alpha\rangle$, where $\{|\alpha\rangle\}$ are complete orthonormal energy eigenstates with eigenvalue spectrum: $\{E_\alpha\}$. We also consider ***generic*** initial states defined by the usual superposition of basis states:

$$|\psi(0)\rangle = \sum_\alpha C_\alpha|\alpha\rangle, \tag{1.1.19}$$

where $\sum_\alpha |C_\alpha|^2 = 1$ but subject to the key additional constraint that its distribution is sufficiently narrow in energy with a quantum uncertainty:

$$\Delta E \equiv \sqrt{\langle E^2\rangle - \langle E\rangle^2\rangle} \ll \langle E\rangle, \tag{1.1.20}$$

that vanishes in the limit that the linear size of the system L goes to infinity. Such generic initial states can be easily prepared experimentally as well. Naturally, the time-evolved quantum state, $|\psi(t)\rangle$ obeys Schrodinger's equation:

$$|\psi(t)\rangle = \sum_\alpha C_\alpha e^{-i\frac{E_\alpha t}{\hbar}}|\psi_\alpha\rangle. \tag{1.1.21}$$

[1] In (Srednicki, 1994), Berry's conjecture states that each eigenfunction of chosen basis appears to be a superposition of plane waves with random phase and Gaussian random amplitudes with fixed wavelengths. It is believed to hold for quantum systems which exhibit classical chaos in all or at least most of classical phase space.

We are now ready to explore the possibility of quantum thermalization but from the perspective of "special" observables, $\hat{A}$. There is no clear distinction as to what observables are considered "special" but typically they are physically relevant and experimentally measurable, an example being the magnetization in spin systems or the momentum distribution of bosons. It is further worth mentioning that eq. 1.1.20 originates from the condition that

$$(\Delta E)^2 \left| \frac{A''(E)}{A(E)} \right| \ll 1, \tag{1.1.22}$$

where $A(E)$ is a smooth function of energy (Srednicki, 1994). The latter is true if we make the additional assumption that the difference between the neighboring elements: $A_{\alpha+1,\alpha+1} - A_{\alpha\alpha}$ are exponentially small in L (Rigol and Srednicki, 2012) so that $A_{\alpha\alpha}$ is indeed a smooth function of E_α with small eigenstate-to-eigenstate fluctuations.

Now for thermalization to occur, analogous to the classical case, we expect the following equivalence of the time average of the observable $\overline{A}$ with the predictions of the quantum microcanonical ensemble: $\rho_{Q,mc}(E)$, analogous to eq. 1.1.18. To see how this may arise, let us first evaluate the long time average of the expectation value of $\bar{A}$:

$$\begin{aligned}
\overline{A} &\equiv \frac{1}{T} \lim_{T\to\infty} \int_0^T \langle A(t) \rangle dt && (1.1.23)\\
&= \frac{1}{T} \lim_{T\to\infty} \int_0^T \left[\sum_{\alpha,\beta} C_\alpha^* C_\beta A_{\alpha\beta} e^{-i(E_\alpha - E_\beta)t/\hbar} \right] dt && (1.1.24)\\
&= \sum_\alpha |C_\alpha|^2 A_{\alpha\alpha} + i\hbar \lim_{T\to\infty} \sum_{\alpha\neq\beta} \left[\frac{C_\alpha^* C_\beta A_{\alpha\beta}}{E_\beta - E_\alpha} \left(\frac{e^{-i(E_\beta - E_\alpha)T/\hbar} - 1}{T} \right) \right] && (1.1.25)\\
&= \sum_\alpha |C_\alpha|^2 A_{\alpha\alpha}. && (1.1.26)
\end{aligned}$$

The final expression is referred to in the literature as the expectation of the *diagonal ensemble* and is exact as long as the cross terms can be safely ignored. Interestingly, we see that time plays a different role in classical and quantum systems. Due to the chaotic origins in classical systems, time constructs the thermal state as it maps out the energy hypersurface. In QM systems however, time serves to reveal the quantum state as the cross terms in eq. 1.1.25 vanish. However, eq. 1.1.26 is not solely due to temporal dephasing. Let us look more closely at the second term in eq. 1.1.25. using L'hopital's rule to evaluate the limit we note that:

$$i\hbar \lim_{T\to\infty} \sum_{\alpha\neq\beta} \left[\frac{C_\alpha^* C_\beta A_{\alpha\beta}}{E_\beta - E_\alpha} \left(\frac{e^{-i(E_\beta - E_\alpha)T/\hbar} - 1}{T} \right) \right] = \lim_{T\to\infty} \sum_{\substack{\alpha,\beta \\ \alpha\neq\beta}} \left[C_\alpha^* C_\beta A_{\alpha\beta} e^{-i(E_\beta - E_\alpha)T/\hbar} \right], \tag{1.1.27}$$

where we have taken the derivative with respect to T in the numerator and denominator of the cross terms. Following the arguments of (Rigol et al., 2008), we note that the dephasing factors only scale as the square root of the number of terms, then $\sum_{\alpha,\beta;\alpha\neq\beta} e^{i(E_\alpha - E_\beta)T/\hbar} \sim \sqrt{N_b^2}$, where N_b is the number of basis states. Furthermore, assuming that the initial state has a finite overlap with a substantial number of eigenstates of the final Hamiltonian (as is usually the case), then the typical

overlap amplitude $C_\alpha \sim 1/\sqrt{N_b}$. Taken together then, we see that

$$\sum_{\substack{\alpha,\beta \\ \alpha \neq \beta}} \left[C_\alpha^* C_\beta A_{\alpha\beta} e^{-i(E_\beta - E_\alpha)T/\hbar} \right] \sim \sqrt{N_b^2} \frac{1}{N_b} A_{\alpha\beta}^{\text{typical}} \tag{1.1.28}$$

$$= A_{\alpha\beta}^{\text{typical}}, \tag{1.1.29}$$

where $A_{\alpha\beta}^{\text{typical}}$ is the typical value of an off-diagonal element. We therefore see that it is necessary to make the additional assumption that:

$$A_{\alpha\beta}^{\text{typical}} \ll A_{\alpha\alpha}^{\text{typical}} \tag{1.1.30}$$

to obtain the diagonal ensemble result of eq. 1.1.26. There is indeed strong numerical evidence for this condition to be true (Rigol et al., 2008).

The microcanonical ensemble on the other hand requires that for an energy window: $I(E) \equiv [\langle E \rangle - \Delta E, \langle E \rangle + \Delta E]$, the expectation value is given by:

$$\langle A \rangle_{Q,mc} = \frac{1}{N'} \sum_{\alpha : E_\alpha \in I} A_{\alpha\alpha} \tag{1.1.31}$$

where N' is the number of states in the interval $I(E)$. Thermalization requires the agreement of eq. 1.1.26 and eq. 1.1.31, so that:

$$\sum_{\alpha : E_\alpha \in I} |C_\alpha|^2 A_{\alpha\alpha} = \frac{1}{N'} \sum_{\alpha : E_\alpha \in I} A_{\alpha\alpha} \tag{1.1.32}$$

However, eq. 1.1.32 appears to be paradoxical. The LHS of eq. 1.1.32 depends on the initial conditions through the coefficients: $\{C_\alpha\}$, while the RHS of eq. 1.1.32 only depends on $\langle E \rangle$, which could be the same for different sets of $\{C_\alpha\}$. In order for this to be true, the most likely possibility is that $A_{\alpha\alpha}$ is roughly constant for eigenstates that are close in energy, i.e. in the energy interval (although non-generic possibilities can also arise (Rigol and Srednicki, 2012)), in which case eq. 1.1.32 is justified since we can now rewrite it as

$$A_{\alpha\alpha} \sum_{\alpha : E_\alpha \in I} |C_\alpha|^2 = \frac{1}{N'} A_{\alpha\alpha} \sum_{\alpha : E_\alpha \in I} 1 \tag{1.1.33}$$

$$A_{\alpha\alpha} = \frac{1}{N'} A_{\alpha\alpha} N', \tag{1.1.34}$$

where $A_{\alpha\alpha}$ represents a typical value in the interval $I(E)$. In addition, it is also necessary to show that temporal fluctuations are small. This can be quantified by the formula:

$$\overline{(A_t - \bar{A})^2} \equiv \lim_{T \to \infty} \frac{1}{T} \int_0^T (A_t - \bar{A})^2 dt, \tag{1.1.35}$$

which can be explicitly evaluated to be:

$$\overline{(A_t - \bar{A})^2} = \sum_{\alpha \neq \beta} |C_\alpha|^2 |C_\beta|^2 |A_{\alpha\beta}|^2. \tag{1.1.36}$$

This condition is guaranteed by the second assumption of the ETH in eq. 1.1.30 that was earlier mentioned, providing further evidence that the observable is indeed well described by its microcanonical ensemble and therefore thermal. To summarise, the ETH tells us that thermalization in quantum systems generically happens at the level of individual eigenstates such that:

$$A_{\alpha\alpha} = \langle A \rangle_{Q,mc}(E_\alpha) \forall \alpha \in I(E). \tag{1.1.37}$$

Additionally, this can only occur for initial states that are sufficiently narrow in energy so that eq. 1.1.20 is satisfied.

Review of literature

The ETH is a widely accepted paradigm responsible for quantum thermalization and has been shown to hold for a number of non-integrable systems (Rigol et al., 2008, Rigol, 2009a,b, Santos and Rigol, 2010b,a). In particular, the pioneering work of Rigol et al (Rigol et al., 2008) elegantly demonstrated the validity of the ETH in a system of 2D network of hardcore bosons with weak nearest-neighbour repulsion after a quench using exact diagonalization. Details of the geometry and the quench protocol can be found in (Rigol et al., 2008). The measured observable was the asymptotic momentum distribution and was shown to conform unequivocally with the predictions of the ETH.

It does however beg the question on its limitations, in particular, does the ETH hold for near-integrable (albeit marginally non-integrable) systems as well, or is there a threshold amount of non-integrability that has to be present? This line of research was primarily motivated by the ground breaking experiments of Kinoshita et al (Kinoshita et al., 2006), where the near ideal realization of the integrable Lieb-Liniger gas with point-like collisions, failed to thermalize even after thousands of collisions, thereby behaving like a quantum Newton's cradle. Despite the pristine nature of optical lattice experiments, experimental imperfections such as anharmonicities or the axial trap potential ensures that the system is only nearly-integrable. However contrary to expectation, these effects were unable to bring about thermalization. To address this, let us consider a quench experiment that mimics the conditions of the experiments of Kinoshita et al. Let us introduce an integrable quantum system (with a tunable parameter, λ, such as the strength of an external field) that is made non-integrable by explicitly introducing integrability-breaking terms, whose strength can be parametrized by the parameter, λ_2. In this scenario, one can then as the question: "Is the ETH satisfied for arbitrarily small λ_2 or does a threshold strength: $\lambda_{2,c}$ exist before integrability is restored?".

The numerical experiments on a system of integrable 1D HC bosons by Rigol et al (Rigol, 2009a) were aimed at elucidating the nature of this phenomena. To this end, integrability breaking terms taking the form of next-nearest neighbour (NNN) interactions terms, quantified by the tunnelling and potential energy parameters (t', V'), were added. When $(t', V') = (0, 0)$, the system is perfectly integrable. Using the long-time momentum distribution as the measured observable, the breakdown of the ETH was quantified by calculating the difference between the predictions of the diagonal

ensemble and the ETH for a series of instantaneous quenches of the NN parameters: $(t_{ini}, V_{ini}) \rightarrow (t_{final}, V_{final})$ with different values of (t', V'). The deviations were observed to become appreciable once $t' = V' < 0.1$ signifying the absence of thermalization.

To further pin down the breakdown of the ETH, the distribution of $n(k=0)_{\alpha,\alpha}$ versus energy E_α was studied. Recall that the ETH requires it to be smooth with minimal fluctuations between adjacent states. Close to integrability $(t' = V' = 0.03)$, it was indeed observed that state to state fluctuations of $n(k=0)_{\alpha,\alpha}$ were noticeably large for the entire spectrum and thermalization is absent. Far from integrability $(t' = V' = 0.24)$ however, there exists an extended region where the fluctuations are suppressed in addition to a region with large fluctuations. Naturally the farther away the system is from integrability, one would expect the suppressed fluctuation region to grow, suggesting that there exists a smooth crossover to thermalization. However since the numerical experiments were performed using exact diagonalizaton, it is possible that this smooth crossover is a finite-size effect. It would be interesting to investigate how this behaviour scales with system size and if thermalization will occur for a sufficiently large system arbitrarily close to the the integrable point or if a sharp cut-off exists at some finite critical value.

Recently, a similar study on quantum spin chains, more specifically the spin-1/2 Heisenberg model have reached similar conclusions within the limitations of small system sizes as well (Steinigeweg et al., 2013). In this study, next-nearest neighbor (NNN) Ising interaction terms: $\left\{S_i^z S_{i+2}^z\right\}$ were used to break integrability instead. Other measures of identifying the breakdown of ETH include observing the crossover of level-spacing statistics of the eigen spectrum from Poisson to Wigner-Dyson statistics in the integrable and non-integrable limits (Rabson et al., 2004).

1.1.4 Integrable systems: the generalized Gibbs ensemble (GGE)

Thus far, our definitions of thermalization have relied on the standard statistical mechanic ensembles as a measure. In that sense, integrable systems do not thermalize. It is then reasonable to ask: Does there exist some other ensemble that the system can equilibrate to? An example of such an ensemble is the generalized Gibbs ensemble (GGE). To derive this ensemble, we follow the standard prescription of statistical mechanics that one should maximize the entropy:

$$S = k_B T \mathrm{Tr}\left[\rho \ln(1/\rho)\right], \tag{1.1.38}$$

(where k_B is Boltzmann's constant) but take into consideration all the integrals of motion of the model: $\{J_m\}$. This yields the GGE:

$$\hat{\rho} = Z^{-1} e^{-\sum_m \lambda_m \hat{J}_m}, \tag{1.1.39}$$

where $Z = \mathrm{Tr}\left[-\sum_m \lambda_m \hat{J}_m\right]$ and the set $\{\lambda_m\}$ are Lagrange multipliers that are determined by the initial condition: $\mathrm{Tr}\left[\hat{J}_m \hat{\rho}\right] = \langle \hat{J}_m \rangle (t=0)$. If only the energy is conserved, such that $\hat{J}_1 = \hat{H}$ then we obtain the canonical ensemble as expected.

Using the GGE, Rigol (Rigol et al., 2007b) et al correctly calculated the asymptotic momentum distribution of a completely integrable system of 1d HC bosons by performing two numerical quench experiments with different initial conditions. In the first experiment, the system is prepared in the ground state of the box of size L, which is then abruptly brought out of equilibrium by a sudden increase to $L' > L$. As expected, the grand-canonical ensemble was incapable of predicting the

momentum distribution of the relaxed state, but instead showed excellent agreement with the fully-constrained GGE. The second experiment closely mimicked the experiments of Kinoshita (Kinoshita et al., 2006) et al and initialized in a quantum superposition of opposite momentum states. In particular, the well-defined peaks in the initial momentum distribution were seen to persist throughout the simulations, instead of degrading into a single Gaussian distribution, as would be expected for a thermal system. Remarkably, the GGE was able to capture the resilience of the initial momentum distribution, a feature absent when using standard ensembles. The mechanism responsible for the applicability of the GGE in integrable system was conjectured to take the form of a generalized-ETH (GETH) (Cassidy et al., 2011). A general microcanonical ensemble (GME) was created using eigenstates with expectation values of conserved currents (instead of energy as in the standard ME), i.e.

$$\langle A\rangle_{GME} \equiv \frac{1}{N_{J'_m}} \sum_{\alpha: J_{m,\alpha\alpha}\in I'} A_{\alpha\alpha}, \tag{1.1.40}$$

fell within a certain window, $I' = [\langle J_m\rangle_o - \delta_{GME}, \langle J_m\rangle_o + \delta_{GME}]$, where $\langle J_m\rangle_o$ is the initial expectation of the conserved charge and δ_{GME} is variable window [2]. This approach showed impressive agreement with the expectation values of a diagonal ensemble and GGE (Cassidy et al., 2011). Yet there are instances where the GGE is known to fail. The GGE for instance is incapable of predicting the asymptotic state for a generic non-translationally invariant initial state (Caneva et al., 2011). The quench of an anisotropic spin-1/2 Heisenberg chain (Wouters et al., 2014) and spin-1/2 XXZ chain (Pozsgay, 2014, Pozsgay et al., 2014, Goldstein and Andrei, 2014), also show a similar discrepancy that has been attributed to a breakdown of the GETH. One possible explanation is that local conserved charges have typically been used to construct the GGE and it has been suggested that a GGE incorporating non-local charges may be necessary (Mierzejewski et al., 2014).

[2] The actual criteria used to construct the GME is actually more involved and the reader is encouraged to refer to (Cassidy et al., 2011) for technical details.

CHAPTER 2

THE POSITIVE-P REPRESENTATION

2.1 Quantum phase space methods: Wigner representation

Quantum phase space techniques are designed to provide a classical interpretation of quantum mechanics by mapping quantum degrees of freedom onto equivalent classical phase space variables. A notable example of such a technique is the pioneering semi-classical Wigner representation (Wigner, 1932, Moyal, 1949) which we will briefly outline to provide a general idea of phase space techniques. The Wigner representation begins by mapping the quantum density operator, $\hat{\rho} = |\psi\rangle\langle\psi|$, onto a phase space distribution using the transformation:

$$f_W(\vec{q},\vec{p}) = \int d\vec{s} e^{\frac{i\vec{p}.\vec{s}}{\hbar}} \langle \vec{q} - \frac{\vec{s}}{2}|\psi\rangle\langle\psi|\vec{q} + \frac{\vec{s}}{2}\rangle, \tag{2.1.1}$$

where $\vec{p}$ and $\vec{q}$ are momentum and position states and $f_W(\vec{q},\vec{p})$ is called the Wigner distribution, that is reminiscent of a joint probability distribution of $\vec{p}$ and $\vec{q}$. Using this basis, we now have a $D = 6N$-dimensional continuous phase space spanned by the variables $\{\vec{p},\vec{q}\}$. A strong case for interpreting f_W as a joint probability distribution can be made if we evaluate the marginal distributions of eq. 2.1.1 individually to yield

$$\int \frac{dp}{(2\pi\hbar)^{D/2}} f_W(q,p) = |\psi(q)|^2 \tag{2.1.2}$$

and

$$\int \frac{dq}{(2\pi\hbar)^{D/2}} f_W(q,p) = |\psi(p)|^2, \tag{2.1.3}$$

(where $|\psi(p)|^2$ and $|\psi(q)|^2$ are the momentum and position probability distributions respectively) and further take into consideration the fact that it is normalized, i.e.:

$$\int f_W(q,p)\frac{dqdp}{(2\pi\hbar)^D} = 1. \tag{2.1.4}$$

Despite having such attractive properties of a conventional probability distribution however, one must be cautious in adopting such an interpretation and note that $f_W(q,p)$ is in fact only a quasi-probability distribution. As much as one would hope, it does not satisfy a cardinal property of semi-positive definiteness. Regardless, the usefulness of the Wigner representation is evident when we wish to calculate observables. Just as we performed a transformation on the density operator to yield the Wigner function, one can also carry out the same transformation on a generic operator, $\hat{O}(\hat{p},\hat{q})$ that is a function of the momentum and position operators:

$$O_W(\vec{q},\vec{p}) = \frac{1}{2\pi\hbar}\int_{-\infty}^{\infty} e^{\frac{i\vec{p}.\vec{s}}{\hbar}}\langle \vec{q} - \frac{\vec{s}}{2}|\hat{O}(\hat{\vec{p}},\hat{\vec{q}})|\vec{q} + \frac{\vec{s}}{2}\rangle ds, \tag{2.1.5}$$

to yield the Weyl symbol, $O_W(\vec{q},\vec{p})$, of the operator, $\hat{O}(\hat{\vec{p}},\hat{\vec{q}})$. Strictly speaking then, the Wigner function is nothing more than the Weyl symbol of the density operator. While eq. 2.1.5 might seem like a cumbersome expression, it is surprisingly easy to evaluate if $\hat{O}(\vec{p},\vec{q})$ is a symmetrized operator. For example, consider the operator: $\hat{A}(\hat{\vec{p}},\hat{\vec{q}}) = \frac{1}{2}\left(\hat{\vec{q}}.\hat{\vec{p}} + \hat{\vec{p}}.\hat{\vec{q}}\right)$, its Weyl symbol can be automatically obtained by making the direct substitution: $(\hat{\vec{p}},\hat{\vec{q}}) \rightarrow (\vec{p},\vec{q})$ so that $A_W(\vec{p},\vec{q}) = \vec{q}.\vec{p}$. A more general and equally simpler approach to calculating the Weyl symbols for general operators can also be achieved using Bopp operators (Polkovnikov et al., 2011), where instead the substitution: $\left(\hat{\vec{p}},\hat{\vec{q}}\right) \rightarrow \left(\vec{p} - \frac{i\hbar}{2}\frac{\partial}{\partial\vec{q}}, \vec{q} + \frac{i\hbar}{2}\frac{\partial}{\partial\vec{p}}\right)$ is made. The classical nature of the Wigner formalism is most evident when calculating expectations values, where quantum mechanical expectation values now take the form of neat statistical expressions instead, i.e.

$$\langle\hat{O}(\hat{\vec{q}},\hat{\vec{p}})\rangle = \int\int \frac{d\vec{p}d\vec{q}}{(2\pi\hbar)^D} f_W(\vec{q},\vec{p})O_W(\vec{q},\vec{p}). \tag{2.1.6}$$

Furthermore, if we are interested in the dynamics of the system, this can be taken into account by evolving the $\vec{p},\vec{q}$ variables using Hamilton's classical equation of motion

$$\frac{d\vec{q}}{dt} = \{\vec{q}, H(\vec{p},\vec{q})\}, \tag{2.1.7}$$

and

$$\frac{d\vec{p}}{dt} = \{\vec{p}, H(\vec{p},\vec{q})\} \tag{2.1.8}$$

where H is the classical version of the Hamiltonian and

$$\{O_1, O_2\} \equiv \frac{\partial O_1}{\partial q}\frac{\partial O_2}{\partial p} - \frac{\partial O_1}{\partial p}\frac{\partial O_2}{\partial q} \tag{2.1.9}$$

defines the Poisson bracket. Quantum mechanics is then incorporated into the system only through quantum fluctuations that are mimicked by sampling initial conditions from the Wigner distribution (which typically has a finite width). This therefore necessitates an averaging over all possible initial

conditions, which modifies eq. 2.1.6 to:

$$\langle \hat{O}(\hat{\vec{q}},\hat{\vec{p}})\rangle = \int\int \frac{d\vec{p}_0 d\vec{q}_0}{(2\pi\hbar)^D} f_W(\vec{q}_0,\vec{p}_0) O_W(\vec{q}(t),\vec{p}(t)), \tag{2.1.10}$$

where $\vec{p}_0$ and $\vec{q}_0$ are the initial conditions of the system obtained from sampling the Wigner function. This approach however is only justified when the Wigner function is semi-positive definite which is only guaranteed for specific initial density operators (Olsen and Bradley, 2009), otherwise one would run into a similar type of 'sign-problem' as Monte-Carlo techniques.

While we have introduced phase space methods using the Wigner representation, other phase space methods include the Q-distribution, Husimi distribution, the Glauber-Sudarshan's P-representation (or P-representation for short) (see (Lee, 1995) for a review) and most recently Bosonic and Fermionic Gaussian phase space representations (Corney and Drummond, 2006, 2004, 2003). We are however, interested in the method called the positive-P distribution (Drummond and Gardiner, 1980) (cf section 2.4) as the title of this chapter suggests, which is in effect a more generalized extension of the P-representation (cf section 2.3).

Finally we note that there is of course nothing special about the conjugate operators $\vec{q}$ and $\vec{p}$ and they were only chosen in our discussion of the Wigner representation so as to draw parallels with classical physics. For Hamiltonians comprising of the Bosonic creation ($\hat{a}^\dagger$) and annihilation ($\hat{a}$) operators, as is commonplace in quantum optics, the Bosonic coherent states is a more appropriate choice. It is indeed the conventional basis chosen for P-representations (including the positive-P) and as such we have decided it worthwhile to review some of its key properties.

2.2 Bosonic coherent states

This section will only cover certain properties of coherent states that are relevant to PP formalism. We would like to point out however, that there are many more properties (Carmichael, 2002) that have been omitted for brevity.

1. A coherent state is a quantum mechanical state that is parameterized by a single complex number, $\alpha \in \mathbf{C}$ so that every point in the complex plane represents a unique state. The mathematical definition of a normalized coherent state has the following equivalent forms:

$$|\alpha\rangle = e^{-\frac{1}{2}\alpha^*\alpha} e^{\alpha\hat{a}^\dagger}|0\rangle, \tag{2.2.1}$$

which tells us that it can be generated by the action of the creation operator $\hat{a}^\dagger$ on the vacuum state $|0\rangle$ or alternatively:

$$|\alpha\rangle = e^{-\frac{1}{2}\alpha^*\alpha} \sum_{n=0}^{\infty} \frac{\alpha^n}{\sqrt{n!}}|n\rangle, \quad n = 0,1,2,\ldots, \tag{2.2.2}$$

which expresses it as a superposition of Fock or number states.

2. It is the eigenstate of the destruction operator

$$\hat{a}|\alpha\rangle = \alpha|\alpha\rangle, \qquad \langle\alpha|\hat{a}^\dagger = \langle\alpha|\alpha^*, \tag{2.2.3}$$

with a complex eigenvalue $\alpha \in \mathbb{C}$.

3. The set of Coherent states are non-orthogonal. This implies that two different states $|\alpha\rangle$ and $|\beta\rangle$ have a non-zero overlap given by:

$$\langle\alpha|\beta\rangle = e^{-\frac{1}{2}|\alpha^2|}e^{-\frac{1}{2}|\beta^2|}e^{\alpha^*\beta} \tag{2.2.4}$$

4. Coherent states are overcomplete and so that an integration over the entire complex plane does not yield the identity, instead:

$$\int d^2\alpha|\alpha\rangle\langle\alpha| = \pi, \tag{2.2.5}$$

.

5. Using a Coherent state basis, it is possible to express any operator in terms of just diagonal terms i.e. any operator is determined by its expectation value in all Coherent states. We can show this by using eq. 2.2.2 to calculate

$$\langle\alpha|\hat{T}|\alpha\rangle = \sum_{m,n}\langle n|\hat{T}|m\rangle e^{-|\alpha|^2}(\alpha^*)^n(\alpha)^m\frac{1}{\sqrt{n!m!}}, \tag{2.2.6}$$

which upon simple differentiation with respect to α and α^* gives

$$\langle n|\hat{T}|m\rangle = \sqrt{m!n!}\frac{\partial^n}{\partial\alpha^{*n}}\frac{\partial^m}{\partial\alpha^m}(e^{\alpha\alpha^*}\langle\alpha|\hat{T}|\alpha\rangle). \tag{2.2.7}$$

Thus the matrix elements of any operator, $\hat{T}$ can be expressed in terms of the diagonal elements of $\hat{T}$ in the Coherent state basis.

2.3 Glauber-Sudarshan's P-representation

The P-representation can be thought of as the predecessor of the PPR and was originally developed in 1963 by 2005 Nobel Prize winner, Roy J. Glauber[1] (Sudarshan, 1963, Glauber, 1963). In describing quantum systems, what we are interested in in particular, is the density operator, $\hat{\rho}$ as it contains all the necessary information about the system. According to property 5 in section 2.2, the diagonal matrix elements of any operator in a Coherent state basis, are all we need to span any operator. Using this property then, we can simply expand $\hat{\rho}$ in terms of a sum of diagonal matrix elements using some distribution function $P(\alpha,\alpha^*)$:

$$\hat{\rho} = \int d^2\alpha|\alpha\rangle\langle\alpha|P(\alpha,\alpha^*). \tag{2.3.1}$$

[1]The nobel prize was attributed to his contribution to the quantum theory of optical coherence

This representation of $\hat{\rho}$ is known as the Glauber-Sudarshan P-representation. The benefit in using the P-representation is in calculating expectation values of normal-ordered operators as they take the trivial form:

$$\begin{aligned}\langle \hat{a}^{\dagger p}\hat{a}^{q}\rangle &\equiv tr(\rho\hat{a}^{\dagger p}\hat{a}^{q}) \\ &= tr\left(\int d^2\alpha|\alpha\rangle\langle\alpha|P(\alpha,\alpha^*)\hat{a}^{\dagger p}\hat{a}^{q}\right) \\ &= \int d^2\alpha P(\alpha,\alpha^*)\langle\alpha|\hat{a}^{\dagger p}\hat{a}^{q}|\alpha\rangle \\ &= \int d^2\alpha P(\alpha,\alpha^*)\alpha^{*p}\alpha^{q}, \end{aligned} \tag{2.3.2}$$

which makes it tempting to interpret $P(\alpha,\alpha^*)$ as a probability distribution function, i.e. $P(\alpha) = \langle\alpha|\hat{\rho}|\alpha\rangle$ being the probability of the system occupying the state $|\alpha\rangle$. Note the similarities between the expectation values of a generic observable in P-representation (eq. 2.3.2) and the Wigner representation (eq. 2.1.10) that was discussed in section 2.1, further reinforcing the statistical interpretation of quantum mechanics as is typical of phase space techniques. Furthermore, $P(\alpha,\alpha^*)$ is normalized as well, i.e.

$$\begin{aligned}\int d^2\alpha P(\alpha,\alpha^*) &= \int d^2\alpha\langle\alpha|\alpha\rangle P(\alpha) \\ &= tr\left(\int d^2\alpha|\alpha\rangle\langle\alpha|P(\alpha)\right) \\ &= tr(\hat{\rho}) \\ &= 1, \end{aligned} \tag{2.3.3}$$

where we used the normalization of the trace of $\hat{\rho}$. However, this interpretation must be made with reservation as in the Wigner case. Owing to the overcompleteness of the Coherent states, $P(\alpha,\alpha^*)$ is not unique. It is additionally not guaranteed to be strictly positive and like the Wigner function is instead a quasi-probability distribution function. This is an issue if we wish to calculate the dynamics of the system. Instead of using Hamilton equations of motion, the dynamics of the system in the P-representation can in some cases be mapped exactly onto Langevin-type Ito stochastic differential equations (SDEs) using the theory of stochastic calculus (Arnold, 1974). This exact mapping only exists if the P -function remains strictly positive semi-definite throughout its evolution, a property which is not generally guaranteed.

2.4 The positive-P representation

In 1980 however, Drummond and Gardiner (Drummond and Gardiner, 1980) formulated the positive-P representation of the density operator which circumvents the problems associated with the P-representation, in particular the P- function being only a quasi distribution function. The PPR for the density operator, $\hat{\rho}$ is now instead given by the expansion

$$\hat{\rho} = \int d^2\alpha d^2\alpha^+ \frac{|\alpha\rangle\langle(\alpha^+)^*|}{\langle(\alpha^+)^*|\alpha\rangle}P(\alpha,\alpha^+) = \int d^2\alpha d^2\alpha^+ \hat{\Lambda}(\alpha,\alpha^+)P(\alpha,\alpha^+), \tag{2.4.1}$$

where $|\alpha\rangle$ is the bosonic coherent state and $P(\alpha,\alpha^+)$ is a distribution function over a doubled complex phase space of variables α and α^+ and

$$\hat{\Lambda}(\alpha,\alpha^+) = \frac{|\alpha\rangle\langle(\alpha^+)^*|}{\langle(\alpha^+)^*|\alpha\rangle} \tag{2.4.2}$$

is called the projection operator or the kernel of the density operator. Note that α and α^+ are two independent complex variables and *not* the complex conjugate of each other. This certainly introduces an extra degree of freedom since according to property 5 in section 2.2, a diagonal kernel: $|\alpha\rangle\langle\alpha|$ would have sufficed. The upshot of using the kernel in eq. 2.4.2 however, is that an explicit form for the distribution always exists and is given by the expression:

$$P(\alpha,\alpha^+) = \frac{1}{4\pi^2} e^{-|\alpha-\alpha^{+*}|^2/4} \langle \frac{(\alpha+(\alpha^+)^*)}{2} |\hat{\rho}| \frac{(\alpha+(\alpha^+)^*)}{2} \rangle. \tag{2.4.3}$$

If $\hat{\rho}$ is a positive-definite operator (which is the case for physical density operators) then $P(\alpha,\alpha^+)$ is also real and positive by definition and given the way that $P(\alpha,\alpha^+)$ appears in eq. 2.4.1, it has the reminiscent properties of a probability distribution. This is further evidenced by evaluating the unit trace of the density operator which demonstrates that P is properly normalized over the α-α^+ complex phase space:

$$\begin{aligned} tr(\hat{\rho}) &= \int P(\alpha,\alpha^+) d^2\alpha d^2\alpha^+ \\ &= 1. \end{aligned} \tag{2.4.4}$$

Furthermore, the expression for the expectation value of normal-ordered operators has a probabilistic interpretation:

$$\begin{aligned} \langle \hat{a}^{\dagger p} \hat{a}^q \rangle &\equiv tr(\hat{\rho}\hat{a}^{\dagger p}\hat{a}^q) \\ &= \int d^2\alpha d^2\alpha^+ P(\alpha,\alpha^+)(\alpha^+)^p \alpha^q, \end{aligned} \tag{2.4.5}$$

where $p,q \in \mathbb{R}^+$. In essence, the beauty of the PPR is the mapping of quantum degrees of freedom onto a simplified classical phase space so that a true probabilistic (and not quasi probabilistic as in the P-representation and Wigner representation) interpretation emerges.

2.5 Simulating dynamics

Having described what the PPR is, we now put it to practical use. We note that the PP-formalism can in principle be used for both real and imaginary time dynamics. Deriving SDEs for the real time case is relatively straightforward and is treated as the conventional application of the PPR. Imaginary-time evolution requires a modification of the real-time approach as well as the use of stochastic gauges, which is covered in section 2.6.1.

2.5.1 Real time dynamics: Master equation

Our starting point is the equation of motion governing the unitary evolution of the density operator: $\hat{\rho}$ for an isolated system in real time:

$$\frac{d}{dt}\hat{\rho} = -\frac{i}{\hbar}\left[\hat{H},\hat{\rho}\right], \tag{2.5.1}$$

which we will refer to as the Master equation. A corresponding Fokker-Planck equation can be derived by first substituting eq. 2.4.1 into eq. 2.5.1 to obtain:

$$\begin{aligned}\int \frac{\partial}{\partial t}P(\alpha,\alpha^+)\hat{\Lambda}(\alpha,\alpha^+)d^2\alpha d^2\alpha^+ &= -\frac{i}{\hbar}\int P(\alpha,\alpha^+)\Big[\hat{H}(\hat{a},\hat{a}^\dagger)\hat{\Lambda}(\alpha,\alpha^+) \\ &\quad -\hat{\Lambda}(\alpha,\alpha^+)\hat{H}(\hat{a},\hat{a^\dagger})\Big]d^2\alpha d^2\alpha^+,\end{aligned} \tag{2.5.2}$$

where we have made the additional assumption that our Hamiltonian: $\hat{H}(\hat{a},\hat{a}^\dagger)$ consists of bosonic annihilation and creation operators. This is an operator equation that is usually difficult to solve. Fortunately, there exist correspondence relations which will allow us to write the master equation in terms of a partial differential equation for α and α^+ in place of an operator equation for a and $\hat{a}^\dagger$. In general, the master equation will contain combinations of $\hat{a}$ and $\hat{a}^\dagger$ on the left hand side (LHS) and right hand side (RHS) of the projection operator: $\hat{\Lambda}(\alpha,\alpha^+)$ which are then replaced with algebraic operations using the correspondence relations. The two obvious correspondence relations are given by the action of $\hat{a}$ and $\hat{a}^\dagger$ on the LHS and RHS of $\hat{\Lambda}(\alpha,\alpha^+)$ respectively:

$$\begin{aligned}\hat{a}\hat{\Lambda} &= \frac{(\hat{a}|\alpha\rangle)\langle\alpha^{+*}|}{\langle\alpha^{+*}|\alpha\rangle} \\ &= \alpha\hat{\Lambda}\end{aligned} \tag{2.5.3}$$

and

$$\begin{aligned}\hat{\Lambda}\hat{a}^\dagger &= \frac{|\alpha\rangle\langle(\alpha^{+*}|\hat{a}^\dagger)}{\langle\alpha^{+*}|\alpha\rangle} \\ &= \alpha^+\hat{\Lambda},\end{aligned} \tag{2.5.4}$$

which can be seen from a direct application of eq. 2.2.3. We can therefore replace $\hat{a}$ and $\hat{a}^\dagger$ by complex phase space variables α and α^+ when this type of ordering appears. To obtain expressions for the reverse orderings, we take our expression for $\hat{\Lambda}$ and use eq. 2.2.1 and the overlap relation in eq. 2.2.4 to write it explicitly as:

$$\begin{aligned}\hat{\Lambda}(\alpha,\alpha^+) &= \frac{|\alpha\rangle|\langle\alpha^{+*}|}{\langle\alpha^{+*}|\alpha\rangle} \\ &= e^{(\alpha\hat{a}^\dagger-\alpha\alpha^+)}|0\rangle\langle 0|e^{\alpha^+\hat{a}}.\end{aligned} \tag{2.5.5}$$

We then differentiate eq. 2.5.5 with respect to α

$$\begin{aligned}\frac{\partial}{\partial\alpha}\hat{\Lambda} &= \frac{\partial}{\partial\alpha}(e^{(\alpha\hat{a}^\dagger-\alpha\alpha^+)})|0\rangle\langle 0|e^{\alpha^+\hat{a}} \\ &= (\hat{a}^\dagger-\alpha^+)\hat{\Lambda}(\alpha,\alpha^+),\end{aligned} \tag{2.5.6}$$

and carry out a simple rearrangement to get

$$\hat{a}^\dagger\hat{\Lambda} = (\alpha^+ + \frac{\partial}{\partial\alpha})\hat{\Lambda}. \tag{2.5.7}$$

On the other hand, by taking the derivative with respect to α^+ and rearranging we get:

$$\hat{\Lambda}\hat{a} = (\alpha + \frac{\partial}{\partial\alpha^+})\hat{\Lambda}. \tag{2.5.8}$$

To summarize then, the correspondence relations for the positive-P representation are:

$$\begin{aligned}\hat{\Lambda}\hat{a}^\dagger &= \alpha^+\hat{\Lambda}. \\ \hat{a}\hat{\Lambda} &= \alpha\hat{\Lambda}. \\ \hat{a}^\dagger\hat{\Lambda} &= (\alpha^+ + \frac{\partial}{\partial\alpha})\hat{\Lambda} \\ \hat{\Lambda}\hat{a} &= (\alpha + \frac{\partial}{\partial\alpha^+})\hat{\Lambda}.\end{aligned} \tag{2.5.9}$$

which can be thought of as its defining feature.

2.5.2 Deriving the Fokker-Planck equation

Upon subsitituting the correspondence relations. 2.5.9 into the Master equation in eq. 2.5.1, it is generally possible to convert the latter to the standard form:

$$\begin{aligned}\frac{\partial\hat{\rho}}{\partial t} &= \int\int\hat{\Lambda}(\alpha,\alpha^+)\frac{\partial P(\alpha,\alpha^+)}{\partial t}d^2\alpha d^2\alpha^+ \\ &= \int\int P(\alpha,\alpha^+)\left\{(A^\mu(\alpha)\frac{\partial}{\partial\alpha^\mu}+\frac{1}{2}D^{\mu\nu}(\alpha)\frac{\partial}{\partial\alpha^\mu}\frac{\partial}{\partial\alpha^\nu})\hat{\Lambda}(\alpha)\right\}d^2\alpha d^2\alpha^+,\end{aligned} \tag{2.5.10}$$

where μ is an index over stochastic variables. In the case of a single mode system described by $\hat{a}$, we denote $\alpha^0=\alpha, \alpha^1=\alpha^+$. Already, this is reminiscent of a Fokker-Planck equation (FPE) (Risken, 1989), which by definition is the equation of motion for a conditional probability distribution function, and we can intuitively identify the first term $A(\alpha,\alpha^+)$ as the drift vector and the second term: $D(\alpha,\alpha^+)$ as the diffusion matrix. The next key step is an integration by parts of eq. 2.5.10 with the assumption that boundary terms vanish.

For now we focus on the drift terms, for which an integration by parts yields:

$$\int\int P(\alpha,\alpha^+)A^\mu(\alpha,\alpha^+)\frac{\partial}{\partial\alpha^\mu}\hat{\Lambda}(\alpha,\alpha^+)d^2\alpha d^2\alpha^+ = \int d^2\alpha^+\Big[P(\alpha,\alpha^+)A^0(\alpha,\alpha^+) \tag{2.5.11}$$

$$\hat{\Lambda}(\alpha,\alpha^+)\big]\,|_{\alpha=boundaries} + \int d^2\alpha\left[P(\alpha,\alpha^+)A^1(\alpha,\alpha^+)\hat{\Lambda}(\alpha,\alpha^+)\right]|_{\alpha^+=boundaries}$$
$$-\int\int \hat{\Lambda}(\alpha,\alpha^+)\frac{\partial}{\partial\alpha^\mu}\left[A^\mu P(\alpha,\alpha^+)\right]d^2\alpha d^2\alpha^+,$$

where there is an implied summation in the last term. If we have an unbounded phase space, then the first two terms are evaluated at the regions $|\alpha|,|\alpha^+|\to\infty$ which we will assume to vanish. The effect of integrating by parts then is the introduction of a negative sign to the drift term and a transfer of derivatives away from the projection operator $\hat{\Lambda}(\alpha,\alpha^+)$, i.e.:

$$\int\int P(\alpha,\alpha^+)A^\mu(\alpha,\alpha^+)\frac{\partial}{\partial\alpha^\mu}\hat{\Lambda}(\alpha,\alpha^+)d^2\alpha d^2\alpha^+ = -\int\int \hat{\Lambda}(\alpha,\alpha^+)\frac{\partial}{\partial\alpha^\mu}\left[A^\mu P(\alpha,\alpha^+)\right]d^2\alpha d^2\alpha^+. \tag{2.5.12}$$

If we repeat this process for the diffusion term, then we see that there is no change in sign since we integrate by parts twice. However, the derivatives will also be removed from $\hat{\Lambda}(\alpha,\alpha^+)$ and transferred to the remaining terms: $D^{\mu\nu}P(\alpha)$. The final result is eq. 2.6.3 being converted to:

$$\begin{aligned}&\int\int \hat{\Lambda}(\alpha,\alpha^+)\left\{\frac{\partial P(\alpha,\alpha^+)}{\partial t}\right\}d^2\alpha d^2\alpha^+\\ &=\int\int \hat{\Lambda}(\alpha,\alpha^+)\left\{-\frac{\partial}{\partial\alpha^\mu}A^\mu(\alpha,\alpha^+)+\frac{1}{2}\frac{\partial}{\partial\alpha^\mu}\frac{\partial}{\partial\alpha^\nu}D^{\mu\nu}(\alpha)\right\}P(\alpha)d^2\alpha d^2\alpha^+\end{aligned} \tag{2.5.13}$$

from which we can tell that at least one solution that exists is given by:

$$\frac{\partial P(\alpha,\alpha^+)}{\partial t} = \left[-\frac{\partial}{\partial\alpha^\mu}A^\mu(\alpha,\alpha^+)+\frac{1}{2}\frac{\partial}{\partial\alpha^\mu}\frac{\partial}{\partial\alpha^\nu}D^{\mu\nu}(\alpha,\alpha^+)\right]P(\alpha,\alpha^+). \tag{2.5.14}$$

Eq. 2.5.14 has the conventional form of a Fokker-Planck equation (FPE). Since we have established that $P(\alpha,\alpha^+)$ in section 2.4 does have the properties of probability distribution then this interpretation is valid as long as $\mathbf{D}$ is symmetric and positive semi-definite. The symmetricalness of $\mathbf{D}$ depends on the form of the master equation whereas its positive semi-definiteness is automatically guaranteed by use of the PP kernel (Drummond and Gardiner, 1980).

2.5.3 Deriving Ito stochastic differential equations

Solving the FPE analytically is usually impossible with some notable exceptions (Risken, 1989) and a numerical solution is highly non-trivial. A simpler approach is to map the dynamics of an FPE onto a set of Ito Stochastic differential equations (SDEs) (Arnold, 1974) which is then much simpler to integrate numerically. The equivalent Ito SDEs that describe the evolution of our phase space variables are given by:

$$d\alpha^\mu = A^\mu(\alpha,\alpha^+)dt + B^{\mu\nu}(\alpha,\alpha^+)dW^\nu(t) \tag{2.5.15}$$

where $\mathbf{B}$ is the noise matrix that is related to the diffusion matrix via the following factorization:

$$\mathbf{D}(\alpha,\alpha^+) = \mathbf{B}(\alpha,\alpha^+)\mathbf{B}^T(\alpha,\alpha^+). \tag{2.5.16}$$

The condition imposed by eq. 2.5.16 grants us the freedom in constructing a noise matrix with a variable second dimension, N_w. Thus if $\mathbf{D}$ is an $N \times N$ matrix then $\mathbf{B}$ has dimensions: $N \times N_w$. The terms $dW^\nu(t)$, where $\nu = 1 \ldots N_w$, are independent Wiener increments or white noise terms with the statistical properties that

$$\begin{aligned} \langle dW^\mu(t) \rangle &= 0 \\ \langle dW^\mu(t) dW^\nu(t') \rangle &= \delta_{\mu\nu}\delta(t-t')dt. \end{aligned} \tag{2.5.17}$$

and can be easily numerically generated using a Gaussian distribution with mean 0 and variance dt, i.e. $\sim N(0,dt)$ which can be related to a standard normal random variable, $N(0,1)$ via the relation

$$dW^\mu(t) \sim \sqrt{dt}N(0,1). \tag{2.5.18}$$

It is important to make the distinction that we have derived *Ito* SDEs and a technical point is that is necessary to evaluate the noise matrix using the value of the stochastic variables at the beginning of the time step (see Appendix A in (Ng, 2010) for an abridged treatment of SDEs.). They also obey a modified calculus (Arnold, 1974) which necessitates the inclusion of second order differential terms:

$$d(xy) = ydx + xdy + dxdy, \tag{2.5.19}$$

in contrast to the rules of ordinary calculus where dx,dy are Ito differentials.

2.5.4 Stratonovich correction terms

In practice, it is the Stratonovich form of the SDEs that are numerically integrated due to better numerical convergence (Drummond and Mortimer, 1991). To obtain these, one simply needs to include correction terms in the drift terms of the Ito SDEs:

$$A^\mu_{Strat} = A^\mu_{Ito} - \frac{1}{2}\sum_{\nu\gamma} B^{\gamma\nu}(\vec{\alpha},\vec{\alpha}^+)\frac{\partial}{\partial x_\gamma}B^{\mu\nu}(\vec{x}). \tag{2.5.20}$$

whereas the form of the noise terms are unchanged. It is however necessary to evaluate the noise matrix at the midpoint of each time step interval as opposed to the start. The benefit of using Stratonovich SDE is that they obey the rules of ordinary calculus, so that:

$$d(xy) = xdy + ydx, \tag{2.5.21}$$

where the differentials dx,dy are now in Stratanovich form and which allows for more intuitive algebraic manipulation. For a generic Stratonovich differential dx, we denote the Stratanovich noise by the symbol $\circ$, where $d\vec{x} = A(\vec{x})dt + B(\vec{x}) \circ d\vec{W}$.

2.5.5 Noise matrix factorization

In general for non-diagonal diffusion matrices, finding the noise matrix $\mathbf{B}$ that satisfies eq. 2.5.16 is not an easy task, especially so for the multidimensional case. There are two ways to go about this.

The first way utilizes the symmetry of $\mathbf{D}$, i.e. since

$$\mathbf{D} = \mathbf{D}^T = \mathbf{B}\mathbf{B}^T \tag{2.5.22}$$

then we can write

$$\mathbf{D} = \mathbf{B}^2 \tag{2.5.23}$$

and a straightforward decomposition is given by the square root of the diffusion matrix:

$$\mathbf{B} = \sqrt{\mathbf{D}}, \tag{2.5.24}$$

which can be carried out using common symbolic manipulation software such as *Maple* or *Mathematica*.

Alternatively we could makes use of the ambiguity of the second dimension of $\mathbf{B}$. Note that since $\mathbf{D}$ is an $N \times N$ matrix then any noise matrix of dimension $N \times N_w$, will preserve the dimensionality of $\mathbf{D}$. It is generally possible to break up $\mathbf{D}$ into N_c constituents such that:

$$\mathbf{D} = \sum_{i=1}^{N_c} \mathbf{D^{(i)}}. \tag{2.5.25}$$

Of course, one should be strategic in choosing these constituents so that factorizing each $\mathbf{D}^{(i)}$ is a considerably easier task. Mathematically this means finding an $N \times N_w^i$ matrix, $\mathbf{B^{(i)}}$ so that $\mathbf{D^{(i)}} = \mathbf{B^{(i)}}\mathbf{B^{(i)T}}$. Using this strategy then, the total noise matrix is given by

$$\mathbf{B} = \left[\mathbf{B}^1\mathbf{B}^2 \ldots\ldots \mathbf{B}^{N_c}\right] \tag{2.5.26}$$

since

$$\begin{aligned}
\mathbf{B}\mathbf{B}^{\mathbf{T}} &= \left[\mathbf{B^{(1)}}\mathbf{B^{(2)}} \cdots + \mathbf{B^{(N_c)}}\right] \begin{bmatrix} \mathbf{B^{(1)T}} \\ \mathbf{B^{(2)T}} \\ \vdots \\ \vdots \\ \mathbf{B^{(N_c)T}} \end{bmatrix} \\
&= \mathbf{B^{(1)}}\mathbf{B^{(1)T}} + \mathbf{B^{(2)}}\mathbf{B^{(2)T}} + \cdots + \mathbf{B^{(N_c)}}\mathbf{B^{(N_c)T}} \\
&= \mathbf{D^{(1)}} + \mathbf{D^{(2)}} + \cdots + \mathbf{D^{(N_c)}} \\
&= \mathbf{D}
\end{aligned} \tag{2.5.27}$$

as required. The benefit of using the square root factorization is that we only require $4N$ noise terms (recall eq. 2.5.15), at the cost of a (usually) much more complicated expression for the noise matrix. On the other hand, using the latter trick we end up introducing $\sum_i N_w^{(i)} \geq N$ noise terms. In the case of multiplicative noise, this can have unfavourable effects such as a rapid growth of the variances of the stochastic variables which can lead to numerical instabilities (Deuar and Drummond, 2006).

2.5.6 Diffusion gauges

Due to the structure of the noise decomposition, another possible choice for noise matrix is given by:

$$\mathbf{B}' = \mathbf{BO}, \tag{2.5.28}$$

where $\mathbf{O}$ is an orthognal matrix satisfying $\mathbf{OO}^{\mathbf{T}} = \mathbf{I}$. This choice of noise matrix is also known as a diffusion gauge (Plimak et al., 2001), since it directly modifies the form of the noise terms, which originate from the diffusion components of the FPE. For a single mode system, a possible choice of $\mathbf{O}$ is given by:

$$\mathbf{O} = \begin{bmatrix} \cos(g) & -\sin(g) \\ \sin(g) & \cos(g) \end{bmatrix}, \tag{2.5.29}$$

where g is an arbitrary parameter. In some instances such as in the anharmonic oscillator (Plimak et al., 2001), it has been shown to enhance the numerical stability in the SDEs.

2.5.7 Initial distribution

A salient point that we have not yet addressed is the initialization of the stochastic variables before evolving them according to eq. 2.5.15. In reality, all one has to do is to calculate the PP-distribution using eq. 2.4.3 for an initial density operator: $\hat{\rho}$. This step is analogous to calculating the Wigner function in the truncated Wigner semiclassical technique (Polkovnikov et al., 2011).

Coherent state

The simplest state to initialize the system however is that of a generic coherent state, $|\gamma\rangle\langle\gamma|$ such that $\gamma \in \mathbb{R}^+$ with average particle number: $|\gamma|^2$. In the PP formalism, this can be simply achieved by setting the positive-P function in eq. 2.4.1:

$$\hat{\rho} = \int P(\alpha,\alpha^+)\hat{\Lambda}(\alpha,\alpha^+)d^2\alpha d^2\alpha^+ \tag{2.5.30}$$

to the following delta function:

$$P(\alpha,\alpha^+) = \delta(\alpha-\gamma)\delta(\alpha^+-\gamma). \tag{2.5.31}$$

This distribution function can also be used to set the vacuum state of the system by setting $\gamma = 0$ ().

Fock state

Now suppose for a single mode system, we would like to initialise our system in a, i.e. $\hat{\rho} = |n\rangle\langle n|$. This can be achieved by introducing the change of variables: $\mu = \frac{\alpha+(\alpha^+)^*}{2}$ and $\gamma = \frac{\alpha-(\alpha^+)^*}{2}$ which we can then substitute into eq. 2.4.3 to get

$$P(\mu,\nu) = \frac{1}{4\pi^2}\,|\langle\mu|n\rangle\langle n|\mu\rangle|\,e^{-|\gamma|^2}|J(\alpha,\alpha^+)|, \tag{2.5.32}$$

where $J(\alpha,\alpha^+)$ is the Jacobian matrix:

$$J(\alpha,\alpha^+) = \begin{bmatrix} \frac{\partial\alpha}{\partial\mu} & \frac{\partial\alpha}{\partial\gamma} \\ \frac{\partial(\alpha^+)^*}{\partial\mu} & \frac{\partial(\alpha^+)^*}{\partial\gamma} \end{bmatrix} = \left| \begin{bmatrix} 1 & 1 \\ 1 & -1 \end{bmatrix} \right| = 2. \tag{2.5.33}$$

Note that: $\alpha = \mu + \gamma$ and $(\alpha^+)^* = \mu - \gamma$.

Using the overlap between a coherent state $|\mu\rangle = e^{-\frac{|\mu|^2}{2}} \sum_{m=0}^{\infty} \frac{\mu^m}{\sqrt{m!}} |m\rangle$ and an arbitrary fock state $|n\rangle$, the distribution function $P(\mu,\gamma)$ is then given by

$$\begin{aligned} P(\mu,\gamma) &= \frac{1}{4\pi^2} \sum_{m,m'} \left| \frac{(\mu^*)^m}{\sqrt{m!}} \frac{(\mu)^{m'}}{\sqrt{m'!}} e^{-\frac{|\mu|^2}{2}} e^{-\frac{|\mu|^2}{2}} \langle m|n\rangle \langle m'|n\rangle \right| e^{-|\gamma|^2} 4 \\ &= \frac{1}{\pi^2} \sum_{m,m'} \left| \frac{(\mu^*)^m}{\sqrt{m!}} \frac{(\mu)^{m'}}{\sqrt{m'!}} e^{-|\mu|^2} \right| \delta_{mn}\delta_{m'n} e^{-|\gamma|^2} \\ &= \frac{1}{\pi^2} \left| \frac{(\mu^*)^n}{\sqrt{n!}} \frac{(\mu)^{2n}}{\sqrt{n!}} e^{-|\mu|^2} \right| e^{-|\gamma|^2} \\ &= \left(\frac{e^{-|\gamma|^2}}{\pi} \right) \left(\frac{|\mu|^{2n} e^{-|\mu|^2}}{\pi n!} \right) \end{aligned} \tag{2.5.34}$$

or more succinctly

$$P(\mu,\gamma) = \frac{e^{-|\gamma|^2}}{\pi} \frac{\Gamma(|\mu|^2, n+1)}{\pi}, \tag{2.5.35}$$

where

$$\Gamma(x,n) = \frac{e^{-x} x^{n-1}}{(n-1)!} \tag{2.5.36}$$

is the Gamma distribution. So we see that in order to sample a fock state, we need to sample the real number $z = |\mu|^2$ using a gamma distribution and the real and imaginary parts of γ using a Gaussian distribution, i.e.:

$$\gamma = \frac{1}{\sqrt{2}} (n_1 + i n_2) \tag{2.5.37}$$

where $n_1, n_2 \sim N(0,1)$ are independent Gaussian random variables and μ is given by

$$\mu = \sqrt{z} e^{i\theta}, \tag{2.5.38}$$

with θ being drawn from a uniform distribution: $\theta \in [0, 2\pi)$. The gamma distribution can be easily coded and efficient algorithms are readily available (Marsaglia and Tsang, 2000). Once we sample, μ and γ then the original phase space variables can be easily obtained from the equations:

$$\alpha = \mu + \gamma \tag{2.5.39}$$

$$\alpha^+ = \mu^* - \gamma^*. \tag{2.5.40}$$

A variety of initial states can also be set up within the PPR and this has been well detailed in (Olsen

and Bradley, 2009).

2.6 Imaginary time dynamics

The PP can also be reformulated to obtain ground state properties. We will use a canonical ensemble in the following derivations, although calculations in the grand canonical ensemble are possible as well (Deuar et al., 2009). To do so, we construct an analogous equation of motion but in imaginary time, $\beta = 1/k_B T$ instead, for the unnormalized thermal density operator: $\rho = e^{-\beta \hat{H}}$. T is the temperature of the system and k_B is Boltzmann's constant. A simple differentiation yields:

$$\frac{d}{d\beta}\hat{\rho} = \frac{1}{2}\left[\hat{H}\hat{\rho} + \hat{\rho}\hat{H}\right]. \tag{2.6.1}$$

By applying the same procedure in section 2.5.1- 2.5.3, a subtle issue arises. In the imaginary time master equation, the different permutations of $\hat{\rho}\hat{H}$ are added instead of subtracted. The result is that constant terms ($C(\alpha,\alpha^+)$) arise, yielding an equation that no longer fits the canonical form of a FPE:

$$\frac{\partial \hat{\rho}}{\partial \beta} = \int\int \hat{\Lambda}(\alpha,\alpha^+)\frac{\partial P(\alpha,\alpha^+)}{\partial t} d^2\alpha d^2\alpha^+ \tag{2.6.2}$$

$$= \int\int P(\alpha,\alpha^+)\left\{(A^\mu(\alpha)\frac{\partial}{\partial \alpha^\mu} + \frac{1}{2}D^{\mu\nu}(\alpha)\frac{\partial}{\partial \alpha^\mu}\frac{\partial}{\partial \alpha^\nu}) + C(\alpha,\alpha^+)\right\}\hat{\Lambda}(\alpha) d^2\alpha d^2\alpha^+. \tag{2.6.3}$$

2.6.1 The Gauge-P representation

In order to remove the constant term, $C(\alpha,\alpha^+)$, we will have to make use of the gauge-P representation (Deuar and Drummond, 2002) that allows for arbitrary modifications in eq. 2.4.2 by introducing an extra complex variable, Ω in the stochastic kernel. Ω plays the role of a weight term.

The modified kernel is:

$$\hat{\Lambda}_g = \Omega\hat{\Lambda} = \Omega\frac{|\alpha\rangle\langle\alpha^{+*}|}{\langle\alpha^{+*}|\alpha\rangle}, \tag{2.6.4}$$

from which we can introduce an extra correspondence gauge relation.

$$\left(\Omega\frac{\partial}{\partial\Omega} - 1\right)\Lambda_g C(\alpha,\alpha^+,\Omega) = 0, \tag{2.6.5}$$

where $C(\alpha,\alpha^+,\Omega)$ is any arbitrary function. Adding this gauge into eq. 2.6.3, we get:

$$\frac{\partial\hat{\rho}}{\partial\beta} = \int\int\int \hat{\Lambda}_g \frac{\partial P(\alpha,\alpha^+,\Omega)}{\partial\beta} d^2\alpha d^2\alpha^+ d\Omega$$

$$= \int\int P(\alpha,\alpha^+,\Omega)\left\{A^\mu(\alpha)\frac{\partial}{\partial\alpha^\mu} + \frac{1}{2}D^{\mu\nu}(\alpha)\frac{\partial}{\partial\alpha^\mu}\frac{\partial}{\partial\alpha^\nu} + C(\alpha,\alpha^+,\Omega)\right\}\hat{\Lambda}_g(\alpha,\Omega)d^2\alpha d^2\alpha^+ d^2\Omega.$$
$$+ \int\int P(\alpha,\alpha^+,\Omega)\left\{(\frac{\partial}{\partial\Omega} - 1)C(\alpha,\alpha^+,\Omega)\right\}\hat{\Lambda}_g(\alpha)d^2\alpha d^2\alpha^+ d^2\Omega$$

$$= \int\int P(\alpha,\alpha^+,\Omega)\left\{A^\mu(\alpha)\frac{\partial}{\partial\alpha^\mu} + \frac{1}{2}D^{\mu\nu}(\alpha)\frac{\partial}{\partial\alpha^\mu}\frac{\partial}{\partial\alpha^\nu} + \frac{\partial}{\partial\Omega}C(\alpha,\alpha^+,\Omega)\right\}\hat{\Lambda}_g(\alpha,\Omega)d^2\alpha d^2\alpha^+ d^2\Omega. \tag{2.6.6}$$

Remarkably, the simple addition of an extra "weight" term allows us to arbitrarily remove constant terms above. The stochastic evolution for Ω is determined by the unwanted constant terms and has the form:

$$d\Omega/\Omega = C(\alpha,\alpha^+,\Omega)d\beta. \tag{2.6.7}$$

Meanwhile, the evolution of the α,α^+ variables are left unchanged.

2.6.2 Drift gauges

The gauge-P representation in fact grants us even more flexibility in altering the FPE other than for the removal of constant terms. Consider the choice:

$$C(\alpha,\alpha^+,\Omega) = A'^\mu(\vec{\alpha})\frac{\partial}{\partial\alpha^\mu}, \tag{2.6.8}$$

which has the overall effects of both modifying the corresponding drift terms of the $\vec{\alpha}$ variables

$$\int\int P(\alpha,\alpha^+,\Omega)\left\{(A^\mu(\alpha) - A'^\mu(\alpha)\right\}\frac{\partial}{\partial\alpha^\mu}\hat{\Lambda}_g(\alpha,\Omega)d^2\alpha d^2\alpha^+ d^2\Omega. \tag{2.6.9}$$

as well as generating diffusion terms.:

$$\int\int P(\alpha,\alpha^+,\Omega)A'^\mu\frac{\partial}{\partial\Omega}\frac{\partial}{\partial\alpha^\mu}\hat{\Lambda}_g(\alpha,\Omega)d^2\alpha d^2\alpha^+ d^2\Omega. \tag{2.6.10}$$

Note that this will have effect of generating SDEs that couple Ω and $\vec{\alpha}$ variables through common noise terms. The term drift gauges refers to the use of the gauge-P representation in this above fashion and is formalized in (Deuar and Drummond, 2002). It has been known to have a stabilizing effect when applied to the single mode anharmonic oscillator for example (Deuar and Drummond, 2006).

2.7 Stochastic averages of observables

2.7.1 Standard PPR

The advantage of using SDEs is in the relative ease in calculating normal ordered expectation values. As mentioned in section 2.5.2, the calculation of quantum mechanical normal ordered observables is given by the statistical expression in eq. 2.4.5:

$$\langle \hat{a}^\dagger(t)^p \hat{a}(t)^q \rangle = \int P(\alpha,\alpha^+)\alpha(t)^{+p}\alpha(t)^q d^2\alpha d^2\alpha^+. \tag{2.7.1}$$

where $p,q \in \mathbb{R}^+$ and we see that the dynamics is implicitly built in to the stochastic evolution of the variables, $\alpha(t)$ and $\alpha^+(t)$. Furthermore, from the correspondence relations in eq. 2.5.9, we see that there is a direct relation between the bosonic operators: $\hat{a}^\dagger$ and $\hat{a}$ with α^+ and α, respectively. There also exists an exact correspondence between the quantum mechanical average and the stochastic average of their respective phase space variable functions, i.e.:

$$\langle \hat{a}^{\dagger p}(t)\hat{a}^q(t))\rangle = \lim_{ntraj\to\infty} \langle\langle \alpha^+(t)^p\alpha(t)^q)\rangle\rangle_{ntraj}, \tag{2.7.2}$$

in the limit of an infinite number of trajectories, n_{traj}, where

$$\langle\langle \alpha^+(t)^p,\alpha(t)^q\rangle\rangle_{ntraj} \equiv \frac{1}{ntraj}\sum_{i=1}^{ntraj}\left[\alpha_i^+(t)^p\alpha_i(t)^q\right] \tag{2.7.3}$$

and i labels the individual realization of each trajectory of the phase space variables. The dynamics of any normal ordered operator can therefore be monitored by numerically integrating SDEs of the form 2.5.15 and calculating simple stochastic averages. Although the exact correspondence is achieved in the limit that the total number of trajectories tends to infinity, in practice it is usually sufficient to use $\sim 10^4 - 10^7$ trajectories, depending on the nature of the problem.

2.7.2 Gauge-P

Within the gauge-P representation, the normalization is no longer preserved and instead, we find that:

$$Tr(\Lambda_g) = \Omega. \tag{2.7.4}$$

Observables expression are then modified in the following way:

$$\langle O(\hat{a}(t),\hat{a}^\dagger(t))\rangle = \frac{\langle\langle \Omega(t)O(\alpha(t),\alpha^+(t))\rangle\rangle}{\langle\langle \Omega(t)\rangle\rangle}. \tag{2.7.5}$$

This expression gives further credence to the reason that Ω is called the "weight" term. The Gauge-P representation brings to light a salient point. If an unnormalized kernel is used, the trace of the density operator has to be explicitly taken into account. It manifest itself in the denominator of our stochastic estimators in our observable calculations as seen in eq. 2.7.4.

2.8 Multimode case

Although our discussion carried out so far has been explicitly used for the single mode case, the PPR can also be generalized to a system with N-modes, taking the form:

$$\hat{\rho} = \int \hat{\Lambda}(\vec{\alpha},\vec{\alpha}^{+})P(\vec{\alpha},\vec{\alpha}^{+})d^{2}\vec{\alpha}d^{2}\vec{\alpha}^{+} \tag{2.8.1}$$

where the generalized off-diagonal Coherent state projection operator is obtained from a direct product of single mode kernels:

$$\hat{\Lambda}(\vec{\alpha},\vec{\alpha^{+}}) = \prod_{i}^{N}\otimes\frac{|\alpha_i\rangle\langle(\alpha_i^{+})^{*}|}{|(\alpha_i^{+})^{*}\rangle\langle\alpha_i|} \tag{2.8.2}$$

and α_i and α_i^{+} for $i = 1\ldots N$ are independent complex variables. The quantum mechanical average of normal ordered moments can be analogously calculated via:

$$\langle\prod_{i}^{N}(\hat{a}_i^{\dagger})^{p_i}(\hat{a}_i)^{q_i}\rangle = \int P(\vec{\alpha},\vec{\alpha^{+}})\prod_{i}^{N}(\alpha_i)^{p_i}(\alpha_i^{+})^{q_i}d^{2}\vec{\alpha}d^{2}\vec{\alpha^{+}} \tag{2.8.3}$$

which is also equivalent to the stochastic average and an implicit time dependence in the stochastic variables are implied but not explicitly written out for brevity.

$$\lim_{ntraj\to\infty}\langle\langle\prod_{i}^{N}(\alpha_i)^{p_i}(\alpha_i^{+})^{q_i}\rangle\rangle_{ntraj}. \tag{2.8.4}$$

The PPR can therefore be easily generalized to multimode systems and that the number of variables required to simulate the system scales linearly with N. In this respect, exact many-body dynamics is reduced to a tractable one that is not computationally exhaustive.

2.9 Short lifetimes and spiking

In principle, the PPR allows us to simulate the exact dynamics of a Bosonic system and seems to be a very powerful method. However, there is a notorious problem associated with the method; its short simulation lifetime: t_{life}. This means that beyond $t > t_{life}$, simulations fail to produce correct results. The single most defining feature is the onset of "spiking" in observable calculations. This is an indication that the stochastic differential equations are stiff and the ensuing evolution is systematically incorrect. In the extreme case, this can result in numerical overflow.

As detailed in (Deuar, 2005), spiking simulations are features that arise when two types of boundary errors occur. In deriving the FPE, we carried out an integration by parts and discarded boundary terms in the process, assuming they were negligible. This is true granted that the $P(\alpha,\alpha^{+})$ distribution function does not develop fat tails, in which case the entire formalism breaks down. Such an error is called a Type-I boundary error. It is usually not possible to evaluate these boundary terms but there are tell-tale signs for when they could be a problem. Examples of which include: Moving singularities in the drift, i.e. a set of solutions of measure zero that diverge in a finite time.

The location of the pole depends on the initial conditions and is moving in that sense. An overly broad initial probability distribution (Gilchrist et al., 1997) has also been observed to have undesirable effects. A very general criteria that was outlined in (Deuar, 2005) states that drift and noise instabilities arise unless the two conditions:

$$\lim_{|\alpha_j|\to\infty} \frac{A_j}{|\alpha_j|} = 0 \tag{2.9.1}$$

and

$$\lim_{|\alpha_j|\to\infty} \frac{B_{jk}}{|\alpha_j|} = 0, \tag{2.9.2}$$

for all k are satisfied. This simple check will give us a good idea if simulation of our SDEs will be the victim of early peril or not. The type-II boundary error (Deuar, 2005) occurs at the level of our observable estimates. The quantum mechanical average given by the integral

$$\langle \hat{O} \rangle = \frac{\int P(\alpha,\alpha^+)\Re\left[\mathrm{Tr}(\hat{O}\hat{\Lambda}(\alpha,\alpha^+))\right]}{\int P(\alpha,\alpha^+)\Re\left[\mathrm{Tr}(\hat{\Lambda}(\alpha,\alpha^+))\right]} \tag{2.9.3}$$

may fail to converge when either $\hat{O}$ or Λ in the numerator, grows faster than $P(\alpha,\alpha^+)$ close to the boundaries of phase space. Note that in eq. 2.9.3, we have assumed an unnormalized kernel for generality.

Typically, there is no way apriori to know what t_{life} will be or how many trajectories are needed to obtain convergence. The latter usually ranges from $10^4 - 10^7$ depending on the problem and the nature of the SDEs, and has to be determined empirically. The positive-P representation is therefore a method that is particularly useful in simulating many-body systems where the interesting physics occur at short time scales before spiking occurs. In essence, most of the issues with spiking arises as a result of a sub-optimal normalization for the kernel chosen. In the PPR in particular, the kernel:

$$\Lambda = \frac{|\alpha\rangle\langle\alpha^{+*}|}{\langle\alpha^{+*}|\alpha\rangle} \tag{2.9.4}$$

while well defined in the diagonal limit, i.e. $\alpha = \alpha^{+*}$ is ill-equipped to represent off-diagonal elements in an orthogonal basis. For instance, suppose Λ takes the form $|n\rangle\langle m|$ in the fock basis and $|n\rangle, |m\rangle$ are Fock states. The denominator in this case approaches zero and is ill-defined for such non-hermitian operators. Points in phase space with a vanishing normalization is ironically favored by trajectories which are drawn over to compensate by their sheer numbers. On the other hand, points in phase space with a large normalization are avoided since they have a higher weight (Deuar, 2015) and fewer trajectories are required. Ideally one must find an optimal normalization that abates such extreme behavior, which is a non-trivial task. Regardless, for times $t < t_{life}$, exact quantum dynamics are still amenable.

2.10 General recipe

To summarise then, the PPR is the expansion of the quantum density operator, $\hat{\rho}$, in terms of an off-diagonal kernel, $\hat{\Lambda}$ formed from Bosonic coherent states. The benefit of doing so is that in this form, the equation of motion for $\hat{\rho}$ may take the form of a Fokker-Planck Equation (FPE), which can then be mapped onto a set of Ito SDES, that are relatively easy to simulate. This is the final goal of using the PPR i.e. being able to derive Ito SDEs that just as equivalently describe the quantum system.

2.11 Example: Quench dynamics of the Bose-Hubbard Hamiltonian

As an example, let us consider the quench dynamics of the 1D BH model in an external parabolic potential. It is described by the Hamiltonian:

$$\hat{H} = \sum_j \left[-J\left(\hat{a}_j^\dagger \hat{a}_{j+1} + \hat{a}_{j+1}^\dagger \hat{a}_j\right) + \frac{U}{2}\hat{n}_j\left(\hat{n}_j - 1\right) + \frac{K}{2}\hat{n}_j j^2 \right], \tag{2.11.1}$$

where U is the onsite repulsion energy and $K = m\omega^2 d^2$, represents the external potential. ω is the trapping frequency of the harmonic trap and d is the lattice spacing. We follow closely the quench protocol carried out in (Trotzky et al., 2012). At an initial time t_o, the system is prepared in the $U \to \infty$ ground state at half filling described by the state: $|\psi(0)\rangle = |1,0,1,0,1,0,\ldots\rangle$. At $t > t_0$, the system is instantaneously quenched to a new set of values $\{J,U,K\}$ and allowed to evolve under the full Hamiltonian 2.11.1. The dynamics of the system is monitored by a series of observables that are both experimentally and numerically calculable using t-DMRG.

2.11.1 Application of the PPR

We now derive the SDEs for Hamiltonian 2.11.1 as a contemporary, instructive example to elucidate the PP-formalism. We shall also explore its limitations as highlighted in 2.9. Our starting point is the master equation:

$$\frac{d}{dt}\hat{\rho} = -\frac{i}{\hbar}\left[\hat{H},\hat{\rho}\right], \tag{2.11.2}$$

which we will use to first obtain a FPE by mapping the operator equation onto a differential equation. Let us deal with the terms individually. Using the correspondence relations in eq. 2.5.9, the tunnelling

term maps to:

$$\begin{aligned}
\frac{d}{dt}\hat{\rho} &\sim -\frac{i}{\hbar}\left[-J\left(\hat{a}_j^\dagger \hat{a}_{j+1} + \hat{a}_{j+1}^\dagger \hat{a}_j\right), \hat{\rho}\right] \\
&= \frac{iJ}{\hbar}\left(\hat{a}_j^\dagger \hat{a}_{j+1}\hat{\Lambda} - \hat{\Lambda}\hat{a}_j^\dagger \hat{a}_{j+1} + \hat{a}_{j+1}^\dagger \hat{a}_j \hat{\Lambda} - \hat{\Lambda}\hat{a}_{j+1}^\dagger \hat{a}_j\right) \\
&= \frac{iJ}{\hbar}\left(\alpha_j\left(\beta_i + \frac{\partial}{\partial \alpha_i}\right) - \beta_i\left(\alpha_j + \frac{\partial}{\partial \beta_j}\right) + \alpha_i\left(\beta_j + \frac{\partial}{\partial \alpha_j}\right) - \beta_j\left(\alpha_i + \frac{\partial}{\partial \beta_i}\right)\right) \\
&= \frac{iJ}{\hbar}\left(\alpha_j\frac{\partial}{\partial \alpha_i} - \beta_i\frac{\partial}{\partial \beta_j} + \alpha_i\frac{\partial}{\partial \alpha_j} - \beta_j\frac{\partial}{\partial \beta_i}\right) \\
&= \frac{iJ}{\hbar}\left((\alpha_{i+1} + \alpha_{i-1})\frac{\partial}{\partial \alpha_i} - (\beta_{i+1} + \beta_{i-1})\frac{\partial}{\partial \beta_i}\right),
\end{aligned} \tag{2.11.3}$$

where we have suppressed summation and integration notations. For the on-site repulsion term, we can first simplify it by using the commutation relations for bosons

$$\text{onsite repulsion} = \frac{U}{2}\hat{a}_i^\dagger \hat{a}_i\left(\hat{a}_i^\dagger \hat{a}_i - 1\right) \tag{2.11.4}$$

$$= \frac{U}{2}\left(\hat{a}_i^\dagger(1 + \hat{a}_i^\dagger \hat{a}_i)\hat{a}_i - \hat{a}_i^\dagger \hat{a}_i\right) \tag{2.11.5}$$

$$= \frac{U}{2}\hat{a}_i^{\dagger 2}\hat{a}_i^2 \tag{2.11.6}$$

which corresponds to a local anharmonic oscillator (Dowling et al., 2007). Applying the correspondence relations yields:

$$\frac{d}{dt}\hat{\rho} \sim -\frac{i}{\hbar}\left[\frac{U}{2}\hat{a}^{\dagger 2}\hat{a}^2, \hat{\rho}\right] \tag{2.11.7}$$

$$= -\frac{iU}{2\hbar}\left[\hat{a}^{\dagger 2}\hat{a}^2, \hat{\rho}\right] \tag{2.11.8}$$

$$= -\frac{iU}{2\hbar}\left(\hat{a}_i^{\dagger 2}\hat{a}_i^2\hat{\Lambda} - \hat{\Lambda}\hat{a}_i^{\dagger 2}\hat{a}_i^2\right) \tag{2.11.9}$$

$$= -\frac{iU}{2\hbar}\left(\alpha_i^2\left(\beta_i + 2\beta_i\frac{\partial}{\partial \alpha_i} + \frac{\partial^2}{\partial \alpha_i^2}\right) - \beta_i^2\left(\alpha_i + 2\alpha_i\frac{\partial}{\partial \beta_i} + \frac{\partial^2}{\partial \beta_i^2}\right)\right) \tag{2.11.10}$$

$$= -\frac{iU}{\hbar}\left(\alpha_i^2\beta_i\frac{\partial}{\partial \alpha_i} + \frac{1}{2}\alpha_i^2\frac{\partial^2}{\partial \alpha_i^2} - \alpha_i\beta_i^2\frac{\partial}{\partial \beta_i} - \frac{1}{2}\beta_i^2\frac{\partial^2}{\partial \beta_i^2}\right) \tag{2.11.11}$$

Lastly, we focus on the external harmonic potential term, which gives

$$\frac{d}{dt}\hat{\rho} \sim -\frac{i}{\hbar}\left[\frac{K}{2}\hat{a}^{\dagger}\hat{a}j^2,\hat{\rho}\right] \tag{2.11.12}$$

$$= -i\frac{j^2K}{2\hbar}\left(\hat{a}_j^{\dagger}\hat{a}_j\hat{\Lambda} - \hat{\Lambda}\hat{a}_j^{\dagger}\hat{a}_j\right) \tag{2.11.13}$$

$$= -i\frac{j^2K}{2\hbar}\left(\alpha_j\left(\beta_j + \frac{\partial}{\partial\alpha_j}\right) - \beta_j(\alpha_j + \frac{\partial}{\partial\beta_j})\right) \tag{2.11.14}$$

$$= -i\frac{j^2K}{2\hbar}\left(\alpha_j\frac{\partial}{\partial\alpha_j} - \beta_j\frac{\partial}{\partial\beta_j}\right). \tag{2.11.15}$$

Gathering the three different terms we get the resulting FPE:

$$\frac{d}{dt}P(\vec{\alpha},\vec{\beta}) = \sum_j\left[\frac{iJ}{\hbar}\left((\alpha_{j+1}+\alpha_{j-1})\frac{\partial}{\partial\alpha_j} - (\beta_{j+1}+\beta_{j-1})\frac{\partial}{\partial\beta_j}\right)\right. \tag{2.11.16}$$

$$-\frac{iU}{\hbar}\left(\alpha_j^2\beta_j\frac{\partial}{\partial\alpha_j} + \frac{1}{2}\alpha_j^2\frac{\partial^2}{\partial\alpha_j^2} - \alpha_i\beta_j^2\frac{\partial}{\partial\beta_j} - \frac{1}{2}\beta_j^2\frac{\partial^2}{\partial\beta_j^2}\right) \tag{2.11.17}$$

$$\left.-i\frac{j^2K}{2\hbar}\left(\alpha_j\frac{\partial}{\partial\alpha_j} - \beta_j\frac{\partial}{\partial\beta_j}\right)\right]P(\vec{\alpha},\vec{\beta}), \tag{2.11.18}$$

which (in units of $\hbar = 1$) yields the corresponding SDEs:

$$d\alpha_j = iJ\left(\alpha_{j+1}+\alpha_{j-1}\right)dt - iU\alpha_j^2\beta_j dt - i(\frac{j^2K}{2})\alpha_j dt + i\sqrt{iU}\alpha_j\xi_j dt \tag{2.11.19}$$

$$d\beta_j = -iJ\left(\beta_{j+1}-\beta_{j-1}\right)dt + iU\beta_j^2\alpha_j dt + i(\frac{j^2K}{2})\beta_j dt + \sqrt{iU}\beta_j\eta_j dt \tag{2.11.20}$$

where we have introduced two independent noise terms: $\eta_i,\xi_i \sim \frac{1}{\sqrt{dt}}N(0,1)$. Since the diffusion matrices are diagonal, obtaining a noise matrix decomposition (see section: 2.5.3) is trivially obtained by taking the square root of the diagonal elements. The Stratonovich correction terms can be calculated using the formula:

$$S_j = -\frac{1}{2}\sum_{l,k}\frac{\partial B_{jk}}{\partial x_l}B_{lk}. \tag{2.11.21}$$

and are especially easy to calculate for a diagonal diffusion matrix, e.g. for $j = \alpha_j$:

$$S_{\alpha_j} = -\frac{1}{2}\frac{\partial B_{\alpha_j\alpha_j}}{\partial\alpha_j}B_{\alpha_j\alpha_j} \tag{2.11.22}$$

$$= -\frac{1}{2}i\sqrt{iU}i\sqrt{iU}\alpha_j \tag{2.11.23}$$

$$= i\frac{U}{2}\alpha_j \tag{2.11.24}$$

and similarly

$$S_{\beta_j} = -i\frac{U}{2}\beta_j \tag{2.11.25}$$

The Stratonovich form of the equations is then given by

$$\begin{aligned} d\alpha_j &= iJ\left(\alpha_{j+1}+\alpha_{j-1}\right)dt - iU\alpha_j^2\beta_j dt - i(\frac{j^2K}{2}-\frac{U}{2})\alpha_j dt + i\sqrt{iU}\alpha_j \circ \xi_j dt \\ d\beta_j &= -iJ\left(\beta_{j+1}-\beta_{j-1}\right)dt + iU\beta_j^2\alpha_j dt + i(\frac{j^2K}{2}-\frac{U}{2})\beta_j dt + \sqrt{iU}\beta_j \circ \eta_j dt, \end{aligned} \tag{2.11.26}$$

with an appropriately modified drift term. In most cases, it is often better to work with log variables as they exhibit better convergent properties. As a demonstration of Stratonovich calculus, it would be instructive to go through this change of variables procedure. In particular we choose to work with the variables:

$$\theta_j = \frac{1}{2}\ln(\alpha_j\beta_j) \tag{2.11.27}$$

and

$$\phi_j = \frac{1}{2i}\ln(\frac{\alpha_j}{\beta_j}), \tag{2.11.28}$$

and derive SDEs for it. In the Stratonovich form, we can treat the variables using the rules of regular calculus so that:

$$d\theta_j = \frac{1}{2\alpha_j\beta_j}\left(d\alpha_j\beta_j + d\beta_j\alpha_j\right) \tag{2.11.29}$$

$$= \frac{1}{2}\left(\frac{d\alpha_j}{\alpha_j}+\frac{d\beta_j}{\beta_j}\right) \tag{2.11.30}$$

$$= \frac{1}{2}\left(iJ\left(\frac{\alpha_{j+1}+\alpha_{j-1}}{\alpha_j}-\frac{\beta_{j+1}+\beta_{j-1}}{\beta_j}\right)dt + \sqrt{iU}\left(\xi_j+i\eta_j\right)dt\right) \tag{2.11.31}$$

which only retains the tunneling term in the drift. We should now express α,β in terms of the log variables. Note that since:

$$\alpha_j = e^{\theta_j+i\phi_j} \tag{2.11.32}$$

$$\beta_j = e^{\theta_j-i\phi_j} \tag{2.11.33}$$

the tunneling term can be rewritten as:

$$\begin{aligned} &\frac{\alpha_{j+1}+\alpha_{j-1}}{\alpha_j} - \frac{\beta_{j+1}+\beta_{j-1}}{\beta_j} = \frac{e^{\theta_{j+1}+i\phi_{j+1}}+e^{\theta_{j-1}+i\phi_{j-1}}}{e^{\theta_j+i\phi_j}} - \frac{e^{\theta_{j+1}-i\phi_{j+1}}+e^{\theta_{j-1}-i\phi_{j-1}}}{e^{\theta_j-i\phi_j}} \\ &= e^{\Delta\theta_j^+}e^{i\Delta\phi_j^+} + e^{\Delta\theta_j^-}e^{i\Delta\phi_j^-} - e^{\Delta\theta_j^+}e^{-i\Delta\phi_j^+} - e^{\Delta\theta_j^-}e^{-i\Delta\phi_j^-} \\ &= e^{\Delta\theta_j^+}\left(e^{i\Delta\phi_j^+}-e^{-i\Delta\phi_j^+}\right) + e^{\Delta\theta_j^-}\left(e^{i\Delta\phi_j^-}-e^{-i\Delta\phi_j^-}\right) \\ &= 2ie^{\Delta\theta_j^+}\sin(\Delta\phi_j^+) + 2ie^{\Delta\theta_j^-}\sin(\Delta\phi_j^-), \end{aligned} \tag{2.11.34}$$

where $\Delta\theta_j^{\pm} = \theta_{j\pm1} - \theta_j$ and $\Delta\phi_j^{\pm} = \phi_{j\pm1} - \phi_j$. For later reference, we will also calculate the addition of the tunnelling term

$$\begin{aligned}
&\frac{\alpha_{j+1}+\alpha_{j-1}}{\alpha_j} + \frac{\beta_{j+1}+\beta_{j-1}}{\beta_j} = \frac{e^{\theta_{j+1}+i\phi_{j+1}} + e^{\theta_{j-1}+i\phi_{j-1}}}{e^{\theta_j+i\phi_j}} + \frac{e^{\theta_{j+1}-i\phi_{j+1}} + e^{\theta_{j-1}-i\phi_{j-1}}}{e^{\theta_j-i\phi_j}} \\
&= e^{\Delta\theta_j^+} e^{i\Delta\phi_j^+} + e^{\Delta\theta_j^-} e^{i\Delta\phi_j^-} + e^{\Delta\theta_j^+} e^{-i\Delta\phi_j^+} + e^{\Delta\theta_j^-} e^{-i\Delta\phi_j^-} \\
&= e^{\Delta\theta_j^+} \left(e^{i\Delta\phi_j^+} + e^{-i\Delta\phi_j^+}\right) + e^{\Delta\theta_j^-} \left(e^{i\Delta\phi_j^-} + e^{-i\Delta\phi_j^-}\right) \\
&= 2e^{\Delta\theta_j^+} \cos(\Delta\phi_j^+) + 2e^{\Delta\theta_j^-} \cos(\Delta\phi_j^-),
\end{aligned} \tag{2.11.35}$$

The Stratonovich SDEs for the θ_j variable is then given by

$$d\theta_j = -J\left(e^{\Delta\theta_j^+} \sin(\Delta\phi_j^+) + e^{\Delta\theta_j^-} \sin(\Delta\phi_j^-)\right) dt + \frac{1}{2}\sqrt{iU}\left(i\xi_j + \eta_j\right) dt \tag{2.11.36}$$

We can similarly derive SDES for the $\phi = \frac{1}{2i}\ln(\frac{\alpha}{\beta})$ variable:

$$\begin{aligned}
d\phi_j &= \frac{1}{2i}\frac{\beta}{\alpha}\left(\frac{d\alpha}{\beta} - \frac{\alpha}{\beta^2}d\beta\right) && (2.11.37)\\
&= \frac{1}{2i}\left(\frac{d\alpha}{\alpha} - \frac{d\beta}{\beta}\right) && (2.11.38)\\
&= \frac{1}{2i}\left(J\left(\frac{\alpha_{j+1}+\alpha_{j-1}}{\alpha_j} + \frac{\beta_{j+1}+\beta_{j-1}}{\beta_j}\right) dt - 2iU\alpha_j\beta_j dt - i\left(j^2K - U\right) dt \right. \\
&\quad \left. + \sqrt{iU}(i\xi_j - \eta_j)\right) dt && (2.11.39)\\
&= -iJ\left(e^{\Delta\theta_j^+} \cos(\Delta\phi_j^+) + e^{\Delta\theta_j^-} \cos(\Delta\phi_j^-)\right) dt - Ue^{2\theta_j} dt - \frac{1}{2}\left(j^2K - U\right) dt \\
&\quad + \frac{1}{2}\sqrt{iU}\left(\xi_j + i\eta_j\right) dt && (2.11.40)
\end{aligned}$$

Taken together, the SDEs to integrate are

$$\begin{aligned}
d\theta_i &= -J\left(e^{\Delta\theta_j^+} \sin(\Delta\phi_j^+) + e^{\Delta\theta_j^-} \sin(\Delta\phi_j^-)\right) dt + \frac{i}{2}\sqrt{iU}\Xi_j^* dt \\
d\phi_i &= -iJ\left(e^{\Delta\theta_j^+} \cos(\Delta\phi_j^+) + e^{\Delta\theta_j^-} \cos(\Delta\phi_j^-)\right) dt - Ue^{2\theta_j} dt - \frac{1}{2}\left(j^2K - U\right) dt + \frac{1}{2}\sqrt{iU}\Xi_j dt
\end{aligned} \tag{2.11.41}$$

where we define the complex noise: $\Xi_j = \left(\xi_j + i\eta_j\right)$. Note that we can also take diffusion gauges into

consideration. Following the receipe in section 2.5.3, the noise matrix can be modified as:

$$\underline{B}\,\vec{\xi} = \underline{B_o}.\underline{O}\,\vec{\xi} \tag{2.11.42}$$

$$= \frac{\sqrt{iU}}{2}\begin{bmatrix} i & 1 \\ 1 & i \end{bmatrix}\begin{bmatrix} \cosh(A) & -i\sinh(A) \\ i\sinh(A) & \cosh(A) \end{bmatrix}\begin{bmatrix} \xi_j \\ \eta_j \end{bmatrix} \tag{2.11.43}$$

$$= \frac{\sqrt{iU}}{2}\begin{bmatrix} i & 1 \\ 1 & i \end{bmatrix}\begin{bmatrix} \cosh(A)\xi_j - i\sinh(A)\eta_j \\ i\sinh(A)\xi_j + \cosh(A)\eta_j \end{bmatrix} \tag{2.11.44}$$

which means that our original noise terms are affected in the following way: $\xi_j \to \cosh(A)\xi_j + i\sinh(A)\eta_j$ and $\eta_j \to i\sinh(A)\xi_j + \cosh(A)\eta_j$. The equations are changed in the following way:

$$\begin{aligned} d\theta_i &= -J\left(e^{\Delta\theta_j^+}\sin(\Delta\phi_j^+) + e^{\Delta\theta_j^-}\sin(\Delta\phi_j^-)\right)dt + \frac{i}{2}\sqrt{iU}e^{A}\Xi_j^* dt \\ d\phi_i &= -iJ\left(e^{\Delta\theta_j^+}\cos(\Delta\phi_j^+) + e^{\Delta\theta_j^-}\cos(\Delta\phi_j^-)\right)dt - Ue^{2\theta_j}dt - \frac{1}{2}\left(j^2K - U\right)dt + e^{-A}\frac{1}{2}\sqrt{iU}\Xi_j dt \end{aligned} \tag{2.11.45}$$

where A is an arbitrary constant and determined empirically so as to maximize simulation lifetimes. From eq. 2.11.45, we can see how the diffusion gauge stabilizes the equations. Its effect is such that for $A > 0 (A < 0)$, the noise terms in ϕ_j decrease (increase) whereas for θ_j increasing (decreasing). An optimal value of A can therefore be chosen so as to minimize the variances of θ_j or ϕ_j (Plimak et al., 2001, Deuar and Drummond, 2006). In principle, it could also be generalized to a function of stochastic variables, in which case it would be necessary to properly take into consideration Stratonovich correction terms.

2.11.2 Results for the non-interacting case: $U = 0$

For a test quench protocol, we perform an extreme quench to the non-interacting limit: $U_i = \infty \to U_f = 0$ and evolve the system using the pure Superfluid Hamiltonian, starting from the Mott state of $|\psi(t)\rangle = |1,0,1,0,\ldots\rangle$. Note that this requires the use of the gamma distribution function to model the Fock state as mentioned in section 2.5.7. The results in this section were performed using the α_i, β_i variables and subsequently setting $U = 0$ in eq. 2.11.26. In the non-interacting regime, the thermodynamics limit of several observables can be calculated analytically (Flesch et al., 2008) and serve as a benchmark to compare our results against. The main observable is given by the average occupation number for odd and even site

$$\begin{aligned} \langle\hat{n}_i(t)\rangle &= \frac{1}{2} - \frac{(-1)^i}{2L}\sum_{k=1}^{L} e^{4iJt\cos(2\pi k/L)} \\ &\to \frac{1}{2} - \frac{(-1)^i}{2}J_0(4Jt), \end{aligned} \tag{2.11.46}$$

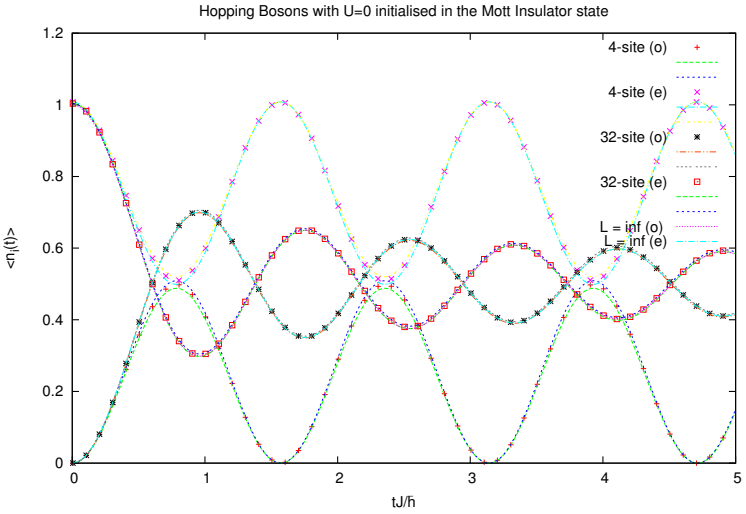

Figure 2.1: Average occupation number of even/ odd site ($\langle n_i(t)\rangle$) vs $tJ/\hbar$. The results are for $N=4$ (even and odd) and $N=32$ (even and odd). The exact results for an infinite lattice with $(U=0)$ are also shown in the plot. Simulations parameters: $T=5.0, dt=0.005, N_{bins}=100, N_{sample}=100$.

.

where $J_0(x)$ is the bessel J function of the first kind, i is either even or odd and L is the number of sites. The complex phase space function associated with the number operator is given by:

$$\langle\langle \hat{n}_i\rangle\rangle = \Re\left[\frac{1}{(N/2)}\sum_i(\beta_i\alpha_i)\right] \tag{2.11.47}$$

Next we calculate the correlators or green's function between sites j and k, which in the thermodynamic limit has the exact result:

$$f_{j,k} \equiv \langle \hat{b}_j^\dagger(t)\hat{b}_k(t)\rangle = \frac{1}{2}\delta_{jk} - \frac{(-1)^j i^{k-j}}{2} J_{k-j}(4Jt) \tag{2.11.48}$$

so that the nearest neighbor and the next nearest neighbor correlators are given by:

$$\begin{aligned} f_{j+1,j} &= \frac{1}{2}\delta_{j+1,j} - \frac{(-1)^{j+1} i^{j-(j+1)}}{2} J_{j-(j+1)}(4Jt) && (2.11.49)\\ &= -\frac{(-1)(-1)^j}{2}(i^{-1})J_{-1}(4Jt) && (2.11.50)\\ &= \frac{(-1)^j}{2i}J_{-1}(4Jt) && (2.11.51)\end{aligned}$$

Using the property of Bessel functions that: $J_{-n} = (-1)^n J_n(x)$, where $n \in Z$ we get:

$$f_{j+1,j} = -\frac{(-1)^j}{2i}J_1(4Jt), \tag{2.11.52}$$

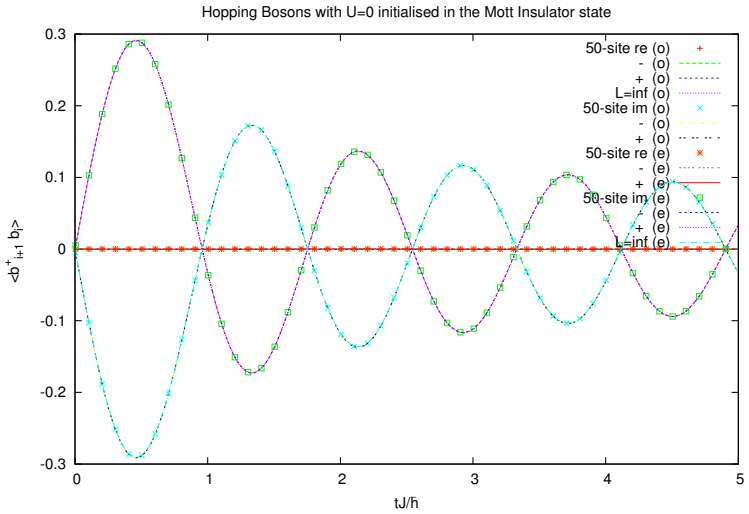

Figure 2.2: Nearest neighbor correlators for lattice averaged even/ odd site $\langle \hat{b}^{\dagger}_{i+1}\hat{b}_i \rangle$ vs $tJ/\hbar$. The real and imaginary parts of $\langle \hat{b}^{\dagger}_{i+1}\hat{b}_i \rangle$ are shown.The results are for $N = 50$ (even and odd). The exact results for an infinite lattice with $(U = 0)$ are also shown in the plot. Simulations parameters: $T = 5.0, dt = 0.005, N_{bins} = 100, N_{sample} = 100$.

.

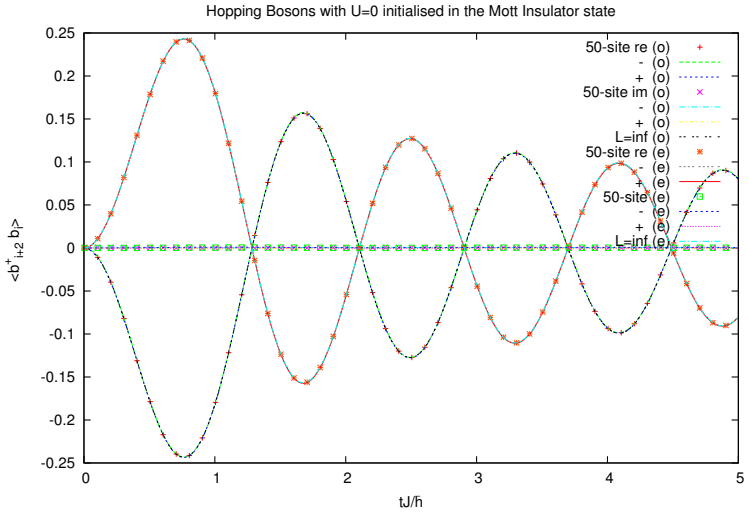

Figure 2.3: Next nearest neighbor correlators for lattice averaged even/ odd site $\langle \hat{b}^{\dagger}_{i+2}\hat{b}_i \rangle$ vs $tJ/\hbar$. The real and imaginary parts of $\langle \hat{b}^{\dagger}_{i+2}\hat{b}_i \rangle$ are shown.The results are for $N = 50$ (even and odd). The exact results for an infinite lattice with $(U = 0)$ are also shown in the plot. Simulations parameters: $T = 5.0, dt = 0.005, N_{bins} = 100, N_{sample} = 100$.

.

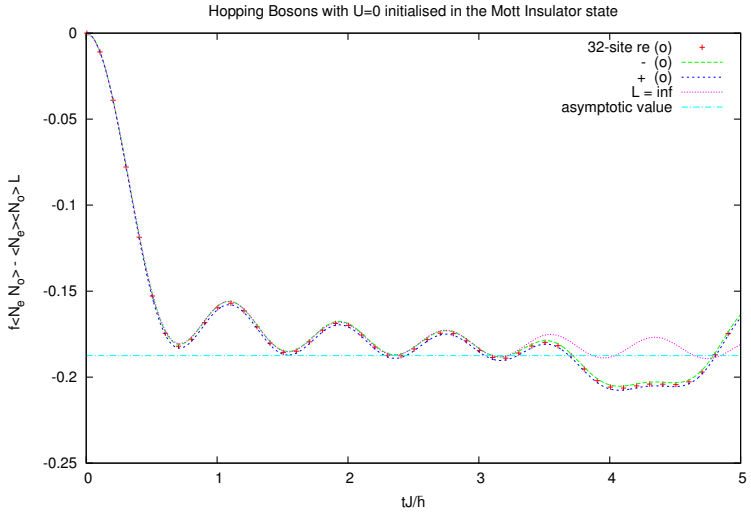

Figure 2.4: Global density-density correlators: $\frac{\left(\hat{N}_e(t)\hat{N}_o(t)\rangle - \langle\hat{N}_e(t)\rangle\langle\hat{N}_o(t)\right)}{L}$ vs $tJ/\hbar$. The results are for $N = 32$ (even and odd). The exact results for an infinite lattice with $(U = 0)$ are also shown in the plot. The agreement is not as good but can be improved by using larger lattice sizes. Simulations parameters: $T = 5.0, dt = 0.005, N_{bins} = 100, N_{sample} = 100$.

.

which depends on the evenness and oddness of j. Note that this quantity is pure imaginary as well and so the calculation of the real part should yield zero. This is indeed observed in fig. 2.2. Similarly the next-nearest-neighbor (NNN) correlator is given by

$$f_{j+2,j} = \frac{1}{2}\delta_{j+2,j} - \frac{(-1)^{j+2}i^{j-(j+2)}}{2}J_{j-(j+2)}(4Jt) \tag{2.11.53}$$

$$= -\frac{(-1)(-1)^j}{2}(i^{-2})J_{-2}(4Jt) \tag{2.11.54}$$

$$= \frac{(-1)^j}{2}J_{-2}(4Jt) \tag{2.11.55}$$

and in contrast to the NN correlator in eq. 2.11.51, this is a real quantity. The general expression for the stochastic estimator of the correlators are

$$\Re\left[\langle\langle\hat{b}^\dagger_{i+1}\hat{b}_i\rangle\rangle\right] = \Re\left[\frac{1}{(N/2)}\sum_{i\in e \text{ or } o}\beta_{i+1}\alpha_i\right] \tag{2.11.56}$$

and

$$\Im\left[\langle\langle\hat{b}^\dagger_{i+1}\hat{b}_i\rangle\rangle\right] = \Im\left[\frac{1}{(N/2)}\sum_{i\in e \text{ or } o}\beta_{i+1}\alpha_i\right]. \tag{2.11.57}$$

It is important to note that i is either even or odd and does not simply run over the entire lattice. The last observable which we calculated is the global density density correlator defined in the large

L limit as:

$$\langle \hat{N}_e(t)\hat{N}_o(t)\rangle - \langle \hat{N}_e(t)\rangle\langle \hat{N}_o(t)\rangle \to -\frac{L}{16}\left\{3 + J_0(8Jt) - 4\left[J_0(4Jt)\right]^2\right\}, \tag{2.11.58}$$

where $N_{e,o}(t) = \sum_{i\in e,o} n_i$ is the total number of particles in the even/odd sites. The stochastic estimator of the first term has to be evaluated as a single expression and one should be careful not to take the real part of the even and odd terms individually. Namely, we want to calculate the stochastic average of

$$\langle\langle N_e(t)N_o(t)\rangle\rangle = \Re\left[\sum_{i\in e}\sum_{j\in o}\beta_j\alpha_j\beta_i\alpha_i\right], \tag{2.11.59}$$

and not

$$\Re\left[\sum_{j\in e}\beta_j\alpha_j\right]\Re\left[\sum_{i\in o}\beta_i\alpha_i\right], \tag{2.11.60}$$

which is instead the stochastic estimator for the second term on the LHS of eq. 2.11.58.

In Fig 2.1-Fig 2.4, we have compared the exact analytic results with PPR simulations for all observables discussed above. Even though in the non-interacting regime, the SDEs reduce to ordinary differential equations, stochasticity is still present in the sampling of the initial state and is necessary to reproduce the exact dynamics. Despite the simplicity of this treatment, it demonstrates excellent agreement with the exact results while requiring only a small number of trajectories.

2.11.3 The interacting case: $U \neq 0$

Needless to say, it would be more interesting to examine the evolution of the Mott state for $U \neq 0$. First of all since such quenches have no known analytic solution, its dynamics have to be determined either by numerical simulations or experiments (Trotzky et al., 2012). Secondly, it also serves as an illustrative demonstration of spiking in numerical simulations and the limitations of the PP formalism. Our results for the odd and even site occupation number are plotted in Fig. 2.5 for a series of U values ranging from $0.1 - 1.0$. The simulation lifetime for each U value is taken as the time at which the first sign of spiking is observed. Such spiking is expected since the drift terms arising from the anharmonic contributions in eq. 2.11.26 violates eq. 2.9.1. The appearance of the standalone single mode anharmonic oscillator: $\hat{H}_i = \hat{a_i}^{\dagger 2}\hat{a_i}^2$ is the root of this behavior and several attempts have been made to circumvent it. These include Monte-Carlo techniques (Dowling et al., 2007), adhoc modifications to the SDEs themselves (Perret and Petersen, 2011) and the use of a combination of drift and diffusion gauges (Deuar, 2005). Gauges are arguably the most effective and reliable way for improving the simulation lifetimes of the single mode anharmonic oscillator. However when coupling between modes is present, their positive effects are neutralized. See (Deuar and Drummond, 2006) for a detailed study. From our simulations, we find that that including interactions severely reduces the lifetimes of the bare PPR simulations and decays exponentially with U as seen in Fig. 2.6. We also note that the use of log variables or drift and diffusion gauges were unsuccessful in improving simulation lifetimes.

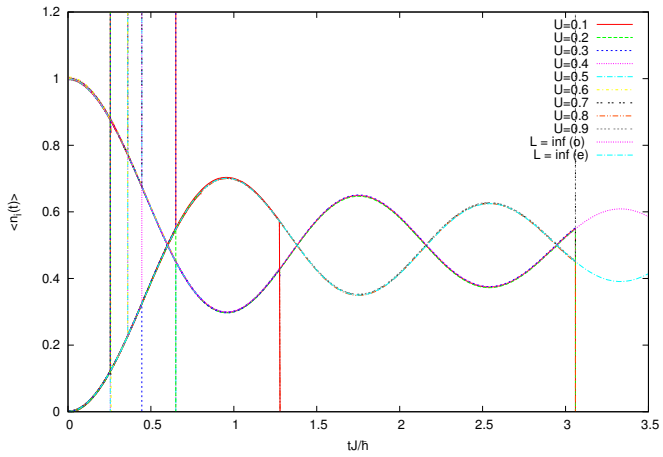

Figure 2.5: $\langle n_i(t)\rangle$ vs U for $N = 32$ site Bose-Hubbard model. Spiking for different interaction strength U, can be seen in the form of sharp vertical lines.

.

2.12 The transverse Ising model

In this thesis, we are interested in simulating the quench dynamics of quantum spin systems. As a test system, we focus primarily on the paradigmatic spin-1/2 transverse Ising model (TIM) (Pfeuty, 1970) defined by:

$$\hat{H} = -J\sum_{\langle i,j\rangle}\hat{S}_i^z\hat{S}_j^z - h\sum_i \hat{S}_i^x, \tag{2.12.1}$$

in 1D and 2D for quantum dynamic simulations, although we have also attempted to calculate the dynamics of the more general transverse field anisotropic Heisenberg model as well (Ng, 2010). In eq. 2.12.1, $\left\{\hat{S}^\alpha\right\}|_{\alpha=x,y,z}$ are the usual Pauli matrices multiplied by a factor of $\frac{1}{2}$ and $\langle i,j\rangle$ denotes nearest-neighbour sites. The 1D TIM is an integrable model and can be diagonalized using Jordan-Wigner transformation (Sachdev, 2011). In higher dimensions however, no known exact solution exists which makes it dynamics only accessible either by numerical efforts or experiments. Despite its simplicity, it manifests several interesting dynamical properties (Heyl et al., 2013, Rossini et al., 2009, Silva, 2008) and its asymptotic temporal properties after a quench have only recently been calculated (Calabrese et al., 2011, 2012a,b). This is largely in part owing to the shifting interest of research efforts to that of non-equilibrium phenomena and the successful emulation of spin systems in optical lattices (Simon et al., 2011, Friedenauer et al., 2008, Porras and Cirac, 2004, Britton et al., 2012). The publication included in section 2.13 presents our first application of the PPR on simulating the quench dynamics of transverse field spin systems in 1D. Majority of the derivations can be found in the paper to follow and explicit details can be found in (Ng, 2010).

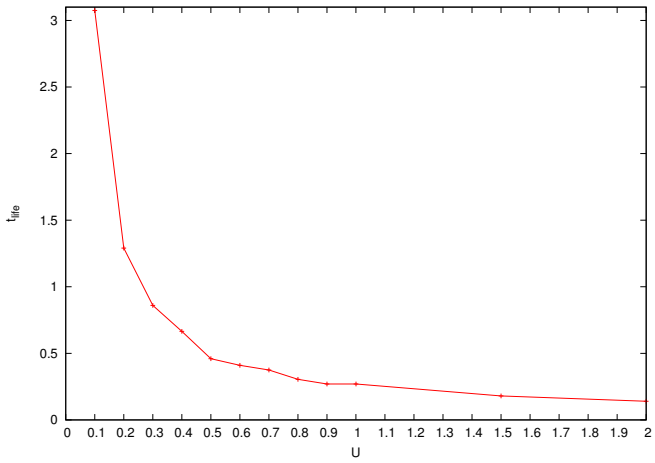

Figure 2.6: t_{life} vs U for $N = 32$ site Bose-Hubbard model. t_{life} is taken as the first sign that spiking occurs at each interaction strength U.

.

2.13 Paper 1: Exact real-time dynamics of quantum spin systems using the positive-P representation

Exact Real-Time Dynamics of Quantum Spin Systems Using the Positive-P Representation
– *Ray Ng and Erik S. Sørensen*

J. Phys. A: Math. Theor. 44 065305

doi: 10.1088/1751-8113/44/6/065305

Calculations: I performed all the simulations and produced all the figures.

Manuscript: I wrote the bulk of the manuscript. Erik S. Sørensen helped to refine and edit the Introduction.

In this publication, we set out to answer the following questions:

- Is the PPR amenable to quantum spin systems in particular: the transverse field spin-1/2 XXZ and transverse-field Ising model?
- To what extent are we able to simulate the real time dynamics of spin system following a quantum quench?
- What are the largest system sizes that we can simulate?
- What are the largest time scales that can be achieved (without gauges)?
- What are the causes of the limitations (if any) of the PPR in the context of spin systems?

IOP PUBLISHING JOURNAL OF PHYSICS A: MATHEMATICAL AND THEORETICAL

J. Phys. A: Math. Theor. **44** (2011) 065305 (23pp) doi:10.1088/1751-8113/44/6/065305

Exact real-time dynamics of quantum spin systems using the positive-P representation

R Ng and E S Sørensen

Department of Physics and Astronomy, McMaster University, 1280 Main St W, L8S4LM, Hamilton, ON, Canada

E-mail: ngry@mcmaster.ca

Received 27 September 2010, in final form 17 December 2010
Published 17 January 2011
Online at stacks.iop.org/JPhysA/44/065305

Abstract
We discuss a scheme for simulating the *real-time* quantum quench dynamics of interacting quantum spin systems within the positive-P formalism. As model systems we study the transverse field Ising model as well as the Heisenberg model undergoing a quench away from the classical ferromagnetic ordered state and the antiferromagnetic Néel state, depending on the sign of the Heisenberg exchange interaction. The connection to the positive-P formalism as it is used in quantum optics is established by mapping the spin operators on to Schwinger bosons. In doing so, the dynamics of the interacting quantum spin system is mapped onto a set of Ito stochastic differential equations the number of which scales *linearly* with the number of spins, N, compared to an exact solution through diagonalization that, in the case of the Heisenberg model, would require matrices exponentially large in N. This mapping is *exact* and can be extended to higher dimensional interacting systems as well as to systems with an explicit coupling to the environment.

PACS numbers: 05.10.Gg, 75.10.Pq, 75.10.Jm

(Some figures in this article are in colour only in the electronic version)

1. Introduction

The *real-time* quantum dynamics following a quench [1–15] is a problem of considerable current interest. Here, our focus is on methods applicable to this problem that are in principle exact (up to controllable errors) and we leave approximate methods aside. Unfortunately, standard quantum Monte Carlo techniques yield results in the imaginary time domain and require an explicit analytic continuation to access real times, a notoriously difficult procedure. For lattice-based models it is possible to perform exact diagonalization but for an N site quantum spin system the size of the Hilbert space is exponential in N, severely limiting

1751-8113/11/065305+23$33.00

the applicability of this method. In recent years, methods rooted in the density matrix renormalization group (DMRG) such as TEBD [16] and t-DMRG [17] have been developed to study real-time dynamics of one-dimensional systems. Most recently the infinite size TEBD (iTEBD) has been tuned to yield results for the time dependence of the transverse field Ising model (TFIM) out to relatively large times of order $tJ/\hbar \sim 6$–10 [18] as well as in the XXZ and related spin chain models $tJ/\hbar \sim 20$ [5, 9] and often times scales of order $tJ/\hbar \sim 100$ can be accessed [19]. How well such methods will perform in higher dimensions or in the presence of a coupling to the environment is presently a point of intense research and very promising progress has been made [20–23]. Here we investigate an alternative approach for studying the dynamics of interacting quantum spin systems using quantum phase space methods, in particular, the positive-P representation (PPR) [24] of the density operator. As model systems we have studied the one-dimensional TFIM as well as the Heisenberg model. This approach is quite general and can be extended to higher dimensional interacting quantum spin systems and to open systems with an explicit coupling to the environment.

In general, quantum phase space methods map the dynamics of bosonic operators onto the stochastic evolution of complex phase space variables [24]. Using the PPR, we can easily calculate the expectation values of any normal-ordered products of creation and annihilation operators by calculating the stochastic averages of their equivalent representation in terms of phase-space variables. This is carried out in two steps; first we use Schwinger bosons to replace the Heisenberg spin operators, then employ the PPR. The PPR converts the master equation into a Fokker–Planck equation (FPE) which can then be mapped onto a set of coupled, complex Ito stochastic differential equations (SDEs). The number of SDEs to simulate scales linearly with the number of spins in the system, N, in contrast to an exact diagonalization approach.

To illustrate the feasibility of this approach we study the dynamics of the TFIM as well as the isotropic ferromagnetic (FM) Heisenberg model subject to a quantum quench at $T = 0$. The different models are related through the anisotropy parameter, Δ/J. The spin chains are prepared in the FM state at $t = 0$ whenever we assume a FM Heisenberg model, and evolved by including the transverse magnetic field term at $t \geqslant 0$. We calculate the time evolution of the expectation values of the spin operators: $[S^x]$, $[S^y]$ $[S^z]$, which is an average of the individual components over the entire lattice. The averaging is allowed because of the translational symmetry of the system. In addition, we also calculate the results of $\hat{S}_z$ nearest-neighbor correlation functions: $\left[\hat{S}_i^z \hat{S}_{i+1}^z\right]$ for the TFIM. In order to verify the validity of our results, we in all cases compare them with results from exact diagonalization obtaining the excellent agreement.

In a bid to fully take advantage of the PPR, we also attempt to explore finite size effects by simulating lattice sizes of up to 100 spins for the FM isotropic model and 10 spins for the antiferromagnetic (AFM) anisotropic model. Finite size effects are more noticeable in the AFM Hamiltonian, and for the latter the natural choice for an initial state is the classical Néel state.

Since the PPR is well established in quantum optics, we will relegate the details of the formalism to appendix A. Readers who are already familiar with the PPR may continue to section 2 where Schwinger bosons are employed to map the spin operators onto bosonic operators. The resulting SDEs are derived in this section with more explicit details laid out in appendic C. In section 3, the results of the TFIM ($\Delta/J = 0.0$) and the isotropic ($\Delta/J = 1.0$) Heisenberg model are compared with exact diagonalization calculations. We also carry out a brief discussion on the possibility of extending simulation life times by potentially using the gauge-P representation [25] instead. In section 3.1, we present our results for finite-size effects in both the anisotropic AFM and the isotropic FM Hamiltonian and discuss our findings.

Results and a short discussion on the correlation functions can be found in section 3.2. The conclusion is presented in section 4.

2. Using Schwinger bosons to derive SDEs

The PPR is based on bosonic coherent states and is only directly applicable to Hamiltonians written in terms of bosonic annihilation and creation operators. In order to apply it to the Heisenberg model or any spin Hamiltonian, we therefore need to rewrite the spin operators in terms of bosonic operators. A convenient way of doing this is by employing the Schwinger boson representation [26, 27] and we will demonstrate how it can be applied to the Heisenberg model. A similar approach, based on Schwinger bosons, was previously applied to the study of spontaneous emission non-interacting two-level atoms [28] in quantum optics.

The Heisenberg Hamiltonian with FM ($J > 0$) or AFM interaction ($J < 0$) subject to a quench in the x-direction at $t \geqslant 0$ is given by

$$\hat{H} = -J \sum_{\langle i,j \rangle} \hat{\mathbf{S}}_i \cdot \hat{\mathbf{S}}_j - h(t) \sum_i \hat{S}_i^x, \qquad h(t) = \begin{cases} h, & t \geqslant 0 \\ 0, & t < 0 \end{cases} \tag{1}$$

and can be written in terms of the usual raising and lowering operators, $\hat{\mathbf{S}}^{\pm} = \hat{\mathbf{S}}^{\mathbf{x}} \pm \mathrm{i}\hat{\mathbf{S}}^{\mathbf{y}}$. If we allow anisotropy in the transverse direction[1], then the Hamiltonian takes the following form:

$$\hat{H}_{\mathrm{Heis}} = -\sum_{\langle i,j \rangle} \left[J \hat{S}_i^z \hat{S}_j^z + \Delta \frac{1}{2} \left(\hat{S}_i^+ \hat{S}_j^- + \hat{S}_i^- \hat{S}_j^+ \right) \right] - \frac{1}{2} h(t) \sum_i \left[\hat{S}_i^+ + \hat{S}_i^- \right] \tag{2}$$

where $\langle i, j \rangle$ indicates nearest-neighbor pairs and Δ/J is a measure of anisotropy. The two models which we first examined were the (i) TFIM ($\Delta/J = 0$):

$$\hat{H}_{\mathrm{TFIM}} = -\sum_{\langle i,j \rangle} \left[J \hat{S}_i^z \hat{S}_j^z \right] - \frac{1}{2} h(t) \sum_i \left[\hat{S}_i^+ + \hat{S}_i^- \right] \tag{3}$$

and the (ii) isotropic Heisenberg model (see equation (2)) with an anisotropy of $\Delta/J = 1.0$.

The Schwinger boson representation of spins (setting $\hbar = 1$) is given by

$$\hat{S}^+ \to \hat{b}\hat{a}^\dagger, \qquad \hat{S}^- \to \hat{b}^\dagger \hat{a}, \qquad \hat{S}^z \to \tfrac{1}{2}(\hat{a}^\dagger \hat{a} - \hat{b}^\dagger \hat{b}). \tag{4}$$

where $\hat{a}$ and $\hat{b}$ represent two types of bosons and the following commutation relations:

$$\begin{aligned} \left[\hat{S}^+, \hat{S}^-\right] &\to \left[\hat{a}^\dagger \hat{b}, \hat{b}^\dagger \hat{a}\right] = \hat{a}^\dagger \hat{a} - \hat{b}^\dagger \hat{b} \to 2\hat{S}^z, \\ \left[\hat{S}^+, \hat{S}^z\right] &\to \left[\hat{a}^\dagger \hat{b}, \frac{1}{2}(\hat{a}^\dagger \hat{a} - \hat{b}^\dagger \hat{b})\right] = -\hat{a}^\dagger \hat{b} \to -\hat{S}^+, \\ \left[\hat{S}^-, \hat{S}^z\right] &\to \left[\hat{b}^\dagger \hat{a}, \frac{1}{2}(\hat{a}^\dagger \hat{a} - \hat{b}^\dagger \hat{b})\right] = \hat{b}^\dagger \hat{a} \to \hat{S}^- \end{aligned} \tag{5}$$

demonstrate that the commutation relations of the spin operators are indeed preserved. This is a necessary requirement for a successful mapping. With the Schwinger representation, the two states of a spin-1/2 particle are now described by either an $\hat{a}$-boson or a $\hat{b}$-boson per site. A spin-up state: $|\uparrow\rangle$ is the same as having a single $\hat{a}$-boson whereas a spin down-state: $|\downarrow\rangle$ is the same as having a single $\hat{b}$-boson. We can therefore replace the spin operators in equations (2) and (3) with the bosonic mapping in equation (4) without altering the physics.

[1] The transverse direction is relative to the quantization axis which we have taken to be the z-axis.

As the PPR is well established[2], we will relegate a brief review of the formalism to appendix A. Additional technical details pertaining to the specific examples in this paper can be found in appendix C. For brevity we will present the derivations for only the TFIM (see equation (3)) where $\Delta/J = 0$.

Using equation (4), the equivalent bosonic Hamiltonian for the TFIM is given by

$$\hat{H} = -\frac{J}{4}\sum_{\langle i,j\rangle}\left(\hat{a}_i^\dagger\hat{a}_i\hat{a}_j^\dagger\hat{a}_j - \hat{a}_i^\dagger\hat{a}_i\hat{b}_j^\dagger\hat{b}_j - \hat{b}_i^\dagger\hat{b}_i\hat{a}_j^\dagger\hat{a}_j + \hat{b}_i^\dagger\hat{b}_i\hat{b}_j^\dagger\hat{b}_j\right) - \left(h(t)\sum_i \hat{a}_i^\dagger\hat{b}_i + \hat{b}_i^\dagger\hat{a}_i\right). \quad (6)$$

Now if we take our system to be closed, its dynamics can be captured via the master equation for the density operator, i.e.

$$\frac{\mathrm{d}}{\mathrm{d}t}\hat{\rho} = -\frac{\mathrm{i}}{\hbar}\left[\hat{H},\hat{\rho}\right], \quad (7)$$

which allows us to use a generalized prescription of the PPR. In principle, it is also possible to calculate open system dynamics by including a Liouvillan term in equation (7): $\hat{L}[\hat{\rho}]$,[3] and so this approach is by no means limited to closed system.

To proceed, we first write our density operator in terms of a direct product of projection operators for each site, i.e.

$$\hat{\Lambda}(\vec{\alpha},\vec{\alpha}^+,\vec{\beta},\vec{\beta}^+) = \prod_{i=0}^{N-1}\otimes\frac{|\alpha_i\rangle\langle\alpha_i^{+*}|}{\langle\alpha_i^{+*}|\alpha_i\rangle}\otimes\frac{|\beta_i\rangle\langle\beta_i^{+*}|}{\langle\beta_i^{+*}|\beta_i\rangle} \quad (8)$$

where $\vec{\alpha} = (\alpha_0,\ldots,\alpha_{N-1})$, $\vec{\alpha}^+ = (\alpha_0^+,\ldots,\alpha_{N-1}^+)$, $\vec{\beta} = (\beta_0,\ldots,\beta_{N-1})$ and $\vec{\beta}^+ = (\beta_0^+,\ldots,\beta_{N-1}^+)$ so that

$$\hat{\rho} = \int P(\vec{\alpha},\vec{\alpha}^+,\vec{\beta},\vec{\beta}^+)\hat{\Lambda}(\vec{\alpha},\vec{\alpha}^+,\vec{\beta},\vec{\beta}^+)\mathrm{d}^2\vec{\alpha}\mathrm{d}^2\vec{\alpha}^+\mathrm{d}^2\vec{\beta}\mathrm{d}^2\vec{\beta}^+. \quad (9)$$

We can then use the usual correspondence relations (see equation (A.3)) to obtain an FPE (see equation (A.4)) for the PPR distribution function: $P(\vec{\alpha},\vec{\alpha}^+,\vec{\beta},\vec{\beta}^+)$. A particular factorization of the diffusion matrix results in a noise matrix which gives us a set of Ito SDEs for $4N$ of our phase space variables, i.e.

$$\begin{aligned}\mathrm{d}\alpha_i &= \left\{\frac{\mathrm{i}J}{4\hbar}\alpha_i\left[\left(n_{i+1}^\alpha - n_{i+1}^\beta\right) + \left(n_{i-1}^\alpha - n_{i-1}^\beta\right)\right] + \frac{\mathrm{i}h(t)}{2\hbar}\beta_i\right\}\mathrm{d}t \\ &+ \frac{1}{2}\sqrt{\frac{\mathrm{i}J}{2\hbar}}\left[-\sqrt{\alpha_i\alpha_{i+1}}\left(\mathrm{d}W_{2i}^\alpha + \mathrm{i}\,\mathrm{d}W_{2i+1}^\alpha\right) - \sqrt{\alpha_i\alpha_{i-1}}\left(\mathrm{d}W_{2i-2}^\alpha - \mathrm{i}\,\mathrm{d}W_{2i-1}^\alpha\right)\right] \\ &+ \frac{\mathrm{i}}{2}\sqrt{\frac{\mathrm{i}J}{2\hbar}}\left[-\sqrt{\alpha_i\beta_{i-1}}\left(\mathrm{d}W_{2i-2}^{\alpha\beta} + \mathrm{i}\,\mathrm{d}W_{2i-1}^{\alpha\beta}\right) - \sqrt{\alpha_i\beta_{i+1}}\left(\mathrm{d}W_{2i}^{\beta\alpha} - \mathrm{i}\,\mathrm{d}W_{2i+1}^{\beta\alpha}\right)\right] \end{aligned} \quad (10)$$

$$\begin{aligned}\mathrm{d}\beta_i &= \left\{\frac{\mathrm{i}J}{4\hbar}\beta_i\left[\left(n_{i+1}^\beta - n_{i+1}^\alpha\right) + \left(n_{i-1}^\beta - n_{i-1}^\alpha\right)\right] + \frac{\mathrm{i}h(t)}{2\hbar}\alpha_i\right\}\mathrm{d}t \\ &+ \frac{1}{2}\sqrt{\frac{\mathrm{i}J}{2\hbar}}\left[-\sqrt{\beta_i\beta_{i+1}}\left(\mathrm{d}W_{2i}^\beta + \mathrm{i}\,\mathrm{d}W_{2i+1}^\beta\right) - \sqrt{\beta_i\beta_{i-1}}\left(\mathrm{d}W_{2i-2}^\beta - \mathrm{i}\,\mathrm{d}W_{2i-1}^\beta\right)\right] \\ &+ \frac{\mathrm{i}}{2}\sqrt{\frac{\mathrm{i}J}{2\hbar}}\left[-\sqrt{\alpha_{i+1}\beta_i}\left(\mathrm{d}W_{2i}^{\alpha\beta} - \mathrm{i}\,\mathrm{d}W_{2i+1}^{\alpha\beta}\right) - \sqrt{\alpha_{i-1}\beta_i}\left(\mathrm{d}W_{2i-2}^{\beta\alpha} + \mathrm{i}\,\mathrm{d}W_{2i-1}^{\beta\alpha}\right)\right] \end{aligned} \quad (11)$$

[2] See [28–33] for successful applications of the PPR.

[3] The Liouvillian term models the effect of the environment on the system.

$$\begin{aligned}
\mathrm{d}\alpha_i^+ &= \left\{\frac{\mathrm{i}J}{4\hbar}\alpha_i^+\left[\left(n_{i+1}^{\beta}-n_{i+1}^{\alpha}\right)+\left(n_{i-1}^{\beta}-n_{i-1}^{\alpha}\right)\right]-\frac{\mathrm{i}h(t)}{2\hbar}\beta_i^+\right\}\mathrm{d}t\\
&+\frac{\mathrm{i}}{2}\sqrt{\frac{\mathrm{i}J}{2\hbar}}\left[-\sqrt{\alpha_i^+\alpha_{i+1}^+}\left(\mathrm{d}W_{2i}^{\alpha^+}+\mathrm{i}\,\mathrm{d}W_{2i+1}^{\alpha^+}\right)-\sqrt{\alpha_i^+\alpha_{i-1}^+}\left(\mathrm{d}W_{2i-2}^{\alpha^+}-\mathrm{i}\,\mathrm{d}W_{2i-1}^{\alpha^+}\right)\right]\\
&+\frac{1}{2}\sqrt{\frac{\mathrm{i}J}{2\hbar}}\left[-\sqrt{\alpha_i^+\beta_{i-1}^+}\left(\mathrm{d}W_{2i-2}^{\alpha^+\beta^+}+\mathrm{i}\,\mathrm{d}W_{2i-1}^{\alpha^+\beta^+}\right)-\sqrt{\alpha_i^+\beta_{i+1}^+}\left(\mathrm{d}W_{2i}^{\beta^+\alpha^+}-\mathrm{i}\,\mathrm{d}W_{2i+1}^{\beta^+\alpha^+}\right)\right] \qquad (12)
\end{aligned}$$

$$\begin{aligned}
\mathrm{d}\beta_i^+ &= \left\{\frac{\mathrm{i}J}{4\hbar}\beta_i^+\left[\left(n_{i+1}^{\alpha}-n_{i+1}^{\beta}\right)+\left(n_{i-1}^{\alpha}-n_{i-1}^{\beta}\right)\right]-\frac{\mathrm{i}h(t)}{2\hbar}\alpha_i^+\right\}\mathrm{d}t\\
&+\frac{\mathrm{i}}{2}\sqrt{\frac{\mathrm{i}J}{2\hbar}}\left[-\sqrt{\beta_i^+\beta_{i+1}^+}\left(\mathrm{d}W_{2i}^{\beta^+}+\mathrm{i}\,\mathrm{d}W_{2i+1}^{\beta^+}\right)-\sqrt{\beta_i^+\beta_{i-1}^+}\left(\mathrm{d}W_{2i-2}^{\beta^+}-\mathrm{i}\,\mathrm{d}W_{2i-1}^{\beta^+}\right)\right]\\
&+\frac{1}{2}\sqrt{\frac{\mathrm{i}J}{2\hbar}}\left[-\sqrt{\alpha_{i+1}^+\beta_i^+}\left(\mathrm{d}W_{2i}^{\alpha^+\beta^+}-\mathrm{i}\,\mathrm{d}W_{2i+1}^{\alpha^+\beta^+}\right)-\sqrt{\alpha_{i-1}^+\beta_i^+}\left(\mathrm{d}W_{2i-2}^{\beta^+\alpha^+}+\mathrm{i}\,\mathrm{d}W_{2i-1}^{\beta^+\alpha^+}\right)\right], \qquad (13)
\end{aligned}$$

where $i = 0 \ldots N-1$ labels the vector components and we have defined $n_i^{\alpha} = \alpha_i^+\alpha_i$ and $n_i^{\beta} = \beta_i^+\beta_i$, which are complex phase space functions representing the number of $\hat{a}$ and $\hat{b}$-bosons (per site i), respectively. With this particular choice of noise matrix, we have introduced eight $2N \times 1$ Wiener increment vectors with the usual statistical properties that $\langle \mathrm{d}W_i^x \mathrm{d}W_j^y\rangle = \mathrm{d}t\delta_{xy}\delta_{ij}$ and $\langle \mathrm{d}W_i^x\rangle = 0$, where $i = 0 \ldots N-1$ and $x, y = \alpha, \alpha^+, \beta, \beta^+, \beta\alpha, \alpha\beta, \beta^+\alpha^+, \alpha^+\beta^+$ labels each Wiener increment vector. We would like to point out that the subscript labels of the Wiener increment vector are not unique and the labeling scheme[4] was chosen simply for convenience (see appendix C).

2.1. Inclusion of anisotropy

Had we begun with the full anisotropic Hamiltonian in equation (2) instead and carried out the same steps as in section 2, it would have been shown that anisotropy is included by adding the following expressions into the drift terms of equations (10)–(13):

$$\mathrm{d}\alpha_i \sim +\frac{\mathrm{i}\Delta}{2\hbar}\beta_i\left(m_{i-1}+m_{i+1}\right)\mathrm{d}t \qquad (14)$$

$$\mathrm{d}\beta_i \sim +\frac{\mathrm{i}\Delta}{2\hbar}\alpha_i\left(m_{i-1}^+ + m_{i+1}^+\right)\mathrm{d}t \qquad (15)$$

$$\mathrm{d}\alpha_i^+ \sim -\frac{\mathrm{i}\Delta}{2\hbar}\beta_i^+\left(m_{i-1}^+ + m_{i+1}^+\right)\mathrm{d}t \qquad (16)$$

$$\mathrm{d}\beta_i^+ \sim -\frac{\mathrm{i}\Delta}{2\hbar}\alpha_i^+\left(m_{i-1}^+ + m_{i+1}^+\right)\mathrm{d}t \qquad (17)$$

where the following shorthand $m_i = \alpha_i\beta_i^+, m_i^+ = \alpha_i^+\beta_i$ was used. For the stochastic terms, however, only the mixed derivative diffusion terms (i.e. those containing $\alpha\beta$ and $\alpha^+\beta^+$) are modified in the following way:

$$\mathrm{d}\alpha_i \sim +\frac{\mathrm{i}}{2}\sqrt{\frac{\mathrm{i}}{2\hbar}}\left[-\sqrt{J\alpha_i\beta_{i-1}-2\Delta\beta_i\alpha_{i-1}}(\ldots\ldots)-\sqrt{J\alpha_i\beta_{i+1}-2\Delta\alpha_{i+1}\beta_i}(\ldots\ldots)\right] \qquad (18)$$

[4] Note that with the inclusion of periodic boundary conditions: $\alpha_{-1} \to \alpha_{N-1}$ and $\alpha_N \to \alpha_0$. However, since there are $2N \times 1$ Wiener increments, then it is periodic in $2N$ instead. For example $\mathrm{d}W_{-1}^x = \mathrm{d}W_{2N-1}^x$ and $\mathrm{d}W_{2N}^x = 0$.

$$\mathrm{d}\beta_i \sim +\frac{\mathrm{i}}{2}\sqrt{\frac{\mathrm{i}}{2\hbar}}\left[-\sqrt{J\beta_i\alpha_{i+1}-2\Delta\beta_{i+1}\alpha_i}(\ldots\ldots)-\sqrt{J\beta_i\alpha_{i-1}-2\Delta\alpha_i\beta_{i-1}}(\ldots\ldots)\right] \tag{19}$$

$$\mathrm{d}\alpha_i^+ \sim +\frac{\mathrm{i}}{2}\sqrt{\frac{\mathrm{i}}{2\hbar}}\left[-\sqrt{J\beta_{i-1}^+\alpha_i^+-2\Delta\beta_i^+\alpha_{i-1}^+}(\ldots\ldots)-\sqrt{J\beta_{i+1}^+\alpha_i^+-2\Delta\alpha_{i+1}^+\beta_i^+}(\ldots\ldots)\right] \tag{20}$$

$$\mathrm{d}\beta_i^+ \sim +\frac{\mathrm{i}}{2}\sqrt{\frac{\mathrm{i}}{2\hbar}}\left[-\sqrt{J\beta_i^+\alpha_{i-1}^+-2\Delta\beta_{i-1}^+\alpha_i^+}(\ldots\ldots)-\sqrt{J\beta_i^+\alpha_{i+1}^+-2\Delta\alpha_i^+\beta_{i+1}^+}(\ldots\ldots)\right] \tag{21}$$

where the terms in $(\ldots\ldots)$ represent the same Wiener increment combinations as in equations (10)–(13). The Ito SDEs we have derived are able to describe other types of spins models such as the XY model and the XYZ model (to name a few), just by adjusting or including a few parameters. For the last two cases, we would have to take a trivial generalization in the derivations by introducing two different anisotropy terms in equation (2). An informative review article on the the quantum quench dynamics of other variants of the Heisenberg Hamiltonian using other numerical methods can be found in [9].

3. Results and discussion

To test our formalism, we first simulated the FM ($J > 0$) spin Hamiltonian for the TFIM ($\Delta/J = 0$) and the isotropic Heisenberg Hamiltonian ($\Delta/J = 1.0$) in equation (2) for high ($h/J = 10$) and low ($h/J = 0.5$) field values. This was compared to results from exact diagonalization calculations using a small system with $N = 4$ spins. The Stratanovich version of the SDES[5] in equations (10)–(13) were simulated using a semi-implicit Stratanovich algorithm as they are known to exhibit superior convergence properties [34]. To track the dynamics of the system, we calculated the expectation values of all three spin components at each site i: $\langle S_i^x\rangle$, $\langle S_i^y\rangle$, $\langle S_i^z\rangle$. Using the translation symmetry of the system, we further averaged them over the entire lattice to obtain an average expectation value of the spin components per site: $[S^x]$, $[S^y]$, $[S^z]$. These expectation values were calculated using the stochastic averages of their respective phase space functions, i.e.

$$[S^x] = \sum_{i=0}^{N-1}\left\langle\frac{1}{2}(\hat{a}_i^\dagger\hat{b}_i+\hat{b}_i^\dagger\hat{a}_i)\right\rangle = \sum_{i=0}^{N-1}\left\langle\left\langle\frac{1}{2}(\alpha_i^+\beta_i+\beta_i^+\alpha_i)\right\rangle\right\rangle, \tag{22}$$

$$[S^y] = \sum_{i=0}^{N-1}\left\langle\frac{1}{2\mathrm{i}}(\hat{a}_i^\dagger\hat{b}_i-\hat{b}_i^\dagger\hat{a}_i)\right\rangle = \sum_{i=0}^{N-1}\left\langle\left\langle\frac{1}{2\mathrm{i}}(\alpha_i^+\beta_i-\beta_i^+\alpha_i)\right\rangle\right\rangle, \tag{23}$$

$$[S^z] = \sum_{i=0}^{N-1}\left\langle\frac{1}{2}(\hat{a}_i^\dagger\hat{a}_i-\hat{b}_i^\dagger\hat{b}_i)\right\rangle = \sum_{i=0}^{N-1}\left\langle\left\langle\frac{1}{2}(\alpha_i^+\alpha_i-\beta_i^+\beta_i)\right\rangle\right\rangle, \tag{24}$$

where $\langle\langle\cdot\rangle\rangle$ denotes a stochastic average.

The initial state of the system was taken to be the classical FM state: $|\uparrow\uparrow\ldots\uparrow\rangle$ and the dynamics were observed for $t \geqslant 0$ during which a transverse field is turned on. The results for the TFIM are shown in figures 1 and 2 for different field strengths while the results for the isotropic ($\Delta/J = 1.0$) model are shown in figures 3 and 4. Both models show a good agreement with exact diagonalization calculations.

[5] The Stratanovich correction terms worked out to be zero and hence the Stratanovich form of the SDEs from equations (10)–(13) have the exact same form as the derived Ito SDEs.

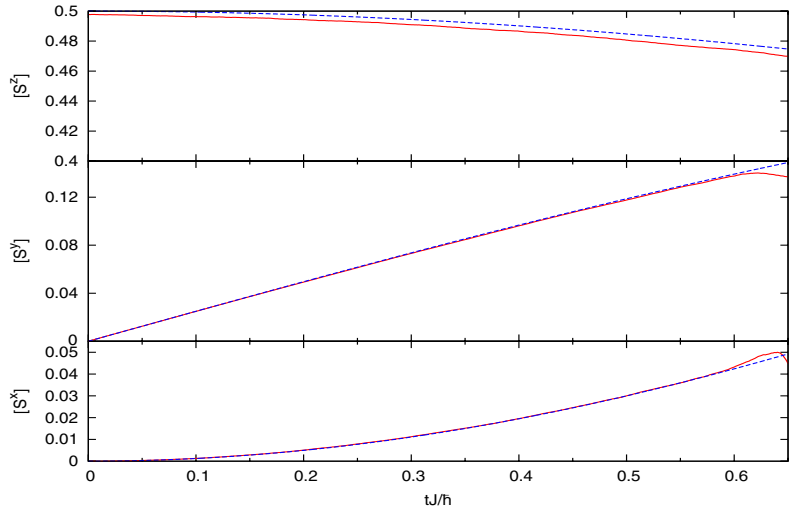

Figure 1. TFIM following a transverse quench. From top to bottom: plots of $[S^x]$, $[S^y]$, $[S^z]$ versus $tJ/\hbar$, respectively. The stochastic averages, $\langle\langle\cdot\rangle\rangle$ are given by red solid lines while exact diagonalization results are represented by green dashed lines. Simulation parameters: $N = 4, n_{\text{traj}} = 10^6, \mathrm{d}t = 0.001, h/J = 0.5, \Delta/J = 0.0$. The agreement remains good until approximately $tJ/\hbar = 0.6$.

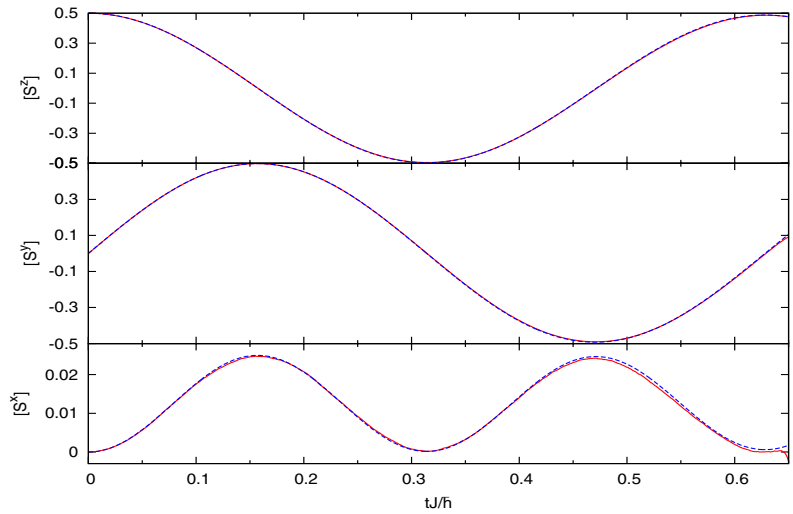

Figure 2. TFIM following a transverse quench. From top to bottom: plots of $[S^x]$, $[S^y]$, $[S^z]$ versus $tJ/\hbar$, respectively. The stochastic averages, $\langle\langle\cdot\rangle\rangle$ are given by red solid lines while exact diagonalization results are represented by the green dashed lines. Simulation parameters: $N = 4, n_{\text{traj}} = 2 \times 10^5, \mathrm{d}t = 0.001, h/J = 10.0, \Delta/J = 0.0$. Agreement remains good until approximately $tJ/\hbar = 0.65$.

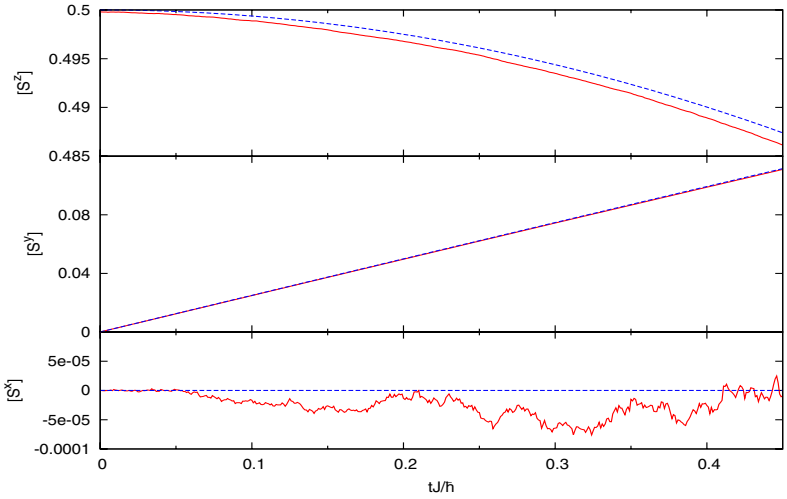

Figure 3. Isotropic Heisenberg model following a transverse quench. From top to bottom: plots of $[S^x]$, $[S^y]$, $[S^z]$ versus $tJ/\hbar$, respectively. The stochastic averages, $\langle\langle\cdot\rangle\rangle$ are given by red solid lines while exact diagonalization results are represented by green dashed lines. Simulation parameters: $N = 4, n_{\text{traj}} = 10^6, \mathrm{d}t = 0.001, h/J = 0.5, \Delta/J = 1.0$. The agreement remains good and both results are nearly indistinguishable. The simulations diverge at approximately $tJ/\hbar = 0.45$.

The only drawback of the PPR is that the simulations are usually valid only for relatively short lifetimes (roughly $tJ/\hbar \sim 0.45$–0.65 for the models examined) before sampling errors caused by diverging trajectories take over. In figure 1 for example, the onset of the effects of diverging trajectories can be seen at around $tJ/\hbar \sim 0.58$ where a deviation of the SDE results and exact calculations begin to appear. However, for the time scales where the simulations remain finite, it does yield good results.

One should not be alarmed as this is a common problem associated with using the PPR and can be attributed to the nature of the SDEs derived and not due to a non-converging numerical algorithm [35–37]. In fact, Deuar [38] examined this issue when applying the PPR to the exact dynamics of many-body systems. If we abide by Deuar's findings strictly, we see that there are no drift and noise divergences present in the SDEs in equations (10)–(13). However, we suspect drift terms of the form $\sim \mathrm{i}X_i\big[\big(\mp n^{\alpha}_{i+1} \pm n^{\beta}_{i+1}\big) + \big(n^{\alpha}_{i-1} \pm n^{\beta}_{i-1}\big)\big]$, where $X_i = \alpha_i, \alpha_i^+, \beta, \beta^+$ can be problematic. This is because if we take into consideration the translational symmetry of the system, then we can approximately say that

$$\mathrm{i}X_i\big[\big(\mp n^{\alpha}_{i+1} \pm n^{\beta}_{i+1}\big) + \big(\mp n^{\alpha}_{i-1} \pm n^{\beta}_{i-1}\big)\big] \approx 2\mathrm{i}X_i\big(\mp n^{\alpha}_{i} \pm n^{\beta}_{i}\big), \tag{25}$$

which now clearly exhibits offending terms [38] that cause trajectories to escape to infinity, since $\mathrm{d}X_i \sim X_i^2\,[\cdots]\,\mathrm{d}t + \cdots$.

The gauge-P representation [25, 37–40] was developed to specifically deal with such drift instabilities. In the gauge-P representation, arbitrary gauge functions, $\{g_k\}$ can be introduced into the SDEs whose effect is a modification of the deterministic evolution. This can be done at the expense of introducing another stochastic variable (Ω), in $\hat{\Lambda}$, which manifests itself as

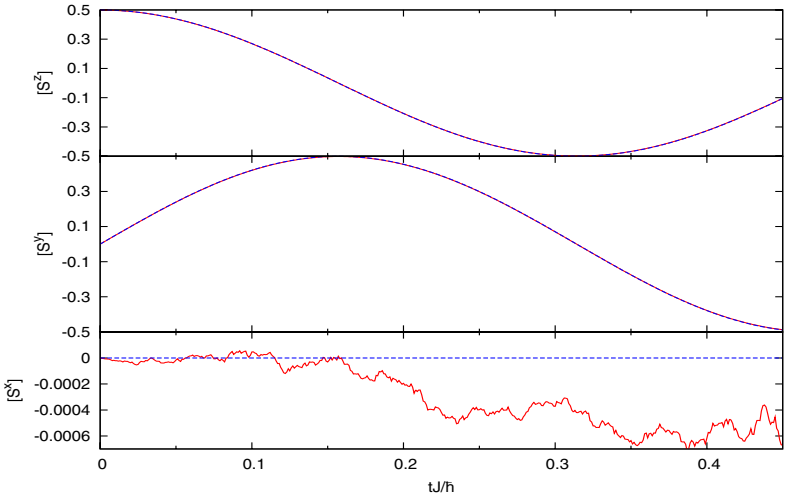

Figure 4. Isotropic Heisenberg model following a transverse quench. From top to bottom: plots of $[S^x]$, $[S^y]$, $[S^z]$ versus $tJ/\hbar$, respectively. The stochastic averages, $\langle\langle\cdot\rangle\rangle$ are given by red solid lines while exact diagonalization results are represented by green dashed lines. Simulation parameters: $N = 4, n_{\text{traj}} = 10^5, \mathrm{d}t = 0.001, h/J = 10.0, \Delta/J = 1.0$. The agreement remains good and both results are nearly indistinguishable. The simulations diverge at approximately $tJ/\hbar = 0.45$.

a weight term when calculating stochastic averages. To be more specific using the gauge-P representation [25], the Ito SDEs are altered such that

$$\mathrm{d}\alpha_i = \left(A_i^+ - g_k B_{jk}\right)\mathrm{d}W_k \tag{26}$$

$$\mathrm{d}\Omega = \Omega\left(V\,\mathrm{d}t + g_k\mathrm{d}W_k\right), \tag{27}$$

where summation over k is implied and V is the constant term that may appear after substituting the correspondence relations into an equation of motion for $\hat{\rho}$.

The gauge-P representation has been very successful in simulating the dynamics of many-mode Bose gases [41–43] partly because such systems result in neat diagonal noise matrices that are easier to handle as seen in equation (26). However, it is evidently not as straightforward to apply it in our case as we have a much more complicated non-diagonal noise matrix. The true complication arises when we attempt to calculate Stratonovich correction terms as it is the Stratanovich version of the SDEs that are simulated. We believe that the application of the gauge-P is possible in principle but requires a bit more thought for Heisenberg systems when using the Schwinger boson approach.

3.1. Finite size effects

The main advantage of the PPR is the linear scaling with the number of spins, N, as compared to the exponentially large matrices needed for an exact solution. We first demonstrate the capabilities of the PPR at simulating large system sizes by showing results for the FM isotropic Heisenberg case at a field value of $h/J = 10$, prepared in the initial FM state

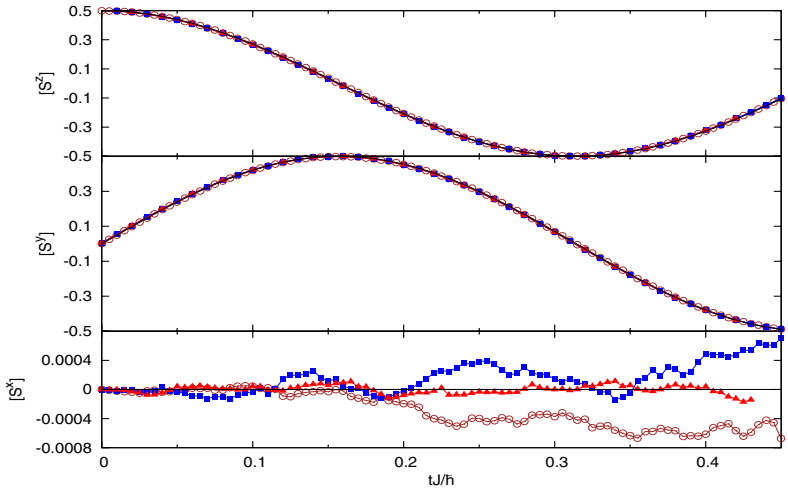

Figure 5. Isotropic Heisenberg model following a transverse-field quench at $tJ/\hbar = 0$ from $h/J = 0.0$ to $h/J = 10.0$, beginning in the FM ground state: $|\uparrow\uparrow \ldots \uparrow\rangle$. FM interactions assumed: $\mathrm{sign}(J) = +1$. From top to bottom: plots of $[S^x]$, $[S^y]$, $[S^z]$ versus $tJ/\hbar$, respectively. The stochastic averages, $\langle(\cdot)\rangle$ are for $N = 4$: (—■—), $N = 10$: (—○—), $N = 100$: (—▲—), while exact diagonlization results for $N = 4$ are represented by the black solid line. Simulation parameters: $n_{\mathrm{traj}}^{(N=4)} = 10^5$, $n_{\mathrm{traj}}^{(N=10)} = 2 \times 10^5$, $n_{\mathrm{traj}}^{(N=100)} = 5 \times 10^4$, $\mathrm{d}t = 0.001$, $\Delta/J = 1.0$. The agreement remains good and finite size effects are negligible. The simulations diverge at approximately $tJ/\hbar \sim 0.45$.

as in figure 4. As expected, we do not observe any finite size effects within the life time of the stochastic simulations. Even with a chain consisting of 100 spins (figure 5), the dynamics exhibited are similar to that of a 4-spin chain. The simulations are compared against the exact diagonalization results for an $N = 4$ system and exhibit identical real-time evolution of the spin components for a 1D chain with FM interactions, i.e. finite size effects are negligible.

This is not the case for a 1D AFM ($J < 0$), however. A quantum quench in this model with $h = 0$ starting from the Néel state has previously been extensively studied [5]. In order to verify that in our approach finite size effects do exist, we performed $N = 4$ and $N = 10$ exact calculations for the anisotropic AFM with different values of anisotropy: Δ/J. Two sample exact calculations are shown in figures 6 and 7, respectively, for $\Delta/J = -0.8$ and $\Delta/J = -1.5$ for low field values of $h/J = 0.5$. For the AFM Heisenberg Hamiltonian, the system is initialized in the classical AFM Néel state: $|\uparrow\downarrow \ldots \uparrow\downarrow\rangle$.

An immediate observation is that increasing the value of Δ, reduces the time, t_{finite}, which we define as the time that significant finite size effects are noticeable. A natural progression to make in order to take advantage of the SDES we have derived, is to increase the value Δ/J till $t_{\mathrm{finite}} < t_{\mathrm{life}}$, thereby allowing us to explore the finite size effects of macroscopically large systems.

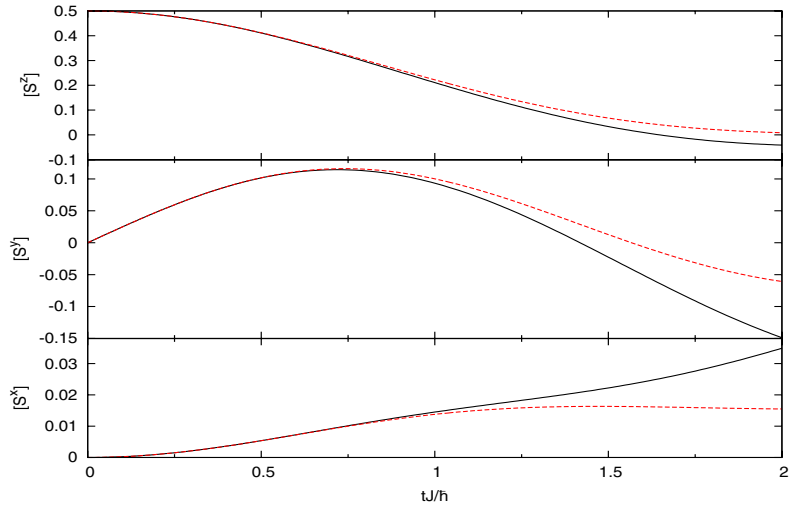

Figure 6. Anisotropic Heisenberg model following a transverse-field quench at $tJ/\hbar = 0$ from $h/J = 0.0$ to $h/J = 10.0$, beginning in the AFM Néel state: $|\uparrow\downarrow \ldots \uparrow\downarrow\rangle$. AFM interactions assumed: $\mathrm{sign}(J) = -1$. From top to bottom: plots of $[S^x]$, $[S^y]$, $[S^z]$ versus $tJ/\hbar$, respectively. The exact calculations for the $N = 4$ (solid black lines) and $N = 10$ (dashed red lines) are compared. We observe $t_{\mathrm{finite}}J/\hbar \sim 0.8$ for $\Delta/J \sim -0.8$.

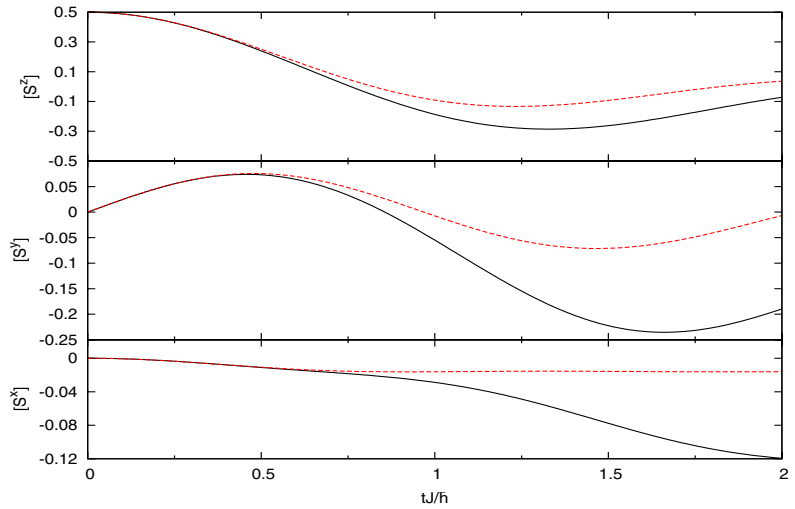

Figure 7. Anisotropic Heisenberg model following a transverse-field quench at $tJ/\hbar = 0$ from $h/J = 0.0$ to $h/J = 10.0$, beginning in the AFM Néel state: $|\uparrow\downarrow \ldots \uparrow\downarrow\rangle$. AFM interactions assumed: $\mathrm{sign}(J) = -1$. From top to bottom: plots of $[S^x]$, $[S^y]$, $[S^z]$ versus $tJ/\hbar$, respectively. The exact calculations for the $N = 4$ (solid black lines) and $N = 10$ (dashed red lines) are compared. We observe $t_{\mathrm{finite}}J/\hbar \sim 0.5$ for a given anisotropy of $\Delta/J \sim -1.5$.

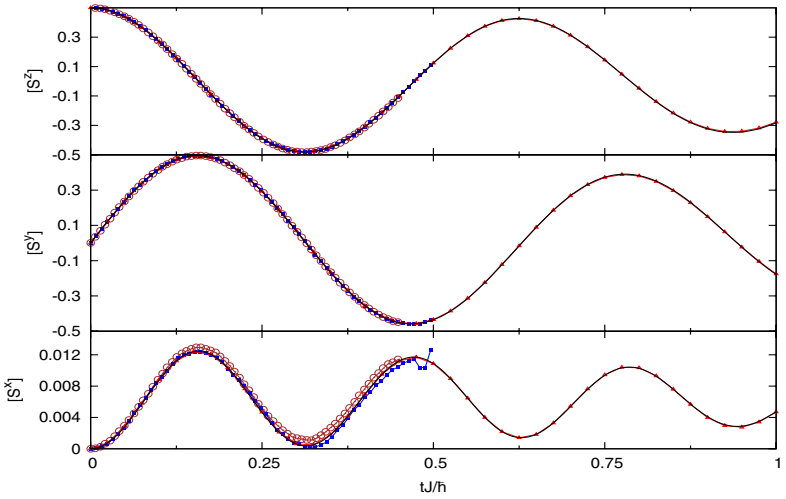

Figure 8. Anisotropic Heisenberg model following a transverse-field quench at $tJ/\hbar = 0$ from $h/J = 0.0$ to $h/J = 10.0$, beginning in the AFM ground state: $|\uparrow\downarrow \ldots \uparrow\downarrow\rangle$. AFM interactions assumed: $\mathrm{sign}(J) = -1$. From top to bottom: plots of $[S^x]$, $[S^y]$, $[S^z]$ versus $tJ/\hbar$, respectively. The stochastic averages, $\langle\langle\cdot\rangle\rangle$ are for $N = 4$: (—■—) and $N = 10$: (—○—), while exact diagonalization results are for $N = 4$: (black solid lines) and $N = 10$: (—▲—). Simulation parameters: $n_{\mathrm{traj}}^{(N=4)} = 10^6$, $n_{\mathrm{traj}}^{(N=10)} = 10^5$, $\mathrm{d}t = 0.001$, $\Delta/J = -0.5$. The agreement remains good and finite size effects are unnoticeable up to $tJ\hbar = 1$. The SDEs diverge at $t_{\mathrm{life}}J/\hbar \sim 0.48$.

We observe finite size effects through the same observables as in equations (22) to (24). However for the initial Néel state, it is more meaningful to take into consideration the alternating sign of spins when calculating the averaged spin components[6], i.e.

$$[S^x] = \sum_{i=0}^{N-1} \left\langle \frac{1}{2}\left(\hat{a}_i^\dagger \hat{b}_i + \hat{b}_i^\dagger \hat{a}_i\right) \right\rangle = \sum_{i=0}^{N-1} \left\langle\!\left\langle \frac{1}{2}\left(\alpha_i^+ \beta_i + \beta_i^+ \alpha_i\right) \right\rangle\!\right\rangle, \tag{28}$$

$$[S^y] = \sum_{i=0}^{N-1} \left\langle \frac{1}{2i}(-1)^i\left(\hat{a}_i^\dagger \hat{b}_i - \hat{b}_i^\dagger \hat{a}_i\right) \right\rangle = \sum_{i=0}^{N-1} (-1)^i \left\langle\!\left\langle \frac{1}{2i}\left(\alpha_i^+ \beta_i - \beta_i^+ \alpha_i\right) \right\rangle\!\right\rangle, \tag{29}$$

and

$$[S^z] = \sum_{i=0}^{N-1} \left\langle \frac{1}{2}(-1)^i\left(\hat{a}_i^\dagger \hat{a}_i - \hat{b}_i^\dagger \hat{b}_i\right) \right\rangle = \sum_{i=0}^{N-1} (-1)^i \left\langle\!\left\langle \frac{1}{2}\left(\alpha_i^+ \alpha_i - \beta_i^+ \beta_i\right) \right\rangle\!\right\rangle. \tag{30}$$

Increasing Δ/J however has the adverse effect of decreasing t_{life} significantly. Thus, while it is possible to simulate macroscopically large system sizes, we find that the SDE simulations diverge much sooner than t_{finite}. Figure 8 ($\Delta/J = -0.5$, $h/J = 10.0$) reinforces our claim that t_{finite} decreases with Δ/J as no finite size effects are observed up to $tJ/\hbar = 1$, in sharp comparison to figure 6 ($\Delta/J = -0.8$) and figure 7 ($\Delta/J = -1.5$), albeit for $h/J = 0.5$.

[6] Note that there exists an exception. There is no need to account for a sign change for the observable: $[S_x]$.

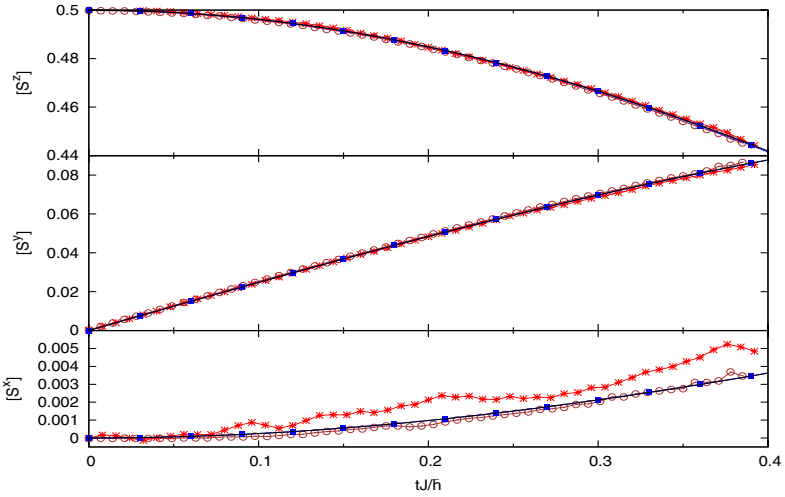

Figure 9. Anisotropic Heisenberg model following a transverse-field quench at $tJ/\hbar = 0$ from $h/J = 0.0$ to $h/J = 0.5$, beginning in the AFM ground state: $|\uparrow\downarrow \ldots \uparrow\downarrow\rangle$. AFM interactions assumed: sign$(J) = -1$. From top to bottom: plots of $[S^x]$, $[S^y]$, $[S^z]$ versus $tJ/\hbar$, respectively. The stochastic averages, $\langle(\cdot)\rangle$ are for $N = 4$: (—○—) and $N = 10$: (—✳—), while exact diagonalization results are for $N = 4$: (black solid lines) and $N = 10$: (—■—). Simulation parameters: $n_{\text{traj}}^{(N=4)} = 10^6, n_{\text{traj}}^{(N=10)} = 10^5, \mathrm{d}t = 0.001, \Delta/J = -0.8$. Finite size effects are unnoticeable at $t_{\text{life}}J/\hbar \sim 0.4$.

Our last effort to observe finite size effects was to increase Δ/J to -0.8 with hopes that $t_{\text{life}} > t_{\text{finite}}$. As seen in figure 9, our simulations do not survive beyond t_{finite}. Since t_{finite} depends on the anisotropy Δ/J, increasing the system size while possible will result in t_{life} of the same order. In general, we find that increasing Δ/J will *decrease* t_{life} as well as t_{finite} such that $t_{\text{life}} < t_{\text{finite}}$ always holds true. This thwarts our efforts to examine finite size effects for the AFM case. Furthermore, we find that using an initial Néel state results in poor convergence for the observable: $[S^x]$ as seen in figure 8 (and even more so in figure 9) compared to an initial FM ground state and it is likely that we have used an insufficient number of trajectories in our simulations. Nevertheless, we have demonstrated the applicability of the PPR to AFM systems.

3.2. Nearest-neighbor correlation functions

Correlation functions are generally of greater interest seeing as they are experimentally accessible quantities. In order to demonstrate the applicability of the PPR in this respect, we calculate the nearest-neighbor spin correlation functions for the z-component, which is defined as

$$\left[\hat{S}_i^z \hat{S}_{i+1}^z\right] = \sum_{i=0}^{N-1} \frac{\langle \hat{S}_i^z \hat{S}_{i+1}^z \rangle}{N} = \frac{1}{4} \sum_{i=0}^{N-1} \frac{\left\langle\!\left\langle \left(n_i^\alpha - n_i^\beta\right)\left(n_{i+1}^\alpha - n_{i+1}^\beta\right) \right\rangle\!\right\rangle}{N}, \tag{31}$$

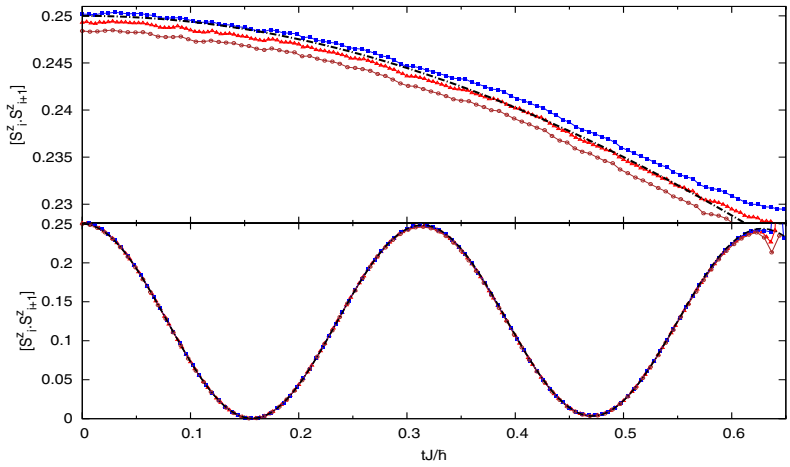

Figure 10. TFIM following a transverse-field quench at $tJ/\hbar = 0$ from $h/J = 0.0$ to $h/J = 0.5$ (top) and $h/J = 0.0$ to $h/J = 10.0$ (bottom) beginning in the FM ground state: $|\uparrow\uparrow \ldots \uparrow\uparrow\rangle$. FM interactions assumed: $\mathrm{sign}(J) = 1$. Plots of $\left[\hat{S}_i^z \hat{S}_{i+1}^z\right]$ versus $tJ/\hbar$, respectively. The stochastic averages, $\langle\langle\cdot\rangle\rangle$ for $N = 4$ are represented by solid red lines (—▲—) while the averages plus and minus one standard deviation are presented by (—■—) and (—○—) lines, respectively. Exact diagonalization results are given by dot-dashed black curves. Simulation parameters: $n_{\mathrm{traj}} = 10^6 \mathrm{d}t = 0.001$, $\Delta/J = 0.0$.

where periodic boundary conditions apply and as before the following shorthand has been used: $n_i^\alpha = \alpha_i^+\alpha_i, n_i^\beta = \beta_i^+\beta_i$. Our calculations in figure 10 compares the stochastic averages of correlation functions with the results from exact diagonalization. It is because the correlation function shows poorer convergence than the spin components that we include error bars for this calculation. Error bars can be calculated from a simple binning analysis of the trajectories and applying the central limit theorem [32]. It is not surprising to find poorer convergence for the correlation functions since they amount to higher order moments of the complex phase space variables. Due to the noise terms in the SDEs, the phase space variables are exponentials of Gaussian random numbers which are known to diverge sooner for higher moments.

4. Conclusion

We have shown how the real-time quantum quench dynamics of spin systems can be simulated via the use of SDEs. This was done by writing the Heisenberg spin operators in terms of Schwinger bosons and deriving a Fokker–Planck Equation using the PPR for the density operator. This in turn allows us to obtain Ito SDEs which can be used to calculate the expectation values of normally ordered bosonic operators. An attractive feature of this prescription is that the number of SDEs scale linearly as N and can in principle be used to simulate macroscopic system sizes. In addition, our method is generalizable to higher dimensions and other geometries as well and explicit couplings to the environment can be included.

The main drawback of the PPR, however, is its notoriously short life time which prevents us from obtaining useful results beyond a certain time: t_{life}. For the TFIM and the anisotropic Heisenberg model, we found a bare application of the PPR to have $t_{\text{life}}J/\hbar \sim 0.45$–$0.65$. We suspect that this is due to drift instability terms present in the SDEs that cause trajectories to diverge within this time scale.

We also attempted to explore finite size effects which were more significant for the anisotropic AFM Hamiltonian beginning in the classical Néel state. For the FM case, no finite size effects were observed even for a lattice size of 100 spins within its lifetime. We find that the more negative the anisotropy parameter in the AFM Hamiltonian, the sooner finite size effects are observed, i.e. t_{finite} decreases. However, this has the adverse effect of decreasing t_{life} such that $t_{\text{life}} < t_{\text{finite}}$ for the simulations that we have carried out.

Finally, we would like to point that in cases where the underlying Hamiltonian has conserved properties, such as the models addressed in this paper, then it could be advantageous to use projection methods instead [44, 45]. This ensures the use of a more efficient basis set which will lead to improved simulation performances. In particular, there exists the PPR approach which uses the SU(n) spin coherent states [46] as a basis set instead.

An obvious future direction of our research involves applying the gauge-P representation in a bid to extend simulation life times and to examine the efficient of the other methods suggested above. Also the study of systems in higher dimensions with and without couplings to the environment would be of considerable interest.

Acknowledgments

This research has been made possible with the support of an NSERC research grant. We would also like to thank Piotr Deuar and Murray Olsen for helpful discussions.

Appendix A. The positive-P representation

In this section, we will review the PPR [24] that has been applied to both quantum optics [28–30] and exact many-body simulations of Bose gases [33, 47–49] successfully. The PPR is already well established and our aim for including this review is simply to provide a self-contained paper for readers who are not as familiar with it.

In short, the PPR is an expansion of the density operator in terms of an off-diagonal coherent state basis:

$$\hat{\rho} = \int P(\alpha, \alpha^+)\,\hat{\Lambda}(\alpha, \alpha^+)\,\mathrm{d}^2\alpha\,\mathrm{d}^2\alpha^+ = \int P(\alpha, \alpha^+)\,\frac{|\alpha\rangle\langle\alpha^{+*}|}{\langle\alpha^{+*}|\alpha\rangle}\,\mathrm{d}^2\alpha\,\mathrm{d}^2\alpha^+ \quad \text{(A.1)}$$

where $|\alpha\rangle = \mathrm{e}^{-\frac{1}{2}|\alpha|^2}\sum_{n=0}^{\infty}\frac{\alpha^n}{n!}|n\rangle$ is the standard bosonic coherent state [50] that are eigenstates of the annihilation operator $\hat{a}$. $P(\alpha, \alpha^+)$ plays the role of a distribution function in the phase space spanned by $\{\alpha, \alpha^+\}$ and can be chosen such that it remains real and positive. In addition, due to the normalization factor in the denominator of equation (A.1) and using the fact that $\mathrm{Tr}[\hat{\rho}] = 1$, we see that

$$\int P(\alpha, \alpha^+)\,\mathrm{d}^2\alpha\,\mathrm{d}^2\alpha^+ = 1 \quad \text{(A.2)}$$

i.e. the distribution is normalized over the entire complex phase space. Simply put, we can interpret $P(\alpha, \alpha^+)$ as a probability distribution function for the variables α and α^+, hence the name positive-P.

A hallmark of the PPR is that the off-diagonal projection operators, $\hat{\Lambda}(\alpha, \alpha^+)$ satisfies the following correspondence relations:

$$\begin{aligned}
\hat{a}\hat{\Lambda} &= \alpha\hat{\Lambda} \\
\hat{a}^\dagger\hat{\Lambda} &= \left(\alpha^+ + \frac{\partial}{\partial\alpha}\right)\hat{\Lambda} \\
\hat{\Lambda}\hat{a}^\dagger &= \alpha^+\hat{\Lambda} \\
\hat{\Lambda}\hat{a} &= \left(\alpha + \frac{\partial}{\partial\alpha^+}\right)\hat{\Lambda},
\end{aligned} \tag{A.3}$$

which allows us to map complicated operator equations consisting of bosonic annihilation and creation operators onto differential equations of phase space variables α, α^+. The correspondence relation is typically used in an equation of motion for $\hat{\rho}$, which after integration by parts and ignoring of boundary terms allows us to obtain a FPE:

$$\frac{\partial P(\vec{x})}{\partial t} = \left\{-\frac{\partial}{\partial x^\mu}A^\mu(\vec{x}) + \frac{1}{2}\frac{\partial}{\partial x^\mu}\frac{\partial}{\partial x^\nu}D^{\mu\nu}(\vec{x})\right\}P(\vec{x}), \quad \mu, \nu = 0\ldots N-1, \tag{A.4}$$

where $\vec{x} = \{\vec{\alpha}, \vec{\alpha}^+\}$, A^μ is called the drift vector and $D^{\mu\nu}$ is called the diffusion matrix (which is symmetric and positive semi-definite by definition). Due to the doubling of phase space, the diffusion matrix is guaranteed to be positive semi-definite [24]. This then allows one to convert the FPE to a set of Ito SDEs proportional to the number of bosonic modes of the system, i.e.

$$\mathrm{d}x^\mu = A^\mu \mathrm{d}t + B^{\mu\nu}\mathrm{d}W^\nu, \qquad \mu = 0\ldots N-1, \nu = 0\ldots N_w, \tag{A.5}$$

where $\mathrm{d}W^\nu$ is a vector of Wiener increments with N_w components and $B^{\mu\nu}$ is a noise matrix that must satisfy the factorization

$$\mathbf{D} = \mathbf{B}\mathbf{B}^T. \tag{A.6}$$

This factorization is not unique and any noise matrix that satisfies equation (A.6) will produce the same stochastic averages in the limit of an infinite number of trajectories. This ambiguity in the choice of $\mathbf{B}$ may affect the performance of stochastic simulations [36, 38].

Since $\mathbf{D} = \mathbf{D}^T$, an obvious factorization to use would be the square root of the diffusion matrix, i.e. $\mathbf{B} = \sqrt{\mathbf{D}}$, which is easily accomplished by using common mathematical software such as Matlab or Maple. While this is the most convenient procedure, it does not necessarily produce the most elegant noise matrix. On the other hand, it is possible to decompose a single diffusion matrix into different diffusion processes [38]: $\mathbf{D} = \mathbf{D_1} + \mathbf{D_2} + \mathbf{D_3} + \cdots$ that may be more easily factorized, i.e. the factorization $\mathbf{D}_i = \mathbf{B_i}\mathbf{B_i^T}$ is trivial. Using this procedure, an equivalent noise matrix that also results in $\mathbf{D}$ is given by

$$\mathbf{B} = [\mathbf{B_1}\ \mathbf{B_2}\ \mathbf{B_3}\ldots]. \tag{A.7}$$

Despite possibly taking on a more elegant form, equation (A.7) introduces $N_w(> N)$ Wiener increments and with that the possibility of larger sampling errors. So we see that there are advantages and disadvantages of the two factorization methods.

The convenience in using the PPR is in calculating the expectation values of normal-ordered operators as they can be replaced by simple stochastic averages over their corresponding phase space functions. The equivalence is as follows:

$$\langle(\hat{a})^\dagger)^m(\hat{a})^n\rangle = \langle\langle(\alpha^+)^m(\alpha)^n\rangle\rangle \tag{A.8}$$

where $\langle\cdot\rangle$ is the usual quantum mechanical expectation value and $\langle\langle\cdot\rangle\rangle$ represents an average over stochastic trajectories. In the limit that the number of trajectories goes to infinity, we get

16

an exact correspondence, although an average over 10^4–10^6 trajectories usually gives good agreement[7] before sampling errors cause divergences [35].

The main downside of the PPR is its notoriously short simulation life times. This is typically caused by instabilities in the drift or diffusion term [25] that cause trajectories to diverge in a finite time, when a finite number of trajectories are used to calculate expectation values. That being said, the PPR is best used for systems where the interesting physics occur at short timescales. Nonetheless, this does not deter us from our our current aim of demonstrating the possibility of simulating real-time spin dynamics using SDEs, even if only for short times.

Appendix B. Initial distribution

An important point in simulating SDEs would be using the right initial values for the phase space variables, α, α^+. For any density matrix, a particular form of the positive-P distribution function [24] that always exists is given by

$$P(\alpha, \alpha^+) = \frac{1}{4\pi^2} \langle (\alpha + (\alpha^+)^*)/2 | \hat{\rho} | (\alpha + (\alpha^+)^*)/2 \rangle \, \mathrm{e}^{-|\alpha - (\alpha^+)^*|^2/4}. \tag{B.1}$$

It has been shown in [51] that using equation (B.1), it is possible to initialize the phase space variables for a variety of initial states such as: coherent states, Fock states or crescent states to name a few. Of interest to us is the initial positive P-distribution for number states: $|n\rangle\langle n|$ which takes the form

$$P(\mu, \gamma) = \frac{\mathrm{e}^{-|\gamma|^2}}{\pi} \frac{\Gamma(|\mu|^2, n+1)}{\pi}, \tag{B.2}$$

where

$$\Gamma(x, n) = \frac{\mathrm{e}^{-x} x^{n-1}}{(n-1)!} \tag{B.3}$$

is the Gamma distribution. Our phase space variables are related to γ and μ via the relation $\alpha = \mu + \gamma$ and $\alpha^+ = \mu^* - \gamma^*$ and so by sampling γ and μ using the appropriate distribution functions in equation (B.2) (i.e. gamma distribution for μ and Gaussian distribution for γ), we can invert them to find the numerical values for α and α^+ that represents the Fock state $|n\rangle\langle n|$. Although, we have only outlined the steps for initializing the distribution of a Fock state, more explicit details can be found in the useful article in [51].

While in this paper, we initialize the system in either the FM ground state or the AFM, it is in principle possible to initialize the system in a general entangled state, which is described by the following density operator:

$$\hat{\rho} = \frac{1}{N} \left(w_1 | \uparrow \rangle + w_0 | \downarrow \rangle \right) \left(\langle \uparrow | w_1 + \langle \downarrow | w_0 \right), \tag{B.4}$$

where $N = w_0^2 + w_1^2$ and w_0 and w_1 represent the probabilities of the entangled state being spin down and spin up state, respectively. Or in the language of $\hat{a}$ and $\hat{b}$ bosons:

$$\hat{\rho} = \frac{1}{N} \left(w_1 | 1, 0 \rangle + w_0 | 0, 1 \rangle \right) \left(\langle 1, 0 | w_1 + \langle 0, 1 | w_0 \right). \tag{B.5}$$

The general entangled state is of interest as it is the ground state of the random field Ising model (RFIM), which our formalism is also able to address. Substituting equation (B.5) into

[7] This is just a general observation of the number of trajectories used in different articles when applying the PPR. See [28, 29, 33] for example.

equation (B.1), the coherent state basis results in the following expression for the probability distribution:

$$P(\mu_{\vec{\alpha}}, \gamma_{\vec{\alpha}}, \mu_{\vec{\beta}}, \gamma_{\vec{\beta}}) = \frac{1}{N}\left[w_0^2 \Gamma(|\mu_{\vec{\alpha}}|^2, 2)\frac{\mathrm{e}^{-|\gamma_{\vec{\alpha}}|^2}}{\pi}\delta(\mu_{\vec{\beta}}) + w_1^2\delta(\mu_{\vec{\alpha}})\Gamma(|\mu_{\vec{\beta}}|^2, 2)\frac{\mathrm{e}^{-|\gamma_{\vec{\beta}}|^2}}{\pi}\right.$$
$$\left. w_0 w_1 \left(\frac{\mathrm{e}^{-|\mu_\alpha|^2}|\mu_{\vec{\alpha}}|}{\pi}\frac{\mathrm{e}^{-|\gamma_{\vec{\alpha}}|^2}}{\pi}\right)\left(\frac{\mathrm{e}^{-|\mu_\beta|^2}|\mu_{\vec{\beta}}|}{\pi}\frac{\mathrm{e}^{-|\gamma_{\vec{\beta}}|^2}}{\pi}\right) 2\cos(2\eta)\right], \tag{B.6}$$

where $\mu_{\vec{\alpha}} = |\mu_{\vec{\alpha}}|\ \mathrm{e}^{\mathrm{i}(\eta+\xi)} = |\mu_{\vec{\alpha}}|\ \mathrm{e}^{\mathrm{i}(\xi+\eta)}$ and $\mu_{\vec{\beta}} = |\mu_{\vec{\beta}}|\ \mathrm{e}^{\mathrm{i}(\eta+\xi)} = |\mu_{\vec{\beta}}|\ \mathrm{e}^{\mathrm{i}(\xi-\eta)}$. Note that we have made a similar change of variables as above, i.e.

$$\mu_{\vec{\alpha}} = \frac{\alpha + (\alpha^+)^*}{2}, \qquad \gamma_{\vec{\alpha}} = \frac{\alpha - (\alpha^+)^*}{2}$$
$$\mu_{\vec{\beta}} = \frac{\beta + (\beta^+)^*}{2}, \qquad \gamma_{\vec{\beta}} = \frac{\beta - (\beta^+)^*}{2}. \tag{B.7}$$

The PPR based on the SU-(n) coherent states [46] seems more tailored to dealing with superposition states, as they can be more easily initialized with delta functions.

Appendix C. Fokker–Planck equation for Heisenberg Hamiltonian

If we were to apply formalism outlined in appendix A, we obtain the following FPE for the TFIM in equation (3):

$$\frac{\partial P(\vec{\alpha}, \vec{\alpha}^+, \vec{\beta}, \vec{\beta}^+)}{\mathrm{d}t} = \sum_i \left(-\frac{\partial}{\partial\alpha_i}\left\{\frac{\mathrm{i}J}{4\hbar}\alpha_i\left[(n^\alpha_{i+1} - n^\beta_{i+1}) + (n^\alpha_{i-1} - n^\beta_{i-1})\right] + \frac{\mathrm{i}h(t)}{2\hbar}\beta_i\right\}\right.$$
$$- \frac{\partial}{\partial\alpha_i^+}\left\{\frac{\mathrm{i}J}{4\hbar}\alpha_i^+\left[(n^\beta_{i+1} - n^\alpha_{i+1}) + (n^\beta_{i-1} - n^\alpha_{i-1})\right] - \frac{\mathrm{i}h(t)}{2\hbar}\beta_i^+\right\}$$
$$- \frac{\partial}{\partial\beta_i}\left\{\frac{\mathrm{i}J}{4\hbar}\beta_i\left[(n^\beta_{i+1} - n^\alpha_{i+1}) + (n^\beta_{i-1} - n^\alpha_{i-1})\right] + \frac{\mathrm{i}h(t)}{2\hbar}\alpha_i\right\}$$
$$- \frac{\partial}{\partial\beta_i^+}\left\{\frac{\mathrm{i}J}{4\hbar}\beta_i^+\left[(n^\alpha_{i+1} - n^\beta_{i+1}) + (n^\alpha_{i-1} - n^\beta_{i-1})\right] - \frac{\mathrm{i}h(t)}{2\hbar}\alpha_i^+\right\}$$
$$+ \frac{1}{2}\left(\frac{\mathrm{i}J}{4\hbar}\right)\left[\frac{\partial^2}{\partial\alpha_i\partial\alpha_{i+1}}\alpha_i\alpha_{i+1} + \frac{\partial^2}{\partial\alpha_{i+1}\partial\alpha_i}\alpha_i\alpha_{i+1} - \frac{\partial^2}{\partial\alpha_i^+\partial\alpha_{i+1}^+}\alpha_i^+\alpha_{i+1}^+\right.$$
$$- \frac{\partial^2}{\partial\alpha_{i+1}^+\partial\alpha_i^+}\alpha_i^+\alpha_{i+1}^+\frac{\partial^2}{\partial\beta_i\partial\beta_{i+1}}\beta_i\beta_{i+1} + \frac{\partial^2}{\partial\beta_{i+1}\partial\beta_i}\beta_i\beta_{i+1} - \frac{\partial^2}{\partial\beta_i^+\partial\beta_{i+1}^+}\beta_i^+\beta_{i+1}^+$$
$$- \frac{\partial^2}{\partial\beta_{i+1}^+\partial\beta_i^+}\beta_i^+\beta_{i+1}^+\frac{\partial^2}{\partial\alpha_i^+\partial\beta_{i+1}^+}\alpha_i^+\beta_{i+1}^+ + \frac{\partial^2}{\partial\beta_{i+1}^+\partial\alpha_i^+}\alpha_i^+\beta_{i+1}^+ + \frac{\partial^2}{\partial\alpha_{i+1}^+\partial\beta_i^+}\alpha_{i+1}^+\beta_i^+$$
$$+ \frac{\partial^2}{\partial\beta_i^+\partial\alpha_{i+1}^+}\alpha_{i+1}^+\beta_i^+ - \frac{\partial^2}{\partial\alpha_i\partial\beta_{i+1}}\alpha_i\beta_{i+1} - \frac{\partial^2}{\partial\beta_{i+1}\partial\alpha_i}\alpha_i\beta_{i+1}$$
$$\left.\left. - \frac{\partial^2}{\partial\alpha_{i+1}\partial\beta_i}\alpha_{i+1}\beta_i - \frac{\partial^2}{\partial\beta_i\partial\alpha_{i+1}}\alpha_{i+1}\beta_i\right]\right) P(\vec{\alpha}, \vec{\alpha}^+, \vec{\beta}, \vec{\beta}^+), \tag{C.1}$$

where we have already carried out an integration by parts and assumed that boundary terms vanish. By inspecting equation (C.1), the diffusion matrix (which is a $4N \times 4N$ matrix) has matrix elements that are specified by the functions associated with their derivatives.

Obviously, calculating the noise matrix is not a trivial task and comprises the bulk of the analytical work. Instead of simply taking the straightforward $\mathbf{B} = \sqrt{\mathbf{D}}$ choice, we used

the trick mentioned in appendix A and decomposed our diffusion matrix into eight different constituents, i.e.

$$\mathbf{D} = \mathbf{D}^{\alpha} + \mathbf{D}^{\beta} + \mathbf{D}^{\alpha^+} + \mathbf{D}^{\beta^+} + \mathbf{D}^{\beta\alpha} + \mathbf{D}^{\alpha\beta} + \mathbf{D}^{\beta^+\alpha^+} + \mathbf{D}^{\alpha^+\beta^+} \tag{C.2}$$

where the obvious choice for these constituents would be

$$\begin{aligned}
(\mathbf{D}^{\alpha})_{i,i+1} &= (\mathbf{D}^{\alpha})_{i+1,i} = \frac{\mathrm{i}J}{4\hbar}\alpha_i\alpha_{i+1} \\
(\mathbf{D}^{\beta})_{i,i+1} &= (\mathbf{D}^{\beta})_{i+1,i} = \frac{\mathrm{i}J}{4\hbar}\beta_i\beta_{i+1} \\
(\mathbf{D}^{\alpha^+})_{i,i+1} &= (\mathbf{D}^{\alpha^+})_{i+1,i} = -\frac{\mathrm{i}J}{4\hbar}\alpha_i^+\alpha_{i+1}^+ \\
(\mathbf{D}^{\beta^+})_{i,i+1} &= (\mathbf{D}^{\beta^+})_{i+1,i} = -\frac{\mathrm{i}J}{4\hbar}\beta_i^+\beta_{i+1}^+ \\
(\mathbf{D}^{\beta\alpha})_{i,i+1} &= (\mathbf{D}^{\beta\alpha})_{i+1,i} = -\frac{\mathrm{i}J}{4\hbar}\alpha_i\beta_{i+1} \\
(\mathbf{D}^{\alpha\beta})_{i,i+1} &= (\mathbf{D}^{\alpha\beta})_{i+1,i} = -\frac{\mathrm{i}J}{4\hbar}\beta_i\alpha_{i+1} \\
(\mathbf{D}^{\beta^+\alpha^+})_{i,i+1} &= (\mathbf{D}^{\beta^+\alpha^+})_{i+1,i} = \frac{\mathrm{i}J}{4\hbar}\alpha_i^+\beta_{i+1}^+ \\
(\mathbf{D}^{\alpha^+\beta^+})_{i,i+1} &= (\mathbf{D}^{\alpha^+\beta^+})_{i+1,i} = \frac{\mathrm{i}J}{4\hbar}\beta_i^+\alpha_{i+1}^+.
\end{aligned}$$

The idea is that instead of factorizing one complicated diffusion matrix, $\mathbf{D}$, we can instead factorize eight relatively simpler looking noise matrices, i.e. solving $\mathbf{B}^{\mathbf{x}}\left(\mathbf{B}^{\mathbf{x}}\right)^T = \mathbf{D}^{\mathbf{x}}$. To make things slightly more transparent we will write out the general form for the first constituent, i.e. $x = \alpha$:

$$\mathbf{D}^{\alpha} = \frac{\mathrm{i}J}{4\hbar}\begin{bmatrix}
\begin{bmatrix}
0 & \alpha_0\alpha_1 & 0 & \cdots & t\alpha_0\alpha_{N-1} \\
\alpha_1\alpha_0 & 0 & \alpha_1\alpha_2 & \cdots & 0 \\
0 & \alpha_2\alpha_1 & 0 & \ddots & 0 \\
\vdots & 0 & \ddots & \cdots & 0 \\
\alpha_{N-1}\alpha_0 & 0 & \cdots & \cdots & 0
\end{bmatrix} & & & \\
 & \mathbf{0} & & & \mathbf{0}\ \mathbf{0}\ \mathbf{0} \\
 & & \mathbf{0} & & \mathbf{0}\ \mathbf{0}\ \mathbf{0} \\
 & & & \mathbf{0} & \mathbf{0}\ \mathbf{0}\ \mathbf{0}
\end{bmatrix} \tag{C.3}$$

where $\mathbf{0}$ represents an $N \times N$ null matrix. If it were possible to find $\mathbf{B}^x$ for all x, then the total noise matrix takes the form of equation (A.7).

Unfortunately, using the obvious choice $\sqrt{B^x}$ would still be messy and it would appear that we have not made things any easier. However, we can apply the same trick once more and decompose each $\mathbf{D}^{\mathbf{x}}$ into N subconstituents: $\{\mathbf{D}^{\mathbf{x}}_{\mathbf{j}},\ \ j = 0 \ldots N-1\}$. Once again taking the $x = \alpha$ matrix as an example, the intuitive way of choosing the subconstituents is

$$\mathbf{D}^{\alpha} = \mathbf{D}^{\alpha}_{\mathbf{0}} + \mathbf{D}^{\alpha}_{\mathbf{1}} + \cdots + \mathbf{D}^{\alpha}_{\mathbf{N-1}} \tag{C.4}$$

$$= \frac{iJ}{4\hbar}\begin{bmatrix} 0 & \alpha_0\alpha_1 & \dots & \dots & 0 \\ \alpha_1\alpha_0 & 0 & \cdots & \cdots & \\ \vdots & \vdots & \ddots & \dots & \vdots \\ \vdots & \vdots & \ddots & \dots & \vdots \\ 0 & 0 & \cdots & \cdots & 0 \end{bmatrix} + \frac{iJ}{4\hbar}\begin{bmatrix} 0 & 0 & \cdots & \cdots & 0 \\ 0 & 0 & \alpha_1\alpha_2 & \dots & \\ 0 & \alpha_2\alpha_1 & \ddots & \cdots & \\ \vdots & \vdots & \dots & \ddots & \vdots \\ 0 & \dots & \dots & \dots & 0 \end{bmatrix} + \cdots$$
$$+\frac{iJ}{4\hbar}\begin{bmatrix} 0 & \cdots & \cdots & \cdots & \alpha_0\alpha_{N-1} \\ 0 & \cdots & \vdots & \cdots & \\ \vdots & \cdots & \ddots & \cdots & \\ \vdots & \vdots & \cdots & \ddots & \vdots \\ \alpha_{N-1}\alpha & \cdots & \cdots & \cdots & 0 \end{bmatrix}, \tag{C.5}$$

where the only non-trivial matrix elements of $\mathbf{D}^{\alpha}_{\mathbf{j}}$ are given by

$$(\mathbf{D}^{\alpha}_{\mathbf{j}})_{i,i+1} = (\mathbf{D}^{\alpha}_{\mathbf{j}})_{i+1,i} = \frac{iJ}{4\hbar}\alpha_j\alpha_{j+1}. \tag{C.6}$$

Each subconstituent diffusion matrix $\mathbf{D}^{\alpha}_{i}$ can then be individually factorized. This reduces the original problem to the much more trivial problem of factorizing matrices of the following form:

$$\mathbf{D}' = \begin{bmatrix} 0 & X \\ X & 0 \end{bmatrix} \tag{C.7}$$

for which we can easily show that either

$$\mathbf{B}' = \begin{bmatrix} -\sqrt{X/2} & -i\sqrt{X/2} \\ -\sqrt{X/2} & i\sqrt{X/2} \end{bmatrix} \tag{C.8}$$

or

$$\mathbf{B}'' = \begin{bmatrix} -\sqrt{X/2} & i\sqrt{X/2} \\ -\sqrt{X/2} & -i\sqrt{X/2} \end{bmatrix} \tag{C.9}$$

satisfies the necessary relation in equation (A.6). Now, granted that the decomposition for each $\mathbf{D}^{\alpha}_{i}$ exists, we can write equation (C.4) as

$$\mathbf{D}^{\alpha} = \mathbf{B}^{\alpha}_{\mathbf{0}}\left(\mathbf{B}^{\alpha}_{\mathbf{0}}\right)^{T} + \mathbf{B}^{\alpha}_{\mathbf{1}}\left(\mathbf{B}^{\alpha}_{\mathbf{1}}\right)^{T} + \cdots + \mathbf{B}^{\alpha}_{\mathbf{N-1}}\left(\mathbf{B}^{\alpha}_{\mathbf{N-1}}\right)^{T} \tag{C.10}$$

so that according to equation (A.7), the total noise matrix for $\mathbf{D}^{\alpha}$ takes the obvious form:

$$\mathbf{B}^{\alpha} = \begin{bmatrix} | & | & | & | & | & | \\ \mathbf{B}^{\alpha}_{\mathbf{0}} & \mathbf{B}^{\alpha}_{\mathbf{1}} & \dots & \mathbf{B}^{\alpha}_{\mathbf{j}} & \dots & \mathbf{B}^{\alpha}_{\mathbf{N-1}} \\ | & | & | & | & | & | \end{bmatrix} \tag{C.11}$$

obviously satisfying equation (A.6), with the only non-zero elements being:

$$\left(\mathbf{B}^{\alpha}_{\mathbf{j}}\right)_{j,2j} = -\frac{1}{2}\sqrt{\frac{iJ}{4\hbar}}\sqrt{\alpha_j\alpha_{j+1}}$$
$$\left(\mathbf{B}^{\alpha}_{\mathbf{j}}\right)_{j,2j+1} = -\frac{i}{2}\sqrt{\frac{iJ}{4\hbar}}\sqrt{\alpha_j\alpha_{j+1}}$$
$$\left(\mathbf{B}^{\alpha}_{\mathbf{j}}\right)_{j+1,2j} = -\frac{1}{2}\sqrt{\frac{iJ}{4\hbar}}\sqrt{\alpha_j\alpha_{j+1}}$$
$$\left(\mathbf{B}^{\alpha}_{\mathbf{j}}\right)_{j+1,2j+1} = \frac{i}{2}\sqrt{\frac{iJ}{4\hbar}}\sqrt{\alpha_j\alpha_{j+1}},$$

where $j = 0 \ldots N-1$. As an explicit example, the $N = 4$ case of equation (C.11) is shown below:

$$\mathbf{B}^{\alpha} = \tfrac{1}{2}\sqrt{\tfrac{\mathrm{i}J}{4\hbar}} \begin{bmatrix} \begin{bmatrix} -\sqrt{\alpha_0\alpha_1} & -\mathrm{i}\sqrt{\alpha_0\alpha_1} \\ -\sqrt{\alpha_0\alpha_1} & +\mathrm{i}\sqrt{\alpha_0\alpha_1} \\ 0 & 0 \\ 0 & 0 \\ \vdots & \vdots \\ 0 & 0 \end{bmatrix} \begin{bmatrix} 0 & 0 \\ -\sqrt{\alpha_1\alpha_2} & -\mathrm{i}\sqrt{\alpha_1\alpha_2} \\ -\sqrt{\alpha_1\alpha_2} & \mathrm{i}\sqrt{\alpha_1\alpha_2} \\ 0 & 0 \\ \vdots & \vdots \\ 0 & 0 \end{bmatrix} \begin{bmatrix} 0 & 0 \\ 0 & 0 \\ -\sqrt{\alpha_2\alpha_3} & -\mathrm{i}\sqrt{\alpha_2\alpha_3} \\ -\sqrt{\alpha_2\alpha_3} & \mathrm{i}\sqrt{\alpha_2\alpha_3} \\ \vdots & \vdots \\ 0 & 0 \end{bmatrix} \\ \begin{bmatrix} -\sqrt{\alpha_0\alpha_3} & -\mathrm{i}\sqrt{\alpha_0\alpha_3} \\ 0 & 0 \\ 0 & 0 \\ -\sqrt{\alpha_0\alpha_3} & +\mathrm{i}\sqrt{\alpha_0\alpha_3} \\ \vdots & \vdots \\ 0 & 0 \end{bmatrix} \end{bmatrix} \tag{C.12}$$

(C.13)

which is an $4N \times 2N$ matrix with most elements being trivial. This noise matrix would therefore introduce $2N$ independent Wiener increments (see equation (A.5)) can be stored as the components of the Wiener increment vector: $\mathrm{d}\vec{W}^{\alpha}$. In this fashion, the noise terms for the SDEs in equations (10) to (13) can be derived. If we label $\mathrm{d}\vec{W}^{\alpha}$ in the conventional way[8] then

$$\mathrm{d}\vec{W}^{\alpha} = \begin{bmatrix} \mathrm{dW}_0^{\alpha} \\ \mathrm{d}W_1^{\alpha} \\ \vdots \\ \vdots \\ \mathrm{d}W_{N-1}^{\alpha} \end{bmatrix}, \tag{C.14}$$

and the resulting stochastic terms only contribute to $\mathrm{d}\vec{\alpha}$, i.e.:

$$\mathrm{d}\alpha_i \propto -\sqrt{\alpha_i\alpha_{i+1}}\,(\mathrm{d}W_{2i} + \mathrm{i}\,\mathrm{d}W_{2i+1}) - \sqrt{\alpha_i\alpha_{i-1}}(\mathrm{d}W_{2i-2} + \mathrm{i}\,\mathrm{d}W_{2i-1}), \tag{C.15}$$

where we assumed 'periodic boundary conditions' for the Wiener increment vectors in the sense that $\mathrm{d}W_{-i} = \mathrm{d}W_{N-i}$ where $i \in [0, N-1]$.

References

[1] Calabrese P and Cardy J 2007 Quantum quenches in extended systems *J. Stat. Mech.* P06008

[2] Calabrese P and Cardy J 2007 Entanglement and correlation functions following a local quench: a conformal field theory approach *J. Stat. Mech.* P10004

[3] Kollath C, Läuchli A M and Altman E 2007 Quench dynamics and nonequilibrium phase diagram of the Bose–Hubbard model *Phys. Rev. Lett.* **98** 180601

[4] Manmana S R, Wessel S, Noack R M and Muramatsu A 2007 Strongly correlated fermions after a quantum quench *Phys. Rev. Lett.* **98** 210405

[5] Barmettler P, Punk M, Gritsev V, Demler E and Altman E 2009 Relaxation of antiferromagnetic order in spin-1/2 chains following a quantum quench *Phys. Rev. Lett.* **102** 130603

[6] Roux G 2009 Quenches in quantum many-body systems: one-dimensional Bose–Hubbard model re-examined *Phys. Rev.* A **79** 21608

[8] The labeling for $\mathrm{d}W^{\alpha\beta}$, $\mathrm{d}W^{\beta\alpha}$, $\mathrm{d}W^{\beta^+\alpha^+}$ and $\mathrm{d}W^{\alpha^+\beta^+}$ does not follow the usual convention and can be deduced from the corresponding noise terms in equations (10)–(13).

[7] Langer S, Heidrich-Meisner F, Gemmer J, McCulloch I P and Schollwöck U 2009 Real-time study of diffusive and ballistic transport in spin-1/2 chains using the adaptive time-dependent density matrix renormalization group method *Phys. Rev.* B **79** 214409

[8] Roux G 2010 Finite-size effects in global quantum quenches: examples from free bosons in an harmonic trap and the one-dimensional Bose–Hubbard model *Phys. Rev.* A **81** 053604

[9] Barmettler P, Punk M, Gritsev V, Demler E and Altman E 2010 Quantum quenches in the anisotropic spin-1/2 Heisenberg chain: different approaches to many-body dynamics far from equilibrium *New J. Phys.* **12** 055017

[10] Prosen T 2008 Third quantization: a general method to solve master equations for quadratic open Fermi systems *New J. Phys.* **10** 043026

[11] Calabrese P, Faribault A and Caux J-S 2009 Bethe ansatz approach to quench dynamics in the Richardson model *J. Math. Phys.* **50** 095212

[12] Faribault A, Calabrese P and Caux J-S 2009 Quantum quenches from integrability: the fermionic pairing model *J. Stat. Mech.* P03018

[13] Rizzi M, Montangero S and Vidal G 2008 Simulation of time evolution with multiscale entanglement renormalization ansatz *Phys. Rev.* A **77** 052328

[14] Fioretto D and Mussardo G 2010 Quantum quenches in integrable field theories *New J. Phys.* **12** 055015

[15] Fagotti M and Calabrese P 2008 Evolution of entanglement entropy following a quantum quench: analytic results for the xy chain in a transverse magnetic field *Phys. Rev.* A **78** 010306

[16] Daley A J, Kollath C, Schollwöck U and Vidal G 2004 Time-dependent density-matrix renormalization-group using adaptive effective Hilbert spaces *J. Stat. Mech.* P04005

[17] White S R and Feiguin A E 2004 Real-time evolution using the density matrix renormalization group *Phys. Rev. Lett.* **93** 76401

[18] Bañuls M C, Hastings M B, Verstraete F and Cirac J I 2009 Matrix product states for dynamical simulation of infinite chains *Phys. Rev. Lett.* **102** 240603

[19] Gobert D, Kollath C, Schollwoeck U and Schuetz G 2005 Real-time dynamics in spin-1/2 chains with adaptive time-dependent density matrix renormalization group *Phys. Rev.* E **71** 36102

[20] Verstraete F, García-Ripoll J J and Cirac J I 2004 Matrix product density operators: simulation of finite-temperature and dissipative systems *Phys. Rev. Lett.* **93** 207204

[21] Zwolak M and Vidal G 2004 Mixed-state dynamics in one-dimensional quantum lattice systems: a time-dependent superoperator renormalization algorithm *Phys. Rev. Lett.* **93** 207205

[22] Hartmann M J, Prior J, Clark S R and Plenio M B 2009 Density matrix renormalization group in the Heisenberg picture *Phys. Rev. Lett.* **102** 057202

[23] Clark S R, Prior J, Hartmann M J, Jaksch D and Plenio M B 2010 Exact matrix product solutions in the Heisenberg picture of an open quantum spin chain *New J. Phys.* **12** 025005

[24] Drummond P D and Gardiner C W 1980 Generalised P-representations in quantum optics *J. Phys. A: Math. Gen.* **13** 2353–68

[25] Deuar P and Drummond P D 2002 Gauge P-representations for quantum-dynamical problems: removal of boundary terms *Phys. Rev.* A **66** 033812

[26] Van Dam H and Biedenharn L C 1965 *Quantum Theory of Angular Momentum* (New York: Academic)

[27] Sakurai J J 1994 *Modern Quantum Mechanics* (Reading, MA: Addison-Wesley)

[28] Olsen M K, Plimak L I, Rebic S and Bradley A S 2005 Phase-space analysis of Bosonic spontaneous emission *Opt. Commun.* **254** 271–81

[29] Smith A M and Gardiner C W 1989 Simulations of nonlinear quantum damping using the positive-P representation *Phys. Rev.* A **39** 3511–24

[30] McNeil K J and Craig I J D 1990 Positive-P representation for second-harmonic generation: analytic and computational results *Phys. Rev.* A **41** 4009–18

[31] Steel M J, Olsen M K, Plimak L I, Drummond P D, Tan S M, Collett M J, Walls D F and Graham R 1998 Dynamical quantum noise in trapped Bose–Einstein condensates *Phys. Rev.* A **58** 4824–35

[32] Deuar P and Drummond P D 2006 First-principles quantum dynamics in interacting Bose gases: I. The positive-P representation *J. Phys. A: Math. Gen.* **39** 1163–81

[33] Deuar P and Drummond P D 2007 Correlations in a bec collision: first-principles quantum dynamics with 150 000 atoms *Phys. Rev. Lett.* **98** 120402

[34] Drummond P D and Mortimer I K 1991 Computer simulations of multiplicative stochastic differential equations *J. Comput. Phys.* **93** 144–70

[35] Gilchrist A, Gardiner C W and Drummond P D 1997 Positive-P representation: application and validity *Phys. Rev.* A **55** 3014–32

[36] Plimak L I, Olsen M K and Collett M J 2001 Optimization of the positive-P representation for the anharmonic oscillator *Phys. Rev.* A **64** 025801

[37] Deuar P and Drummond P D 2006 First-principles quantum dynamics in interacting bose gases: II. Stochastic gauges *J. Phys. A: Math. Gen.* **39** 2723–55

[38] Deuar P 2005 First-principles quantum simulations of many-mode open interacting Bose gases using stochastic gauge methods arXiv:cond-mat/0507023

[39] Deuar P and Drummond P D 2001 Stochastic gauges in quantum dynamics for many-body simulations *Comput. Phys. Commun.* **142** 442–5

[40] Drummond P D and Deuar P 2003 Quantum dynamics with stochastic gauge simulations *J. Opt. B: Quantum Semiclass. Opt.* **5** S281–9

[41] Drummond P D, Deuar P and Kheruntsyan K V 2004 Canonical Bose gas simulations with stochastic gauges *Phys. Rev. Lett.* **92** 040405

[42] Ghanbari S, Corney J F and Kieu T D 2010 Finite temperature correlations in the Bose–Hubbard model: application of the Gauge-P representation arXiv:1002.4735

[43] Deuar P, Sykes A G, Gangardt D M, Davis M J, Drummond P D and Kheruntsyan K V 2009 Nonlocal pair correlations in the one-dimensional Bose gas at finite temperature *Phys. Rev.* A **79** 043619

[44] Carusotto I, Castin Y and Dalibard J 2001 n-Boson time-dependent problem: a reformulation with stochastic wave functions *Phys. Rev.* A **63** 023606

[45] Aimi T and Imada M 2007 Does simple two-dimensional Hubbard model account for high-t_c superconductivity in copper oxides? *J. Phys. Soc. Japan* **76** 113708

[46] Barry D W and Drummond P D 2008 Qubit phase space: $su(n)$ coherent-state P-representations *Phys. Rev.* A **78** 052108

[47] Drummond P D and Corney J F 1999 Quantum dynamics of evaporatively cooled Bose–Einstein condensates *Phys. Rev.* A **60** R2661–4

[48] Ögren M and Kheruntsyan K V 2009 Atom–atom correlations in colliding Bose–Einstein condensates *Phys. Rev.* A **79** 021606

[49] Mølmer K, Perrin A, Krachmalnicoff V, Leung V, Boiron D, Aspect A and Westbrook C I 2008 Hanbury Brown and Twiss correlations in atoms scattered from colliding condensates *Phys. Rev.* A **77** 033601

[50] Glauber R J 1963 The quantum theory of optical coherence *Phys. Rev.* **130** 2529–39

[51] Olsen M K and Bradley A S 2009 Numerical representation of quantum states in the positive-P and Wigner representations *Opt. Commun.* **282** 3924–9

CHAPTER 3

SPIN COHERENT STATES

3.1 Motivation

A central requirement when using the PPR is an overcomplete basis. In our first look at simulating spin dynamics, we utilized a bosonic coherent state basis that was made possible by implementing a Schwinger Boson transformation (Sakurai, 1993). This choice was primarily used for historic reasons and while successful, produced relatively short simulation lifetimes. In addition, introducing two independent Schwinger bosons per spin resulted in a phase space with $4N$ complex degrees of freedom instead of the usual $2N$. An obvious extension and possible improvement for this technique was to investigate the use of SU(2) spin coherent states (SCS) basis (Radcliffe, 1971) instead which is a more intuitive choice for spin systems. Furthermore, since it is parametrized by a single complex variable, it immediately reduces the complex degrees of freedom to 2N as desired. This new basis was previously used to simulate the imaginary time dynamics of the 2D classical Ising model (Barry and Drummond, 2008) and has recently been used to simulate the real time dynamics of a *Dicke Network* (Mandt et al., 2014) - an N interacting large spin system coupled to a single mode cavity. The effects of dissipation of both the spin and bosonic degrees of freedom were also considered in the latter work. At the time that this research was carried out, we were unaware of any other PP real time simulations that utilized a SCS basis.

A straightforward application of the PPR (even with this new basis) while interesting, would inevitably inherit the usual limitations of short simulation life times as discussed in section 2.9. Beyond this time scale, no meaningful results are obtainable and some optimization procedure is clearly essential. In 2012, Deuar (Deuar et al., 2009) once again made headway in optimizing the PP by utilizing an extrapolation scheme to calculate the quantum dynamics (QD) of colliding BECs. The results obtained were not only exact but also had a simulation life time that was significantly longer than the bare t^{PP}_{life}. The Implementation of this novel technique, which we will outline in section 3.7 constitutes the premise of our second publication (Ng et al., 2013). In what follows, we will provide

the derivation of the formalism using SU(2) coherent states and derive the SDEs for the transverse Ising model as a test system.

3.2 SU(2) Coherent states

While the bosonic coherent state is defined by $\alpha \in \mathbb{C}$ such that $|\alpha\rangle \sim e^{\alpha \hat{S}^+}|0\rangle$, where $|0\rangle$ is the vacuum state, we can analogously define an SU(2) coherent state as $|w\rangle \sim e^{\hat{S}^+ w}|s,-s\rangle$, where $|s,-s\rangle$ has the minimum spin projection. We will however follow the parametrization of (Barry and Drummond, 2008) such that our unnormalized SU(2) SCS for a spin-1/2 system takes the form:

$$|z\rangle = e^{-Sz}e^{\hat{S}^+ e^z}|0\rangle = \begin{bmatrix} e^{z/2} \\ e^{-z/2} \end{bmatrix}, \tag{3.2.1}$$

where we obtain the second expression by expanding the exponential operator to first order: $e^{\hat{S}^+ e^z} = (1 + \hat{S}^+ e^z)$. The SU(2) coherent state can be equivalently visualised as point on the surface of the unit Bloch sphere and there exists a one to one mapping of the complex plane on to the surface of the Bloch sphere. If we imagine the Bloch sphere located right above the complex plane, with its south pole located at the origin, the mapping is achieved by wrapping the complex plane over the sphere. Mathematically, this can be effected by the change of variables:

$$e^z = e^{i\phi}\tan(\theta/2), \tag{3.2.2}$$

where $\theta \in [0,\pi]$ is the azimuthal angle extending from the south-pole and $\phi \in [0,\pi]$ is the polar one. Using this variable change, there is only one problematic point that is located at the north pole (i.e. $\theta = \pi/2$), which corresponds to the infinite regions of the complex plane. Physically, the south pole represent the spin down state while the north pole represents the spin up state. We will further address how to deal with this improper map in section 3.6. An additional important property of the SCS is their non-orthogonality with a non-zero overlap that can be evaluated to be:

$$\mathscr{N} \equiv \langle z'^*|z\rangle = 2\cosh(R), \tag{3.2.3}$$

where $R = \frac{z+z'}{2}$.

3.3 Correspondence relations

It is now essential to derive new correspondence relations. The kernel, $\hat{\Lambda}(z,z')$ that we will use in the PP expansion:

$$\hat{\rho} = \int P(z,z')\hat{\Lambda}(z,z')d^z d^2 z' \tag{3.3.1}$$

is analogously defined as:

$$\hat{\Lambda}(z,z') \equiv \frac{\hat{\Lambda}_o}{\mathscr{N}} = \frac{|z\rangle\langle z'^*|}{\mathscr{N}}, \tag{3.3.2}$$

where $\hat{\Lambda}_o$ is the unnormalised kernel and our choice of $\mathscr{N} = \langle z'^* | z \rangle$ ensures that $\mathrm{Tr}(\hat{\Lambda}) = 1$. Before we derive the correspondence relations for the full kernel $\hat{\Lambda}$, it would be useful to perform the same steps for $\hat{\Lambda}_o$. It is trivial to show that $\hat{\Lambda}_o$ obeys the following correspondence relations:

$$\hat{S}^z \hat{\Lambda}_o = \frac{\partial}{\partial z} \hat{\Lambda}_o \tag{3.3.3}$$

$$\hat{S}^+ \hat{\Lambda}_o = e^{-z} \left[\frac{1}{2} + \frac{\partial}{\partial z} \right] \hat{\Lambda}_o \tag{3.3.4}$$

$$\hat{S}^- \hat{\Lambda}_o = e^{z} \left[\frac{1}{2} - \frac{\partial}{\partial z} \right] \hat{\Lambda}_o. \tag{3.3.5}$$

Using the standard definition for the transverse spin operators, i.e.

$$\hat{S}^x = \frac{1}{2} \left(\hat{S}^+ + \hat{S}^- \right) \tag{3.3.6}$$

$$\hat{S}^y = \frac{1}{2i} \left(\hat{S}^+ - \hat{S}^- \right), \tag{3.3.7}$$

we can use eq. 3.3.4 and eq. 3.3.5 to obtain:

$$\hat{S}^x \hat{\Lambda}_o = \left[\frac{1}{2} \cosh(z) - \sinh(z) \frac{\partial}{\partial z} \right] \hat{\Lambda}_o \tag{3.3.8}$$

$$\hat{S}^y \hat{\Lambda}_o = \left[\frac{i}{2} \sinh(z) - i \cosh(z) \frac{\partial}{\partial z} \right] \hat{\Lambda}_o. \tag{3.3.9}$$

In the PP formalism, one can implement an adhoc mathematical operation to expedite derivations. For instance, in order to obtain the left ordering of the correspondence relations, i.e. $\hat{\Lambda}\hat{O}$ from its right ordering $\hat{O}\hat{\Lambda}$(or vice versa), we simply take the hermitian conjugate of the operator on the LHS and carry out a modified complex conjugate operation on the differential operator, denoted as $c.c.'$ on the RHS. The essence of $c.c'$ is that complex constants are conjugated and complex stochastic variables are replaced by their primed counterparts, i.e. $z \leftrightarrow z'$. The kernel itself is non-hermitian and to be left alone. As an example, under this operation, eq. 3.3.5 becomes:

$$\left[\hat{S}^- \hat{\Lambda}_o \right]^\dagger = \left[e^{z} \left[\frac{1}{2} - \frac{\partial}{\partial z} \right] \hat{\Lambda}_o \right] |_{c.c'} \tag{3.3.10}$$

$$\hat{\Lambda}_o \hat{S}^+ = e^{z'} \left[\frac{1}{2} - \frac{\partial}{\partial z'} \right] \hat{\Lambda}_o. \tag{3.3.11}$$

Similarly we can derive the left ordering operators for eq. 3.3.3 and eq. 3.3.4.

Another important relation we need is the derivative of the inverse norm: $\mathscr{N}^{-1}$. For an N-site (as mentioned in section 2.8) spin system, the kernel generalizes to its direct product: $\Lambda_o(\hat{z}, z') = \prod_{j=1}^{N} \frac{\hat{\Lambda}(z_j, z'_j)}{\mathscr{N}_i} \otimes$, where we have now restored site indices so that

$$\mathscr{N} \equiv \langle z'^* | z \rangle = \prod_{j=1}^{N} 2 \cosh\left(R_j \right) \tag{3.3.12}$$

Note that z_j and z_j' appear in a symmetric fashion and so its derivative (which will be used later on) is given by:

$$\begin{aligned}\frac{\partial}{\partial z_i}\left(\langle z'^{*}|z\rangle\right)^{-1} &= \tfrac{\partial}{\partial z_i}\mathscr{N}^{-1} = \left(\prod_{j\neq i}2^{-1}\mathrm{sech}(R_j)\right)\left(-2^{-1}\mathrm{sech}(R_i)\tanh(R_i)\frac{1}{2}\right)\\ &= -\frac{1}{2}\tanh(R_i)\mathscr{N}^{-1} \qquad (3.3.13)\end{aligned}$$

since $\frac{d}{dz}\mathrm{sech}(z) = -\mathrm{sech}(z)\tanh(z)$. We are now ready to derive the correspondence relations. As a starting example, we will fill in the details for the derivations for the $\hat{S}_z$ correspondence relation by taking a derivative of $\hat{\Lambda}$ and further using eq. 3.3.3 and eq. 3.3.13. This yields

$$\begin{aligned}\frac{\partial}{\partial z_i}\hat{\Lambda} &= \mathscr{N}^{-1}\frac{\partial}{\partial z_i}\hat{\Lambda}_o + \hat{\Lambda}_o\frac{\partial}{\partial z_i}\mathscr{N}^{-1}\\ &= \mathscr{N}^{-1}\hat{S}_i^z\hat{\Lambda}_o + \hat{\Lambda}_o(-\mathscr{N}^{-1}\frac{1}{2}\tanh(R_i))\\ &= \hat{S}_i^z\hat{\Lambda} - \frac{1}{2}\tanh(R_i)\hat{\Lambda} \qquad (3.3.14)\end{aligned}$$

or

$$\hat{S}_i^z\hat{\Lambda} = \frac{\partial}{\partial z_i}\hat{\Lambda} + \frac{1}{2}\tanh(R_i)\hat{\Lambda}, \qquad (3.3.15)$$

thereby completing our derivation for our new correspondence relation for $\hat{S}^z$. Note that eq 3.3.15 also tells us that it is possible to replace derivatives of the unweighted kernel, $\hat{\Lambda}_o$ in terms of the new normalized ones, $\hat{\Lambda}$, i.e. either

$$\mathscr{N}^{-1}\frac{\partial}{\partial z_i}\hat{\Lambda}_o = \frac{\partial}{\partial z_i}\hat{\Lambda} + \frac{1}{2}\tanh(R_i)\hat{\Lambda}. \qquad (3.3.16)$$

or

$$\mathscr{N}^{-1}\frac{\partial}{\partial z_i'}\hat{\Lambda}_o = \frac{\partial}{\partial z_i'}\hat{\Lambda} + \frac{1}{2}\tanh(R_i)\hat{\Lambda}, \qquad (3.3.17)$$

where we have made use of $c.c'$ to obtain eq. 3.3.17. The last two identities will allow us to derive the correspondence relations for the less trivial case of $\hat{S}^+\hat{\Lambda}$ for example where some algebraic manipulation is in order. To begin, we simply multiply eq. 3.3.4 on both sides by $\mathscr{N}^{-1}$ and replace derivatives of the unnormalized kernel with derivatives of the full kernel by substituting eq. 3.3.16 where necessary, i.e.:

$$\mathscr{N}^{-1}\hat{S}_i^+\hat{\Lambda}_o = \mathscr{N}^{-1}e^{-z_i}\left[\frac{1}{2} + \frac{\partial}{\partial z_i}\right]\hat{\Lambda}_o \qquad (3.3.18)$$

so that

$$\begin{aligned}\hat{S}_i^+\hat{\Lambda} &= \left[\frac{e^{-z_i}}{2}\hat{\Lambda} + e^{-z_i}\mathscr{N}^{-1}\frac{\partial}{\partial z_i}\hat{\Lambda}_o\right]\\ &= \left[\frac{e^{-z_i}}{2}\hat{\Lambda} + e^{-z_i}\left(\frac{\partial}{\partial z_i}\hat{\Lambda} + \frac{1}{2}\tanh(R_i)\hat{\Lambda}\right)\right] \qquad (3.3.19)\\ &= \left[\frac{e^{-z_i}}{2}\hat{\Lambda} + e^{-z_i}\frac{\partial}{\partial z_i}\hat{\Lambda} + \frac{e^{-z_i}}{2}\tanh(R_i)\hat{\Lambda}\right]. \qquad (3.3.20)\end{aligned}$$

Applying the $c.c'$ operation then immediately yields the left ordering for $\hat{S}_i^-$:

$$\hat{\Lambda}\hat{S}_i^- = \frac{e^{-z_i'}}{2}\hat{\Lambda} + e^{-z_i'}\frac{\partial}{\partial z'}\hat{\Lambda} + \frac{e^{-z'}}{2}\hat{\Lambda}\tanh(R_i). \tag{3.3.21}$$

Note that complex functions where z and z' appear symmetrically as in $\tanh(R_i)$ are unchanged under $c.c'$. The remaining correspondence relations can be derived in a similar fashion and we will skip further derivations for brevity. A summary of the important relations however are listed below. The right ordering gives:

$$\hat{S}^z\hat{\Lambda} = \left[\frac{\partial}{\partial z_i} + \frac{1}{2}\tanh(R_i)\right]\hat{\Lambda} \tag{3.3.22}$$

$$\hat{S}^+\hat{\Lambda} = \left[\frac{e^{-z}}{2} + e^{-z}\frac{\partial}{\partial z} + \frac{e^{-z}}{4}\tanh(R)\right]\hat{\Lambda}. \tag{3.3.23}$$

$$\hat{S}^-\hat{\Lambda} = \left[\frac{e^{z}}{2} - e^{z}\frac{\partial}{\partial z} - \frac{e^{z}}{4}\tanh(R_i)\right]\hat{\Lambda} \tag{3.3.24}$$

$$\hat{S}^x\hat{\Lambda} = \left[-\sinh(z)\frac{\partial}{\partial z} + \frac{1}{2}\cosh(z) - \frac{1}{2}\sinh(z)\tanh(R)\right]\hat{\Lambda} \tag{3.3.25}$$

$$\hat{S}^y\hat{\Lambda} = \left[-i\cosh(z)\frac{\partial}{\partial z} + \frac{i}{2}\sinh(z) - \frac{i}{2}\cosh(z)\tanh(R)\right]\hat{\Lambda} \tag{3.3.26}$$

while the left ordering gives

$$\hat{\Lambda}\hat{S}^z = \left[\frac{\partial}{\partial z_i'} + \frac{1}{2}\tanh(R_i)\right]\hat{\Lambda} \tag{3.3.27}$$

$$\hat{\Lambda}\hat{S}^+ = \left[\frac{e^{z'}}{2} - e^{z'}\frac{\partial}{\partial z_i'} - \frac{e^{z'}}{2}\tanh(R_i)\right]\hat{\Lambda} \tag{3.3.28}$$

$$\hat{\Lambda}\hat{S}^- = \left[\frac{e^{-z'}}{2} + e^{-z'}\frac{\partial}{\partial z'} + \frac{e^{-z'}}{2}\tanh(R_i)\right]\hat{\Lambda} \tag{3.3.29}$$

$$\hat{\Lambda}\hat{S}^x = \left[-\sinh(z')\frac{\partial}{\partial z'} + \frac{1}{2}\cosh(z') - \frac{1}{2}\sinh(z')\tanh(R)\right]\hat{\Lambda} \tag{3.3.30}$$

$$\hat{\Lambda}\hat{S}^y = \left[i\cosh(z')\frac{\partial}{\partial z'} - \frac{i}{2}\sinh(z) + \frac{i}{2}\cosh(z')\tanh(R)\right]\hat{\Lambda} \tag{3.3.31}$$

3.3.1 Observables

For spin systems, the observables that are typically of interest are the spin components and the correlation functions. It is possible to once again use the correspondence relations to derive the equivalent phase space functions for the expectation values. For instance, the expectation value for

the S_z spin component is given by the following expression:

$$\begin{aligned}
\langle \hat{S}_i^z \rangle &= \mathrm{Tr}\left(\hat{S}_i^z \hat{\rho}\right) \\
&= \mathrm{Tr}\left(\int\int P(z,z')\hat{S}_i^z \hat{\Lambda} d^2z d^2z'\right) \quad \textit{use correspondence relations} \\
&= \mathrm{Tr}\left(\int P(z)\left(\partial_i + \frac{1}{2}\tanh(R_i)\right)\hat{\Lambda} d^2z\right) \\
&= \int P(z)\left(\partial_i + \frac{1}{2}\tanh(R_i)\right) tr(\hat{\Lambda}) d^2z \quad \textit{recall that the kernel is normalized} \\
&= \int P(z)\left(\frac{1}{2}\tanh(R_i)\right) d^2z \\
&= \langle\langle \frac{1}{2}\tanh(R_i)\rangle\rangle \qquad (3.3.32) \\
&= \langle\langle S_i^z\rangle\rangle \qquad (3.3.33)
\end{aligned}$$

where we have introduced the notation $S_i^z = \frac{1}{2}\tanh(R_i)$ and $\langle\langle \ldots \rangle\rangle$ denotes a stochastic averaging. Note that single derivative terms acting on $\hat{\Lambda}$ present in the correspondence relations will vanish in the stochastic estimator. Adopting the abbreviation: $\{c_i, s_i, T_i\} = \{\cosh(z_i), \sinh(z_i), \tanh(R_i)\}$ and $\{c_i', s_i'\} = \{\cosh(z_i'), \sinh(z_i')\}$, one can trivially to show that:

$$\begin{aligned}
\langle \hat{S}_i^y \rangle &= tr\left(\hat{S}_i^y \hat{\rho}\right) \qquad (3.3.34) \\
&= \langle\langle \frac{i}{2}(s_i - c_i T_i)\rangle\rangle \qquad (3.3.35) \\
&= \langle\langle S_i^y\rangle\rangle \qquad (3.3.36)
\end{aligned}$$

and

$$\begin{aligned}
\langle \hat{S}_i^x \rangle &= tr\left(\hat{S}_i^x \hat{\rho}\right) \qquad (3.3.37) \\
&= \langle\langle \frac{1}{2}(c_i - s_i T_i)\rangle\rangle \qquad (3.3.38) \\
&= \langle\langle S_i^x\rangle\rangle \qquad (3.3.39)
\end{aligned}$$

where we have further introduced the aptly named expressions

$$S_i^y = \frac{1}{2}\left(\cosh(z_i) - \sinh(z_i)\tanh(R_i)\right) \qquad (3.3.40)$$

and

$$S_i^x = \frac{i}{2}\left(\sinh(z_i) - \cosh(z_i)\tanh(R_i)\right). \qquad (3.3.41)$$

And so we see that the expectation value of the operators: $\left\{\hat{S}_i^\alpha\right\}$ map directly on to the phase space functions: $\left\{S_i^\alpha\right\}$ where $\alpha = x, y, z$ and are therefore aptly named. The correlation functions can be also calculated analogously more attention has to be paid to the extra derivatives which now appear. Calculating the S^y-correlations between sites i and j for example and using the cyclic property of

the trace, we can write:

$$\begin{aligned}
\langle \hat{S}_i^y \hat{S}_j^y \rangle &= \mathrm{Tr}\left(\hat{S}_j^y \hat{\rho} \hat{S}_i^y\right) \\
&= \mathrm{Tr}\left(\int P(z)\left(-S_i^{y\prime} + ic_i'\partial_i'\right)\left(S_j^y - ic_j\partial_j\right)\hat{\Lambda} d^2z\right) \\
&= \mathrm{Tr}\left(\int P(z)\left(-S_i^{y\prime}S_j^y + ic_i'\partial_i' S_j^y + iS_i^{y\prime}c_j\partial_j + c_i'c_j\partial_i'\partial_j\right)\hat{\Lambda} d^2z d^2z'\right) \\
&= \langle\langle -S_i^{y\prime}S_j^y\rangle\rangle + i\langle\langle c_i'\partial_i' S_i^y\rangle\rangle\delta_{ij} \\
&= \langle\langle -S_i^{y\prime}S_j^y\rangle\rangle + \frac{i\delta_{ij}}{4}\langle\langle \frac{c_i'c_i}{C_i^2}\rangle\rangle,
\end{aligned} \tag{3.3.42}$$

where $C_i = \cosh(R_i)$ and the second term is only included for on-site correlations. Similarly we can show that:

$$\langle \hat{S}_i^x \hat{S}_j^x \rangle = \langle\langle S_i^{x\prime} S_j^x\rangle\rangle + \frac{\delta_{ij}}{4}\langle\langle \frac{s_i' s_i}{C_i^2}\rangle\rangle \tag{3.3.43}$$

and

$$\langle \hat{S}_i^z \hat{S}_j^z \rangle = \frac{1}{4}\langle\langle S_i^z S_j^z\rangle\rangle + \frac{\delta_{ij}}{4}\langle\langle \frac{1}{C_i^2}\rangle\rangle. \tag{3.3.44}$$

Following the above steps, it is easy to derive general expressions for other non-diagonal correlators: $\langle \hat{S}^\alpha \hat{S}^\beta\rangle|_{\alpha\neq\beta}$ where $\alpha,\beta = x,y,z$ can be derived as well.

3.4 Deriving SDEs for the transverse Ising model

The correspondence relations for the normalized kernel, $\hat{\Lambda}$ in eq. 3.3.22-eq. 3.3.31 in the master equation:

$$\frac{d}{dt}\hat{\rho} = -\frac{i}{\hbar}\left[\hat{H},\hat{\rho}\right] \tag{3.4.1}$$

can now be used to derive SDEs as was done for the 1D BH model in section 2.11. We derive the results for a transverse Ising spin-1/2 model given by the usual Hamiltonian:

$$\hat{H} = -J\sum_{\langle i,j\rangle}\hat{S}_i^z\hat{S}_j^z - h\sum_i \hat{S}^x, \tag{3.4.2}$$

where $J>0$ is the strength of the Ising interaction and h is the external field along the transverse x-axis. Let us sketch out the derivations term by term. First let us treat the Ising term:

$$\begin{aligned}
&\frac{d}{dt}\hat{\rho} \sim \frac{iJ}{\hbar}\left[\hat{S}_i^z\hat{S}_j^z\hat{\Lambda} - \hat{\Lambda}\hat{S}_i^z\hat{S}_j^z\right] \\
&= \frac{iJ}{\hbar}\left[\left(\frac{\partial}{\partial z_j} + S_j^z\right)\left(\frac{\partial}{\partial z_i} + S_j^z\right) - \left(\frac{\partial}{\partial z_j'} + S_j^z\right)\left(\frac{\partial}{\partial z_i'} + S_i^z\right)\right]\hat{\Lambda} \\
&= \frac{iJ}{\hbar}\left[\partial_i\partial_j + S_j^z\partial_i + S_j^z\partial_i - \partial_i'\partial_j' - S_j^z\partial_i' - S_j^z\partial_i'\right]\hat{\Lambda},
\end{aligned} \tag{3.4.3}$$

where we have made the substitution $S_i^z = \tanh(R_i)$ and taken advantage of the fact that it is insensitive to the $c.c.'$ operation, and formally speaking: $S_i^z = S_i^{z\prime}$. The drift terms arising from the Ising interactions can be immediately read off, i.e.

$$dz_i \sim \frac{iJ}{\hbar} \sum_{j \in n(i)} S_j^z. \tag{3.4.4}$$

where $n(i)$ is the list of sites connected to i. For a 1D system with NN bonds for example, $n(i) = \{i-1, i+1\}$. Similarly, the diffusion matrix can be further decomposed so that every bond $b(i,j)$ connecting site i and j corresponds to a unique matrix:

$$D_{b(i,j)} = iJ \begin{array}{c} \begin{array}{cc} \textit{site } i & \textit{site } j \end{array} \\ \begin{bmatrix} 0 & 1 \\ 1 & 0 \end{bmatrix} \end{array} \begin{array}{l} \textit{site } i \\ \\ \textit{site } j \end{array}, \tag{3.4.5}$$

with the following noise decomposition:

$$B_{b(i,j)} = \sqrt{\frac{iJ}{2}} \begin{array}{c} \begin{array}{cc} \textit{site } i & \textit{site } j \end{array} \\ \begin{bmatrix} 1 & -i \\ 1 & i \end{bmatrix} \end{array} \begin{array}{l} \textit{site } i \\ \\ \textit{site } j \end{array}, \tag{3.4.6}$$

as well as its own noise terms $\eta_b^r, \eta_b^{im} \in N(0, 1/dt)$. This results in the following stochastic contribution to the SDEs:

$$\frac{d}{dt} \begin{bmatrix} z_i \\ \\ z_j \end{bmatrix} \sim \sqrt{\frac{iJ}{2}} \begin{bmatrix} 1 & i \\ \\ 1 & -i \end{bmatrix} \begin{bmatrix} \eta_b^r \\ \\ \eta_b^{im} \end{bmatrix} = \sqrt{\frac{iJ}{2}} \begin{bmatrix} \tilde{\eta}_b \\ \\ \tilde{\eta}_b^* \end{bmatrix}, \tag{3.4.7}$$

where $\tilde{\eta}_b = \eta_b^r + i\eta_{im}^r$. This can be further simplified by noting that $\sqrt{\frac{i}{2}} = \frac{1}{2}(1+i)$ and expanding out the noise terms so that:

$$\begin{aligned} \sqrt{\frac{iJ}{2}}(\eta_b^r \pm i\eta_b^{im}) &= \frac{\sqrt{J}}{2}(1+i)(\eta_b^r \pm i\eta_b^{im}) && (3.4.8) \\ &= \frac{\sqrt{J}}{2}([\eta_b^r \mp \eta_b^{im}] + i[\eta_b^r \pm \eta_b^{im}]) && (3.4.9) \\ &= \sqrt{J}(\eta_b^{\mp} + i\eta_b^{\mp}) && (3.4.10) \end{aligned}$$

where $(\eta_b^-, \eta_b^+) = \left(\frac{1}{2}(\eta_b^r - \eta_b^{im}), \frac{1}{2}(\eta_b^r + \eta_b^{im})\right)$ are statistically distributed such that $\eta_b^{\pm} \in N(0, \frac{1}{2dt})$. If we further define the complex noise:

$$\eta_b = \eta_b^- + i\eta_b^+, \tag{3.4.11}$$

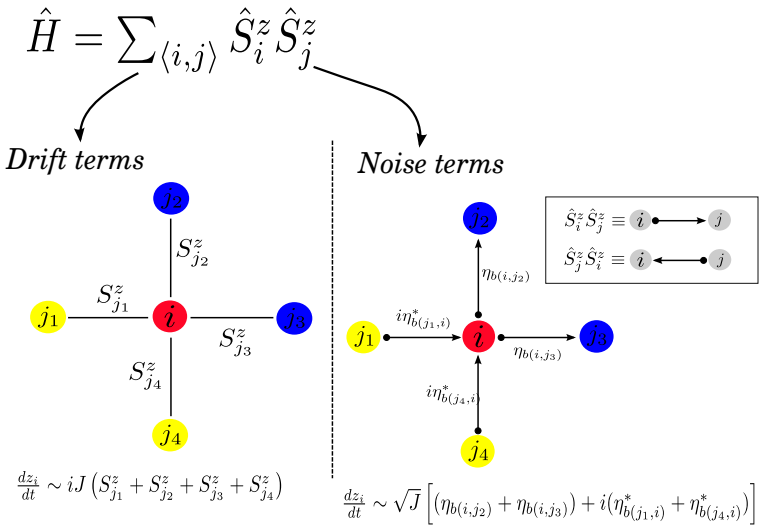

Figure 3.1: Schematic representation of the drift and diffusion terms for a 2D Ising interaction. For the noise terms, there is a directionality indicated by the arrow that depends on how the operators are ordered in the Hamiltonian. The base of the arrow indicates the index of the first operator while the tip of the arrow represents the second operator.

the Ising noise terms in eq. 3.4.7 simplify to:

$$\sqrt{\frac{iJ}{2}} \begin{bmatrix} \tilde{\eta}_b \\ \\ \tilde{\eta}_b^* \end{bmatrix} = \sqrt{J} \begin{bmatrix} \eta_b \\ \\ i\eta_b^* \end{bmatrix}. \tag{3.4.12}$$

It is important to further note that the order in which the indices appear matter and a schematic diagram representing the SDEs associated with a NN Ising system in $2D$ is shown in Fig. 3.1. If the index i precedes j, e.g. $\hat{S}_i^z \hat{S}_j^z$, then it will result in z_i variable adopting the noise η_b while its matching pair z_j takes on its complex conjugate multiplied by i, $i\eta^*_{b(i,j)}$. This noise term is unique to bond pair $b(i,j)$. However, it is also possible for the opposite ordering from a different bond, $b(k,i)$ to arise, for example in the term $S_k^z S_i^z$. In this case, z_i will further take on an independent noise term, $\eta_{b(k,i)}$ with the same statistical properties as eq. 3.4.11 but that is complex conjugated (and multiplied by i), i.e. $i\sqrt{J}\eta^*_{b(k,i)}$ instead, while z_k will yield the non-conjugated pair: $\sqrt{J}\eta_{b(k,i)}$.

Putting all this together the pure Ising terms produce the following SDES:

$$\frac{dz_i}{dt} = \frac{iJ}{\hbar} \sum_{j \in n(i)} S_j^z + \sqrt{J}\left[\sum_j \eta_{b(i,j)} + i\sum_k \eta^*_{b(k,i)}\right], \tag{3.4.13}$$

where there exist as many complex noise terms: $\{\eta_b\}$ as there are bonds, b and there are two different noise contributions depending on the position of site i in the Ising interaction. As such, this formula be easily extended to long range interactions beyond NN. The SDEs for the primed variables follow

immediately by applying the operation $c.c'$:

$$\frac{dz'_i}{dt} = -\frac{iJ}{\hbar}\sum_{j\in n(i)} S^z_j + \sqrt{J}\left[\sum_j \eta'_{b(i,j)} - i\sum_k \eta'^*_{b(k,i)}\right], \tag{3.4.14}$$

where η'_b are independent of η_b despite having the same statistical properties. Lastly, we derive the transverse field contributions to the SDEs starting from the master equation:

$$\begin{aligned}
\frac{d\hat{\rho}}{dt} &\sim \frac{ih}{\hbar}\left[\hat{S}^x_i\hat{\Lambda} - \hat{\Lambda}\hat{S}^x_i\right] && (3.4.15)\\
&\sim \frac{ih}{\hbar}\left[-s_i\frac{\partial}{\partial z_i} + S^x_i + s'_i\frac{\partial}{\partial z'_i} - S^{x\prime}_i\right] && (3.4.16)\\
&\sim \frac{ih}{\hbar}\left[-s_i\frac{\partial}{\partial z_i} + s'_i\frac{\partial}{\partial z'_i}\right], && (3.4.17)
\end{aligned}$$

which only contribute to the drift via:

$$\begin{aligned}
dz_i &\sim -ihs_i dt && (3.4.18)\\
dz'_i &\sim ihs'_i dt. && (3.4.19)
\end{aligned}$$

Note that the constant terms $S^x_i - S^{x\prime}_i$ do indeed eliminate each other although some tedious algebra is required to show this. The final equations are summarized as:

$$\begin{aligned}
\frac{dz_i}{dt} &= -\frac{iJ}{\hbar}\sum_{j\in n(i)} S^z_j + \sqrt{J}\left[\sum_j \eta_{b(i,j)} + i\sum_k \eta^*_{b(k,i)}\right] - ih\sum_i \sinh(z_i) && (3.4.20)\\
\frac{dz'_i}{dt} &= \frac{iJ}{\hbar}\sum_{j\in n(i)} S^z_j + \sqrt{J}\left[\sum_j \eta'_{b(i,j)} - i\sum_k \eta'^*_{b(k,i)}\right] + ih\sum_i \sinh(z'_i). && (3.4.21)
\end{aligned}$$

The steps detailed in thus far provide all the necessary ingredients to carry out the derivation of SDEs for a more generalized spin model, such as the spin-1/2 XXZ chain. This is a straightforward exercise and the final SDEs can be found in our work in section 3.8.

3.5 Bloch sphere parametrization

Recall in section 3.2 that the $|\uparrow\rangle$ state of the Bloch sphere corresponds to the infinite regions of complex phase space and as such cannot be properly mapped. To get around this, we will use a toggling procedure. To begin, let us parametrize the SU(2) states by writing $y = e^{z*}$ and so $|y\rangle = \begin{bmatrix} y \\ 1/y \end{bmatrix}$. The mapping onto the Bloch sphere is given by: $y = e^{-i\phi}\tan(\theta/2)$, where $\phi \in [0, 2\pi]$ and $\theta \in [0, \pi]$ are the azimuthal and polar angles respectively and that θ is measured from the south pole. To obtain the equivalent point corresponding to (θ, ϕ) on the complex plane, we extend a line from the sphere's origin to the complex plane, oriented at an angle $\theta/2$ from the south pole. The point of intersection with the complex plane is the mapping of the Bloch sphere point. This is illustrated as the lower left red point in fig. 3.2(a). Both the point on the Bloch sphere and the

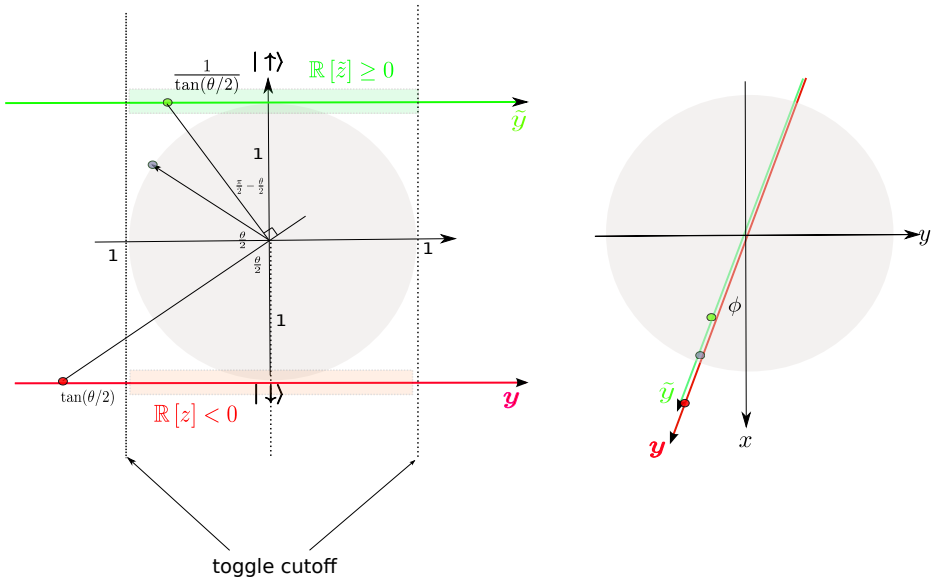

(a) Projection of sphere as viewed down its x-axis. We superimpose the different ϕ-planes where the y and $\tilde{y}$ can belong to. This is similar to the slice $\phi = 0$.

(b) General case when $\phi \neq 0$: Projection of sphere looking down its z-axis / North pole

Figure 3.2: SU(2) sphere

point on the complex plane point share the same azimuthal angle ϕ.

Alternatively, if we use the variable $\tilde{y} = e^{-z}$, so that: $|\tilde{y}\rangle = \begin{bmatrix} 1/\tilde{y} \\ \tilde{y} \end{bmatrix}$, the location of the $\tilde{y}$-complex plane is instead on top the North pole of the Bloch sphere with their origins aligned. The corresponding point on the $\tilde{y}$ complex plane is the line that intersects it, and that originates from the center of the Bloch sphere at an angle $(\pi - \theta)/2$ from the North pole instead. One can visualize this mapping by physically wrapping the complex $\tilde{y}$-plane over the North pole. In the $\tilde{y}$ parametrization it is the South pole that cannot be properly mapped as it corresponds to the edges of phase space. The corresponding point lies in the same azimuthal plane as the Bloch sphere point as well. This physical interpretation agrees with the expected expression: $\tilde{y} = 1/\tan(\theta/2)e^{-i\phi}$

In figure. 3.2(a), if one looks down the z-axis for any $\phi \neq 0$, the blue point on the Bloch sphere is mapped on to the red and green points on the y and $\tilde{y}$ planes respectively, depending on our parametrization choice. Note that because we defined y through the complex conjugate, $y = e^{z*}$ we see that the same y and $\tilde{y}$ points lie on the same azimuthal planes.

3.6 Toggling procedure

The SU(2)-SDEs even for the TIM case, are highly non-linear and can be unstable to numeric integration as they approach the boundaries of phase space($\pm\infty$). In this region, the SDEs become stiff and numerical overflow typically arises. This is attributed to an improper mapping of a proper

point on the Bloch sphere as mentioned above. To circumvent this, we devise a toggling procedure that alternates between y and $\tilde{y}$ variables wherever it suits our cause so as to avoid such onerous regions. We set a cut off radius $|y_{cutoff}| = |\tilde{y}_{cutoff}| = 1$, which corresponds to the exact location of the hemispheres on the Bloch, i.e. when $\theta/2 = \pi/2$ as an indication for when we are too close to the pole. This is equivalently represented by the unit circle about the origin in the complex plane. The cutoff procedure therefore prevents the stochastic variables from getting too close to the poles i.e. values $|y| > y_{cutoff}$, by controlling its magnitude. Although the cutoff criteria in the y or $\tilde{y}$ variables are the same, they represent different conditions in terms of the original z variables, i.e.

$$|\tilde{y}| \leq 1 \Rightarrow \tilde{z}_r \geq 0, \tag{3.6.1}$$

whereas

$$|y| < 1 \Rightarrow z_r < 0. \tag{3.6.2}$$

In fig. 3.2(a), the accepted regions are denoted by shaded green and red regions for $\tilde{y}$ and y respectively. The outline of the toggling procedure is as follows. Consider the dynamics of a single spin, which would entail keeping track of the two points corresponding to z and z' on independent Bloch spheres. Let us initialize it in the spin down state so that they are relatively close to the south pole. We shall concentrate on the z variable since the same argument applies z' as well. For this initial condition, we assign it a sign: $S = -1$ and use the parametrization $y = e^{z*}$. After some time however, the point on the Bloch sphere may evolve so as to cross the hemisphere towards the North pole, which is onerous. This occurs when $\Re[z] > 0$, in which case, we perform a "toggle" by changing variables to $\tilde{y} = e^{-z}$ instead and updating the sign to $S = 1$. The sign therefore tells us which hemisphere we are in, $+1$ for the northern hemisphere and -1 for the southern hemisphere. This step is repeated when necessary to ensure that the point on the Bloch sphere never approaches the onerous pole that is characteristic of the mapping chosen.

3.6.1 New expressions for hyperbolic functions

Note that the toggling procedure has to be carried out for all $2N$ variables and as a result new expressions for the stochastic functions that appear in the SDES (see eq. 3.4.13 and eq. 3.4.14) have to be calculated. First let us consider local hyperbolic functions. If $S = +1$, then we choose the parametrization $y = e^{-z}$

$$\sinh(z) = \frac{e^z - e^{-z}}{2} \tag{3.6.3}$$

$$= \frac{1 - e^{-2z}}{2e^{-z}} \tag{3.6.4}$$

$$= \frac{1 - y^2}{2y} \tag{3.6.5}$$

and

$$\cosh(z) = \frac{1 + y^2}{2y} \tag{3.6.6}$$

On the other hand, if $S=-1$, we instead choose $y=e^{z*}$ so that

$$\begin{aligned}\sinh(z) &= \frac{e^{z}-e^{-z}}{2} && (3.6.7)\\ &= \frac{e^{2z}-1}{2e^{z}} && (3.6.8)\\ &= \frac{y^{*2}-1}{2y^{*}} && (3.6.9)\end{aligned}$$

and

$$\cosh(z)=\frac{1+y^{*2}}{2y^{*}}. \quad (3.6.10)$$

For multivariable functions such as $\tanh(R_i)$, slightly more algebra is required since it depends on both z and z' which can switch sign independently. This therefore gives us four possible forms for this term. Note as well the useful identity: $\tanh(\ln(x^c))=\frac{x^{2c}-1}{x^{2c}+1}$ and that: $S=+1 \implies [z=-\ln y]$ and $S=-1 \implies [z=\ln y^{*}]$ The four cases are defined by the signs (S,S') so that when $S=+1,S'=+1$, then

$$\begin{aligned}\tanh\frac{z+z'}{2} &= \tanh(\frac{-\ln y-\ln y'^{*}}{2}) && (3.6.11)\\ &= \tanh(\ln[yy']^{-\frac{1}{2}}) && (3.6.12)\\ &= \frac{(yy')^{-1}-1}{(yy')^{-1}+1} && (3.6.13)\\ &= \frac{1-yy'}{1+yy'}, && (3.6.14)\end{aligned}$$

and when $S=+1,S'=-1$ then,

$$\begin{aligned}\tanh\frac{z+z'}{2} &= \tanh(\frac{-\ln y+\ln y'^{*}}{2}) && (3.6.15)\\ &= \tanh(\ln[\frac{y'^{*}}{y}]^{\frac{1}{2}}) && (3.6.16)\\ &= \frac{(y'^{*}/y)-1}{(y'^{*}/y)+1} && (3.6.17)\\ &= \frac{y'^{*}-y}{y'^{*}+y}, && (3.6.18)\end{aligned}$$

and when $S=-1, S'=+1$, then

$$\tanh\frac{z+z'}{2} = \tanh(\frac{\ln y^* - \ln y'}{2}) \tag{3.6.19}$$
$$= \tanh(\ln[\frac{y^*}{y'}]^{\frac{1}{2}}) \tag{3.6.20}$$
$$= \frac{(y^*/y')-1}{(y^*/y')+1} \tag{3.6.21}$$
$$= \frac{y^*-y'}{y^*+y'}, \tag{3.6.22}$$

and lastly if $S=-1, S'=-1$, then

$$\tanh\frac{z+z'}{2} = \tanh(\frac{\ln y^* + \ln y'^*}{2}) \tag{3.6.23}$$
$$= \tanh(\ln[y^* y'^*]^{\frac{1}{2}}) \tag{3.6.24}$$
$$= \frac{(y^* y'^*)-1}{(y^* y'^*)+1}. \tag{3.6.25}$$

It is then more convenient to define the function: $\zeta_i(S_i, S_i')$, which combines these four cases depending on the sign of (S, S') and that is now equivalent to the stochastic estimator S_i^z:

$$\zeta_i(S_i,S_i') = \begin{cases} \text{if } [+,+]: & \frac{1}{2}\frac{1-y_i y_i'}{1+y_i y_i'} \\ \text{if } [+,-]: & \frac{1}{2}\frac{y_i'^*-y_i}{y_i'^*+y_i} \\ \text{if } [-,+]: & \frac{1}{2}\frac{y_i^*-y'}{y_i^*+y_i'} \\ \text{if } [-,-]: & \frac{1}{2}\frac{y_i^* y_i'^*-1}{y_i^* y_i'^*+1} \end{cases} \tag{3.6.26}$$

The Stratanovich SDEs transforms as: $\dot{z}_i = -\dot{y}_i/y_i$ if $S=+1$ and $\dot{z}_i = \dot{y_i^*}/y_i^*$ if $S_i=-1$ and a simple change of variables gives us the new expressions:

$$\frac{dy_i}{dt} = \begin{cases} -iy_i\sum_{j\in n(i)}\zeta_j(S_i,S_i') + \frac{i\hbar}{2}\left(1-y_i^2\right) - y_i\left(\sum_j \eta_{b(i,j)} + i\sum_k \eta^*_{b(k,i)}\right) & \text{if } S_i=1 \\ -iy_i\sum_{j\in n(i)}\zeta_j(S_i,S_i')^* - \frac{i\hbar}{2}\left(1-y_i^2\right) + y_i\left(\sum_j \eta^*_{b(i,j)} - i\sum_k \eta_{b(k,i)}\right) & \text{if } S_i=1 \end{cases} \tag{3.6.27}$$

and

$$\frac{dy_i'}{dt} = \begin{cases} iy_i'\sum_{j\in n(i)}\zeta_j^*(S_i,S_i') - \frac{i\hbar}{2}\left(1-y_i'^2\right) - y_i'\left(\sum_j \eta'_{b(i,j)} + i\sum_k \eta'^*_{b(k,i)}\right) & \text{if } S_i'=1 \\ iy_i'\sum_{j\in n(i)}\zeta_j^*(S_i,S_i') + \frac{i\hbar}{2}\left(1-y_i'^2\right) + y_i'\left(\sum_j \eta'^*_{b(i,j)} - i\sum_k \eta'_{b(k,i)}\right) & \text{if } S_i'=1 \end{cases} \tag{3.6.28}$$

Thus in this way, we are able to prevent numerical overflow. It does not however remove systematic bias and spiking. To deal with these issues, we used a noise extrapolation scheme which will be explained in section 3.7 and detailed in section 3.8.

3.6.2 Numerical integration with toggling

Some care has to be exercised when numerically integrating the SDEs in eq. 3.6.27 and eq. 3.6.28. The numerical integration of the SDEs can be broken down into a few steps:

1. First, we need to check the sign: S_i and S_i' which is determined from z_i^r and $z_i^{r\prime}$.
2. Evolve $\{y_i\}$ and $\{y_i'\}$ using the SDEs depending on the sign S_i', S_i
3. Since we are using Stratonovich calculus, we self-consistently determine a midpoint solution, $\{y_{i+1/2}\}$ and $\left\{y'_{i+1/2}\right\}$.
4. Iterate for $\{y_{i+1}\}$ and $\{y'_{i+1}\}$ using $\{y_{i+1/2}\}$ and $\left\{y'_{i+1/2}\right\}$.
5. At the end of each time step, check for the values of S_i and S_i'. If $|y_i| > 1.$ then we update the sign: $S_i = -S_i$ make the transformation: $y_i = 1/y_i^*$. The same update scheme applies to the primed variables as well.
6. Observables are calculated by transforming back to $\left\{z_i, z_i'\right\}$ variables for convenience.

3.6.3 Initial conditions

An interesting point to note that is that with the y, y' variables, we are now able to access the full spin up or spin down state. This is simply given by setting $y = y' = 0.$ and choosing either a $S = 1$ or $S' = -1$ parametrization. Previously, we could only approximate the fully polarized state by setting z, z' to be a large number. The range $z, z' \in [5, 10]$ proved to be adequate for spin up or the range $[-10, -5]$ for the spin down state.

3.7 Extrapolation scheme

The extrapolation scheme (Deuar et al., 2009) is a clever technique that can be used to obtain longer simulation lifetimes. It is carried out in two key steps, which we will now qualitatively describe. The first step necessitates the construction of a blended formalism, which is the hybridization of an exact formalism labelled H_Q and an approximate formalism labelled: H_A. The PPR was used as the exact formalism and therefore limited by short simulation lifetimes, whereas the approximate formalism despite having no limitations on its simulation times, has the characteristic of producing only qualitatively correct results. A blended formalism is then formally constructed by writing:

$$H_{\text{blend}} = \lambda H_Q + (1 - \lambda) H_A, \tag{3.7.1}$$

where a single parameter: $\lambda \in [0,1]$ measures the contribution from each formalism. Setting $\lambda = 1$ corresponds to the exact quantum dynamics while setting $\lambda = 0$ corresponds to the approximate scheme. One would therefore expect the simulation lifetime to be a monotonically decreasing function of λ as H_Q is approached. An illustration of this can be found in fig. 3.3 which are results taken from (Deuar et al., 2009). The evolution of the number of scattered atoms as well as the halo density, after the BEC collision were calculated. Two different blends were constructed using a (i) mean-field Gross-Pitaevskii (GP) description and a (ii) semi-classical Truncated Wigner Approximation (TWA) as the approximate formalism.

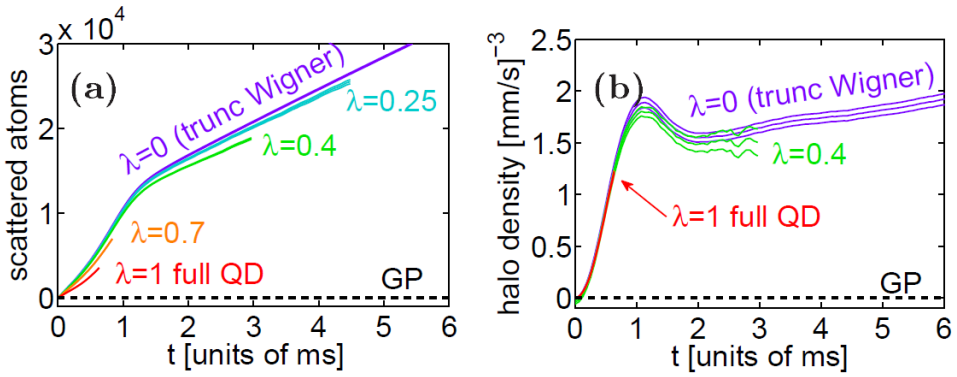

Figure 3.3: *(Figure taken from (Deuar et al., 2009)).* Demonstration of extrapolation scheme from $\lambda = 0$ to $\lambda = 1$. The two approximate schemes for the BEC collision are the mean-field Gross-Pitaevskii equation and the semi-classical Truncated Wigner Approximation (TWA). The full quantum dynamics (QD) is carried out using the PPR and has an expected short simulation lifetime compared to the approximate methods.

Since the dynamics generated from the series: $\{\lambda\} \neq 1$ do not produce exact results, we instead use the λ-series to extrapolate towards $\lambda = 1$ at a fixed time: t'. This entails the second step of the extrapolation scheme. Considering a generic observable: $O(\lambda, t')$, one assumes a series expansion in λ of arbitrary power n, i.e.

$$O(\lambda, t) = \sum_{i=0}^{n} a_i(t)\lambda^i(t). \tag{3.7.2}$$

It is worth mentioning that the order of the expansion is *not* universal and systematically chosen so as to minimize the root mean square (rms) deviations, although typically, a quadratic or cubic fit is sufficient. Using an adequate number of λ values then, the coefficients $\{a_i(t)\}$ can be reliably determined and the desired exact result at $\lambda = 1$ obtained. This procedure can be carried out for a range of times: $t > t^{PP}_{\text{sim}}$ depending on the number of λ-values available at a given time. The results of the full implementation of the toggling procedure and the specifics of the extrapolation scheme can be found in our publication (Ng et al., 2013) included in the next section.

3.8 Paper 2: Simulation of the dynamics of many-body quantum spin systems using phase-space techniques

Simulation of the dynamics of many-body quantum spin systems using phase-space techniques
– *Ray Ng, Erik S. Sørensen, and Piotr Deuar*

Phys. Rev. B 88, 14430 (Editor's suggestion)

DOI: 10.1103/PhysRevB.88.144304

Calculations: I performed all stochastic simulations and produced half of the figures. Piotr Deuar carried out the extrapolation calculations and produced the figures that resulted from that numerical effort.

Manuscript: I wrote approximately 50% the manuscript and 50% of the figures. Erik S. Sørensen helped to refine and edit the paper.

In this publication, we set out to answer the following questions:

- Can the PP be reformulated using a spin coherent state basis?

Using the spin-1/2 transverse Ising model as a test system:

- What are the longest time scales, t_{life} that can be achieved (without gauges)?
- How does t_{life} depend on the parameters of the system?
- Can the extrapolation scheme further increase simulation lifetimes? And if so:
  - How much of an improvement can we achieve?

PHYSICAL REVIEW B **88**, 144304 (2013)

Simulation of the dynamics of many-body quantum spin systems using phase-space techniques

Ray Ng* and Erik S. Sørensen
Department of Physics and Astronomy, McMaster University 1280 Main Street West, Hamilton, Ontario, Canada L8S 4M1

Piotr Deuar
Institute of Physics, Polish Academy of Sciences (PAN), Al. Lotnikw 32/46 02-668 Warszawa, Poland
(Received 17 July 2013; published 4 October 2013)

We reformulate the full quantum dynamics of spin systems using a phase-space representation based on SU(2) coherent states which generates an exact mapping of the dynamics of any spin system onto a set of stochastic differential equations. This representation is superior in practice to an earlier phase-space approach based on Schwinger bosons, with the numerical effort scaling only linearly with system size. By also implementing extrapolation techniques from quasiclassical equations to the full quantum limit, we are able to extend useful simulation times severalfold. This approach is applicable in any dimension including cases where frustration is present in the spin system. The method is demonstrated by simulating quenches in the transverse-field Ising model in one and two dimensions.

DOI: 10.1103/PhysRevB.88.144304 PACS number(s): 75.10.Dg, 78.55.−m, 75.40.Gb

I. INTRODUCTION

With the development of cold-atom experiments, the nonequilibrium dynamics of closed quantum systems has become a focus of attention.[1] In these experiments, it has become feasible to prepare a model system in a specific eigenstate of H_i and study the ensuing real-time dynamics when the system evolves under a controllable Hamiltonian H_f. This can be viewed as a realization of a quantum quench.[2–9]

Here, we focus on how these effects occur in closed quantum spin systems[10–22] neglecting couplings to the environment. The dynamics of quantum spin systems is of particular interest for two reasons. First, it forms a cornerstone of condensed matter physics with many open problems, in particular for models with frustration, where even the equilibrium state is a matter of debate and little is known about the dynamics. Second, using cold-atom systems it has become conceivable to implement quantum simulators[23–29] using atomic degrees of freedom to mimic the quantum spin and their interactions. Recent experiments[30–39] have shown significant progress towards realizing such a quantum simulator capable of simulating quantum spin systems. Following the initial proposal[24] to implement such a simulator using trapped ions, it was experimentally realized with two spins,[30] three spins,[31] and up to nine spins.[34,36] Recently, a system of ∼300 spins with Ising interactions was realized with trapped ions[38] and similar system sizes have been reached using neutral atoms in optical lattices.[35,40] As a model system, several of these experiments[30,32,34,38] model the transverse-field Ising model (TFIM) (Ref. 41):

$$\hat{H} = -J \sum_{\langle i,j \rangle} \hat{S}_i^z \hat{S}_j^z - h(t) \sum_i \hat{S}_i^x, \tag{1}$$

which is the model that we focus on here.

Calculating the quantum dynamics of condensed matter spin systems is a notoriously difficult problem due to the macroscopic number of degrees of freedom. In this limit, the size of the Hilbert space scales exponentially, deeming it intractable in most cases. While some models can be solved analytically, they are often not generalizable to higher dimension and the solution is often model specific. For instance, the TFIM (Ref. 41) can be solved exactly in one dimension using the Jordan-Wigner transformation, but this is not possible in higher dimensions.

From a numerical perspective, the standard condensed matter computational toolbox is remarkably successful but not completely general. For instance, the direct "brute force" approach by way of exact diagonalization (ED), while always applicable, can only accommodate relatively small system sizes of $N \sim 48$ (for a spin-$\frac{1}{2}$ system). Quantum Monte Carlo (QMC) methods[42] are extremely useful for calculating ground-state properties, but only in the absence of any frustration. However, for the study of dynamics, QMC techniques are usually limited to imaginary times or, equivalently, imaginary frequencies. Other methods, such as those rooted in the density matrix renormalization group (DMRG),[43–45] are the dominant techniques for one-dimensional systems[43] but are much harder to apply in two dimensions due to scaling issues associated with the area law.[46] Currently, DMRG techniques are restricted to one-dimensional systems and quasi-two-dimensional strips. Nonetheless, time-dependent DMRG (tDMRG) (Refs. 47 and 48) has been very successful for one-dimensional systems where the real-time dynamics of quantum spin systems can be treated out to $tJ/\hbar \sim 100$.[10] Using time-evolving block decimation (TEBD),[49] the infinite-size TEBD (iTEBD) (Ref. 50) has yielded results out to $tJ/\hbar \sim 6$–10 (Ref. 51) for the TFIM and $tJ/\hbar \sim 20$ (Refs. 11 and 12) for the XXZ spin chain and related models. It would therefore be quite worthwhile to explore techniques for calculating real-time dynamics that are generally applicable to quantum spin systems in any dimension even in the presence of frustration.

Another branch of numerical techniques falls under the category of quantum phase-space methods.[52–57] They can be summarized by the following expression for the density operator:

$$\hat{\rho} = \int P(\vec{\lambda}) \hat{\Lambda}(\vec{\lambda}) d\vec{\lambda}, \tag{2}$$

where $\vec{\lambda}$ are parameters, $P(\vec{\lambda})$ plays the role of a distribution, and $\hat{\Lambda}(\vec{\lambda})$ is the operator kernel. Quantum phase-space methods

have recently begun to gain exposure in condensed matter systems. For instance, Polkovnikov *et al*.[57] have applied the path-integral formalism of the truncated Wigner representation to simulate quantum quenches. Aimi *et al*.[58] extended the work by Corney *et al*.[53] by successfully calculating the imaginary-time dynamics of the Hubbard Hamiltonian in the high-interaction limit using fermionic Gaussian phase-space methods.[59] This was done by implementing symmetry projection techniques[60] as well as Monte Carlo methods. The high-interaction limit was previously unattainable by QMC techniques.

We focus specifically on the positive-P representation (PPR) which was developed by Drummond and coworkers[61–63] and originally tailored to solve problems in quantum optics, where it has been applied with considerable success, as well as in ultracold bosonic gases. For instance, Deuar *et al*.[64] have successfully implemented the PPR for the purpose of simulating multidimensional Bose gases.[64–66]

The general idea is that the PPR provides an *exact* mapping of the quantum dynamics onto a set of Langevin-type differential equations as long as boundary terms do not arise.[62,67] This mapping is made possible by the existence of correspondence relations, which are characteristic of different phase-space methods. In principle, the PPR can be applied to both real and imaginary times[56] and since the computational effort is proportional to the system size, it is possible to simulate macroscopically large systems. In addition, it is also possible to simulate frustrated systems which makes the PPR particularly appealing. Finally, the PPR can be readily applied in any dimension. The main drawback of the PPR, however, is the possible appearance of short simulation lifetimes signaled by the onset of a divergence in the stochastic averages. Modified formalisms of the PPR based on the gauge-P representation[59,62,68,69] have proven useful in this respect by allowing one to introduce gauge functions that systematically remove unstable terms in the stochastic differential equations (SDEs), and with it the source of divergences. This is typically done at the expense of introducing an extra degree of freedom that plays the role of a complex weight Ω.

We implemented the PPR formalism to the dynamics of many-body spin systems in our earlier work[70] by treating the equivalent Schwinger boson representation of spin chains with the canonical PPR method. It was applied to the real-time dynamics of one-dimensional spin chains under a quantum quench. A conclusion of that work was that the coherent-state basis used in other studies where the PPR has been successful is not very suitable for systems composed of $S = \frac{1}{2}$ quantum spins. It led to both early noise onset, and the need for a broad initial distribution to describe the number state that corresponds to $S = \frac{1}{2}$ spin. The latter issue is particularly onerous as it turns out to preclude efficient sampling of the distribution for large numbers of spins [$\mathcal{O}(100)$], the regime where phase-space methods are particularly advantageous.

In this paper, we choose a different route and describe the system using the SU(2) basis.[71–73] This allows us to develop a PPR-like distribution, which is then used to obtain stochastic differential equations that do not suffer from the broad distribution and sampling issues encountered with PPR in Schwinger bosons. A related approach has been used in the past on an imaginary-time evolution of the Ising model by Barry *et al*.[73] using an unnormalized kernel for the density operator. We will, however, use a normalized kernel, which is more appropriate for simulating dynamics.[54]

The outline of the paper is as follows. The SU(2) coherent state phase-space representation and related formalism is derived in Sec. II. Its basic application to the TFIM is discussed in Sec. III. Even though this approach leads to significantly longer simulation times, limitations are clearly present and we also discuss these later in the section. It is possible to extend the simulation time even further by extrapolating from regimes with reduced quantum fluctuations into the full quantum regime. This *entanglement scaling* technique is described in Sec. IV. This allows us to obtain longer simulation times, similar to typical time scales of the problem. We then conclude in Sec. V and discuss the future direction of this work. Some more technical aspects are relegated to Appendices.

II. FORMALISM

A. SU(2) basis

Traditionally, the PPR formalism is based upon bosonic coherent states,[74] and hence the most natural generalization to spin systems would be the use of SU(2) coherent states.[71,72,75,76] The bosonic coherent states and SU(2) coherent states are analogous and have similar properties such as that of overcompleteness, and in the large-S limit the SU(2) coherent states approach the bosonic coherent states. While the spin versions of other kinds of phase-space representations (the Q representation,[77–79] P representation,[80] and Wigner representation[81]) have been introduced in the past, the advantage of the PPR approach is that the kernel can be made analytic in the phase-space variables, which in turn guarantees that standard stochastic diffusion equations can be obtained for the evolution.[61]

Labeling the spin quantization direction as $\vec{z}$, with operator $\hat{S}^z$, we define the SU(2) coherent states for a spin S as[71,72,75,76]

$$|z\rangle = e^{-zS} e^{e^z \hat{S}^\dagger} |S,-S\rangle, \tag{3}$$

where $S^\dagger$ is the raising operator and $|S,S_z\rangle$ is the state with S_z spin projection onto the quantization direction. The state is parametrized by a single complex variable z (not to be confused with the quantization direction $\vec{z}$). Our interest lies in the spin-$\frac{1}{2}$ case for which (3) reduces to the SU(2) case:

$$|z\rangle = e^{-\frac{z}{2}} e^{e^z \hat{S}^+} |\downarrow\rangle = \begin{bmatrix} e^{z/2} \\ e^{-z/2} \end{bmatrix} \tag{4}$$

with $|\downarrow\rangle = \left[\begin{smallmatrix} 0 \\ 1 \end{smallmatrix}\right]$, and $S^+ = \left[\begin{smallmatrix} 0 & 1 \\ 0 & 0 \end{smallmatrix}\right]$. In this case, $|z\rangle$ has the physical interpretation of being a unit vector pointing to the position (θ,ϕ) on the surface of the Bloch sphere. The transformation that relates the z coordinate to (θ,ϕ) is $e^z = e^{i\phi} \tan(\theta/2)$ where $\theta \in [0,\pi/2]$ is the polar angle and $\phi \in [0,2\pi]$ is the azimuthal one.

B. SU(2) phase-space representation

To obtain stochastic evolution equations with positive diffusion, we follow standard PPR procedure.[52,61,82] For brevity, we will only highlight key aspects of the formalism

and refer interested readers to[70] where a spin system is worked out in detail.

First, we represent the density matrix (2) using an off-diagonal kernel with unit trace constructed from SU(2) coherent states:

$$\hat{\Lambda} = \frac{|z\rangle\langle z'^*|}{\langle z'^*|z\rangle}. \tag{5}$$

For an N-site system, one uses a tensor product of independent kernels for each site i:

$$\hat{\Lambda} = \bigotimes_{i=1}^{N} \hat{\Lambda}_i(z_i, z_i'^*). \tag{6}$$

It is parametrized by the set $\vec{\lambda} = \{z_1, \ldots, z_N, z_1', \ldots, z_N'\}$ of $2N$ independent complex variables.

The dynamics of any system is obtained by evolving the equation of motion for the density operator

$$\frac{d\hat{\rho}}{dt} = -\frac{i}{\hbar}[\hat{H}, \hat{\rho}]. \tag{7}$$

To counteract the exponential complexity of the Hilbert space with large system sizes, there exists an equivalent description of (7) in terms of a Fokker-Planck equation (FPE) for the distribution function $P(\vec{\lambda})$ [cf. Eq. (2)] in the continuous space of the phase-space variables $\vec{\lambda}$. This in turn can be mapped onto stochastic equations for the variables, which is the final result of the formalism. These can be sampled with a chosen ensemble whose size $\mathcal{N}$ controls the numerical effort, trading it off for statistical precision.

The FPE is obtained by using correspondence relations that establish a duality between the action of spin operators and differential operators on the kernel $\hat{\Lambda}$. It is possible to show that spin operators acting from the left of the kernel satisfy the following identities (site index i implied):

$$\hat{S}^x\hat{\Lambda} = \left[-\sinh z\frac{\partial}{\partial z} + S^x\right]\hat{\Lambda}, \tag{8}$$

$$\hat{S}^y\hat{\Lambda} = \left[-i\cosh z\frac{\partial}{\partial z} + S^y\right]\hat{\Lambda}, \tag{9}$$

$$\hat{S}^z\hat{\Lambda} = \left[\frac{\partial}{\partial z} + S^z\right]\hat{\Lambda}, \tag{10}$$

while spin operators acting from the right satisfy

$$\hat{\Lambda}\hat{S}^x = \left[-\sinh z'\frac{\partial}{\partial z'} + S^{x\prime}\right]\hat{\Lambda}, \tag{11}$$

$$\hat{\Lambda}\hat{S}^y = \left[i\cosh z'\frac{\partial}{\partial z'} + S^{y\prime}\right]\hat{\Lambda}, \tag{12}$$

$$\hat{\Lambda}\hat{S}^z = \left[\frac{\partial}{\partial z'} + S^z\right]\hat{\Lambda}, \tag{13}$$

where

$$S^x = \frac{1}{2}(\cosh z - \sinh z\tanh R), \tag{14}$$

$$S^y = \frac{i}{2}(\sinh z - \cosh z\tanh R), \tag{15}$$

$$S^z = \frac{1}{2}\tanh(R), \tag{16}$$

and

$$R = (z + z')/2. \tag{17}$$

The primed counterparts of (14) and (15) are easily obtained by making the substitutions $z \to z', i \to -i$, so that $(S^y)^* = S^{y\prime}$ when $z = z'^*$.

To derive estimators for expectation values $\langle\hat{O}\rangle$ of general observables $\hat{O}$, we start from the usual expression

$$\langle\hat{O}\rangle = \frac{\mathrm{Tr}[\hat{O}\hat{\rho}]}{\mathrm{Tr}[\hat{\rho}]} = \frac{\langle\!\langle \mathrm{Tr}[\hat{O}\hat{\Lambda}]\rangle\!\rangle}{\langle\!\langle \mathrm{Tr}[\hat{\Lambda}]\rangle\!\rangle}, \tag{18}$$

where the right term follows from (2), with $\langle\!\langle\cdots\rangle\!\rangle$ denoting an average over the ensemble that samples $P(\vec{\lambda})$, i.e., $\langle\!\langle\cdots\rangle\!\rangle = \int P(\vec{\lambda})(\cdots)d\vec{\lambda}$. Noting that $\mathrm{Tr}[\hat{\Lambda}] = 1$ and using (8)–(10), one obtains, e.g.,

$$\langle\hat{S}^\alpha\rangle = \langle\!\langle S^\alpha\rangle\!\rangle \tag{19}$$

for $\alpha = x, y, z$. This explains the choice of notation $S^{x,y,z}$ in (8)–(16). Using the cyclic property of the trace in (18) and (11)–(13), one could have just as well have derived the equivalent estimators for the spin components using primed coordinates instead: $\langle\hat{S}^\alpha\rangle = \langle\!\langle S^{\alpha\prime}\rangle\!\rangle$. Either estimator is valid, but in our calculations we chose to use (19) simply as a matter of preference. Notably, since the kernel is normalized the expectation value of its derivative is zero and one can obtain estimators for more complex observables by taking the expectation value of appropriate correspondence relations. Once the FPE is obtained, its mapping onto Ito SDEs is well known,[52] and in doing so, we effectively map the dynamics of N spins onto $\sim N$ complex variables: $\{\vec{\lambda}\}$.

An ensemble of $\mathcal{N}$ realizations $\{\vec{\lambda}^{(i)}\}$, with $i = 1, \ldots, \mathcal{N}$, becomes equivalent to the full quantum mechanical description of the system as the ensemble size becomes large ($\mathcal{N} \to \infty$). In practice, 10^3–10^6 trajectories are typically sufficient for good convergence, depending on the desired precision.

C. Stochastic equations for quantum dynamics

Even though the numerical results that we present later are only for the transverse-field Ising model (1), it is instructive to consider the stochastic equations for slightly more general models. For generality, we therefore consider the Heisenberg Hamiltonian in a transverse field $h(t)$ along the $\vec{x}$ direction:

$$\hat{H} = -J\sum_{\langle i,j\rangle}\left[\hat{S}_i^z\hat{S}_j^z + \Delta\left(\hat{S}_i^y\hat{S}_j^y + \hat{S}_i^x\hat{S}_j^x\right)\right] - h(t)\sum_i \hat{S}_i^x, \tag{20}$$

with each connected-neighbor pair $\langle i, j\rangle$ counted once. Here, J is the hopping strength ($J > 0$ for the ferromagnetic system), Δ governs in-plane anisotropy, $h(t)$ is the transverse-field strength, and we choose units such that $\hbar = 1$. Following Sec. II B, we derive Ito stochastic equations to describe the

dynamics of the system:

$$\frac{dz_i}{dt} = \frac{iJ}{2}\sum_{j\in \mathrm{n}(i)} \tanh R_j - ih(t)\sinh z_i + \sqrt{J}\left[\sum_{j\in \mathrm{n_L}(i)} \eta_{\langle i,j\rangle} + i\sum_{j\in \mathrm{n_R}(i)} \eta^*_{\langle i,j\rangle}\right]$$
$$-i\frac{\Delta J}{2}\sum_{j\in \mathrm{n}(i)} (\mathcal{S}_{ij} + \mathcal{C}_{ij}\tanh R_j) + \sqrt{J\Delta}\left[\sum_{j\in \mathrm{n_L}(i)} \sqrt{\mathcal{C}_{ij}}\,\xi_{\langle i,j\rangle} - i\sum_{j\in \mathrm{n_R}(i)} \sqrt{\mathcal{C}_{ij}}\,\xi^*_{\langle i,j\rangle}\right], \quad (21)$$

$$\frac{dz'_i}{dt} = -\frac{iJ}{2}\sum_{j\in \mathrm{n}(i)} \tanh R_j + ih(t)\sinh z'_i + \sqrt{J}\left[\sum_{j\in \mathrm{n_L}(i)} \eta'_{\langle i,j\rangle} - i\sum_{j\in \mathrm{n_R}(i)} \eta'^*_{\langle i,j\rangle}\right]$$
$$+i\frac{\Delta J}{2}\sum_{j\in \mathrm{n}(i)} (\mathcal{S}'_{ij} + \mathcal{C}'_{ij}\tanh R_j) + \sqrt{J\Delta}\left[\sum_{j\in \mathrm{n_L}(i)} \sqrt{\mathcal{C}'_{ij}}\,\xi'_{\langle i,j\rangle} + i\sum_{j\in \mathrm{n_R}(i)} \sqrt{\mathcal{C}'_{ij}}\,\xi'^*_{\langle i,j\rangle}\right]. \quad (22)$$

The R, $\mathcal{C}$, and $\mathcal{S}$ functions are

$$R_i = \frac{z_i + z'_i}{2}, \quad (23)$$

$$\mathcal{C}_{ij} = \cosh(z_i - z_j), \quad \mathcal{S}_{ij} = \sinh(z_i - z_j), \quad (24)$$

$$\mathcal{C}'_{ij} = \cosh(z'_i - z'_j), \quad \mathcal{S}'_{ij} = \sinh(z'_i - z'_j). \quad (25)$$

The noise η, ξ, η', ξ' takes the form of complex Wiener increments of zero mean, one of each per connected pair $\langle i,j\rangle$. They are all independent of each other, and delta time correlated. That is, the only nonzero second-order moments are

$$\langle\langle x_{\langle i,j\rangle}(t)x^*_{\langle i,j\rangle}(t')\rangle\rangle = \delta(t-t'), \quad (26)$$

where x can stand for any symbol in $\{\eta,\xi,\eta',\xi'\}$. Individual complex noises are easily constructed in practice from two real Gaussian random variables of variance $\frac{1}{2\Delta t}$ at each time step of length Δt (one for the real, one for the imaginary part).

Some notation is also required to keep track of the connectivity: $\mathrm{n}(i)$ indicates the set of connected neighbors for site i. For example, a one-dimensional (1D) chain with nearest-neighbor coupling has $\mathrm{n}(i) = \{i-1, i+1\}$. The noises couple connected sites in such a way that when one member of the pair gets the complex noise η, the other gets $i\eta^*$ or $-i\eta^*$ depending on the details. Hence, if we assign to each such bond $\langle i,j\rangle$ an arbitrary labeling directionality $i \to j$, then the "left" site i gets $\eta_{\langle i,j\rangle}$ noise while the "right" site j gets the conjugate one. The neighbors that are labeled as "left" sites for the $\langle i,j\rangle$ bond are in the set $\mathrm{n_L}(i)$, while those that are labeled as "right" sites are in the set $\mathrm{n_R}(i)$. For the 1D example, one can have $\mathrm{n_L}(i) = \{i-1\}$ and $\mathrm{n_R}(i) = \{i+1\}$. With this notation, the expressions (21) and (22) allow for arbitrary connectivity between the sites, including frustrated systems.

Equations (21) and (22) are equivalent to the Schwinger boson phase-space stochastic equations developed in Ref. 70, but their statistical properties at finite but large ensemble size $\mathcal{N}$ are very different. Importantly, in the present representation, any product state $\otimes_i |z_i^0\rangle$ can be described as a delta-function distribution

$$P(\vec{\lambda}) = \prod_i \delta^{(2)}(z_i - z_i^0)\delta^{(2)}(z_i - z_i'^*). \quad (27)$$

This can be used to initialize the $t = 0$ ensemble in a simple fashion. More importantly, since this is a zero-width distribution, the initial state remains well sampled and compact even for very large systems.

A technical hurdle is encountered for the exact $|\uparrow\rangle$ and $|\downarrow\rangle$ states, which correspond to the limit $z \to \pm\infty$, respectively. Some cut is always required when mapping the surface of a sphere (such as the Bloch sphere for the spin-$\frac{1}{2}$ case) onto a plane, and the in-plane evolution at a cut is singular. In our z mapping, there are two cuts like in a cylindrical map projection. We deal with this issue by reprojection onto a polar coordinate plus a Boolean variable that keeps track of which pole is being used to define the coordinates. This is explained in Appendix A.

D. Thermal calculations

An imaginary-time evolution in the temperature variable $\beta = 1/k_B T$ can also be formulated in principle using the anticommutator[56] $d\hat{\rho}/d\beta = -\frac{1}{2}[\hat{H}\hat{\rho} + \hat{\rho}\hat{H}]$. For the simple ferromagnetic 1D Ising model ($J = 1, h = 0$) considered previously in this context,[73] we obtain, for comparison,

$$\frac{dz_i}{d(\beta/2)} = \frac{1}{2}[\tanh R_{i-1} + \tanh R_{i+1}] + \eta_i + \eta^*_{i-1}, \quad (28)$$

$$\frac{dz'_i}{d(\beta/2)} = \frac{1}{2}[\tanh R_{i-1} + \tanh R_{i+1}] + \eta'_i + \eta'^*_{i-1}, \quad (29)$$

$$\frac{dW}{d(\beta/2)} = \frac{1}{2}W\sum_i \{\tanh R_i \tanh R_{i+1}\} \quad (30)$$

with noise variances $\langle\langle \eta_i(\beta)\eta^*_j(\beta')\rangle\rangle = \delta(\beta-\beta')\delta_{ij}$. The variable W is a trajectory-dependent weight and has to be taken into consideration in Eq. (18). For a general observable $\hat{O}$, $\langle\hat{O}\rangle$ is now given by

$$\langle\hat{O}\rangle = \frac{\langle\langle W\,O(\vec{\lambda})\rangle\rangle}{\langle\langle W\rangle\rangle}, \quad (31)$$

where $O(\vec{\lambda})$ represents the stochastic estimator that is a function of phase-space variables $\vec{\lambda}$. Note that the energy units we choose here are a factor of 2 smaller than in Ref. 73, so that $\beta/2$ is the imaginary time used there. In comparison, the noise terms are the same, but the normalized kernel we use introduces the tanh R drift terms and evolving weights.

A $T = \infty$ initial condition $\hat{\rho} = I/N$ can be obtained in a number of ways. One can have, e.g., a uniform distribution of z_i on the imaginary axis on $[-\pi,\pi]$ as in Ref. 73, or an even random mix of $z = \pm z_0$ with $z_0 \to \infty$. In both cases, $z_i' = z_i^*$. Such freedom is typical for overcomplete representations, and may lead to different statistical properties depending on the initial distribution chosen.

III. DEMONSTRATION OF THE BASIC METHOD

A. Transverse-field quench

We now apply our formalism to the dynamics of a transverse-field quench of the ferromagnetic Ising model ($J = 1$, $\Delta = 0$) [Eq. (1)]. This model is a realistic description of many physical phenomena,[41] and with recent advances in ultracold atoms and the high degree of parameter control, it is now possible to reproduce quenches in isolated quantum systems and to study the ensuing unitary dynamics. In this context, the TFIM is of considerable interest as a model system. There has been much recent work done on this system both theoretically[13,17,18] and experimentally.[30,32,34,38,83]

The quench occurs at $t = 0$ with a time-dependent field given by

$$h(t) = \begin{cases} 0, & t \leqslant 0 \\ h, & t > 0. \end{cases} \tag{32}$$

We choose to start from the $h = 0$ spin-up ground state $|\uparrow\uparrow\cdots\uparrow\rangle$ and quench a 1D spin chain to a value of

$$h = h_c = 0.5. \tag{33}$$

This is the well-known critical point of the spin model, where the correlation length in equilibrium diverges,[84] separating the ferromagnetic and paramagnetic phases.

Rewriting Eqs. (21) and (22), we find that for the 1D TFIM the equations to simulate are

$$\frac{dz_i}{dt} = i\left[S_{i-1}^z + S_{i+1}^z\right] - ih\sinh z_i + \eta_i + i\eta_{i-1}^*, \tag{34}$$

$$\frac{dz_i'}{dt} = -i\left[S_{i-1}^z + S_{i+1}^z\right] + ih\sinh z_i' + \eta_i' - i\eta_{i-1}'^* \tag{35}$$

with estimators (16). We calculate the dynamics of the expectation values of spins $\langle\hat{S}^\alpha\rangle$ and nearest-neighbor spin correlations $\langle\hat{S}_i^\alpha\hat{S}_{i+1}^\alpha\rangle$ in the three orthogonal axis directions: $\alpha = \{x,y,z\}$. Our initial results are shown in Figs. 1 and 2 for an $N = 10$ site chain that is small enough that exact results by way of diagonalization are available for comparison. The stochastic averages are in excellent agreement with the exact results. We use $\mathcal{N} = 10^4$ trajectories distributed among $\mathcal{B} = 100$ equal-sized bins. The statistical uncertainty in the estimators for observables can then be determined with the help of the central limit theorem, i.e., the error bars in the final estimates are obtained by averaging over all bins is $1/\sqrt{B}$ times the standard deviation of the $\mathcal{B}$ single-bin-averaged estimators.

We observe the onset of spiking after a certain time $t_{\rm sim}$, which is a known feature of some PPR-like calculations when the equations are nonlinear. This is also often a sign of the onset of sampling difficulties.[67] Simulations are stopped at $t_{\rm sim}$ which we determine by the criterion (A6) (see Appendix A 2 for details). This time compares favorably to the simulation time of $t_{\rm sim} \approx 0.6$ seen in our earlier Schwinger boson calculations.[70]

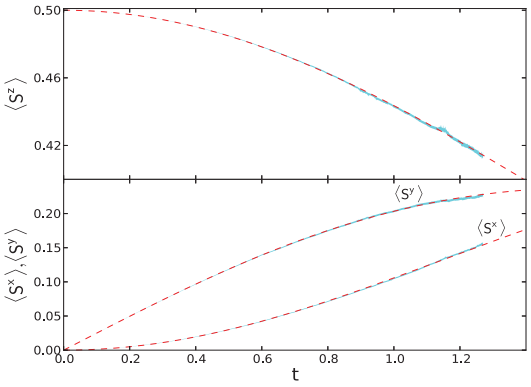

FIG. 1. (Color online) Spin components: $\langle\hat{S}^x\rangle, \langle\hat{S}^y\rangle, \langle\hat{S}^z\rangle$ vs time for the 10-site 1D Ising spin chain with transverse quench from $h = 0$ to $h_c = 0.5$. Red dashed lines show exact diagonalization results. Our calculations including error bars are indicated by the cyan region.

Figure 3 shows a calculation for a two-dimensional (2D) system on a 3×3 square lattice. Again, we use a small system size of 3×3 to allow comparison with exact diagonalization. Much larger systems can be treated, as will be demonstrated in Fig. 8 in Sec. IV.

B. Limitations on simulation time

While real-time simulations now last longer than in Ref. 70 and scale well with system size even in higher dimensions (see Fig. 8), it would be very desirable to obtain much longer simulation times.

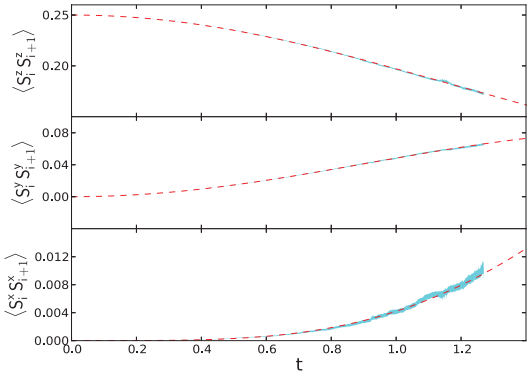

FIG. 2. (Color online) Nearest-neighbor correlation functions $\langle\hat{S}_i^x\hat{S}_{i+1}^x\rangle, \langle\hat{S}_i^y\hat{S}_{i+1}^y\rangle, \langle\hat{S}_i^z\hat{S}_{i+1}^z\rangle$ vs time for a 1D 10-site Ising spin chain with transverse quench from $h = 0$ to $h_c = 0.5$. Red dashed lines show exact diagonalization results. Our calculations including error bars are indicated by the cyan region.

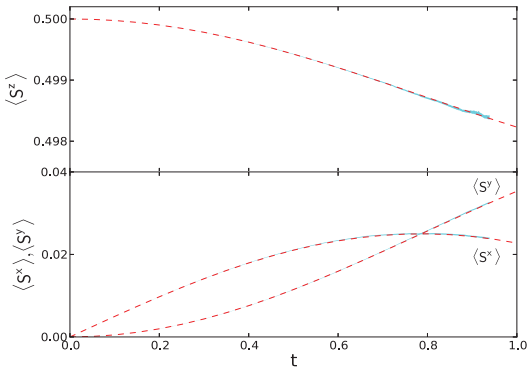

FIG. 3. (Color online) Spin components: $\langle\hat{S}^x\rangle, \langle\hat{S}^y\rangle, \langle\hat{S}^z\rangle$ vs time for the 2D Ising spin model on a 3×3 square lattice with transverse quench from $h = 0$ to 0.1. Red dashed lines show exact diagonalization results.

A major stumbling block is that at the points in phase space where $R_i = \pm i\pi/2$, the factor $\tanh(R_i) = 2S_i^z$ diverges. This is a problem as it appears both in observable calculations (14)–(16) and in the evolution equations (34) and (35). In observables, spiking appears when a trajectory passes close to a pole, which obscures the mean result when it happens often. In the evolution equations, this causes a poorly integrated sudden jump, and in fact can be a symptom of the onset of systematic errors.[67] In the present case, these poles are at the root of the limitations on simulation time.

It is helpful to look at the equations for R and a complementary independent variable

$$Q_i = \frac{z_i - z_i'}{2i}. \tag{36}$$

Consider for now what happens if the transverse field h is turned completely off, the equations are

$$\frac{dR_i}{dt} = \frac{1}{2}[\eta_i + i\eta_{i-1}^* + \eta_i' - i\eta_{i-1}'^*], \tag{37}$$

$$\frac{dQ_i}{dt} = \frac{1}{2}[\tanh R_{i-1} + \tanh R_{i+1}] - \frac{i}{2}[\eta_i + i\eta_{i-1}^* - \eta_i' + i\eta_{i-1}'^*]. \tag{38}$$

The evolution of Q_i becomes singular when either of the R_{i+1} or $R_{i-1} = \pm i\pi/2$. For a small deviation δ_{i+1} or δ_{i-1} from such a pole, as in, e.g., $R_{i+1} = \pm i\pi/2 + \delta_{i+1}$, we have

$$\frac{dQ_i}{dt} \approx \frac{1}{2\delta_{i+1}} + \text{noise}. \tag{39}$$

The evolution of R, on the other hand, is purely complex diffusion, with variances $\text{var}(|R|) = t$. Thus, even if there is no transverse field h, some trajectories will eventually diffuse from z_0 onto the $\pm i\pi/2$ poles in a time $\propto(z_0^2 + \pi^2/4)$. We see that in the ground-state limit of $z_0 \to \infty$, this time becomes ever longer. For finite-h values, there is also a more rapid deterministic drift away from the $h = 0$ ground state due to precession induced by the transverse field. An analysis of t_{sim} that takes into account finite-h values is given in Appendix C.

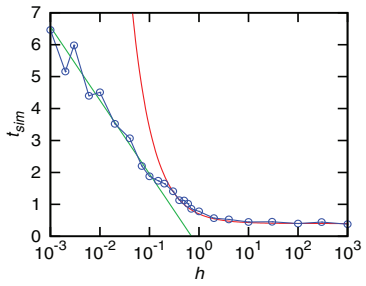

FIG. 4. (Color online) The dependence of simulation time t_{sim} on the quench strength h (blue) for the 1D transverse quench Ising model ($\Delta = 0$). The trends at low h [Eq. (40)] (green line) and at large h [Eq. (41)] (red line) are also shown.

While a fundamental resolution or alleviation of these issues for spin states is beyond our scope here, there is a fairly straightforward procedure that one can use to extract physical information for appreciably longer times than those seen in Figs. 1–4. It is described and demonstrated in the following Sec. IV.

C. Simulation time in the SU(2) basis

Figure 4 shows the dependence of the simulation time t_{sim} on the quench strength h. The trends are logarithmic at small h,

$$t_{\text{sim}} \sim \frac{2}{C} \ln \frac{c_0\sqrt{C}}{h}, \tag{40}$$

and approximately constant

$$t_{\text{sim}} \approx c_1 \frac{1}{C} + \frac{c_2}{h} \tag{41}$$

for large h. C is the number of connections per site ($C = 2$ here), and the constants are $c_0 \approx 0.5$, $c_1 \approx 0.8$, and $c_2 \approx 0.3$. These trends are derived in Appendix C. The simulation time in both regimes is inversely proportional to C, hence also to the dimensionality d.

D. Origin of the poles

For future work in the field, it is instructive to understand why such poles appear in phase space in the first place. Consider the matrix representation of $\hat{\Lambda}$:

$$\hat{\Lambda} = \frac{1}{2\cosh R}\begin{bmatrix} e^R & e^{iQ} \\ e^{-iQ} & e^{-R} \end{bmatrix}. \tag{42}$$

Projectors onto pure states $|z\rangle\langle z|$ correspond to $z' = z^*$, and thus to real values of R and Q. This is the set of all Hermitian kernels, and all such kernels are well behaved. However, non-Hermitian kernels that contain complex R can be singular if the denominator in the normalization approaches zero. The worst case occurs when $\cosh R = \frac{1}{2}\langle z|z'^*\rangle = 0$, i.e., when the kernel causes a transition between orthogonal states. This is the exact location of the unwanted poles in the equations mentioned in the previous section, i.e., when $R_i = \pm in'\frac{\pi}{2}$ and

$n' \in$ odd. Such unwelcome behavior occurs for these states because the present kernel $\hat{\Lambda}$ was explicitly normalized to have unit trace, while such coherences between orthogonal states have zero trace. They are unnormalizable, and pathological behavior ensues.

We have also attempted the obvious idea to use an unnormalized kernel $|z\rangle\langle z'^*|$ which never divides by a zero trace. However, despite having equations of motion with no divergent terms ($\tanh R$ or otherwise), this representation produces a simulation in which systematic errors grow linearly right from $t = 0$. The cause are "type-II" boundary term errors of the kind described in Ref. 54: observable calculations (18) now involve ensemble averages of complex weight factors $\mathrm{Tr}[\hat{\Lambda}] = W = 2\cosh R$, e.g., $\langle \hat{S}_z \rangle = \langle\langle W S^z \rangle\rangle / \langle\langle W \rangle\rangle$, as in (31). The exponential nature of the weight factors leads them to be poorly sampled. This is because the distribution of $W(z,z')$ has very different behavior than the actual Gaussian sample distribution that generates the noise in the evolution equations for z and z'. In particular, trajectories with $\mathrm{Re}[R]$ several standard deviations above the mean are never generated, while their contribution to weights $W(R)$ included may be significant.

The dynamical and normalization behavior described above bears resemblance to similar afflictions seen in PPR simulations of the bosonic anharmonic oscillator $\hat{H} = \hat{a}^{\dagger 2}\hat{a}^2$.[54,63] There, a variable n whose real part is averaged to obtain the occupation number $\langle \hat{a}^\dagger \hat{a} \rangle = \langle\langle n \rangle\rangle$ takes on complex values in the course of the evolution. Unstable regions of phase space are accessed through diffusion into the imaginary part of n, much as here diffusion into the imaginary part of R sets off an instability. Similarly, an unnormalized kernel for the anharmonic oscillator alleviates instability, but makes observable calculations suffer again from type-II boundary terms right from $t = 0$.

This, and past work on Bose systems treated with the original positive-P representation, allow us to speculate that such effects are generic features of PPR-like phase-space methods with analytic kernels constructed from off-diagonal basis states:

(1) Complex parts of variables whose real parts correspond to physical observables mediate instability.

(2) Systematic errors, or at least huge noise, tend to ensue when phase-space evolution accesses regions corresponding to kernels with zero trace.

(3) The use of an unnormalized kernel is not effective, as type-II boundary term errors in the observable calculations tend to result.

IV. EXTENDED SIMULATION TIME BY ENTANGLEMENT SCALING

A. Entanglement scaling

We will apply a technique developed for many-body simulations of Bose gases in tandem with the PPR (Ref. 65) that uses the trend of results from calculations with reduced noise terms to pinpoint the full quantum values. Such a trend can be useful because reduced noise leads to longer simulation times before the onset of spiking. We will call this approach "entanglement scaling" because it is the noise that is responsible for generating new entanglement between the sites. Recall that the kernel is separable, so all entanglement in the system is described by the distribution. Noiseless equations produce no entanglement.

To use the technique, we need several families of stochastic simulations (labeled $m = A, B, \ldots$), parametrized by variables $\lambda_m \in [0,1]$, that interpolate smoothly between long-lasting, reduced-noise equations at $\lambda_m = 0$ and the full quantum description at $\lambda_m = 1$. At least two independent families are required to assess the accuracy of trends extrapolated to $\lambda_m = 1$. Technical details are summarized in Appendix B. The philosophy of this approach is similar to comparing trends of results obtained with different summation techniques in diagrammatic Monte Carlo.[85]

The first family of equations A will be the SU(2) equations (34) and (35) with noise terms multiplied by $\sqrt{\lambda_A}$, so that $\lambda_A = 0$ gives completely noiseless equations with no entanglement. Scaling noise variance linearly with λ_A here tends to give observable estimates that are also nearly linear in λ_A. This aids in making the extrapolation of the trend to $\lambda_A = 1$ well conditioned since few fitting parameters are needed.

The second family B will use the same noise η_i for both z_i and $z_i'^*$ variables at $\lambda_B = 0$. The difference in stochastic equations between $\lambda_B = 0$ and $\lambda_B = 1$ in this family is analogous to that between equations for a boson field under a Glauber-Sudarshan P representation[86,87] and a positive-P representation, respectively. At $\lambda_B = 0$ one now has stable, albeit stochastic, equations, but they do not correspond to full quantum mechanics. The following choice of λ_B dependence gives approximately linear scaling of observable estimates with λ_B:

$$\eta_i' = \sqrt{\lambda_B(2-\lambda_B)}\,\widetilde{\eta}_i + (1-\lambda_B)\,\eta_i^*, \tag{43}$$

where $\widetilde{\eta}_i$ is now an independent Gaussian complex noise with the same properties (26) as the old η_i'.

B. Entanglement scaling performance

Some predictions obtained with the fully deployed entanglement scaling approach are shown in Figs. 5–7. The first of these figures shows some detail of the procedure for the nearest-neighbor correlation $\langle \hat{S}_i^z \hat{S}_{i+1}^z \rangle$ (see also Appendix B and Fig. 10 for more).

One can see that, at longer times, the predictions of both families (green and yellow regions) are much closer to the true value than any of the magenta or cyan lines that were directly simulated. An obvious feature is that the family A prediction gives a much smaller statistical uncertainty than the family B prediction. This is related to the longer range of data in λ_A than in λ_B that is available at a given time (see also Fig. 10). Hence, for the mean final estimate (blue, central line) we use the family A estimate. The uncertainty in our final prediction is taken to be the maximum of three values: the statistical uncertainty from the family A and family B predictions, as well as the absolute difference between the mean family A and family B predictions. The last value takes into account any systematics due to the extrapolations in λ_m without needing to refer to any exact calculations, so that a reasonable uncertainty estimate can be obtained for large systems when no exact result is available.

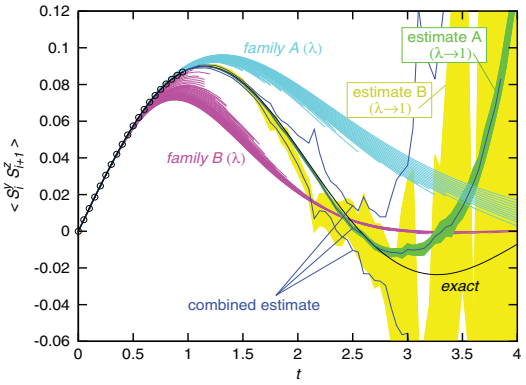

FIG. 5. (Color online) Detail of entanglement scaling shown for the example of the nearest-neighbor correlation $\langle \hat{S}_i^y \hat{S}_{i+1}^z \rangle$ for the $h = 0.5$ Ising quench on $N = 10$ sites of a 1D Ising chain. Cyan/magenta sets of lines show the predictions obtained for different λ_m values with family A and family B equations, respectively. Green and yellow zones show the extrapolation to the full quantum values $\lambda_m = 1$ obtained by each of the two methods, respectively. Vertical width gives the statistical uncertainty. The blue triple lines give the final combined estimate and uncertainty. For comparison, the black markers show the predictions available with $\lambda_A = 1$ direct calculations, while the black line shows the exact value.

Figure 6 further compares the predictions and their uncertainty with the true values, which can still be calculated for $N = 10$. It shows that we obtain useful results until $t \approx 2.8$, which is about three times longer than the plain approach of Sec. III A. This is long enough to access the particularly

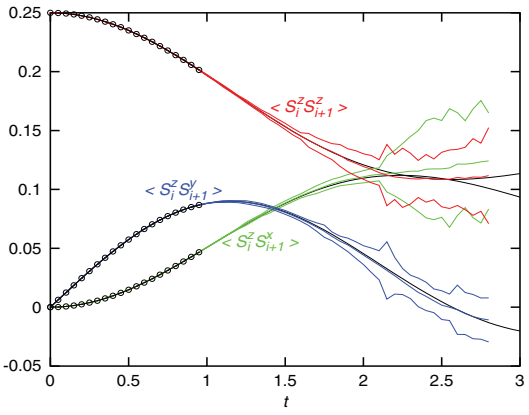

FIG. 6. (Color online) Predictions of the nearest-neighbor correlations involving S^z for the $h = 0.5$ Ising quench on $N = 10$ sites of a 1D Ising chain, as obtained using the entanglement scaling method (triple colored lines), and compared with known exact values (black lines). Black markers show the predictions available with $\lambda_A = 1$ direct calculations.

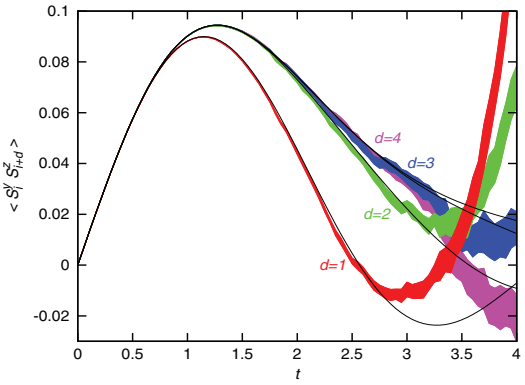

FIG. 7. (Color online) Correlation between $\hat{S}^y$ and $\hat{S}^z$ spin components as a function of site-to-site distance d for a $N = 10$ site 1D lattice at the critical quench value $h = 0.5$, as calculated using family A equations. Statistical uncertainty is shown as width of the color bars, while black lines show the exact results.

important intermediate-time regime of the problem[17] that occurs when $v_{\max} t \sim d$ for correlations between dth neighbors, where $v_{\max} = 2|J|\min[h, 1]$ is the maximum propagation velocity. For our examples here, $v_{\max} = 1$. This is also a characteristic time scale for single-site decoherence in the system such that $|\langle \hat{S} \rangle|$ decays to its typical long-time value over this time.

We see that the match in Fig. 6 is well within the uncertainty reported, and in fact the uncertainty given is quite conservative. The limiting factor is the relatively poor performance of family B in comparison with family A. For this system, the Glauber-Sudarshan–type equations give results further from the full quantum value than the noiseless ones. To reduce the final uncertainty, one needs a substitute, "family C," that gives results that deviate less while retaining a simple dependence on λ_C.

For example, Fig. 7 shows the buildup of correlations at a range as time progresses, when calculated using family A data. One can follow the propagation of the disturbance created by the quench by observing the times at which the correlation values diverge from each other with subsequent d. It would be highly advantageous to have a second family with similar statistical uncertainty, so as to be able to continue to resolve the difference between $d = 2$ and 3 in the final predictions.

C. Large systems

In Fig. 8, we show predictions for two very large systems (a spin chain with $N = 10^4$ sites, and a 2D square lattice with 100×100 sites, inaccessible with direct calculation). Indeed, the full quantum dynamics of a 2D case of the size shown in Fig. 8(b) is presently numerically intractable by any other currently available methods.

Importantly, the lifetime for the 1D spin chain calculations shown in Fig. 6 for $N = 10$ is the same as for $N = 10\,000$ in Fig. 8. This confirms that with these methods the simulation performance need not depend intractably on the system size.

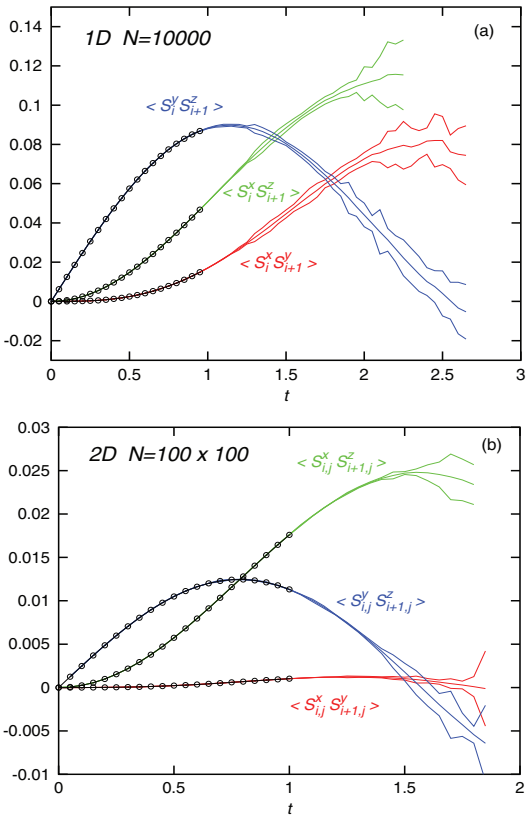

FIG. 8. (Color online) Dynamics of large spin systems after a quench, showing nearest-neighbor correlations between orthogonal spin directions. (a) A $N = 10\,000$ 1D Ising spin chain quenched to $h = 0.5$; (b) a 100×100 spin lattice quenched to $h = 0.1$. Triple lines show prediction and uncertainty obtained via the entanglement scaling method. Black markers show the predictions available with $\lambda = 1$ direct calculations.

Naturally, being able to simulate 10^4 spins would become especially useful for such cases as nonuniform systems or quenches, rather than the uniform test cases shown here.

V. COMMENTS AND CONCLUSIONS

A. Summary

We have implemented a phase-space representation for spin systems based on the SU(2) coherent states and demonstrated that it can be used to simulate the full quantum real-time dynamics of large systems of interacting spins, giving correct results.

A direct application of the representation allowed us to simulate the dynamics for significantly longer times than previous attempts using Schwinger bosons,[70] e.g., an improvement from $\sim 0.6\hbar/J$ (in Ref. 70) to $1.1\hbar/J$ for Ising chains after a transverse field quench to the critical value of $h = 0.5$. By using the entanglement scaling technique, we have been able to extend simulated times further, to times of up to $2.8\hbar/J$, which is long enough to observe the main decoherence effects and the propagation of correlations. Furthermore, initial states are compact so that these representations now exhibit good scaling with system size; the times achievable do not depend on the number of spins in the system, apart from computer resource limitations which scale only linearly with the number of interspin coupling terms. This allows one to access really large systems that are not directly accessible by other methods, such as the 10^4 spins calculations in one and two dimensions demonstrated here.

B. Outlook

This work is a first application of the entanglement scaling approach[65] beyond BEC collisions. Avenues for further improvement of simulated times $t_{\rm sim}$ include diffusion stochastic gauges[68] to reduce diffusion of trajectories into badly normalized regions of phase space such as $\mathrm{Im}[R]$, or a combination of drift and diffusion gauges of the kind presented by Dowling *et al.*[88] with Metropolis sampling of the resulting real weights. For application of entanglement scaling, stabilization of the equations may be useful by the use of just drift gauges[56,62] or the methods presented in Perret *et al.*[89] Finding a third family of equations, "family C," which more closely matches the full evolution at $\lambda_m = 0$ than family B, would strongly improve the precision of the final estimates.

Perhaps the most promising avenue to consider is to build a different kind of kernel that is more closely suited to the natural states of the Hamiltonian (20), especially some variety that builds nearest-neighbor correlations into the basis. To this end, the conjectures at the end of Sec. III D are points to remember when formulating new kinds of phase-space descriptions.

Within the existing time limitations, there is a range of problems for which short-time spin dynamics can tell us a lot. This includes quantum quenches in general, the study of critical behavior, and the pinpointing of phase transitions by analysis of the Loschmidt echo.[90] The coherence properties of a system can be investigated with echo sequences of external forcing parameters,[91–94] something that is especially useful for lossy systems because it alleviates the need for evolution over long times. The representations developed here can be used to simulate such situations without imposing approximations or projections onto the Hamiltonian, especially in 2D and 3D systems, something for which efficient methods have been lacking.

ACKNOWLEDGMENTS

We are grateful to P. Drummond and J. Pietraszewicz for helpful discussions. We also acknowledge financial support from the EU Marie Curie European Reintegration Grant No. PERG06-GA-2009-256291, the Polish Government Grant No. 1697/7PRUE/2010/7, as well as from NSERC. This work was made possible by the facilities of the Shared Hierarchical Academic Research Computing Network (SHARCNET:www.sharcnet.ca) and Compute/Calcul Canada.

APPENDIX A: REMAPPING THE VARIABLES ONTO A SEAMLESS SPACE

1. Polar and Boolean variables

To allow the representation of the $|\uparrow\rangle$, $|\downarrow\rangle$ states polarized in the $\vec{z}$ direction, and avoid the stiffness of the equations near these points in phase space, we make a change of variables that prevents such infinite values. While the surface of the Bloch sphere can not be seamlessly mapped onto a plane, hemispheres are easily treated. We make a transformation similar to a polar projection centered on the nearest pole, and introduce a Boolean variable s that keeps track of which pole is being used for a given trajectory.

For a state $|z\rangle$ we implement the following transformation to a complex variable y:

$$y = \begin{cases} e^{-z}, & \text{and} \quad s = +1 \quad \text{if} \quad \mathbb{R}[z] > 0 \\ e^{z^*}, & \text{and} \quad s = -1 \quad \text{if} \quad \mathbb{R}[z] \leqslant 0, \end{cases} \tag{A1}$$

where the variable $s = \text{sign}(\mathbb{R}[z])$ tells us which Bloch hemisphere we are in. Under this parametrization, the variable y never leaves the unit circle $|y| \leqslant 1$. The extreme spin values of $S_z = \pm\frac{1}{2}$ are now at the well-behaved $y = 0$ point, with $s = \pm 1$.

Since the branch cut in this parametrization lies on the far pole, the trajectories can never go near this singular region so long as we make sure to change the parametrization whenever the trajectory crosses the "equator." This is implemented by checking at the end of each time step whether $|y|$ has crossed outside the unit circle. If it has, we carry out

$$y \to \frac{1}{y^*} \quad \text{and} \quad s \to -s. \tag{A2}$$

When time steps are small, there is then no risk of approaching the far, pathological, pole. The evolution near the equator of the Bloch sphere is gradual, although swapping between projections occurs.

For the many-mode system, we need separate variables y_i, y_i', s_i, and s_i' for each spin. The SDEs (21) and (22) take on slightly different forms depending on which hemispheres the bra and ket components of the kernel lie. In terms of only the new variables, they are

$$\frac{dy_i}{dt} = \begin{cases} -iy_i\left\{S^z_{i-1} + S^z_{i+1}\right\} + \frac{ih}{2}\left(1 - y_i^2\right) & \text{if} \quad s_i = +1, \\ \quad - y_i[\eta_i + i\eta^*_{i-1}] & \\ -iy_i\left\{S^{z*}_{i-1} + S^{z*}_{i+1}\right\} - \frac{ih}{2}\left(1 - y_i^2\right) & \text{if} \quad s_i = -1 \\ \quad + y_i[\eta^*_i - i\eta_{i-1}] & \end{cases} \tag{A3}$$

and

$$\frac{dy_i'}{dt} = \begin{cases} iy_i'\left\{S^z_{i-1} + S^z_{i+1}\right\} - \frac{ih}{2}\left(1 - y_i'^2\right) & \text{if} \quad s_i' = +1, \\ \quad - y_i'[\eta_i' - i\eta'^*_{i-1}] & \\ iy_i'\left\{S^{z*}_{i-1} + S^{z*}_{i+1}\right\} + \frac{ih}{2}\left(1 - y_i'^2\right) & \text{if} \quad s_i' = -1, \\ \quad + y_i'[\eta'^*_i + i\eta'_{i-1}] & \end{cases} \tag{A4}$$

where the S^z estimator in terms of the new variables is

$$2S_i^z = \tanh R = \begin{cases} \frac{1-y_i y_i'}{1+y_i y_i'} & \text{if} \quad s_i = +1, s_i' = +1, \\ \frac{y_i'^* - y_i}{y_i'^* + y_i} & \text{if} \quad s_i = +1, s_i' = -1, \\ \frac{y_i^* - y_i'}{y_i^* + y'} & \text{if} \quad s_i = -1, s_i' = +1, \\ \frac{y_i^* y_i'^* - 1}{1 + y_i^* y_i'^*} & \text{if} \quad s_i = -1, s_i' = -1. \end{cases} \tag{A5}$$

2. Simulation termination

At times $t \gtrsim t_{\text{sim}}$, as shown in Fig. 4, a pronounced spiking behavior is seen in observable means. It is caused by approaches to the $R = \pm i\pi/2$ poles described in Sec. III B. Spikes are a warning sign that poor sampling of the distribution may be occurring[67] so one should disregard the simulation for times after its onset. With the original z, z' variable equations that have stiff behavior, spikes also lead immediately to numerical inaccuracy and overflow, so that ensemble averages of the estimators also overflow and any actual spiking/systematic error is hidden from view. A similar behavior was seen in positive-P simulations of boson fields.[63] The seamless variables y, y' are less stiff so that overflow does not occur and the bare spiking behavior can in principle be seen. An example is shown in Fig. 9. The results shown in other figures disregard evolution after the appearance of the first spike. We detect spikes by checking whether

$$|S^z| = \tfrac{1}{2}|\tanh R_i| > 1/\epsilon \tag{A6}$$

for any trajectory at any site i, where we choose $\epsilon = 0.04$.

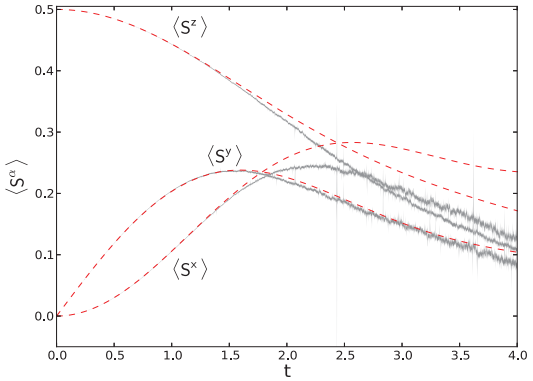

FIG. 9. (Color online) Spin components: $\langle\hat{S}^x\rangle, \langle\hat{S}^y\rangle, \langle\hat{S}^z\rangle$ (bottom to top) vs time for the 10-site Ising spin chain with transverse quench from $h = 0$ to 0.5. Results of simulations using the seamless equations with y, s variables. Here, we do not use the criterion (A6) to stop the simulation, so as to show the bare behavior. $\mathcal{N} = 10^4$ trajectories, $\mathcal{B} = 100$ bins. Error bars and exact results are shown. The criterion (A6) to stop the evolution is achieved at $t_{\text{sim}} \approx 1.1$.

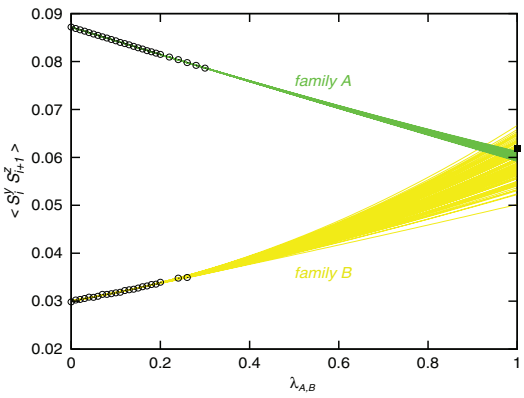

FIG. 10. (Color online) Extrapolation details for the nearest-neighbor correlation $\langle \hat{S}_i^y \hat{S}_{i+1}^z \rangle$ for the data of Fig. 5 at $t = 1.8$. The black circles show observable estimates $O_m(\lambda_m)$ obtained with family A and B equations. The green and yellow lines show the $j = 1, \ldots \mathcal{S} = 100$ ensemble of quadratic fits $f_m^{(j)}(\lambda_m)$ obtained for family A and B, respectively, with the synthetic data sets $O_m^{(j)}(\lambda_m)$. The black square is the exact quantum value obtained through exact diagonalization.

APPENDIX B: ENTANGLEMENT SCALING PROCEDURE

The technique is described in detail in Ref. 65. We proceed as follows:

(1) For an observable of interest $\hat{O}$, we generate observable estimates $O_m(t,\lambda_m) \pm \Delta O_m(t,\lambda_m)$ for a sequence of λ_m values, for each method m. Here, $m = \{A, B\}$. We expect that at long times $t > t_{\rm sim}^m(\lambda_m)$, the data are missing (here, due to rejection because of the onset of spiking) (seen in Figs. 5 and 10).

(2) We use the available λ_m ranges of data to extrapolate to the full quantum predictions $Q_m(t)$ at $\lambda_m = 1$.

(3) We estimate the statistical uncertainty of these extrapolations $\Delta Q_m(t)$.

(4) The final best estimate $Q(t)$ is taken to be the prediction $Q_m(t)$ with the smallest uncertainty among the $\Delta Q_m(t)$.

(5) The final uncertainty $\Delta Q(t)$ is taken to be the maximum among all statistical uncertainties $\Delta Q_m(t)$ and discrepancies $|Q_m(t) - Q(t)|$. The latter takes into account systematics due to poor fits without needing to refer to any exact calculations.

Two or more families m are used to provide a check on each other's accuracy. For this to work, they must make independent estimates of $Q_m(t)$. Since we are in principle free to choose the functional form by which λ_m enters the evolution equations, estimates will only be independent when the $\lambda = 0$ starting points differ to a statistically significant degree.

There is also the matter of choosing fitting functions in the λ_m. In principle, they are unknown *a priori*. In practice, complicated dependencies on λ_m are unacceptable because the extrapolation would become ill conditioned due to poorly constrained fitting parameters. Scaling the noise variance with λ_m tends to give near-linear dependence, when the result at $\lambda_m = 0$ is a noiseless set of equations. We try polynomials up to third order as our fitting functions $f_m(t,\lambda_m)$ in λ_m. In almost all cases, quadratic fits give the best results; linear fits tend to disagree between methods m by more than statistical uncertainty because the dependence is too simple, while cubic fits are usually ill conditioned and give huge uncertainties.

Uncertainty estimates for extrapolations can be found by various means.[95] One relatively straightforward method is to generate a set of synthetic data sets where deviations from the fit are randomized. To do this, we calculate the rms deviation from the fit $\mathcal{R}_m(t)^2 = \frac{1}{N_m(t)} \sum_{\lambda_m} [O_m(t,\lambda_m) - f_m(t,\lambda_m)]^2$, and add random Gaussian noise having this standard deviation to the original data. $N_m(t)$ is the number of λ_m values used. This gives an ensemble of data sets labeled by $j = 1, \ldots, \mathcal{S}$, with values

$$O_m^{(j)}(t,\lambda_m) = O_m(t,\lambda_m) + \mathcal{R}_m^{\rm cap}(t,\lambda_m)\xi_m^{(j)}(t,\lambda_m), \quad \text{(B1)}$$

where the $\xi_m^{(j)}(t,\lambda_m)$ are independent Gaussian random variables with mean zero and variance unity. In practice, we use a deviation that is capped from below $\mathcal{R}_m^{\rm cap}(t,\lambda_m) = \max[\Delta O_m(t,\lambda_m), \mathcal{R}_m(t)]$ to not be smaller than the statistical uncertainty in the data points.

Having these sets, an extrapolation $Q_m^{(j)}(t)$ is made with each one. The uncertainty in our final estimates $\Delta Q_m(t)$ is based on the distribution of $Q_m^{(j)}(t)$. This need not be Gaussian, so instead of using standard deviations we consider percentiles (68.3% in the figures). We use $\mathcal{S} = 100$ such synthetic data sets in each case.

APPENDIX C: SIMULATION TIME FOR NONZERO *h*

Consider the equations (A3) for the "seamless" y variables, and let us stay now generally in the $s = s' = +1$ projection, since what follows is very approximate and this simplification is sufficient to obtain the observed scaling (40) and (41). The poles correspond to the denominator in (A5) going to zero, i.e., for the $s = s'$ case, when $yy' = -1$. Since $|y| \leqslant 1$, this means

$$y' = -y \quad \text{and} \quad |y| = |y'| = 1 \quad \text{(C1)}$$

is the location of the poles, i.e., y and y' lie opposite each other on the unit circle.

To estimate when this can occur, consider that y and y'^* start out equal, and have a similar evolution that differs by some random noise. Hence, the variance of the distance $|y - y'|$ is of the same order as the variance of $|y|$. Poles can occur only when $|y - y'| = 2$, so we expect approaches to the poles to begin when the variance of y is of the order of half (then $\pm 2\sigma$ outliers are separated by a distance of ≈ 2). We will estimate $t_{\rm sim}$ by looking for the time when

$$\text{var}[|y|] = \langle |y|^2 \rangle - |\langle y \rangle|^2 = \Delta_y^2, \quad \text{(C2)}$$

where Δ_y is a constant $\mathcal{O}(1/2)$.

Let us look at the evolution of y. Initially, all the S_{i-1}^z and S_{i+1}^z contributions are negligible because they are multiplied by $y \approx 0$. If we ignore them, the sites decouple, and one has some hope of a simple analysis, so let us proceed in that way. The noises $\eta_{\langle i,j \rangle}$ can be collected together into one larger noise, and the approximate equation is

$$\frac{dy}{dt} = \frac{ih}{2}(1 - y^2) + y\sqrt{C}\eta(t), \quad \text{(C3)}$$

where C is the number of connections per site. For example, $C = 2d$ in d-dimensional square lattices. η has the same statistical properties (26) as one of the η_i.

Initially, $y \approx 0$, and (C3) leads to

$$y(t) \approx i\frac{ht}{2} \tag{C4}$$

so that the trajectories move upwards towards $y \to i$, while starting to acquire fluctuations. There are two extreme possibilities: either the trajectories all move up towards the unit circle without acquiring much noise along the way (large h), or their average stays small while the outliers approach the unit circle (small h). Let us, for now, ignore also the nonlinearity that occurs when $y \sim \mathcal{O}(1)$, and consider the early-time equation

$$\frac{dy}{dt} = \frac{ih}{2} + y\sqrt{C}\eta(t) \tag{C5}$$

which can be solved. For $y(0) = 0$, it is

$$y(t) = \frac{ih}{2}\, e^{-\sqrt{C}f(t)} \int_0^t e^{\sqrt{C}f(s)} ds, \tag{C6}$$

where the function

$$f(t) = \int_0^t \eta(s)ds = f_R(t) + if_I(t) \tag{C7}$$

is an integrated noise that has the following properties:

$$\langle f(t)\rangle = 0, \quad \langle f(t)f(t')\rangle = 0, \quad \langle f^*(t)f(t')\rangle = |t - t'| \tag{C8}$$

and f_R and f_I are the real and imaginary parts, respectively. These are independent and have equal variances of $|t - t'|/2$.

To proceed, we will need the following results,[54] valid for real Gaussian random variables ξ of variance 1 and zero mean:

$$\langle e^{\sigma\xi}\rangle = e^{\sigma^2/2}, \quad \langle e^{i\sigma\xi}\rangle = e^{-\sigma^2/2}. \tag{C9}$$

Let us now evaluate the variance of $|y|$. The expression (C6) for y can be grouped according to independent noises in the exponential, such that

$$y = \frac{ih}{2}\int_0^t ds\, e^{\sqrt{C}[f_R(t)-f_R(s)]}\, e^{i\sqrt{C}[f_I(t)-f_I(s)]}. \tag{C10}$$

Each factor with independent noises can be evaluated independently, so

$$\langle y\rangle = \frac{ih}{2}\int_0^t ds \langle e^{\sqrt{C}[f_R(t)-f_R(s)]}\rangle\langle e^{i\sqrt{C}[f_I(t)-f_I(s)]}\rangle. \tag{C11}$$

The noise difference is $f(t) - f(s) = \int_s^t \eta(s')ds'$ and its real and imaginary parts have a variance of $|t - s|/2$. Then, using (C9) we obtain

$$\langle y\rangle = \frac{iht}{2}. \tag{C12}$$

A similar but slightly more lengthy procedure using the substitution (C10) gives $\langle |y|^2\rangle = \frac{h^2t}{4C}(e^{Ct} - 1)$ so that

$$\mathrm{var}[|y|] = \frac{h^2t}{4C}[e^{Ct} - 1 - Ct], \tag{C13}$$

to be compared with our variance criterion (C2).

The approximate deterministic evolution (C4) is valid as long as $\langle y\rangle$ remains small, i.e., for times $\lesssim t_0 = 2/h$. When h is small, $t_0 \gg 1$, and the variance at this time is $\approx e^{2C/h}(h/2C) \gg 1$. Hence, our variance criterion (C2) for t_{sim} is exceeded while our assumptions hold. Under the $2/h \gg 1$ assumption, $\mathrm{var}[|y|] \approx \frac{h^2t}{4C}e^{Ct}$, so that *for small h* (C2) gives

$$t_{\mathrm{sim}} \approx \frac{2}{C}\ln\left(\frac{2\Delta_y\sqrt{C}}{h}\right) - \frac{1}{C}\ln t_{\mathrm{sim}} \approx \frac{2}{C}\ln\left(\frac{2\Delta_y\sqrt{C}}{h}\right). \tag{C14}$$

The $\ln t$ term is negligible for small enough h, so the observed scaling behavior (40) is recovered. A comparison with the data of Fig. 4 gives a match for $\Delta_y \approx 1/4$.

Different behavior occurs when h is large. In this case, by the "large-y" time of t_0, (C13) gives

$$\mathrm{var}[|y|(t_0)] \approx \frac{C}{h} \ll 1 \tag{C15}$$

so that by the time the linear drift approximation (C4) used to obtain (C13) breaks down, the variance is still small and the $yy' = -1$ poles have not been approached.

At later times, if we continue to ignore the Ising drift terms $\sim yS^z$, then upon reaching $y \approx i$, we make the coordinate change (A2) to obtain $s \to -1$, and $y \to \approx -i$, soon followed by also a complementary flip in s' and y' since the variance of the trajectories is small. The evolution then continues to drift upwards according to $\dot{y} \approx ihy/2$ until we again reach $y \approx +i$, and so on. This basically corresponds to precession invoked by the strong transverse field along the $\vec{x}$ axis. For large h, many such periods will occur before t_{sim} is reached. Let us make a gross approximation that on average the value of $|y|$ is $\overline{y}$ in the time period $t_0 < t < t_{\mathrm{sim}}$, expecting $\overline{y}$ to be $\mathcal{O}(1)$. Then, an approximate equation of motion is

$$\frac{dy}{dt} = \text{ deterministic terms} + \overline{y}\sqrt{C}\eta(t). \tag{C16}$$

The equation of motion for the variance, on the other hand, is (via the Ito calculus)

$$\frac{d}{dt}\mathrm{var}[|y|] = \frac{C|\overline{y}|^2}{2} + \left(\left\langle y^*\frac{dy}{dt}\right\rangle - \left\langle\frac{dy}{dt}\right\rangle\langle y^*\rangle\right) + \text{c.c.} \tag{C17}$$

The covariances on the right-hand side can have a complicated dependence on y, but in the spirit of simplifying down to the bare essentials, let us omit them. With that, we find

$$\mathrm{var}[|y(t)|] \approx \mathrm{var}[|y(t_0)|] + \frac{C|\overline{y}|^2}{2}(t - t_0) \tag{C18}$$

$$\approx C\left[\frac{1}{h} + \frac{|\overline{y}|^2}{2}\left(t - \frac{2}{h}\right)\right], \tag{C19}$$

using also (C15). Applying the criterion (C2), we obtain the following estimate *at large h*:

$$t_{\mathrm{sim}} \approx \frac{2\Delta_y^2}{C|\overline{y}|^2} + \frac{2}{h}\left(1 - \frac{1}{|\overline{y}|^2}\right), \tag{C20}$$

the general behavior being (41). A comparison with the data of Fig. 4 gives a match for $c_1 \approx 0.8$ and $c_2 \approx 0.3$, i.e., $\overline{y} \approx 1.1$ and $\Delta_y \approx 0.7$.

*ngry@mcmaster.ca

[1] A. Polkovnikov, K. Sengupta, A. Silva, and M. Vengalattore, Rev. Mod. Phys. **83**, 863 (2011).
[2] P. Calabrese and J. Cardy, J. Stat. Mech: Theory Exp. (2007) P06008.
[3] P. Calabrese and J. Cardy, J. Stat. Mech: Theory Exp. (2007) P10004.
[4] C. Kollath, A. M. Läuchli, and E. Altman, Phys. Rev. Lett. **98**, 180601 (2007).
[5] S. R. Manmana, S. Wessel, R. M. Noack, and A. Muramatsu, Phys. Rev. Lett. **98**, 210405 (2007).
[6] G. Roux, Phys. Rev. A **79**, 021608(R) (2009).
[7] G. Roux, Phys. Rev. A **81**, 053604 (2010).
[8] J.-S. Bernier, G. Roux, and C. Kollath, Phys. Rev. Lett. **106**, 200601 (2011).
[9] S. Trotzky, Y.-A. Chen, A. Flesch, I. P. McCulloch, U. Schollwöck, J. Eisert, and I. Bloch, Nat. Phys. **8**, 325 (2012).
[10] D. Gobert, C. Kollath, U. Schollwöck, and G. Schütz, Phys. Rev. E **71**, 036102 (2005).
[11] P. Barmettler, M. Punk, V. Gritsev, E. Demler, and E. Altman, Phys. Rev. Lett. **102**, 130603 (2009).
[12] P. Barmettler, M. Punk, V. Gritsev, E. Demler, and E. Altman, New J. Phys. **12**, 055017 (2010).
[13] D. Rossini, A. Silva, G. Mussardo, and G. Santoro, Phys. Rev. Lett. **102**, 127204 (2009).
[14] S. Langer, F. Heidrich-Meisner, J. Gemmer, I. P. McCulloch, and U. Schollwöck, Phys. Rev. B **79**, 214409 (2009).
[15] P. Calabrese, F. H. L. Essler, and M. Fagotti, Phys. Rev. Lett. **106**, 227203 (2011).
[16] U. Divakaran, F. Iglói, and H. Rieger, J. Stat. Mech: Theory Exp. (2011) P10027.
[17] P. Calabrese, F. H. L. Essler, and M. Fagotti, J. Stat. Mech: Theory Exp. (2012) P07016.
[18] P. Calabrese, F. H. L. Essler, and M. Fagotti, J. Stat. Mech: Theory Exp. (2012) P07022.
[19] F. H. L. Essler, S. Evangelisti, and M. Fagotti, Phys. Rev. Lett. **109**, 247206 (2012).
[20] A. Mitra, Phys. Rev. B **87**, 205109 (2013).
[21] M. Rigol, V. Dunjko, V. Yurovsky, and M. Olshanii, Phys. Rev. Lett. **98**, 050405 (2007).
[22] R. Marcos, D. Vanja, and M. Olshanii, Nature (London) **452**, 854 (2008).
[23] R. P. Feynman, Int. J. Theor. Phys. **21**, 467 (1982).
[24] D. Porras and J. I. Cirac, Phys. Rev. Lett. **92**, 207901 (2004).
[25] D. Jaksch and P. Zoller, Ann. Phys. (NY) **315**, 52 (2005).
[26] M. Lewenstein, A. Sanpera, V. Ahufinger, B. Damski, A. Sen De, and U. Sen, Adv. Phys. **56**, 243 (2007).
[27] I. Buluta and F. Nori, Science **326**, 108 (2009).
[28] M. Johanning, A. F. Varón, and C. Wunderlich, J. Phys. B: At. Mol. Opt. Phys. **42**, 154009 (2009).
[29] C. Schneider, D. Porras, and T. Schaetz, Rep. Prog. Phys. **75**, 024401 (2012).
[30] A. Friedenauer, H. Schmitz, J. T. Glueckert, D. Porras, and T. Schaetz, Nat. Phys. **4**, 757 (2008).
[31] K. Kim, M. S. Chang, S. Korenblit, R. Islam, E. E. Edwards, J. K. Freericks, G. D. Lin, L. M. Duan, and C. Monroe, Nature (London) **465**, 590 (2010).
[32] J. Simon, W. S. Bakr, R. Ma, M. E. Tai, P. M. Preiss, and M. Greiner, Nature (London) **472**, 307 (2011).
[33] X.-s. Ma, B. Dakić, W. Naylor, A. Zeilinger, and P. Walther, Nat. Phys. **7**, 399 (2011).
[34] R. Islam, E. E. Edwards, K. Kim, S. Korenblit, C. Noh, H. Carmichael, G. D. Lin, L. M. Duan, C. C. J. Wang, J. K. Freericks, and C. Monroe, Nat. Commun. **2**, 377 (2011).
[35] J. Struck, C. Olschlager, R. Le Targat, P. Soltan-Panahi, A. Eckardt, M. Lewenstein, P. Windpassinger, and K. Sengstock, Science **333**, 996 (2011).
[36] K. Kim, S. Korenblit, R. Islam, E. E. Edwards, M. S. Chang, C. Noh, H. Carmichael, G. D. Lin, L. M. Duan, C. C. Joseph Wang, J. K. Freericks, and C. Monroe, New J. Phys. **13**, 105003 (2011).
[37] C. Roos, Nature (London) **484**, 461 (2012).
[38] J. W. Britton, B. C. Sawyer, A. C. Keith, C. C. J. Wang, J. K. Freericks, H. Uys, M. J. Biercuk, and J. J. Bollinger, Nature (London) **484**, 489 (2012).
[39] R. Blatt and C. F. Roos, Nat. Phys. **8**, 277 (2012).
[40] F. Meinert, M. J. Mark, E. Kirilov, K. Lauber, P. Weinmann, A. J. Daley, and H.-C. Nägerl, Phys. Rev. Lett. **111**, 053003 (2013).
[41] A. Dutta, U. Divakaran, D. Sen, B. K. Chakrabarti, T. F. Rosenbaum, and G. Aeppli, arXiv:1012.0653.
[42] O. F. Syljuåsen and A. W. Sandvik, Phys. Rev. E **66**, 046701 (2002).
[43] S. R. White, Phys. Rev. Lett. **69**, 2863 (1992).
[44] K. A. Hallberg, Adv. Phys. **55**, 477 (2006).
[45] U. Schollwöck, Rev. Mod. Phys. **77**, 259 (2005).
[46] J. Eisert, M. Cramer, and M. B. Plenio, Rev. Mod. Phys. **82**, 277 (2010).
[47] S. R. White and A. E. Feiguin, Phys. Rev. Lett. **93**, 076401 (2004).
[48] U. Schollwöck, Ann. Phys. (NY) **326**, 96 (2011).
[49] A. Daley, C. Kollath, U. Schollwöck, and G. Vidal, J. Stat. Mech: Theory Exp. (2004) P04005.
[50] G. Vidal, Phys. Rev. Lett. **98**, 070201 (2007).
[51] M. C. Bañuls, M. B. Hastings, F. Verstraete, and J. I. Cirac, Phys. Rev. Lett. **102**, 240603 (2009).
[52] C. W. Gardiner, *Quantum Noise* (Springer, Berlin, 1991).
[53] J. F. Corney and P. D. Drummond, Phys. Rev. Lett. **93**, 260401 (2004).
[54] P. Deuar, arXiv:cond-mat/0507023.
[55] J. F. Corney and P. D. Drummond, J. Phys. A: Math. Gen. **39**, 269 (2006).
[56] P. D. Drummond, P. Deuar, and K. V. Kheruntsyan, Phys. Rev. Lett. **92**, 040405 (2004).
[57] A. Polkovnikov, Ann. Phys. (NY) **325**, 1790 (2010).
[58] T. Aimi and M. Imada, J. Phys. Soc. Jpn. **76**, 084709 (2007).
[59] T. Aimi and M. Imada, J. Phys. Soc. Jpn. **76**, 113708 (2007).
[60] F. F. Assaad, P. Werner, P. Corboz, E. Gull, and M. Troyer, Phys. Rev. B **72**, 224518 (2005).
[61] P. D. Drummond and C. W. Gardiner, J. Phys. A: Math. Gen. **13**, 2353 (1980).
[62] P. Deuar and P. D. Drummond, Phys. Rev. A **66**, 033812 (2002).
[63] P. Deuar and P. D. Drummond, J. Phys. A: Math. Gen. **39**, 1163 (2006).
[64] P. Deuar and P. D. Drummond, Phys. Rev. Lett. **98**, 120402 (2007).
[65] P. Deuar, Phys. Rev. Lett. **103**, 130402 (2009).
[66] P. Deuar, J. Chwedenczuk, M. Trippenbach, and P. Zin, Phys. Rev. A **83**, 063625 (2011).
[67] A. Gilchrist, C. W. Gardiner, and P. D. Drummond, Phys. Rev. A **55**, 3014 (1997).
[68] P. Deuar and P. D. Drummond, J. Phys. A: Math. Gen. **39**, 2723 (2006).

[69]P. Deuar, A. G. Sykes, D. M. Gangardt, M. J. Davis, P. D. Drummond, and K. V. Kheruntsyan, Phys. Rev. A **79**, 043619 (2009).
[70]R. Ng and E. S. Sørensen, J. Phys. A: Math. Theor. **44**, 065305 (2011).
[71]J. M. Radcliffe, J. Phys. A: Gen. Phys. **4**, 313 (1971).
[72]W.-M. Zhang and R. Gilmore, Rev. Mod. Phys. **62**, 867 (1990).
[73]D. W. Barry and P. D. Drummond, Phys. Rev. A **78**, 052108 (2008).
[74]R. J. Glauber, Phys. Rev. **130**, 2529 (1963).
[75]F. T. Arecchi, E. Courtens, R. Gilmore, and H. Thomas, Phys. Rev. A **6**, 2211 (1972).
[76]A. Perelomov, Commun. Math. Phys. **26**, 222 (1972).
[77]B. S. Shastry, G. S. Agarwal, and I. R. Rao, Pramana **11**, 85 (1978).
[78]C. T. Lee, Phys. Rev. A **30**, 3308 (1984).
[79]P. D. Drummond, Phys. Lett. A **106**, 118 (1984).
[80]L. A. Narducci, C. A. Coulter, and C. M. Bowden, Phys. Rev. A **9**, 829 (1974).
[81]S. Chaturvedi, E. Ercolessi, G. Marmo, G. Morandi, N. Mukunda, and R. Simon, J. Phys. A: Math. Gen. **39**, 1405 (2006).
[82]P. Drummond and J. Corney, Comput. Phys. Commun. **169**, 412 (2005).
[83]R. Coldea, D. A. Tennant, E. M. Wheeler, E. Wawrzynska, D. Prabhakaran, M. Telling, K. Habicht, P. Smeibidl, and K. Kiefer, Science **327**, 177 (2010).
[84]P. Pfeuty, Ann. Phys. (NY) **57**, 79 (1970).
[85]N. V. Prokof'ev and B. V. Svistunov, Phys. Rev. B **77**, 020408(R) (2008).
[86]R. J. Glauber, Phys. Rev. **131**, 2766 (1963).
[87]E. C. G. Sudarshan, Phys. Rev. Lett. **10**, 277 (1963).
[88]M. R. Dowling, M. J. Davis, P. D. Drummond, and J. F. Corney, J. Comput. Phys. **220**, 549 (2007).
[89]C. Perret and W. P. Petersen, J. Phys. A: Math. Theor. **44**, 095004 (2011).
[90]D. Rossini, T. Calarco, V. Giovannetti, S. Montangero, and R. Fazio, Phys. Rev. A **75**, 032333 (2007).
[91]U. Raitzsch, V. Bendkowsky, R. Heidemann, B. Butscher, R. Löw, and T. Pfau, Phys. Rev. Lett. **100**, 013002 (2008).
[92]K. C. Younge and G. Raithel, New J. Phys. **11**, 043006 (2009).
[93]M. R. Dowling, P. D. Drummond, M. J. Davis, and P. Deuar, Phys. Rev. Lett. **94**, 130401 (2005).
[94]S. Wuster, J. Stanojevic, C. Ates, T. Pohl, P. Deuar, J. F. Corney, and J. M. Rost, Phys. Rev. A **81**, 023406 (2010).
[95]W. H. Press, S. A. Teukolsky, W. T. Vetterling, and B. P. Flannery, *Numerical Recipes*, 3rd ed. (Cambridge University Press, Cambridge, England, 2007).

Part II: Universality Class of the dirty-boson transition in 2d

CHAPTER 4

THE DIRTY-BOSON PROBLEM

4.1 Introduction

Disorder is ubiquitous in condensed matter systems, particularly in real materials and can give rise to non-trivial effects; a classical example of this is the phenomena of Anderson localization (Anderson, 1959) of non-interacting electronic systems in disordered media. Suffice it to say, the interplay between the strength of disorder and interactions adds an extra layer of complexity and is an extremely challenging problem. This is especially due to the shortage of well-controlled approximations for analytical treatments, save for a few exceptions such as weak disorder in 1d. In light of such inherent difficulties, it is only natural to gain insight on the physics of disordered system using numerical tools, such as its quantum critical properties.

There are two common ways of studying disorder physics that are often encountered. One way is to quench a system by incorporating a fixed amount of disorder, followed by tuning an external parameter, (say λ) that is known to induce a quantum phase transition in the disorder-free system. The second way is to instead fix the parameters of the 'clean' system and increase the disorder strength (say Δ). In the latter scenario, one can treat Δ as another dimension of exploration for new quantum critical phenomena. As well, a novel $\Delta - \lambda$ phase diagram can be mapped out. Some novel disorder-induced phenomena include the smearing of a sharp transition (Vojta, 2010), new critical exponents as dictated by the Harris criterion (Harris, 1974) (see section 4.5.1) and of course the manifestation of novel quantum phases such as the spin glass (SG) phase in random bond Ising models (Cho and Fisher, 1997) and the Bose glass phase (BG) in disordered Bosonic models (Fisher et al., 1989).

Of interest to us is the effects of uncorrelated disorder in the 2d Bose-Hubbard (BH) model, dubbed the 'dirty-boson' problem, which was studied in detail in the seminal work of (Fisher et al., 1989) and has since been established as a central reference. It is interesting to note that the interest in disordered

boson physics has been spurred on by several natural experimental platforms, examples of which include ^{4}He in random media such as Vycor (Crowell et al., 1997) or Aerogel (Finotello et al., 1988) and most recently transition metal halogenides (Zheludev and Roscilde, 2013) in place of traditional metal oxide quantum magnets. It has further been successfully emulated using ultra-cold atoms in optical lattices (Sanchez-Palencia and Lewenstein, 2010) using bichromatic potentials (Damski et al., 2003, D'Errico et al., 2014, Roux et al., 2008), speckle potentials (White et al., 2009) or different atomic species to mimic random impurities (Ospelkaus et al., 2006) as well.

Surprisingly to this day, the universality class of the 'dirty-boson' problem, is filled with conflicting results in the literature. In particular the dynamic critical exponent, z, has been proven to be particularly difficult to pin down. In (Fisher et al., 1989), Fisher predicted that $z = d$ in all dimensions, an exact longstanding result that invalidated the existence of an upper critical dimension and has been used as a major assumption in most numerical studies (Runge, 1992, Yu et al., 2008, 2012b, Zhang et al., 1995) since its inception. Oddly enough a series of numerical results demonstrated that an alternate scenario $z < d$ (Álvarez Zúñiga et al., 2014, Priyadarshee et al., 2006, Meier and Wallin, 2012, Kim and Stroud, 2008, Marković et al., 1999) was possible and was further lent credence by the theoretical work of Weichman et al (Weichman, 2008).

Our work in this thesis, details our numerical efforts to determine unequivocally the universality class of the 'dirty-boson' problem, paying special attention to z. To this end, we engage in large-scale QMC simulations making no prior assumptions to the value of z, which traditional simulations heavily relied on (cf. section 4.6.1). For the remainder of this chapter, we aim to elucidate and review the features of the 'clean' and 'dirty' BH model and provide insight on the controversy with regards to the 'dirty-boson' problem, to which our research is targeted at.

4.2 The Insulator-conductor transition in bosonic systems

4.2.1 The Bose-Hubbard model

The Bose-Hubbard model (Fisher et al., 1989) is an approximate description of interacting bosons in a lattice that manifests a conductor-insulator type transition arising from a competition between kinetic energy and potential energy terms. Its Hamiltonian takes the simple form:

$$\hat{H} = -t\sum_{\langle i,j\rangle}(\hat{b}_i^\dagger \hat{b}_j + \hat{b}_j^\dagger \hat{b}_i) - \sum_i \mu \hat{n}_i + \frac{U}{2}\sum_i \hat{n}_i(\hat{n}_i - 1), \tag{4.2.1}$$

where t represents the tunneling amplitude, μ sets the chemical potential and U is the on-site potential energy that penalizes occupancies greater than one. The bosonic operators, $\hat{b}_i, \hat{b}^\dagger$ satisfy the usual commutation relations: $[\hat{b}_i, \hat{b}_i^\dagger] = \delta_{ij}$ and $[\hat{b}_i, \hat{b}^\dagger] = 0$ where δ_{ij} is the kronecker delta function. $\hat{n}_i = \hat{b}_i^\dagger \hat{b}_i$ is the number operator for a given site. It also has a global U(1) symmetry such that $H\left(\left\{\hat{b}_i \to \hat{b}_i e^{-i\theta}, \hat{b}_i^\dagger \to \hat{b}_i^\dagger e^{i\theta}\right\}\right) = H\left(\left\{\hat{b}_i, \hat{b}_i^\dagger\right\}\right)$. We will now discuss its zero temperature properties. The BH model admits a Mott insulator (MI) and a Superfluid (SF) conducting phase and a phase diagram in the t/U-μ/U plane that is uniquely distinguished by the existence of asymmetric Mott lobes surrounded by a SF phase as shown in the schematic phase diagram in fig. 4.1(a).

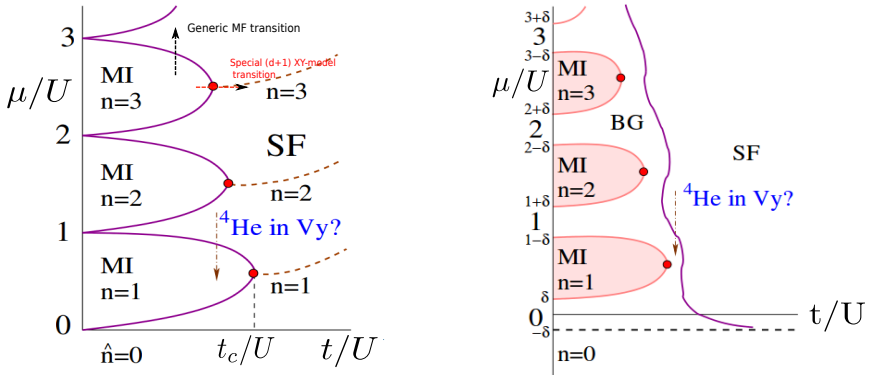

(a) Phase diagram of the clean BH model

(b) Phase diagram of the BH model with disorder, $\delta\mu_i/U = \delta$.

Figure 4.1: Schematic phase diagrams of the BH model adapted from (Weichman, 2008) with and without disorder. The multicritical point is indicated by the red dots. The transition through the latter at fixed μ/V lies in the (d+1) XY universality class. The generic transition can be described by its mean-field values. Experiments involving ^{4}He in random media such as Vycor is an excellent emulator of BH with disorder (Zimanyi et al., 1994) and may be a viable option to probe the transition indicated by the brown dashed arrow.

The Mott insulator (MI) is a gapped phase and characterized by a vanishing compressibility, $\kappa = \frac{\partial \rho}{\partial \mu}$, where ρ is the density of particles. Based on this definition of the compressibility then, in the Mott phase, the density of the system is stuck at commensurate integer filling albeit only for a certain range of values of the chemical potential. One can imagine that a sufficiently large chemical potential will inevitably overcome the energy gap and allow the addition of particles or holes. To visualize how a Mott phase can arise, it is instructive to first study the BH Hamiltonian without tunnelling, i.e. the $t = 0$ limit, which is given by the on-site interaction Hamiltonian

$$\hat{H} = -\sum_i \mu \hat{n}_i + \frac{U}{2} \sum_i \hat{n}_i (\hat{n}_i - 1) \tag{4.2.2}$$

that is diagonal in the Fock basis with eigenstate: $|\psi\rangle = \prod_i \left(\hat{a}^\dagger\right)^n |0\rangle$ where $|0\rangle$ is the vacuum state. The energy per site of the system as a function of μ/U and at different integer fillings are then given by:

$$\begin{aligned} &\text{If } n_i = 0: \quad E_i = 0 \\ &\text{If } n_i = 1: \quad E_i = -\mu \\ &\text{If } n_i = 2: \quad E_i = U - 2\mu \\ &\text{If } n_i = 3: \quad E_i = 3U - 3\mu \\ &\vdots \end{aligned} \tag{4.2.3}$$

and depicted in fig. 4.2. We see that in order to minimize the energy of the system, it is preferred to have n bosons per site for the range of chemical potentials: $\mu/U \in (n-1, n)$. This region represents the aforementioned Mott insulator with a density that is insensitive to changes in μ/U. A crossover

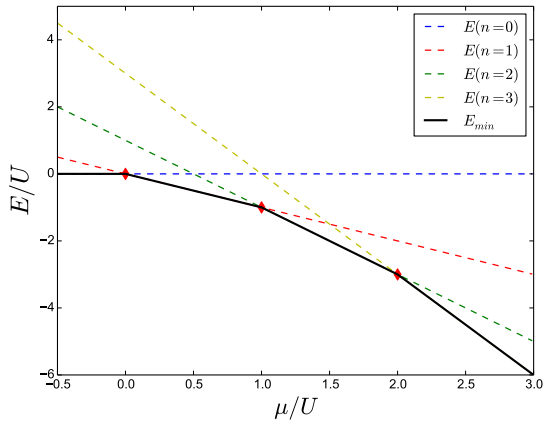

Figure 4.2: Energy per site of the BH model in the absence of hopping. The system is in a Mott phase in commensurate filling with n bosons per site for $\mu/U \in [n, n-1]$. A crossover from density n to $n+1$ occurs at values $\mu'/U = n$ labeled by red diamonds.

to Mott phases of different densities occurs at $\mu/U = n$ precisely when $E(n-1) = E(n)$, implying an energy gap of nU. For finite t however, the system can gain energy by hopping between sites and use it to overcome the energy gap which is of order U. For $t \ll U$, the on-site interaction dominates and the MI phase still persists. On the other hand, for $t \gg U$, the gain in kinetic energy dwarfs the gap and particles/holes can now be added easily. The system is essentially in a gapless superfluid phase. We therefore expect that for intermediate values of t/U, extent of the Mott lobes in the μ-direction which represents the excitation gap, must decrease accordingly, eventually vanishing at a unique point, t_c/U that demarcates the location of the tip of the Mott Lobe.

In the regions between the Mott Lobes, the system is a SF and particles can be added to the system at no energy cost, thereby realizing a gapless phase with finite compressibility. In contrast to the Mott phase, the density increases continuously as the chemical potential is increased. In effect, the on-site interaction strength is completely offset by the gain in kinetic energy. The $T = 0$ wavefunction for the SF state is given by the state with all its bosons in the zero momentum state: $|\psi_{SF}\rangle = \frac{1}{\sqrt{N!}} \left(\hat{b}^\dagger\right)^N |0\rangle$. Additionally it exhibits long-range off-diagonal long-range order and is characterized by a non-zero complex order parameter $\langle \hat{b} \rangle$.

Fascinatingly, the SF-MI transition through the tip of the lobes, induced by varying t/U (and indicated by the red dashed arrow in fig. 4.1(a)), is a special multicritical point at which a "hidden" particle-hole symmetry[1] is restored and belongs to the universality class of the $(d+1)$ classical XY model (Campostrini et al., 2001, Fisher et al., 1989), where $\nu = \nu^{XY}_{d+1}, z = 1$. This particle-hole symmetry implies that particle and hole excitations occur in equal numbers. Meanwhile, the generic transition crossing of the Mott lobe either at constant t/U or constant μ/U (that does not cross the tip) however, is mean field in nature (Fisher et al., 1989) and traversing an upper (lower) branch of a given Mott Lobe, results in only particle (hole) excitations.

[1] We say that this symmetry is "hidden" since it is not explicit in the Hamiltonian in eq. 4.2.1

n_i	$E(\mu,\delta\mu_i=-\Delta,n_i)$	$E(\mu,\delta\mu_i=\Delta,n_i)$
0	0	0
1	$-\mu+\Delta$	$-\mu-\Delta$
2	$-2\mu+U+2\Delta$	$-2\mu+U-2\Delta$

Table 4.1: Energy per site at the extreme values of disorder strength, Δ with no hopping terms.

4.2.2 The effect of disorder

Now let us consider the effects of bounded uncorrelated disorder in the form of a random on-site chemical potential which amounts to the modification:

$$\mu \to \mu + \delta\mu_i \tag{4.2.4}$$

in eq. 4.2.1, where $\delta\mu_i$ is uniformly distributed in the interval $[-\Delta,\Delta]$. Once again, we turn to the $t=0$ limit for insight. The Hamiltonian in this case now reduces to:

$$\hat{H}_i = -(\mu+\delta\mu_i)\hat{n}_i + \frac{U}{2}\hat{n}_i(\hat{n}_i-1) \tag{4.2.5}$$

and at different values of n_i for a given site i, there exists a range of possible energy curves $E(\mu,\delta\mu_i,n_i)$ that are bounded above and below by $\delta\mu_i=\pm\Delta$ respectively that can give rise to a new phase in the region:

$$\mu \in [nU-\Delta, nU+\Delta]. \tag{4.2.6}$$

To elucidate this, one simply has to explicitly write out the possible values of $E(\mu,\delta\mu_i,n_i)$ for the different fillings and the bounds of disorder strength as summarised in table. 4.1 and illustrated in Fig. 4.3. Considering the two extreme cases, $\delta\mu_i=\pm\Delta$, we see the boundaries of eq. 4.2.6 are obtained by solving the equation: $E(\mu,n,\pm\Delta)=E(\mu,n-1,\pm\Delta)$. For general disorder strengths, $\delta\mu_i\in[-\Delta,\Delta]$ however, we can solve for the crossover point μ' at which a transition from an occupancy of n to $n+1$ occurs, by equating:

$$E(\mu',\delta\mu_i,n_i) = E(\mu',\delta\mu_i,n_i+1), \tag{4.2.7}$$

to yield:

$$\mu' = n_iU - \delta\mu_i. \tag{4.2.8}$$

Once μ is tuned past μ' the site occupancy increases from n to $n+1$. The special region of eq. 4.2.6 represents a novel BG phase, which is evidently compressible; the density of the system increases continuously from n to $n+1$ as μ is tuned from $nV-\Delta$ to $nV+\Delta$. In the complementary region:

$$\mu_{Mott} \in [(n-1)+\Delta, n-\Delta] \tag{4.2.9}$$

however, we see that a Mott insulator state persists and so the net effect of disorder on the phase diagram is to shrink the Mott regions uniformly by exactly Δ. As in the clean system, introducing a tunnelling into the system via a nonzero t means that the kinetic energy gained can be used to overcome the energy gap, resulting once again in the tapering of the Mott lobes, till it eventually vanishes at a multi-critical point. Naively, one might expect that the regions originally occupied by the MI, would be replaced by a SF but we now know that this scenario is incorrect and instead a

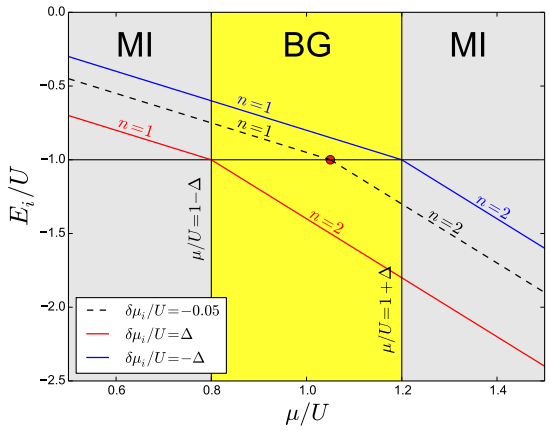

Figure 4.3: Energy for site i of the BH model without hopping but with disorder $\delta\mu_i/U \in [-\Delta,\Delta]$, where $\Delta = 0.2$ as a specific case. This represents the BG phase (yellow region) which exists between the $n=1$ and $n=2$ Mott lobes (grey region) (cf. Fig. 4.1(b)). The red (blue) lines correspond energy profile for maximum (minimum) disorder strength. The dashed line is an example of the energy profile for a general value of $\delta\mu_i$ within the bounds. Depending on the strength of the disorder $\delta\mu_i/U$, site i is either occupied by 1 or 2 bosons at a depending if μ/U is lesser or greater than μ_i'/U indicated by the red circle.

Bose-glass (BG) phase emerges (cf section 4.3).

To obtain a qualitative understanding of the BG phase, we consider the effects of exiting the upper branch of a Mott lobe by increasing the chemical potential at fixed t/U. Fisher (Fisher et al., 1989) argued that when μ/U in eq. 4.2.4 is tuned larger than the upper (lower) branch of the Mott Lobe (see fig. 4.1(b)), excess particles (holes) that are added to the system (on top of the existing Mott Background) must be Anderson localized by the random potential of the disorder: $\{\delta\mu_i\}$. As such, the phase of the system just outside the Mott Lobe cannot be a SF instead we have a peculiar compressible insulator with localized quasiparticles. For sufficiently large μ/U however, the irregular potential is eventually smoothed out as more particles enter the system, eventually admitting a SF phase. A comprehensive summary of the 2d BH phase diagram from stochastic series expansion (SSE) (cf. chp 5) simulations can be found in Fig. 4.4.

4.3 Absence of direct MI-SF transition: Theorem of inclusions

A highly debated issue surrounding the 'dirty-boson' system was if a direct MI-SF transition was possible. Although, Fisher put forth a convincing case that SF cannot generically arise upon exiting a Mott lobe, it did not definitively rule out the possibility of a direct MI-SF transition through the multi-critical points, where the excitation gap exactly vanishes. Curiously, a large number of direct numerical simulations (Krauth et al., 1991, Makivić et al., 1993, Wallin et al., 1994, Pázmándi and Zimányi, 1998, Lee et al., 2001) and some approximate approaches (Zhang and Ma, 1992, Wu and Phillips, 2008, Bissbort and Hofstetter, 2009) observed this unlikely scenario. It was only in 2009 that Pollet et al resolved this controversy by proving the 'Theorem of Inclusions' in all dimensions,

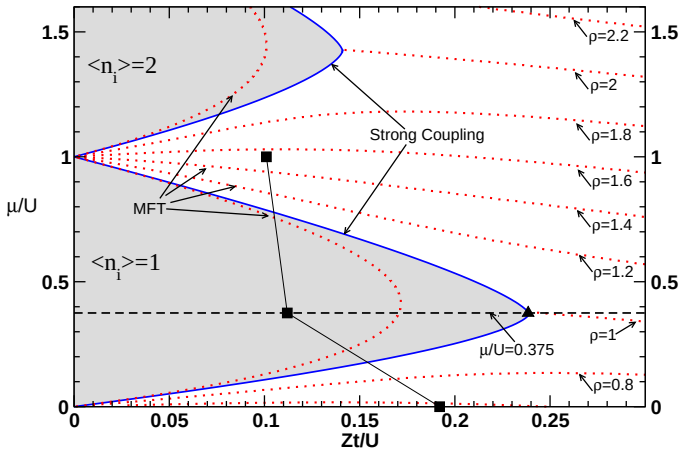

Figure 4.4: The phase diagram of the 2D BH model taken from (Lin et al., 2011). Shaded areas are the Mott insulating phases for zero disorder as determined from strong-coupling expansions in (Elstner and Monien, 1999) and (Niemeyer et al., 1999). The mean-field phase boundaries and constant density profiles for zero disorder are shown as red dotted lines. The dashed line indicates the constant chemical potential $\mu/U = 0.375$. The solid triangle indicates the location of the transition to the Mott phase in the absence of disorder as determined by QMC simulations along the dashed line from (Niemeyer et al., 1999). The three solid squares from bottom up are for the locations of superfluid to Bose-glass transitions with on-site disorder of strength $\Delta/U = 1$ at $\mu/U = 0, 0.375, 1$, respectively, are the results of the QMC simulations of (Lin et al., 2011)

and verified by QMC simulations (Pollet et al., 2009, Söyler et al., 2011).

The theorem of inclusions states that in the presence of generic bounded disorder there exist rare, but arbitrarily large, regions of the competing phase across the transition line. By generic disorder we mean that any particular realization has a non-zero probability density to occur in a finite volume. This theorem immediately implies the absence of a direct SF-MI quantum phase transition. In (Pollet et al., 2009), Pollet et al proved the following two theorems, named theorem I and II. Theorem I states that if the bound on the disorder strength Δ was larger than half the Mott-gap, $E_{g/2}$, then the system must be compressible. In short, if

$$\Delta_c > E_{g/2} \tag{4.3.1}$$

then the transition is to the BG phase and not the MI. Meanwhile, theorem II states that the system must have non-zero compressibility on the SF-I critical line and in its neighborhood in the presence of on-site disorder potentials. Together, theorem I and II proved that a direct SF-MI transition was not possible, putting an end to nearly two decades of controversy.

4.4 General results from scaling theory

Before pressing on, we turn to scaling theory to derive some general results for the insulator-conductor transition of the BH model. Scaling theory (Continentino, 2011, Stanley, 1999, 1987) is a powerful tool that predicts universal scaling relations as a function of proximity to a QCP (of a continuous phase transition) which we denote by $\delta \sim |\lambda - \lambda_c|$, where λ is a generic tuning parameter and λ_c is

the critical point. Remarkably, the heart of it lies in the simple assumption of two diverging length scales (for quantum systems),

$$\begin{aligned} \xi &\sim \delta^{-\nu} \\ \xi_\tau &\sim \delta^{-\nu z}, \end{aligned} \tag{4.4.1}$$

which defines the critical exponents ν and z. A feature of this is that dimensionful observables of a system near a continuous QCP then exhibits scale invariance. Consider the free energy density of the system defined in the $T = 0$ thermodynamic limit:

$$f(\mu, J) \equiv -\lim_{\beta\to\infty}\lim_{L\to\infty}\frac{1}{\beta L^d}\ln Z, \tag{4.4.2}$$

where $Z = \mathrm{Tr}(e^{-\beta\hat{H}})$ is the partition function and N is the spatial dimension of the system, is a homogeneous function. Using a path integral representation, it is trivial to see that $\beta \equiv L_\tau = 1/k_B T$ plays the role of an extra imaginary time dimension. Upon inspection of eq. 4.4.1, we see that there exists an anisotropy in the scaling between space and time. Consequently, under an arbitrary length scale transformation of b such that $L \to L' = bL$ and $L_\tau \to L'_\tau = b^z L'_\tau$, the singular part of the free energy, f_s is a homogeneous function that satisfies the following relation (Fisher et al., 1989):

$$f_s(\delta) \sim b^{-(d+z)} f_s(b^{1/\nu}\delta), \tag{4.4.3}$$

which for the standard choice $b^{1/\nu}\delta = 1$ implies that:

$$f_s(\delta) \sim \delta^{\nu(d+z)}. \tag{4.4.4}$$

By convention, α defines the critical exponent for the free energy such that $f_s \sim \delta^{2-\alpha}$ and reconciliation with eq. 4.4.4 reproduces the quantum hyper-scaling relation:

$$2 - \alpha = \nu(d + z), \tag{4.4.5}$$

in comparison to the classical hyper-scaling relation:

$$2 - \alpha = \nu d. \tag{4.4.6}$$

In quantum systems then, the quantity $d_{eff} = (d + z)$ plays the role of an effective dimensionality.

4.4.1 Compressibility and Superfluid condensate density

Scaling forms for other physical observables can be derived directly from eq. 4.4.4. For instance, choosing the chemical potential as the tuning parameter such that $\delta = \mu - \mu_c$, is is easy to show by simple differentiation that the singular part of the compressibility: $\kappa_s \equiv \partial\rho/\partial\mu = -\partial^2 f/\partial\mu^2$ scales as:

$$\kappa_s \sim \delta^{v(d+z)-2}. \tag{4.4.7}$$

Moreover at criticality, the disorder averaged unequal time green's function defined by:

$$G(r,\tau) \equiv \overline{\langle \hat{a}_r(\tau)\hat{a}_0^\dagger(0)\rangle}, \tag{4.4.8}$$

obeys a power law decay which introduces the anomalous critical exponent, η through the expression:

$$G(r,\tau) \sim \frac{1}{r^{d+z-2+\eta}} g(r/\xi, \tau/\xi^z). \tag{4.4.9}$$

Noting that lengths scale as $\delta^{-\nu}$ and that the order parameter $\langle \hat{a} \rangle$ by definition scales as δ^β, where β is its critical index, we expect that $G(r,\tau) \sim \delta^{2\beta}$. And so ensuring that the dimensionality of the LHS and RHS of eq. 4.4.9 remains consistent, yields the following scaling relation:

$$2\beta = \nu(d + z - 2 + \eta). \tag{4.4.10}$$

Additionally, one can also define a Superfluid density, ρ_s to further distinguish the insulating and SF phase. It is a global quantity that is not accessible by trivial derivatives of the singular free energy. Instead, it is formally related to the change in free energy, Δf_x arising from a spatial phase twist (Fisher et al., 1973) and measures the spatial stiffness of the phase of the SF order parameter: $\langle \hat{a} \rangle$. As such, it can be treated as a rescaled helicity modulus Υ through the definition: $\rho_s = \frac{m^2}{\hbar^2}\Upsilon$. Following Weichman (Weichman, 2008), this energy correction works out to be

$$\Delta f_x = \frac{(\Upsilon)}{2\beta V} \int_0^\beta d\tau \int d^d x |\nabla \phi(x,\tau)|^2, \tag{4.4.11}$$

where $\beta = 1/k_B T$, V is the volume and τ represent imaginary time. $\phi(x,\tau)$ is the phase of the order parameter. $\Delta f_x \sim \delta^{\nu(d+z)}$ (cf eq. 4.4.4) and assuming that the spatial twist is a relevant perturbation then it generates a singular correction so that we can write $\nabla\phi \sim \delta^\nu$. Simple dimensional analysis then tells us that

$$\rho_s \sim \delta^{\nu(d+z-2)}. \tag{4.4.12}$$

Analogously, one can also compute the change in free energy associated with a twist in imaginary time (Fisher et al., 1989), Δf_τ. The helicity modulus associated with this energy change translates directly to the total compressibility, κ_t, of the system. Following (Weichman and Mukhopadhyay, 2007) once more, we can write this as

$$\Delta f_\tau = \frac{\kappa}{2\beta V} \int_0^\beta d\tau \int d^d x (\partial_\tau \phi)^2, \tag{4.4.13}$$

but in this case once again assuming that imaginary time twist is a relevant perturbation, then $\partial_\tau \phi \sim \delta^{-z\nu}$ which means that the compressibility scales as:

$$\kappa_t \sim \delta^{\nu(d-z)} \tag{4.4.14}$$

so as to ensure that eq. 4.4.13 remains dimensionally consistent with eq. 4.4.4.

4.5 Universality class of the SF-BG transition

Determining the universality class of a continuous QPT in general requires knowledge of at least three critical exponents, which can then be used to obtain the remaining exponents using scaling relations such as eq. 4.4.10 and eq. 4.4.5. For disordered systems, obtaining exact values for the critical exponents are especially challenging, however several bounds for the exponents: ν, η and z for the dirty-boson system exist and the derivations of these relations can be found below.

4.5.1 The Harris criterion: lower bound on ν

The Harris criterion (Harris, 1974), a long-standing result in disorder physics is represented by the inequality:

$$\nu \geq \frac{2}{d}, \tag{4.5.1}$$

where d is the dimensionality of the system, which when satisfied dictates that the effect of disorder is an irrelevant perturbation (in the renormalization group (RG) sense) and the critical properties of the clean system persists. When violated however disorder is now relevant and new disorder-induced physics can arise . One possible scenario is that under a coarse graining procedure, the RG flow of the disorder strength approaches a new fixed point that yields new critical exponents that satisfies the Harris criterion. An example of this is the classical 3D Ising model with site diultion (Ballesteros et al., 1998). Alternatively, the RG fixed points can be characterized by infinite disorder strength resulting in exotic exponential (activated) scaling (Fisher, 1992) instead of the usual power law scaling relations of thermodynamic observables. In the latter case, a smearing of an otherwise sharp phase transition (Vojta, 2006) can result, an example being the heat capacity of the McCoy and Wu model (McCoy and Wu, 1968), a special variation of 2d random-bond Ising model that surprisingly has an exact solution.

The derivation of the Harris criterion (Cohen, 1985) starts with the assumption that in a material (at finite temperature) with uncorrelated bond disorder, there exists a unique critical point, T_c at which a diverging correlation length: $\xi \sim (T - T_c)^{-\nu}$ can be defined. At any temperature, T the system can be broken up into independent regions of size ξ comprising of $\sim \xi^d$ bonds in d-dimensions. Furthermore, each block is expected to yield a unique critical temperatures T_c and so the statistical fluctuations of the distribution of the mean of T_c is inversely proportional to the square root of the number of bonds, i.e.:

$$\delta T_c \sim \xi^{-d/2}. \tag{4.5.2}$$

Writing the distance to the unique critical point as:

$$\Delta T \equiv T - T_c \sim \xi^{-1/\nu}, \tag{4.5.3}$$

Harris argued that a sharp transition can only occur if the fluctuations shrink more rapidly than ΔT as ξ approaches infinity, i.e.

$$\delta T_c / \Delta T = \xi^{1/\nu - d/2} \tag{4.5.4}$$

as $\xi \to \infty$. To this end, we require the exponent in eq. 4.5.4 has to be negative. This yields the

Harris criterion of eq. 4.5.1 which establishes a a lower bound on the critical exponent, ν

$$\nu \geq 2/d. \tag{4.5.5}$$

Note that while we have seemingly derived a criteria for sharp transitions with the same clean critical exponents, the Harris criterion actually bears deeper implications. When violated it tells us that the critical properties must change in some way, i.e. either smearing or new critical exponents perhaps. Although the Harris criterion was originally formulated for uncorrelated disorder, this result was generalized to correlated disorder as well. It was further extended by Chayes et al (Chayes et al., 1986) and was shown to be applicable to systems without a "pure" analogue such as in percolation and Anderson location phase transitions, as long as a correlation length: $\xi \sim |\lambda - \lambda_c|^{-\nu}$ could be defined. λ in this case, quantifies the strength of the disorder and λ_c is the critical point beyond which a disorder-induced phase arises.

4.5.2 An upper bound on: η

The equal space green's function can be related to the single-particle density of states, $\rho_1(\epsilon)$ via the formula (Bruus and Flensberg, 2004):

$$\bar{G}(r=0,\tau) = \int_0^\infty d\epsilon e^{-\epsilon|\tau|}\rho_1(\pm\epsilon), \tag{4.5.6}$$

where the sign of ϵ depends on the sign of τ. In what follows, we will derive the scaling behaviour of $\rho_1(\epsilon)$ by considering its asymptotic properties at large τ. First of all, since the excitations in BG phase are localized, the density of states is a constant at low energy. This means that upon evaluating the integral in eq. 4.5.6 in the $\epsilon = 0$ limit yields the following asymptotic long time behaviour:

$$\lim_{\tau\to\infty} \bar{G}(r=0,\tau) \sim \frac{1}{\tau}\rho_{1,BG}(0), \tag{4.5.7}$$

having dimensions of $1/\tau$. Moreover, at the transition and noting that τ scales like r^z, we can deduce from eq. 4.4.9 that

$$\begin{aligned}\bar{G}(r=0,\tau) &\sim \tau^{-(d+z-2+\eta)/z}\tilde{g}(\tau/\xi^z) \\ &= \frac{1}{\tau}\tau^{-(d-2+\eta)/z}\tilde{g}(\tau/\xi^z).\end{aligned} \tag{4.5.8}$$

As highlighted in eq. 4.5.7, the long time behaviour of $\bar{G}$ has to scale as $1/\tau$ and in order for this to be consistent with eq. 4.5.8, we require that the long time behaviour of the scaling function, i.e. $lim_{x\to\infty}\tilde{g(x)}$ scales as $x^{+(d-2+\eta)/z}$ so that the extra τ dependencies cancel out exactly, leaving us with the expression:

$$\bar{G}(r=0,\tau) \sim \frac{1}{\tau}\xi^{2-d-\eta}. \tag{4.5.9}$$

A quick comparison with eq. 4.5.7 leads us to concludes that:

$$\rho_1(0)_{BG} \sim \xi^{2-d-\eta}. \tag{4.5.10}$$

This further tells us that generally at the transition, and at finite energy, ϵ then we have:

$$\rho_1(\epsilon)_{BG} \sim \epsilon^{(d-2+\eta)/z}, \tag{4.5.11}$$

since $\xi \sim \epsilon^{-1/z}$.

Now, in the SF phase, we expect that $\lim_{\tau\to\infty} \bar{G}(r=0,\tau) = M^2$, where $M = \langle \hat{a} \rangle$ is the order parameter. Comparing this with eq. 4.5.6 requires that right at the transition, the SF density of states must be proportional to a delta function in energy $\delta(\epsilon)$, i.e.:

$$\rho_1(\epsilon)_{SF} = M^2\delta(\epsilon), \tag{4.5.12}$$

due to enhanced fluctuations of the condensate. Physically speaking then, one expects that as the SF-BG transition is approached from the BG phase, that $\rho_1(\epsilon)_{BG}$ ought to diverge at $\epsilon = 0$ to match $\rho_1(\epsilon)_{SF}$. In order for this to hold, we must at least have

$$\eta \leq 2 - d \tag{4.5.13}$$

thereby establishing an upper bound for η.

4.5.3 The dynamic critical exponent z

One of the central long-standing results from Fisher et al's seminal work (Fisher et al., 1989) is the exact relation $z = d$ in any dimension, d, for the SF-BG transition. To understand this, one only needs to recall the scaling relation for the total compressibility in eq. 4.4.14, $\kappa_t \sim |\mu - \mu_c|^{\nu(d-z)}$ and the fact that both the SF and BG phases must have a matching finite non-zero compressibility right at the transition. This constrains $z = d$. For completeness however, we shall rule out the other possibilities as well. Suppose we made the assumption $z > d$, implying a diverging compressibility so that $\kappa_t \sim \kappa_s$. Comparing eq. 4.4.14 and eq. 4.4.7 then yields the scaling relation:

$$\nu z = 1, \tag{4.5.14}$$

which in combination with our original assumption $(z > d)$ implies that:

$$\nu < \frac{1}{d}. \tag{4.5.15}$$

However this immediately violates the inequality of Chayes et al that $\nu \geq 2/d$ which was earlier mentioned in section 4.5.1. In light of this contradiction, the assumption $z > d$ must be false. On the other hand, the scenario $z < d$ would require a vanishing compressibility precisely at $\delta = 0$, corresponding to a finite energy gap. Bearing in mind that the SF and BG phase both have finite compressibility at both sides of the critical point, one would expect that this sudden opening of a gap is physically implausible. This then leaves us with the the most likely conclusion $z = d$ which for many decades has been left unchallenged until recently, where the scenario $z \neq d$ has been numerically observed.

To understand how the scenario $z \neq d$ can arise, we have to point out possible flaws in the earlier arguments. A subtle point is that Fisher's argument makes the assumption that the twisted boundary

conditions in both spatial and imaginary time directions generate relevant perturbations and as such, the twists result in singular corrections, i.e. $\nabla\phi(x,\tau) \sim \xi^{-1} \sim \delta^{\nu}$ and $\partial_\tau\phi(x,\tau) \sim \xi^{-\nu z} \sim \delta^{\nu z}$. Upon closer inspection, Weichman (Weichman and Mukhopadhyay, 2007) found this to be the case only for spatial twists because it generates relevant symmetry breaking terms in the Lagrangian. This validates the usual scaling relations for the condensate density. On the other hand, imposing a twist in imaginary time twist: ω_0 only results in a trivial shift of the chemical potential: $\mu \to \mu - i\omega_0$. This is considered an irrelevant perturbation and does not justify the inclusion of singular corrections. As a result, the relation $\partial_\tau\phi(x,\tau) \sim \delta^{\nu z}$ no longer holds and the relation $\kappa \sim \delta^{\nu(d-z)}$ breaks down as well. Instead of eq. 4.4.13, the change in free energy resulting from an imaginary time twist is given by:

$$\delta f_\tau \sim f^0(J,\mu - i\omega_0) - f^0(J,\mu_0), \tag{4.5.16}$$

where $f^0(J,\mu)$ is the free energy with periodic boundary conditions. All contributions to κ therefore come from f^0 which has a singular, f_s^0 and analytic contribution, f_a^0. The singular term results in a contribution to the compressibility: $\kappa_{sing}^0 \sim \delta^{-\alpha}$, where quantum hyperscaling (see eq. 4.4.5) dictates that $\alpha = 2 - (d+z)\nu$. This vanishes under the condition that $\alpha < 0$ or $\nu > \frac{2}{d+z}$ which is guaranteed by the inequality of eq. 4.5.1, $\nu \geq \frac{2}{d}$. We therefore see that the compressibility is dominated by a remaining analytic contribution instead. This conclusion makes no statements about z and therefore leaving it unconstrained, providing an explanation for the unconventional values of z observed in the literature.

4.6 Numerical studies of z

4.6.1 Apriori assumptions of z

Let us highlight the inherent difficulties in extract critical properties from simulations numerical simulations and the importance of apriori knowledge of z, which emphasizes the importance of the exact relation $z = d$. As an example, let us consider the finite-size scaling form for the superfluid density:

$$\rho_s(\delta,L,\beta) \sim L^{-(d+z-2)}\tilde{\rho}(L^{1/\nu}\delta,\beta/L^z), \tag{4.6.1}$$

where $\tilde{\rho}$ is a scaling function and $\delta = \mu - \mu_c$. The quantity $\alpha_\tau \equiv \beta/L^z$ is referred to as the aspect ratio of the simulation, which can be set in simulations via the temperature β, i.e. the size of the $(d+1) - th$ dimension of the equivalent classical model. Once z is known, it is possible to fix α_τ apriori for all simulation sizes L. Now since the numerical effort increases with α_τ, it is beneficial to pick a smaller aspect ratio. However this has to be balanced by a sufficiently large β so as to minimize finite temperature effects. Typically, we find in the literature: $\alpha_\tau \in [0.2,1]$ is used.

Upon picking an aspect ratio, the scaling function immediately reduces to a univariate function. In this situation, a series of plots of the quantity: $L^{d+z-2}\rho_s(\delta,L)|_{\alpha_\tau}$ for different system sizes L, versus μ should cross exactly at the true thermodynamic critical point, $\mu_=\mu_c$. This point is system size independent and at which the scaling function evaluates to: $\tilde{\rho}(0,\alpha_\tau)$. Alternatively, one could also observe data collapse for an appropriate value of the critical exponent ν, when plotting $L^{-(d+z-2)}\rho_s(\delta,L)|_{\alpha_\tau}$ versus $L^{1/\nu}\delta$ for different L's.

Most simulations for the SF-BG transition have adopted either strategies and assumed $z = d$ when

determining the critical properties of the system and are essentially self-consistent checks for the scaling $z = d$. It becomes clear that if z is instead treated as undetermined as suggested by Weichmann (Weichman and Mukhopadhyay, 2007), then the above analysis no longer holds and much more complicated. For instance, we now have a function of two variables and even locating the critical point is no longer trivial. This therefore brings into question a plethora of earlier results in the literature and emphasizes the need for unbiased analysis that make no assumptions on z.

4.6.2 Recent estimates of z

The study of Priyadarshee et al (Priyadarshee et al., 2006), which used path-integral Monte-Carlo (PIMC) to simulate the two-dimensional disordered hardcore boson model (Priyadarshee et al., 2006) produced the numerical estimate: $z \sim 1.4(5)$. The simulations however were fixed at relatively high temperatures of: $\beta = 1/T = L$ so that impressively large system sizes of up to $L = 96$ could be simulated. Since the aspect ratio was not fixed, finite temperature effects may have not been properly accounted for. Furthermore, very few disorder realizations ($\sim 50 - 100$) were used, which leads one to wonder if the average effects of disorder were amply taken into consideration. It is entirely likely that statistically less probable disorder configurations were unsampled, thereby resulting in systematic errors. Most recently, an independent calculation of the critical properties of this exact system were performed using the stochastic series expansion (SSE) and found a different estimate of $z = 1.8(5)$ instead (Álvarez Zúñiga et al., 2014). An analysis of the distribution of the superfluid stiffness showed signs of self-averaging as well.

In 2012, a state-of-the-art PIMC 2d calculation by Meir et al (Meier and Wallin, 2012) produced the first unbiased estimate of $z = 1.80(5)$ for the SF-BG transition. The simulations were performed on an effective (d+1)-dimensional classical equivalent of a link-cluster model that can be derived from quantum rotors via the Villian transformation (Villain, J., 1975). No assumptions were made on the value of z in the simulations. To this end, they constructed a time scale: L_τ, which was the location of the maximum of the quantity: $\langle W^2 \rangle / L\tau^2$ where $\langle W^2 \rangle$ is the squared winding number of the system and determined z by assuming: $L_\tau^* \sim L^{-z}$. This approach was inspired by an earlier work where a similar argument was used to determine the classical critical exponent of the 3D XY model with columnar disorder (Vestergren et al., 2004).

Recent 3d QMC results for a silte-diluted anisotropic spin-1 heisenberg model (Yu et al., 2012b,a) however have found: $z = 3.01$, in agreement with fisher's $z = d$ result. A natural physical realization of this quantum model was found in the quantum magnet Br-DTN (Yu et al., 2012b, 2010), with disorder introduced via doping of magnetic Ni^{2+} sites with non-magnetic Br ions. The simulations were carried out at low enough temperatures so as to allow unbiased estimate for z. Interestingly, a similar simulation protocol on the field induced transition in site-diluted spin-gapped antiferromagnets (Yu et al., 2008) in 2d found $z = 2.0(1)$.

4.7 This thesis

In light of the conflicting results highlighted in section 4.1 and section 4.6.2, our work presents results from state of the art large-scale QMC simulations on **two** different quantum models in 2d making no assumptions on z. In contrast to previous work in the literature, we perform simulation on the

unadulterated quantum mechanical Hamiltonian instead of mapping it on to an effective classical problem. The first model consists of the QR model in the strong disorder scenario, i.e. $\Delta/U = 1/2$ at $\mu/U = 0$. In this regime, the Mott Lobes completely disappear without the complication of special symmetries at multi critical points, and only the generic BG-SF transition remains. The phase diagram then greatly simplified as schematically shown in fig. 5.7. The quantum parameter in this case is given by the tunnelling term in the Hamiltonian. The second model is a 2D hardcore boson model as treated in (Priyadarshee et al., 2006) with disorder modelled as random on-site chemical potential. This can be equivalently expressed as a 2D XY-model with random transverse field and is capable of reproducing the SF-BG transition. The strength of the disorder is used as a tuning parameter in this case. Both of these models and their properties are discussed in Appendix 5.A. Since I was responsible for the simulations on the hardcore version of this model, a brief exposition of the QMC technique used will be outlined in chapter 5, before reverting to our article.

CHAPTER 5

QUANTUM MONTE CARLO TECHNIQUE

In this chapter, we present a brief exposition of the stochastic series expansion (SSE) which was used to obtain results for the disordered quantum XY model. A comprehensive review including pseudo-code of the base method for the Heisenberg model can be found in (Sandvik, 2010).

5.1 The Stochastic Series Expansion

The stochastic series expansion (Sandvik and Kurkijärvi, 1991) is a quantum Monte Carlo method that samples the partition function:

$$Z = \mathrm{Tr}\left[e^{-\beta\hat{H}}\right], \tag{5.1.1}$$

where $\beta = 1/(k_B T)$ sets the temperature of the system. Assuming that the Hamiltonian can be decomposed into M terms, i.e.

$$\hat{H} = \sum_{i=1}^{M} -\hat{H}_i, \tag{5.1.2}$$

and expressing the exponential as an infinite series, eq. 5.1.1 can be rewritten using an appropriate basis $\{|\alpha\rangle\}$as:

$$Z = \sum_{\alpha}\langle\alpha| \sum_{n=0}^{\infty} \frac{(\beta)^n}{n!} \left(\sum_{i=1}^{M} \hat{H}_i\right)^n |\alpha\rangle. \tag{5.1.3}$$

Note that the Hamilton is decomposed such that its constituents, $\left\{\hat{H}_i\right\}$ can only bring about a transformation among the basis states, i.e. $\hat{H}_i|\alpha\rangle = |\beta\rangle, \forall i$ where supposing $|\alpha\rangle$ is a basis state, then $|\beta\rangle$ can only be a basis state and not a superposition of basis states.

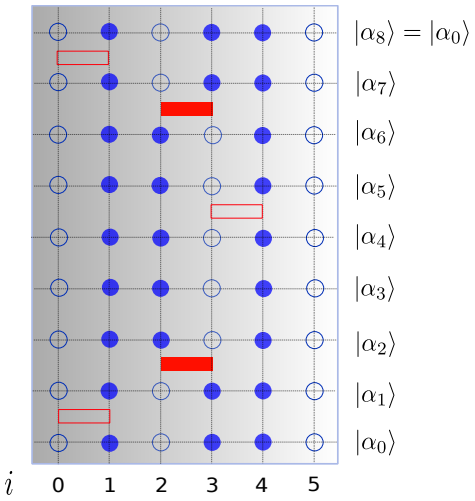

Figure 5.1: Visual representation of a possible configuration of a six-site $s = 1/2$ spin chain with parameters: $n = 5, L = 8$. Filled and unfilled circles represent spin up and down basis states respectively. Filled and unfilled rectangular boxed represent possible H_{l_i} operators that are off-diagonal and diagonal in the basis respectively. The vertical dimension is the expansion order of the operator string with fixed-length L, while the horizontal dimension represents the spatial degrees of freedom.

One may also obtain an equivalent expression for eq. 5.1.3, by rewriting it as a summation over all possible permutations of possible operator strings: S_n comprising terms from $\{\hat{H}_{l_i}\}$, where $l_i \in [1, M]$ and varying lengths n:

$$Z = \sum_{\alpha} \sum_{n=0}^{\infty} \sum_{S_n} \frac{(\beta)^n}{n!} \langle \alpha | \prod_{i=1}^{n} \hat{H}_{l_i} | \alpha \rangle = \sum_{\alpha} \sum_{n=0}^{\infty} \sum_{S_n} W(\alpha, S_n) \tag{5.1.4}$$

where the replacement $W(\alpha, S_n) = \frac{(-\beta)^n}{n!} \langle \alpha | \prod_{i=1}^{n} \hat{H}_{l_i} | \alpha \rangle$ has been made and represents the weight of the configuration (α, S_n). Since we are calculating the trace, only operator strings that leave the bra: $|\alpha\rangle$ in eq. 5.1.4 unchanged contribute to the partition function. In practice, it is numerically convenient to work with non-fluctuating strings. This is done by fixing the length of the operator string at some sufficient large value: L and augmenting strings of order $n (< L)$ with $L - n$ identity operators. A schematic graphical representation of the SSE configuration in the fixed string length representation is shown in fig. 5.1. While this may seem like an approximation, it is important to note that during the equilibration phase of the simulations, L is enforced to be larger than n by a sufficient margin such that $n < L$. Empirically, n eventually plateaus and the stochastic series expansion remains numerically exact. Taking into account equivalent permutations of a given operator string of length n, i.e. $\frac{L!}{(L-n)!n!}$, the final expression for the partition function takes the form

$$Z = \sum_{S_L} \sum_{\alpha} \frac{\beta^n (L-n)!}{L!} \langle \alpha | \prod_{i=0}^{L-1} H_{l_i} | \alpha \rangle = \sum_{S_L} \sum_{\alpha} W(\alpha, S_L), \tag{5.1.5}$$

where $W(\alpha, S_L)$ represents the weight of the configuration. By inserting $L - 1$ closure relations using

the α-basis, eq. 5.2.3 for the partition function can be expressed in an analogous path integral form:

$$Z = \sum_{S_L}\sum_{n} \frac{\beta^n (L-n)!}{L!} \prod_{i=1}^{L} \left\{ \sum_{\alpha_i} \langle \alpha_i | \hat{H}_{l_i} | \alpha_{i-1} \rangle \right\} = \sum_{S_L}\sum_{n} \sum_{\{\alpha(i)\}} \frac{\beta^n (L-n)!}{L!} \prod_{i=1}^{L} \tilde{W}(\alpha_i), \tag{5.1.6}$$

where periodicity of the trace enforces: $|\alpha_L\rangle = |\alpha_0\rangle$ and $\tilde{W}(\alpha_i) = \langle \alpha_i | H_{l_i} | \alpha_{i-1} \rangle$ is the vertex weight depending on the operator H_{l_i}, and the states at consecutive propagation level $i-1$ and i. For operators acting on a particular bond, a vertex comprises of a single operator and four spin states, called the legs of the vertex, as shown in fig. 5.3.

It is important to note however the extra dimension in the SSE represents the expansion order of the series and is not to be confused with that of imaginary time: β, when using a path integral approach. This also raises another salient point, i.e. that the SSE does not suffer from any discretization errors.

5.1.1 Derivation of weights

As an instructive example, let us derive the weights for the spin-1/2 disordered 2D quantum XY model, defined by the Hamiltonian:

$$\hat{H} = -\frac{1}{2} \sum_{\langle i,j \rangle} \left(\hat{S}_i^+ \hat{S}_j^- + \hat{S}_j^- \hat{S}_j^+ \right) - \sum_i h_i \hat{S}_i^z, \tag{5.1.7}$$

where $h_i \in [-h, h]$ is a uniformly distributed random field[1], $\hat{S}^+, \hat{S}^-$ are the spin ladder operators and $\hat{S}^z$ is the usual z- spin component such that $[\hat{S}_i^+, \hat{S}_j^-] = 2\hat{S}^z \delta_{ij}$. The standard notation that $\langle i,j \rangle$ refers to nearest neighbour sites applies here as well. Note that it is the strength of the disorder, h that serves as our tuning parameter and that the system of eq. 5.1.7 is at half filling on average. We choose the S^z-basis and the usual bond decomposition of the Hamiltonian and further categorize them according to whether they are diagonal or non-diagonal in the chosen basis, i.e. in place of eq. 5.1.7, we write

$$\hat{H} = \sum_b -H_{1,b} - H_{2,b}, \tag{5.1.8}$$

such that:

$$H_{1,b} = C_b + h'_{i(b)} S^z_{i(b)} + h'_{j(b)} S^z_{i(b)} \tag{5.1.9}$$

$$H_{2,b} = \frac{1}{2} \left(S^+_{i(b)} S^-_{j(b)} + S^-_{i(b)} S^+_{j(b)} \right). \tag{5.1.10}$$

The first index in $H_{p,b}$ indicates if we have a diagonal or off-diagonal operator in the chosen basis. $p = 1 \implies$ diagonal and $p = 2 \implies$ off-diagonal. $(i(b), j(b))$ denotes the nearest neighbour sites belonging to bond b and the field: $h'_{(i(b))} = h_{i(b)}/(2d)$ is renormalized due to an over-counting in the bond representation. C_b is an arbitrary positive constant that can be added with impunity to ensure a semi positive-definite weight for diagonal operators.

For a spin-1/2 system, there are a total of eight possible vertices: $\tilde{W}(\alpha_i) \in \{W_{b,v}\}$, although only

[1] Note that operationally, we enforce the average value of the field to be precisely zero by calculating the average: $h_{av} = \frac{1}{N}\sum_i h_i$ and then subtracting it explicitly from the field at each site, i.e. $h_i \to h_i - h_{av}$.

six of which (for a given bond, b) will yield non-vanishing weights for the 2d quantum XY model:

$$W_{b,1} = \langle \circ \times |H_{2,b}| \times \circ \rangle = \frac{1}{2} \tag{5.1.11}$$

$$W_{b,2} = \langle \circ \times |H_{1,b}| \circ \times \rangle = \frac{h}{2d} + \epsilon_b - \frac{1}{2}\left(h_{i(b)} - h_{j(b)}\right) \tag{5.1.12}$$

$$W_{b,3} = \langle \times \times |H_{2,b}| \circ \circ \rangle = 0 \tag{5.1.13}$$

$$W_{b,4} = \langle \circ \circ |H_{1,b}| \circ \circ \rangle = \frac{h}{2d} + \epsilon_b - \frac{1}{2}\left(h_{i(b)} + h_{j(b)}\right) \tag{5.1.14}$$

and

$$W_{b,5} = \langle \times \circ |H_{2,b}| \circ \times \rangle = \frac{1}{2} \tag{5.1.15}$$

$$W_{b,6} = \langle \times \circ |H_{1,b}| \times \circ \rangle = \frac{h}{2d} + \epsilon_b + \frac{1}{2}\left(h_{i(b)} - h_{j(b)}\right) \tag{5.1.16}$$

$$W_{b,7} = \langle \circ \circ |H_{2,b}| \times \times \rangle = 0 \tag{5.1.17}$$

$$W_{b,8} = \langle \times \times |H_{1,b}| \times \times \rangle = \frac{h}{2d} + \epsilon_b + \frac{1}{2}\left(h_{i(b)} + h_{j(b)}\right), \tag{5.1.18}$$

where we have set $C_b = h_b + \epsilon_b, \ \ | \ \epsilon_b \geq 0, h_b = h/(2d)$ and $\times$ and $\circ$ represent up and down spins respectively. The reason behind the deliberate inclusion of ϵ_b will be explained in section 5.4.2. Due to the presence of disorder, the weights derived above are bond specific as indicated by the subscript b.

5.2 Observables

Of course, sampling the partition function itself is not useful if we are unable to calculate physical observables. The usual expression for expectation value for a general observable, $\hat{O}$:

$$\langle \hat{O} \rangle = \frac{\mathrm{Tr}\left[e^{-\beta \hat{H}} \hat{O}\right]}{\mathrm{Tr}\left[e^{-\beta \hat{H}}\right]} \tag{5.2.1}$$

is accessible within the SSE formalism if an estimator of $\hat{O}$: $O(\alpha, S_n)$ can be found such that:

$$\langle \hat{O} \rangle = \langle O \rangle_W \equiv \frac{\sum_\alpha \sum_{S_L} O(\alpha, S_L) W(\alpha, S_L)}{\sum_\alpha \sum_{S_L} W(\alpha, S_L)}. \tag{5.2.2}$$

The SSE formalism has been shown to be amenable in calculating a wide variety of observables both diagonal and off-diagonal in the underlying basis and to date, many useful estimators have been derived. For a general understanding, we will only derive a few expressions to give the reader a general idea and simply provide a non-exhauastive list in table 5.1 of other estimators. We refer the interested reader to (Sandvik, 1992, 2010) for details.

5.2.1 Diagonal observables

Diagonal observables are perhaps the easiest to calculate. By direct substitution, the observable expression given by eq. 5.2.1 can be written as:

$$\langle O\rangle = \frac{1}{Z}\sum_{S_L}\sum_{\alpha}\frac{\beta^n(L-n)!}{L!}\langle\alpha|\prod_{i=0}^{L-1}H_{l_i}\hat{O}|\alpha\rangle \tag{5.2.3}$$

Now assuming that the operator: $O = O_d$ is diagonal in the basis such that: $O_d|\alpha\rangle = o(\alpha)|\alpha\rangle$, we obtain the required form in eq. 5.2.2 immediately:

$$\begin{aligned}\langle O\rangle &= \frac{1}{Z}\sum_{S_L}\sum_{\alpha}\frac{\beta^n(L-n)!}{L!}\langle\alpha|\prod_{i=0}^{L-1}H_{l_i}|\alpha\rangle o(\alpha) &(5.2.4)\\ &= \frac{1}{Z}\sum_{S_L}\sum_{\alpha}W_(\alpha,S_L)o(\alpha), &(5.2.5)\end{aligned}$$

making it clear that the estimator for $\hat{O}$ is simply $o(\alpha)$. We can further derive an improved estimator for diagonal expectation values. First let use denote the m-th propagated state as:

$$|\alpha(m)\rangle = \prod_{i=1}^{m}H_{l_i}|\alpha(0)\rangle \tag{5.2.6}$$

Due to the periodicity of the trace however, there is nothing special about the very first state $|\alpha\rangle = |\alpha_0\rangle$ and taking into account all L cyclic permutations of the operator string S_L, we can use the following expression

$$\langle\hat{O}\rangle = \frac{1}{L}\langle\sum_{p=0}^{L-1}o(\alpha(p))\rangle_W \tag{5.2.7}$$

instead.

5.2.2 Off-diagonal observables

Obtaining estimators for off-diagonal observables is often a more involved process. As an example, we derive the estimator for the energy and refer the reader to table 5.1 for other examples. We begin by stating the end result, i.e. that the energy of the system: $\langle E\rangle = \frac{1}{Z}\mathrm{Tr}\left[e^{-\beta H}H\right]$ can be calculated using the estimator:

$$\langle E\rangle = -\frac{\langle n\rangle_W}{\beta}, \tag{5.2.8}$$

which is the average number of non-trivial operators in the operator string. To derive this estimator, we simply perform a series expansion on the exponential: $e^{-\beta H}$ in the trace and manipulate it

Description	Observable	Estimator
Energy	$\langle E \rangle$	$-\frac{\langle n \rangle_W}{\beta}$
Specific heat	$\langle C_v \rangle = \frac{\partial \langle E \rangle}{\partial T}$	$\langle n^2 \rangle_W - \langle n \rangle_W^2 - \langle n \rangle_W$
$H_k =$ single term in $\{H_i\}$	$\langle H_k \rangle$	$-\frac{\langle N(k) \rangle_W}{\beta}$
String of ordered terms in $\{H_i\}$	$\langle \prod_{i=1}^{m} H_{k_i} \rangle$	$\frac{1}{(-\beta)^m} \frac{(n-1)!}{(n-m)!} \langle N(k_1,\ldots,k_m) \rangle_W$
Imaginary time-dependent product of diagonal operators	$\int_0^\beta d\tau \langle O_{1d}(\tau) O_{2d}(0) \rangle$	$\langle \sum_{p=0}^{n-1} \sum_{m=0}^{n} \frac{1}{n} \frac{\beta}{n+1} o_1(\alpha(p)) o_2(\alpha(p+m)) \rangle_W$

Table 5.1: Summary of observables and estimators that can be calculated within the SSE. This is a non-exhaustive list of what can be calculated.

appropriately:

$$\langle E \rangle = \sum_\alpha \sum_n \frac{(-\beta)^n}{n!} \langle \alpha | H^{n+1} | \alpha \rangle \times \frac{-(n+1)/\beta}{-(n+1)/\beta} \tag{5.2.9}$$

$$= \sum_\alpha \sum_{n=0}^{\infty} \frac{n+1}{-\beta} \frac{(-\beta)^{n+1}}{(n+1)!} \langle \alpha | H^{n+1} | \alpha \rangle. \tag{5.2.10}$$

Letting $n' = n+1$, we obtain:

$$\langle E \rangle = \sum_\alpha \sum_{n'=1}^{\infty} \frac{n'}{-\beta} \frac{(-\beta)^{n'}}{n'!} \langle \alpha | H^{n'} | \alpha \rangle \tag{5.2.11}$$

$$= \sum_\alpha \sum_{n'=0}^{\infty} \frac{n'}{-\beta} \frac{(-\beta)^{n'}}{n'!} \langle \alpha | H^{n'} | \alpha \rangle, \tag{5.2.12}$$

where we have reindexed n' to start from 0. Because of the n' factor in the front of eq. 5.2.12, letting $n' = 0$ does not contribute to the summation, thereby allowing a reindexing and giving us the desired result of eq. 5.2.8: $\langle E \rangle = -\langle n/\beta \rangle_W$[2].

The specific heat can now be easily calculated by taking a single derivative of $\langle E \rangle$ with respect to temperature. This yields the expression:

$$C_v = \frac{\partial \langle E \rangle}{\partial T} = \langle n^2 \rangle_W - \langle n \rangle_W^2 - \langle n \rangle_W, \tag{5.2.13}$$

[2]Note that the form of the estimator is insensitive to the fluctuating or fixed-length representation. We have just used the fluctuating length representation out of convenience.

almost similar to the fluctuation of the average number of non-trivial operators with the exception of the subtraction of an extra linear term $\langle n \rangle_W$. If the observable of interest happens to be a term in the decomposition in eq. 5.2.3, i.e. that $\hat{O} = \hat{H}_k, \forall k \in [1, M]$, then its estimator can be shown (Sandvik, 1992) to be:

$$\langle \hat{H}_k \rangle = -\frac{1}{\beta} \langle N(k) \rangle_W, \tag{5.2.14}$$

where $N(k)$ is the number of occurrences of H_k in the operator string.

5.3 Other observables

Other nontrivial observables that can be calculated include the superfluid stiffness and the fidelity susceptibility to name a few. The superfluid stiffness is related to the winding number of the system which can be easily calculated by keeping track of the net particle current along a particular axis as described in (Sandvik, 2010). Detailed instructions for calculating the fidelity susceptibility within the SSE formalism can be found in (Albuquerque et al., 2010), where the critical properties of the 2D transverse ising model were successfully reproduced. The fidelity approach was further used to determine the critical points of a spin-1/2 Heisenberg magnet with one-fifth depletion, a model for the CaVO lattice (Schwandt et al., 2009). Other exotic quantities like the Renyi-entropy (Humeniuk and Roscilde, 2012, Hastings et al., 2010) can also be calculated.

5.4 Configuration sampling

To sample the (α, S_L) configuration space with excellent acceptance rates, we use two types of updates, 1. diagonal and 2. directed loop updates. Diagonal updates insert diagonal operators at different levels of $p \in [0, L-1]$ in the operator string and is the only means to increase the number of non-trivial diagonal operators in the operator string. In order to introduce off-diagonal operators, an obvious option is to introduce pairs of off-diagonal operators located at the same bond but different propagation time slices, to preserve the initial and final states. This algorithm is however somewhat antiquated and a more efficient and extensive update scheme can be achieved using directed loops. In our simulations a single MC step consists of one diagonal update followed by N_l directed loops, where N_l is determined self-consistently during the equilibration phase so that on average $\sim 2\langle n \rangle$ vertices are visited. We now elucidate what diagonal and directed loop updates entail.

5.4.1 Diagonal updates

Diagonal updates (Sandvik, 2002) can be achieved at each propagation level: p depending if it is occupied by a non-identity operator or not. If the occupying operator is off-diagonal, we immediately move on to the next propagation level. On the other hand, if it is occupied by a diagonal operator, then we attempt to remove it with probability:

$$P_{b,remove}(H_b \to I_b) = \frac{L - n + 1}{\beta N_b} W_{b,v}, \tag{5.4.1}$$

where $W_b(v)$ is the weight at bond b of vertex type: v. If we encounter an identity operator however, we pick a bond at random and attempt an insertion of a diagonal operator with probability:

$$P_{b,insert}(I_b \to H_b) = \frac{\beta N_b}{L-n} W_{b,v}. \tag{5.4.2}$$

These are the metropolis solutions (Chib and Greenberg, 1995) chosen to satisfy detailed balance: $W(C)P(C \to C') = W(C')P(C' \to C)$ where C, C' are different configurations which have a difference of ± 1 non-trivial operators.

5.4.2 Directed loop updates

To sample strings with off-diagonal operators, we instead make use of the directed loop algorithm (Syljuåsen and Sandvik, 2002), analogous to worm algorithms (Boninsegni et al., 2006). Fig. 5.2 summarises the procedure we are about to describe. In the original directed loop scheme (Syljuåsen and Sandvik, 2002), a loop is constructed by first uniformly choosing at random, any leg, e belonging to a non-trivial vertex as a starting point.

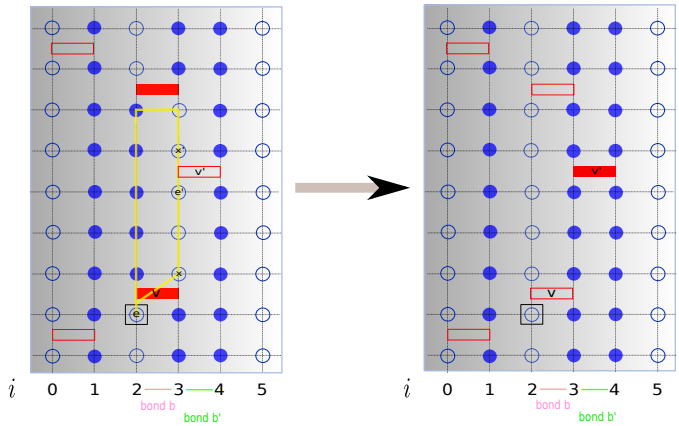

Figure 5.2: (Left) Graphical representation of the path of a directed loop in yellow. (Right) The resulting configuration after implementing changes along path of the loop. While not demonstrated here, one can imagine how directed loops traversing the vertical boundaries can result in a change to $|\alpha_0\rangle$.

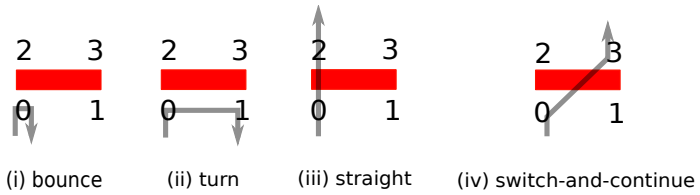

Figure 5.3: The four possible paths of a loop can take during an intra-vertex move. Vertex legs are numbered 0 to 4 accordingly.

We then pick another leg belonging to the same vertex, at random in accordance to a pre-calculated probability table: $p_b(v,e,x)$. This quantity represents the probability of exiting at leg x, assuming

an entrance leg e and that bond b is a vertex of type v. Details on how to calculate $p_b(v,e,x)$ will be provided in section: 5.5 for a Hamiltonian comprising nearest-neighbour bond interactions. Once an exit leg, x is chosen, the loop progresses to the closest vertex, v' that shares a common leg, denoted e', on the same site. A new exit leg,: e' is then chosen according to probability $p_{b'}(v',e',x')$ just like before. This pair of intra- and inter-vertex moves are repeated till the very first leg of the loop is reached. The spins encountered along the path of the loop are then immediately flipped and the vertex type updated accordingly. Typical loops can span the entire extent of the system thereby bringing about a global change in the configuration space. While the operator string length is kept constant during the loop update, it effects change in the configuration space through vertex-type updates as well as modifications of the initial state $|\alpha(0)\rangle$.

5.5 Probability tables

The probability tables can be constructed by ensuring that the fundamental requirement of detailed balance is satisfied (Syljuåsen and Sandvik, 2002), i.e.

$$P(s \to s')W(s) = P(s' \to s)W(s'), \tag{5.5.1}$$

where $P(s \to s')$ is the probability of the transition from configuration s to configuration s' and $W(s)$ is the weight of configuration s. For the procedure outlined in section 5.4.2, one can show that detailed balance is satisfied as long as the following condition is satisfied on each bond b:

$$w_{b,v}(e,x) = w_{b,v'}(x,e). \tag{5.5.2}$$

This states that the weight of the transition, $w_{b,v}(e,x)$, that is brought about by changing states at legs e and x and changes the vertex from v to v' is equal to the weight of the reverse process, $w_{b,v'}(x,e)$, which changes the vertex from v' to v.

In order to ensure that a transition through a vertex always occurs, it is necessary that the sum over all the possible exits legs is equal to the weight of the vertex itself, i.e.:

$$\sum_x w_{b,v}(e,x) = W_{b,v}. \tag{5.5.3}$$

Eq. 5.5.3 can be neatly expressed in graphical form as seen in fig. 5.4. These weights are also related to the probability table mentioned in section 5.4.2 through the relation:

$$p_{b,v}(e,x) = \frac{w_{b,v}(e,x)}{W_{b,v}}. \tag{5.5.4}$$

In total, there are $N_d = N_v \times N_b \times 4 \times 4$ possible weights to solve for subjected to $N_c = 4 \times N_v \times N_b$ constraints, where $N_v \equiv$ number of vertices and $N_b \equiv$ number of bonds. This is therefore an over-specified problem with multiple solutions available (Sandvik, 2002).

To proceed, it is generally accepted though not always true (see (Alet et al., 2005)) that a solution that minimizes the bounce weights is the most efficient choice. This is because bouncing worm trajectories in general cause back-tracking and result in the undoing of earlier changes made to the

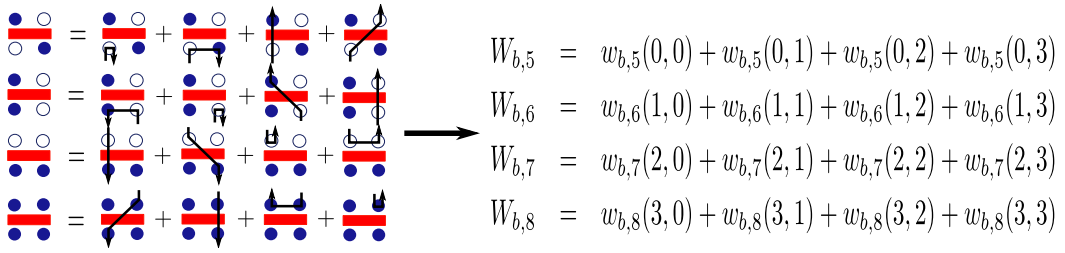

$$
\begin{aligned}
W_{b,5} &= w_{b,5}(0,0) + w_{b,5}(0,1) + w_{b,5}(0,2) + w_{b,5}(0,3) \\
W_{b,6} &= w_{b,6}(1,0) + w_{b,6}(1,1) + w_{b,6}(1,2) + w_{b,6}(1,3) \\
W_{b,7} &= w_{b,7}(2,0) + w_{b,7}(2,1) + w_{b,7}(2,2) + w_{b,7}(2,3) \\
W_{b,8} &= w_{b,8}(3,0) + w_{b,8}(3,1) + w_{b,8}(3,2) + w_{b,8}(3,3)
\end{aligned}
$$

Figure 5.4: Visual representation of a set of related vertices that obey eq. 5.5.3. Detailed balance (see eq. 5.5.2) constrains the vertex matrix to be symmetric. Note that this is one such set out of a total of N_d diagrams, that was generated by picking $v = 6$ and $e = 0$.

SSE configuration. This is counterproductive to the purpose of the directed loop, i.e. to make global changes in the configuration space. To this end, finding a solution of the weights reduces to a linear optimization problem (Alet et al., 2005), where the function we chose to minimize is a superposition of bounce weights over all bonds and vertices,

$$w_{bounce} = \sum_{b=0}^{N_b} \sum_{v=0}^{7} \sum_{e=0}^{3} w_{b,v}(e,e). \tag{5.5.5}$$

subject to the constraints of eq. 5.5.3 and eq. 5.5.2. The set of free constants $\{\epsilon_b\}$ are unconstrained degrees of freedom that can be used during the minimization process. Typically, it is advantageous to further constrain $\{\epsilon_b\}$ to be a small positive number (Sandvik, 2002). The minimization procedure can be carried out very efficiently with the simplex algorithm (Press et al., 2007).

5.6 Equal time Greens functions

For a spin systems, we define the equal time greens function to be:

$$C(r, \tau = 0) = \langle S_0^+ S_r^- \rangle, \tag{5.6.1}$$

which measures the correlation between spins a distance r apart. This quantity can be calculated on-the-fly during the construction of a directed loop with the caveat of single modification (Dorneich and Troyer, 2001). In the standard directed loop (Sandvik, 2002), the start of the loop is chosen to be a random leg on any non-trivial vertex. When calculating greens function however, loops are allowed to start at any point with coordinate (i_o, p_o) in the configuration space, where $i_o \in [0 \ldots N-1]$ and $p_o \in [0, L-1]$. This starting point serves as the reference point. Note that upon insertion, the loop propagates either upwards or downwards with equal probability until the next vertex leg is reached. Even if the reference point belongs to an existing vertex, a direction still has to be sampled.

Specifically for a spin-1/2 system, a measurement of $C(r)$ is obtained by calculating the average number of times the loop crosses the reference level: p_o a distance r away from i_o. For s>1/2 systems, other non-trivial weight factors have to be taken into account (Dorneich and Troyer, 2001). We further note that the calculation of unequal time correlation functions: $\langle S_0^+(0) S_r^-(\tau) \rangle$ are also accessible within the SSE but is much more involved. Details on two equivalent methods can be

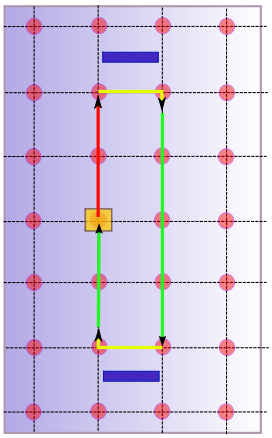

Figure 5.5: Directed loop procedure measuring: $C(r)$. In the loop, a single measurement of $C(r=1)$ is made. The insertion/ reference point: (i_o, p_o) is indicated by the yellow square. Yellow arrows represent intra-vertex moves while green arrows represent inter-vertex move. The red arrow represents the initial direction of the loop, which was chosen with probability half after insertion.

found in (Dorneich and Troyer, 2001) and (Pippan et al., 2009).

5.7 Paper 3: Quantum Critical Scaling of Dirty Bosons in Two Dimensions

Paper 3

Quantum critical scaling of dirty bosons in two dimensions
– *Ray Ng and Erik S. Sørensen*

Phys. Rev. Lett. 114, 255701

DOI: 10.1103/PhysRevLett.114.255701

Calculations: I performed all simulations for the hardcore boson model and produced all the figures.

Manuscript: I wrote approximately 50% the manuscript and produced all the figures. The numerical simulations and results pertaining to the disordered quantum XY model were produced from an original SSE code that I had written myself. Erik S. Sørensen performed all simulations of the quantum rotor model. As such, we were each responsible for the portions of the manuscript addressing the results of our respective models.

In this publication, we set out to answer the following questions pertaining to the quantum rotor model and the hardcore boson model, in the presence of on-site disorder (without apriori assumptions on z in the simulations):

- Where are the exact locations of their critical points ?
- What values of z, ν and η do the models yield?
- Do both the critical exponents obtained from both models agree within errorbars?
- Do both independent models produce a value for ν that satisfies the (quantum) Harris criterion?
- Is Fisher's $z = d$ relation observed?

PRL 114, 255701 (2015) PHYSICAL REVIEW LETTERS week ending 26 JUNE 2015

Quantum Critical Scaling of Dirty Bosons in Two Dimensions

Ray Ng* and Erik S. Sørensen†
Department of Physics and Astronomy, McMaster University, 1280 Main Street West L8S 4M1 Hamilton, Ontario, Canada
(Received 23 January 2015; published 23 June 2015)

We determine the dynamical critical exponent z appearing at the Bose glass to superfluid transition in two dimensions by performing large scale numerical studies of *two* microscopically different quantum models within the universality class: The hard-core boson model and the quantum rotor (soft core) model, both subject to strong on-site disorder. By performing many simulations at different system size L and inverse temperature β close to the quantum critical point, the position of the critical point and the critical exponents, z, ν, and η can be determined *independently* of any implicit assumptions of the numerical value of z, in contrast to most prior studies. This is done by a careful scaling analysis close to the critical point with a particular focus on the temperature dependence of the scaling functions. For the hard-core boson model we find $z = 1.88(8)$, $\nu = 0.99(3)$, and $\eta = -0.16(8)$ with a critical field of $h_c = 4.79(3)$, while for the quantum rotor model we find $z = 1.99(5)$, $\nu = 1.00(2)$, and $\eta = -0.3(1)$ with a critical hopping parameter of $t_c = 0.0760(5)$. In both cases do we find a correlation length exponent consistent with $\nu = 1$, saturating the bound $\nu \geq 2/d$ as well as a value of z significantly larger than previous studies, and for the quantum rotor model consistent with $z = d$.

DOI: 10.1103/PhysRevLett.114.255701 PACS numbers: 67.25.D-, 05.30.Jp, 05.30.Rt, 71.55.Jv

Most familiar quantum critical points (QCPs) are characterized by Lorentz invariance implying a symmetry between correlations in space and time and consequently between the respective correlation lengths $\xi \sim \xi_\tau$ [1]. In turn, the dynamical critical exponent, defined through $\xi_\tau \sim \xi^z$, is simply $z = 1$, such as in the crossing of the special multicritical point of the Bose-Hubbard model [1]. Anisotropic systems where $z \neq 1$, implying different scaling of ξ and ξ_τ, are comparatively less common [1,2]. This quantum critical scaling is particularly intriguing if disorder is present, in which case *nonintegral* values of z have been proposed [3,4]. One model for which it is generally believed that $z \neq 1$ is the Bose glass to superfluid (BG-SF) transition describing interacting bosons subject to disorder, the so-called dirty-boson problem, modeled by the Hamiltonian

$$H_{bh} = -t\sum_{\mathbf{r},\mathbf{e}}(b^\dagger_{\mathbf{r}} b_{\mathbf{r}+\mathbf{e}} + \text{H.c.}) - \sum_{\mathbf{r}} \mu_{\mathbf{r}} \tilde{n}_{\mathbf{r}} + \frac{U}{2}\sum_{\mathbf{r}} \tilde{n}_{\mathbf{r}}(\tilde{n}_{\mathbf{r}} - 1). \tag{1}$$

Here $\mathbf{e} = \mathbf{x}, \mathbf{y}$, and $b^\dagger_{\mathbf{r}}, b_{\mathbf{r}}$ are the boson creation and annihilation operators at site $\mathbf{r}$ with $\tilde{n}_{\mathbf{r}}$ the corresponding number operator. The parameters of the model are the hopping constant t, Hubbard repulsion U, and *site-dependent* chemical potential $\mu_{\mathbf{r}}$, inducing the disorder.

Experimental setups emulating dirty boson physics include optical lattices [5] adsorbed helium in random media [6], Josephson-junction arrays [7], thin-film superconductors [8], and quantum magnets such as doped dichloro-tetrakis-thiourea-nickel(II) (DTN) [9]. For recent reviews, see Refs. [10,11].

The dynamical critical exponent z appearing at the BG-SF transition has proven exceedingly hard to determine. Assuming the validity of the (quantum) Harris criterion for disordered systems $\nu \geq 2/d$ [12], initial theoretical work [13] argued that $z = d$ in *any* dimension. This has intriguing implications since it implies the absence of an upper critical dimension. Although many initial numerical studies [14–19] were consistent with $z = d = 2$, most were biased by implicit assumptions about z, using it to fix the simulation aspect ratio L^z/β. The exponent z was therefore not *truly* independently determined. However, recent theoretical work by Weichman and collaborators [11,20] has challenged the arguments leading to $z = d$ leaving the value of z an open question. A subsequent numerical study [3] of the hard-core version of Eq. (1) found $z = 1.40(2)$, $\nu = 1.10(4)$ while a recent unbiased state-of-the-art study [4] using an effective classical model of Eq. (1) determined a significantly larger value of $z = 1.75(5)$ and $\nu = 1.15(3)$. Both results violate $z = d$. Intriguingly, in three dimensions both numerical [9,19,21] and experimental [22], studies yield evidence for $z = d = 3$, although these numerical estimates cannot be seen as fully unbiased.

At present, the value of z at the dirty-boson QCP along with many of the other exponents most notably ν can therefore best be regarded as ill determined, at least for the fully quantum mechanical model. It is not known to what extent, if any, the relation $z = d$ is violated or if the relation $\nu \geq 2/d$ [12] is satisfied. Here we try to answer some of these questions by performing large-scale simulations on *two* fully quantum mechanical models in two dimensions within the dirty-boson universality class: A hard-core boson model (HCB) modeled as a transverse field *XY*

model and a soft-core quantum rotor model (QR), both subject to strong on-site disorder. In all cases do we find it necessary to use 10^4–10^5 disorder realizations over a large range of temperatures extending down to $\beta = 1024$ for system sizes $L = 12$–32. In contrast to Ref. [3] these dramatically improved statistics allow for a significantly better determination of the critical point of the HCB model. We also note that the use of fully quantum models presents significant advantages over the effective classical model used in Ref. [4]. Finally, through a fully unbiased analysis, without implicit assumptions on z, we find for the first time strong evidence that $z = d = 2$ and that $\nu \geq 2/d$ is satisfied as an equality.

We now briefly summarize some of the theoretical discussion. The arguments leading to the equality $z = d$ start with hyperscaling [23] which states that the singular part of the free energy inside a correlation volume is a *universal* dimensionless number, $(f_s/\hbar)\xi^d\xi_\tau = A$. With $\xi \sim \delta^{-\nu}$ it follows that $f_s \sim \delta^{\nu(d+z)}$ with a finite-size form [1]:

$$f_s(\delta, L, \beta) \sim \delta^{\nu(d+z)} F(\xi/L, \xi_\tau/\beta). \tag{2}$$

Imposing a phase gradient $\partial\phi$ along one of the *spatial* directions will then give rise to a free energy difference $\Delta f_s/\hbar = \frac{1}{2}\rho(\partial\phi)^2$ where ρ is the stiffness (superfluid density). Since Δf_s must obey a form similar to Eq. (2) and since $\partial\phi$ has dimension of inverse length implying $\partial\phi \sim 1/\xi$, it follows that $\rho \sim \xi^2\delta^{\nu(d+z)} \sim \delta^{\nu(d-2+z)}$, with a finite-size scaling form of

$$\rho = L^{2-d-z} R(\delta L^{1/\nu}, \beta/L^z). \tag{3}$$

If an analogous argument is used with a twist in the *temporal* direction scaling as $\partial_\tau\phi \sim 1/\xi_\tau$, Fisher *et al.* [1] argued that the compressibility scales as $\kappa \sim \delta^{\nu(d-z)}$ which they then used to argue that $z = d$. In contrast, Weichman and collaborators [11,20] argue that in the presence of disorder $\partial_\tau\phi \sim 1/\xi_\tau$ should not apply, invalidating the relation $\kappa \sim \delta^{\nu(d-z)}$, leaving z unconstrained. Interestingly, a different theoretical argument [9] favoring $z = d$ has also been put forward.

Models.—The first model we study, closely related to Eq. (1), is the QR model. It is defined in terms of conjugate phase and number operators $\theta_\mathbf{r}$, $n_\mathbf{r}$ satisfying $[\theta_\mathbf{r}, n_{\mathbf{r}'}] = \delta_{\mathbf{r},\mathbf{r}'}$ on a $L \times L$ lattice:

$$H_{\mathrm{qr}} = -\sum_{\mathbf{r},\mathbf{r}+\mathbf{e}} t\cos(\theta_\mathbf{r} - \theta_{\mathbf{r}+\mathbf{e}}) - \sum_\mathbf{r} \mu_\mathbf{r} n_\mathbf{r} + \frac{U}{2}\sum_\mathbf{r} n_\mathbf{r}^2, \tag{4}$$

where U is the on-site repulsion, t is the nearest neighbor tunneling amplitude, and $\mu_r \in [-\Delta, \Delta]$ represents the uniformly distributed on-site disorder in the chemical potential. As before, $\mathbf{e} = \mathbf{x}, \mathbf{y}$. We fix $\Delta = \frac{1}{2}$, $U = 1$, and cross the BG-SF transition by varying t. In contrast to Eq. (1) $n_\mathbf{r}$ can take negative as well as positive values and can be interpreted as deviations from the average filling n_0. For convenience we study Eq. (4) using a link-current representation [24] for which *directed* worm algorithms are available [25]. We use lattices ranging from $L = 12$ to $L = 32$, with 5×10^4 disorder realizations for $L = 12, \ldots, 28$ and 10^4 disorder realizations for $L = 32$. In all cases we average over 6×10^4 Monte-Carlo steps (MCS) per disorder realization. For the simulations of the QR model a temporal discretization of $\Delta\tau = 0.1$ was used, sufficiently small that remaining discretization errors could be neglected.

The second model we consider is the $U \to \infty$ HCB limit of Eq. (1) equivalent to the $S = 1/2$ XY model on an $L \times L$ lattice in a random transverse field:

$$H_{xy} = -\frac{1}{2}\sum_{\mathbf{r},\mathbf{e}} (S^+_\mathbf{r} S^-_{\mathbf{r}+\mathbf{e}} + S^-_\mathbf{r} S^+_{\mathbf{r}+\mathbf{e}}) + \sum_\mathbf{r} h_\mathbf{r} S^z_\mathbf{r}, \tag{5}$$

with $h_\mathbf{r} \in [-h, h]$ uniformly. In this case we traverse the transition by tuning the disorder strength h. We use a directed loop version of the stochastic series expansion (SSE) [26] to simulate this model. This technique is free of discretization errors and efficient directed algorithms [26,27] are available. We further use a beta-doubling scheme [28] that allows for rapid equilibration at large β values. In contrast to the QR model, we employ a microcanonical ensemble for the disorder by constraining each disorder realization to have *exactly* $\sum_\mathbf{r} h_\mathbf{r} = 0$. This facilitates the analysis without affecting the results [29]. We use at least $\sim 10^5$ disorder realizations per data point, a large improvement over [3]. In the following $[\ldots]$ denotes the disorder average and $\langle\ldots\rangle$ the thermal average.

Observables.—Our main focus is the scaling behavior of the superfluid stiffness ρ for which the finite-size scaling form Eq. (3) was derived. For both models we measure ρ as

$$\rho = \frac{[\langle W_x^2 + W_y^2\rangle]}{2\beta}, \tag{6}$$

where W_x and W_y are the winding numbers in the spatial directions. [For the HCB model Eq. (6) is multiplied by π to yield ρ.] From Eq (6), it follows that $\beta\rho = W^2$ has a particularly attractive scaling form when $d = 2$, which we may write

$$W^2 = \frac{\beta}{L^z} W(\delta L^{1/\nu}, L/\beta^{1/z}), \tag{7}$$

where we define $\delta = (t - t_c)$ (QR model) and $\delta = (h - h_c)$ (HCB model). We also make extensive use of the correlation functions, defined as $C(\mathbf{r} - \mathbf{r}', \tau - \tau') = [\langle \exp\{i(\theta_\mathbf{r}(\tau) - \theta_{\mathbf{r}'}(\tau'))\}\rangle]$ for the QR model and as $C(\mathbf{r} - \mathbf{r}', \tau - \tau') = [\langle S^+_\mathbf{r}(\tau)\, S^-_{\mathbf{r}'}(\tau')\rangle]$ for the HCB model.

Results, QR.—A large number of independent simulations of Eq. (4) were carried out at many different L, β close to the QCP. Since we expect ρ to approach zero in an exponential manner as L is increased at *fixed* β and since ρ is likely exponentially suppressed in the insulating phase it

PRL 114, 255701 (2015) PHYSICAL REVIEW LETTERS week ending 26 JUNE 2015

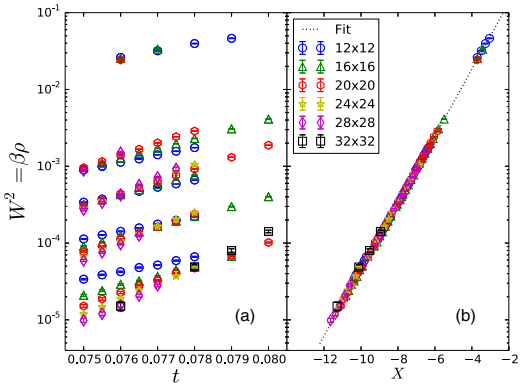

FIG. 1 (color online). Scaling collapse of 142 independent simulations of $W^2 = \beta\rho$ for the QR model. (a) Unscaled data of W^2 versus t. (b) Scaling collapse of the data of panel (a). The data are plotted against the scaling variable $X = \ln(a\beta/L^z) + b(t-t_c)L^{1/\nu} - cL/\beta^{1/z} - d(L/\beta^{1/z})^2$.

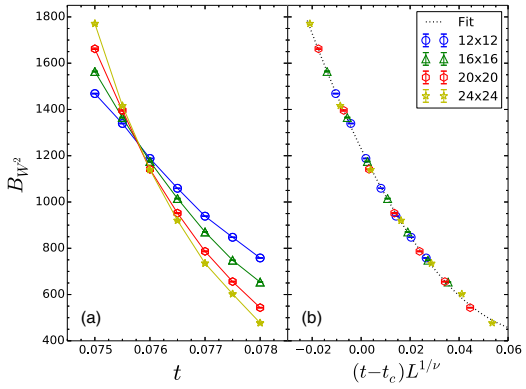

FIG. 2 (color online). The Binder cumulant B_{W^2} for the QR model versus t with $\beta = L^2/4$. (a) Unscaled data showing a crossing close to the critical point $t_c = 0.0760(5)$. (b) Scaling plot versus $(t-t_c)L^{1/\nu}$ obtained by fitting the data in (a) to the form $a + b(t-t_c)L^{1/\nu} + c(t-t_c)^2L^{2/\nu}$ yielding $t_c = 0.758(5)$ and $\nu = 0.98(3)$.

seems reasonable to approximate the function $W(x,y)$ in Eq. (7) as $a\exp[f(x,y)]$ with $x = \delta L^{1/\nu}$, $y = L/\beta^{1/z}$. If the temperature dependence is carefully mapped out [30] one indeed sees that $W(x,y)$ has a clear exponential dependence. As a first step, we then assume $f(x,y) = bx - cy - dy^2$. We can then fit *all* 142 data points to this form determining the coefficients a, b, c, d along with $t_c = 0.0760(5)$ $\nu = 1.00(2)$ and $z = 1.99(5)$. The results are shown in Fig. 1 with a scaling plot using the scaling variable $X = \ln(a\beta/L^z) + b(t-t_c)L^{1/\nu} - cL/\beta^{1/z} - d(L/\beta^{1/z})^2$. A more refined analysis [30] shows that the temperature dependence likely involves a correction term $W^2 = ay^z\exp(bx-cy) + dy^{-w}\exp(bx-c'y)$. The correction term is here proportional to T^w and disappears as T tends to zero. It is straightforward to fit *all* our data to this form which yields identical estimates for t_c, ν, z along with $w = 0.6(2)$. Estimating the AIC (Akaike information criterion) for the two forms heavily favors the latter. We note that our results appear to satisfy $z = d$ and $\nu \geq 2/d$ as equalities in contrast to [4] which finds $z = 1.75(5)$, $\nu = 1.15(3)$.

With a reliable estimate of z we can now *fix* the scaling argument L^z/β. If we then study the Binder cumulant $B_{W^2} = [\langle W^4\rangle]/[\langle W^2\rangle]^2$ we see that at *fixed* L^z/β it should follow a simplified form of Eq. (7), $B_{W^2} = B(\delta L^{1/\nu})$. As shown in Fig. 2, lines for different L will then cross at t_c, thereby confirming our previous estimates.

Our results for the correlation functions for the QR models are shown in Fig. 3 for a $L = 20$ lattice at t_c for a range of temperatures. Asymptotically, one expects [1] $C(\tau) \sim \tau^{-(d-2+z+\eta)/z}$ and $C(\mathbf{r}) \sim r^{-(d-2+z+\eta)}$. Clearly, $C(\mathbf{r})$ drops off much faster than $C(\tau)$ confirming that $z \neq 1$. However, pronounced finite temperature effects are visible in $C(\mathbf{r})$ arising because the limit $\beta \gg L^z$ has not yet been reached which prevents us from reliably determining the power law for $C(\mathbf{r})$. However, from $C(\tau)$ we determine $(z+\eta)/z = y_\tau = 0.85(2)$ and hence $\eta = -0.3(1)$ using our previous estimate $z = 1.99(5)$. This estimate satisfies the rigorous inequality $2-(d+z) < \eta \leq 2-d$ [1] and agrees with the prior result $\eta = -0.3(1)$ [4].

For the QR model we have also verified that the compressibility κ remains finite and independent of L throughout the transition, consistent with $z \leq d$. Furthermore, a direct evaluation of $\partial W^2/\partial t$ directly at t_c for fixed L^z/β, expected from Eq. (7) to scale as $\sim L^{1/\nu}$, yields $\nu = 0.98(4)$ consistent with our previous results.

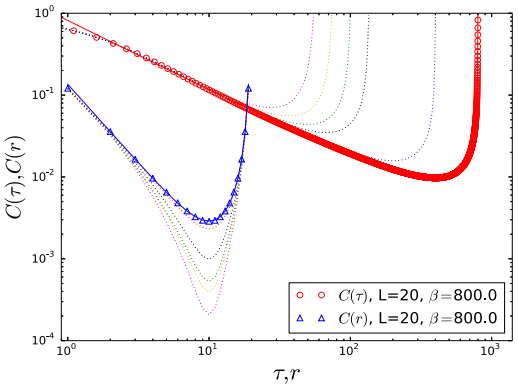

FIG. 3 (color online). The correlation functions $C(\tau)$ and $C(\mathbf{r})$ as a function of τ, $\mathbf{r}$ for a system size $L = 20$. Results are shown for the QR model at the critical point and a range of $\beta = 55, \ldots, 800$. The solid red line is a fit to $\beta = 800$ results for $C(\tau)$ using the form $a[\tau^{-y_\tau} + (\beta-\tau)^{-y_\tau}]$ with pi $(z+\eta)/z = y_\tau = 0.85(2)$.

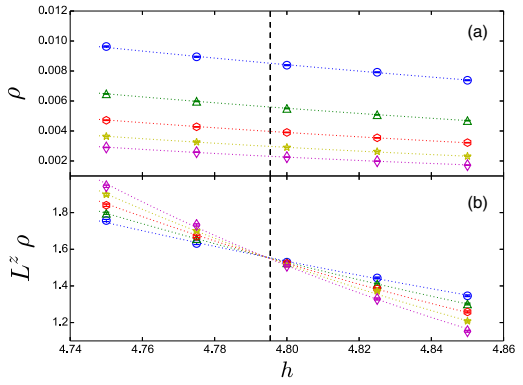

FIG. 4 (color online). Finite-size scaling analysis of the stiffness for the HCB model using data only at $\beta = 512$. (a) ρ vs h. (b) Crossing of the scaling function: $\tilde{R} = L^z\rho$ at the critical point, $h_c = 4.79(3)$ (vertical dashed line). For both panels, the dotted lines are fits to $\tilde{R}(x) = a + bx + cx^2$.

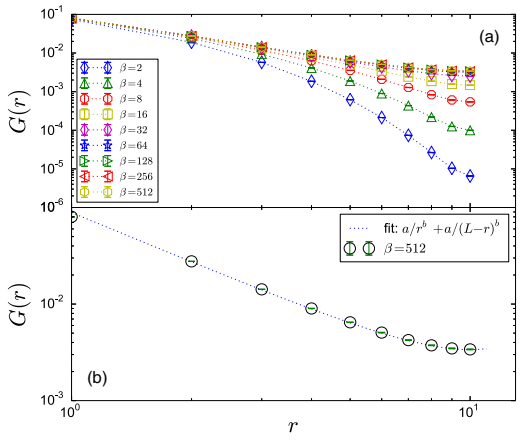

FIG. 5 (color online). The equal-time spatial correlation function, $C(\mathbf{r})$ of a 20×20 lattice for the HCB model at h_c. (a) Convergence of $C(\mathbf{r})$ using the beta-doubling procedure. (b) $C(\mathbf{r})$ (open circles) at $L = 20$, $\beta = 512$ fitted to the form $a(1/r^{y_r} + 1/(L-r)^{y_r})$ (dashed line), yielding $z + \eta = y_r = 1.718(1)$.

Results, HCB.—Because of the hard-core constraint number, fluctuations are dramatically suppressed in the HCB model. Combined with the very effective beta-doubling scheme we can reach much lower temperatures compared to the QR model. Hence, we use a simplified form of Eq. (3),

$$\rho = L^{2-d-z}\tilde{R}(\delta L^{1/\nu}), \tag{8}$$

suppressing the temperature dependence. We have extensively verified that this is permissible for the system sizes used [30] and that our data appear independent of temperature at $\beta = 512$ to within numerical precision. We then fit our data for ρ at $\beta = 512$ to an expansion of $\tilde{R}$ in Eq. (8) to second order $\tilde{R} = a + b\delta L^{1/\nu} + c(\delta L^{1/\nu})^2$, obtaining the estimates $h_c = 4.79(3)$, $z = 1.88(8)$, $\nu = 0.99(3)$ to be contrasted with the values $h_c = 4.42(2)$, $z = 1.40(5)$, and $\nu = 1.10(4)$ determined in Ref. [3] with significantly less statistics. The result of this fit is shown in Fig. 4. In panel b of Fig. 4, we show the crossing of the scaling function $\tilde{\rho}$, at $h_c = 4.79(3)$ as carried out for the QR model in Fig. 1 to yield similar results for z, ν, and h_c.

The correlation functions show a pronounced temperature dependence as shown in Fig. 5(a) for $C(\mathbf{r})$. However, as we lower the temperature, $C(\mathbf{r})$ reaches a stable power-law form at $\beta = 512$ for *all* L studied, showing that the regime $\beta \gg L^z$ is reached, confirming that the temperature dependence can be neglected in Eq. (8). To determine the anomalous dimension η we then fit the results in Fig. 5(a) for $L = 20$, $\beta = 512$ and $h_c = 4.79(3)$ to a power-law form with $z + \eta = y_r = 1.718(1)$ as shown in Fig. 5(b). Using our earlier estimate of z, we obtain $\eta = -0.16(8)$ in reasonable agreement with the QR results. For the HCB model we have also calculated the compressibility κ. It remains roughly constant and independent of L through the transition. We note that our results significantly improve on previous conflicting calculations for the exponents of the HCB model which include $z = 2.0(4)$, $\nu = 0.90(13)$ in [16], $z = 0.5(1)$, $\nu = 2.2(2)$ in [31], and $z = 1.40(2)$, $\nu = 1.10(4)$ in [3].

Conclusion.—Our results for ν for both models studied indicate clearly that $\nu \geq 2/d$ is satisfied as an *equality*. For the dynamical critical exponent z, describing the BG-SF transition, we find a value that is significantly larger than previous estimates. While there is a slight disagreement in the estimate of z for the two models we studied it seems possible that indeed $z = d$. During the final stages of writing this manuscript we became aware of Ref. [32] which for the HCB model reached conclusions similar to ours.

We would like to thank Fabien Alet and Rong Yu for useful discussions. This work was supported by NSERC and made possible by the facilities of the Shared Hierarchical Academic Research Computing Network (SHARCNET [33]) and Compute/Calcul Canada.

*ngry@mcmaster.ca
†sorensen@mcmaster.ca

[1] S. Sachdev, *Quantum phase transitions*, 2nd ed. (Cambridge University Press, Cambridge, 2011); M. P. A. Fisher, P. B. Weichman, G. Grinstein, and D. S. Fisher, Phys. Rev. B **40**, 546 (1989).
[2] T. Barthel, U. Schollwöck, and S. Sachdev, arXiv:1212.3570.
[3] A. Priyadarshee, S. Chandrasekharan, J.-W. Lee, and H. U. Baranger, Phys. Rev. Lett. **97**, 115703 (2006).

[4] H. Meier and M. Wallin, Phys. Rev. Lett. **108**, 055701 (2012).

[5] M. Greiner, O. Mandel, T. Esslinger, T. W. Hansch, and I. Bloch, Nature (London) **415**, 39 (2002); M. Pasienski, D. McKay, M. White, and B. DeMarco, Nat. Phys. **6**, 677 (2010).

[6] P. A. Crowell, F. W. Van Keuls, and J. D. Reppy, Phys. Rev. B **55**, 12620 (1997).

[7] H. S. J. van der Zant, F. C. Fritschy, W. J. Elion, L. J. Geerligs, and J. E. Mooij, Phys. Rev. Lett. **69**, 2971 (1992).

[8] D. B. Haviland, Y. Liu, and A. M. Goldman, Phys. Rev. Lett. **62**, 2180 (1989); H. M. Jaeger, D. B. Haviland, B. G. Orr, and A. M. Goldman, Phys. Rev. B **40**, 182 (1989); Y. Liu, K. A. McGreer, B. Nease, D. B. Haviland, G. Martinez, J. W. Halley, and A. M. Goldman, Phys. Rev. Lett. **67**, 2068 (1991); N. Marković, C. Christiansen, and A. M. Goldman, Phys. Rev. Lett. **81**, 5217 (1998); Y.-H. Lin and A. M. Goldman, Phys. Rev. Lett. **106**, 127003 (2011).

[9] R. Yu, S. Haas, and T. Roscilde, Europhys. Lett. **89**, 10009 (2010); R. Yu, L. Yin, N. S. Sullivan, J. S. Xia, C. Huan, A. Paduan-Filho, O. J. N. F., S. Haas, A. Steppke, C. F. Miclea, F. Weickert, R. Movshovich, E.-D. Mun, B. L. Scott, V. S. Zapf, and T. Roscilde, Nature (London) **489**, 379 (2012); R. Yu, C. F. Miclea, F. Weickert, R. Movshovich, A. Paduan-Filho, V. S. Zapf, and T. Roscilde, Phys. Rev. B **86**, 134421 (2012).

[10] A. Zheludev and T. Roscilde, C.R. Phys. **14**, 740 (2013).

[11] P. Weichman, Mod. Phys. Lett. B **22**, 2623 (2008).

[12] J. T. Chayes, L. Chayes, D. S. Fisher, and T. Spencer, Phys. Rev. Lett. **57**, 2999 (1986).

[13] D. S. Fisher and M. P. A. Fisher, Phys. Rev. Lett. **61**, 1847 (1988); M. P. A. Fisher, G. Grinstein, and S. M. Girvin, Phys. Rev. Lett. **64**, 587 (1990).

[14] W. Krauth, N. Trivedi, and D. Ceperley, Phys. Rev. Lett. **67**, 2307 (1991); K. J. Runge, Phys. Rev. B **45**, 13136 (1992); G. G. Batrouni, B. Larson, R. T. Scalettar, J. Tobochnik, and J. Wang, Phys. Rev. B **48**, 9628 (1993).

[15] E. S. Sørensen, M. Wallin, S. M. Girvin, and A. P. Young, Phys. Rev. Lett. **69**, 828 (1992); M. Wallin, E. S. Sørensen, S. M. Girvin, and A. P. Young, Phys. Rev. B **49**, 12115 (1994).

[16] S. Zhang, N. Kawashima, J. Carlson, and J. E. Gubernatis, Phys. Rev. Lett. **74**, 1500 (1995).

[17] J. Kisker and H. Rieger, Phys. Rev. B **55**, R11981 (1997).

[18] N. V. Prokof'ev and B. Svistunov, Phys. Rev. Lett. **92**, 015703 (2004).

[19] L. Pollet, N. V. Prokof'ev, B. V. Svistunov, and M. Troyer, Phys. Rev. Lett. **103**, 140402 (2009); V. Gurarie, L. Pollet, N. V. Prokof'ev, B. V. Svistunov, and M. Troyer, Phys. Rev. B **80**, 214519 (2009); G. Carleo, G. Boéris, M. Holzmann, and L. Sanchez-Palencia, Phys. Rev. Lett. **111**, 050406 (2013); F. Lin, E. S. Sørensen, and D. M. Ceperley, Phys. Rev. B **84**, 094507 (2011).Y. Wang, W. Guo, A. W. Sandvik, Phys. Rev. Lett. **114**, 105303 (2015).

[20] P. B. Weichman and R. Mukhopadhyay, Phys. Rev. Lett. **98**, 245701 (2007); Phys. Rev. B **77**, 214516 (2008).

[21] P. Hitchcock and E. S. Sørensen, Phys. Rev. B **73**, 174523 (2006); Z. Yao, K. P. C. da Costa, M. Kiselev, and N. V. Prokof'ev, Phys. Rev. Lett. **112**, 225301 (2014).

[22] M. White, M. Pasienski, D. McKay, S. Q. Zhou, D. Ceperley, and B. DeMarco, Phys. Rev. Lett. **102**, 055301 (2009).

[23] D. Stauffer, M. Ferer, and M. Wortis, Phys. Rev. Lett. **29**, 345 (1972); A. Aharony, Phys. Rev. B **9**, 2107 (1974); P. C. Hohenberg, A. Aharony, B. I. Halperin, and E. D. Siggia, Phys. Rev. B **13**, 2986 (1976).

[24] W. Witczak-Krempa, E. S. Sørensen, and S. Sachdev, Nat. Phys. **10**, 361 (2014).

[25] F. Alet and E. S. Sørensen, Phys. Rev. E **67**, 015701 (2003); **68**, 026702 (2003).

[26] A. W. Sandvik and J. Kurkijärvi, Phys. Rev. B **43**, 5950 (1991); O. F. Syljuåsen and A. W. Sandvik, Phys. Rev. E **66**, 046701 (2002).

[27] F. Alet, S. Wessel, and M. Troyer, Phys. Rev. E **71**, 036706 (2005).

[28] A. W. Sandvik, Phys. Rev. B **66**, 024418 (2002).

[29] A. Dhar and A. Young, Phys. Rev. B **68**, 134441 (2003); C. Monthus, Phys. Rev. B **69**, 054431 (2004).

[30] See Supplemental Material at http://link.aps.org/supplemental/10.1103/PhysRevLett.114.255701 for additional simulation details.

[31] M. Makivić, N. Trivedi, and S. Ullah, Phys. Rev. Lett. **71**, 2307 (1993).

[32] J. P. Álvarez Zúñiga, D. J. Luitz, G. Lemarié, and N. Laflorencie, Phys. Rev. Lett. **114**, 155301 (2015).

[33] http://www.sharcnet.ca.

Supplementary material

HCB SIMULATION DETAILS

A central assumption made in our analysis of the HCB results was that a simplified scaling function, Eq.(8), for ρ. In the main text, we showed the convergence of the equal-time spatial correlation function: $C(\mathbf{r})$ in Fig.(5) at the critical point using data from the beta-doubling procedure. For completeness, we show the convergence of the stiffness in the 20×20 system, we need to go up to $\beta = 512$ before finite temperature effects are eliminated. The data indicates that for the simulation of even larger system sizes, one may need to go up to $\beta = 1024$ to validate the use of the simplified scaling form. Note that for each temperature in the beta-doubling scheme, we average over 48 Monte Carlo sweeps (MCS), with each sweep consisting of one diagonal update and N_l directed loop updates. N_l is set during the equilibration phase so that on average $2\langle n_H \rangle$ vertices are visited, where n_H is the number of non-trivial operators in the SSE string.

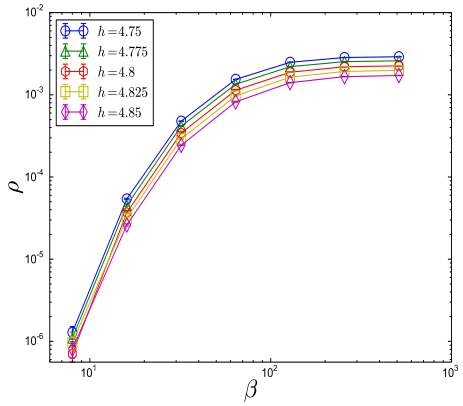

FIG. 1. Demonstration of the convergence of the spin stiffness: ρ versus β using the beta-doubling procedure, for a 32×32 lattice. As β increases, thermal effects can be clearly seen to disappear, thereby justifying the use of the simplified scaling form in Eq.(8).

Another important point that is often overlooked, is the convergence of observable data with the number of disorder realizations, N_r used. For the SSE parameters chosen, we find that it was necessary to use at least $\sim 5 \times 10^4$ disorder samples before disorder fluctuations are reasonably small. This is demonstrated in Fig. 2 for the largest lattice size: 32×32. For reliable data with controlled errorbars, all the HCB data points were averaged over least 10^5 independent disorder realizations. This is contrast to earlier studies [1] most relevant to our work, where only $10^2 - 10^3$ disorder realizations were

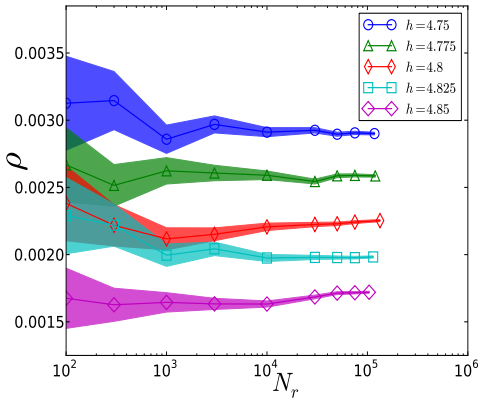

FIG. 2. Convergence of spin stiffness: ρ with number of disorder realizations, N_r, for h values used. The shaded region indicates the errorbars of points which decrease as more samples are used. Note that for the equilibration step size chosen in our simulations, $\sim 10^5$ disorder realizations are necessary to obtain true convergence.

used. We note that it is quite unlikely that self-averaging applies in this model and increasing the lattice size does therefore not decrease the number of disorder realizations needed.

Since different disorder realizations are statistically independent we estimate errorbars using standard binning techniques on the data for different disorder realizations. We have verified that boot-strap methods yield essentially indentical errorbars.

TEMPERATURE DEPENDENCE OF $W^2 = \beta\rho$

Insight into the temperature dependence of W^2 can be gained by first studying ρ for the QR model *without* disorder. A model for which it is know that $z = 1$. Results for ρ for a 40×40 lattice are shown in Fig. 3 for $\beta = 9, \ldots 400$. For $\beta \ll L$ we expect ρ to go to zero in an exponential manner while for $\beta \gg L$ it should approach a constant. The simplest ansatz is therefore:

$$\rho = \frac{a}{L} e^{-c\frac{L}{\beta}}, \tag{1}$$

where we have tentatively included an L dependence. However, as is clearly evident in Fig. 3, ρ has a *maximum* close to $L/\beta = 0.4$. The presence of this maximum signals that there are likely two contributions to ρ describing the $\beta \ll L$ and $\beta \gg L$ regimes. (Although we note that the existence of two terms does not imply a

maximum.) We therefore assume the presence of a correction term proportional to T^y with $y > 0$. Such a term will therefore disappear in the zero temperature limit. For our final ansatz we therefore take:

$$\rho = \frac{a}{L} e^{-c\frac{L}{\beta}} + b\left(\frac{L}{\beta}\right)^y e^{-d\frac{L}{\beta}}. \quad (2)$$

This is the form used in Fig. 3 and it gives an essentially *perfect* fit over the entire range of the figure. We can immediately generalize to a scaling form for $W^2 = \beta\rho$:

$$W^2 = a\frac{\beta}{L} e^{-c\frac{L}{\beta}} + b\left(\frac{L^z}{\beta}\right)^w e^{-d\frac{L}{\beta}}. \quad (3)$$

A fit to this form yields $\omega = 0.97(9)$ in relative good agreement with similar correction terms used in Ref. [2] and estimates for the 3D XY universality class [**?**].

We now turn to the QR model in the presence of disorder. In this case we assume that the scaling variable L/β generalizes to $L/\beta^{1/z}$. We therefore expect to find:

$$W^2 = a\frac{\beta}{L^z} e^{-cL/\beta^{1/z}} + b\left(\frac{L^z}{\beta}\right)^w e^{-dL/\beta^{1/z}}. \quad (4)$$

In Fig. 4 results are shown for W^2 for two different lattice sizes $L = 12, 20$ Assuming $z = 2$ in this case we plot the results against $L/\sqrt{\beta}$ demonstrating that the results fall on a single curve with only slight deviations from a straight line. It is perhaps surprising that it is the variable $L/\beta^{1/z}$ that appears as opposed to L^z/β but this can very clearly be verified from the simulations. Performing a fit to the ansatz we find exceedingly good agreement with the expected form with a correction exponent $w = 0.92(7)$, close to the value for the model without disorder. An inspection of our results for ρ for this system size shows that in this case there is *no* maximum in ρ versus β.

We have performed a similar analysis of W^2 as a function of β for the QR model again clearly confirming the overall exponential dependence and the presence of the two terms.

CROSSING OF $\beta\rho$ FOR THE QR MODEL.

With the z and t_c determined from the fit in Fig.1, $\beta\rho$ plotted for different L at a fixed aspect ratio $\beta = L^z/4$ should also cross at the critical point $t_c = 0.0760(5)$. This is indeed the case and is shown Fig. 5. Since this data is essentially already shown in Fig.1(a) we have in the main text opted to show the crossing using the related quantity $B_{W^2} = [\langle W^4\rangle]/[\langle W^2\rangle]^2$ shown in Fig.2. Note that in simulations of both models two independent replicas α, β of each disorder realization are simulated in parallel to correctly estimate averages like$[\langle\ldots\rangle^2]$ as $[\langle\ldots\rangle_\alpha \langle\ldots\rangle_\beta]$.

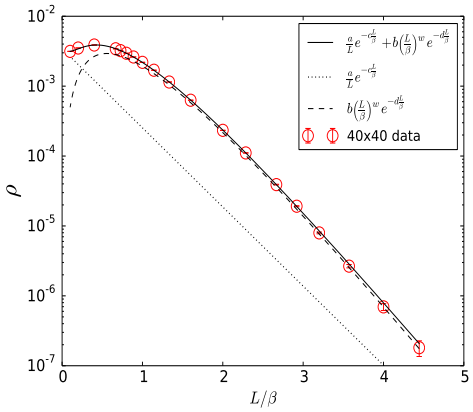

FIG. 3. (Color online) ρ as a function of L/β for the QR model *without* disorder. Results are shown for $L = 40$. The solid black line indicates a fit to the $L = 40$ data of the form $\frac{a}{L}e^{-c\frac{L}{\beta}} + b\left(\frac{L}{\beta}\right)^y e^{-d\frac{L}{\beta}}$ yielding $y = 1.97(9)$. The dotted line indicates the first part of this fit while the dashed line shows the second part.

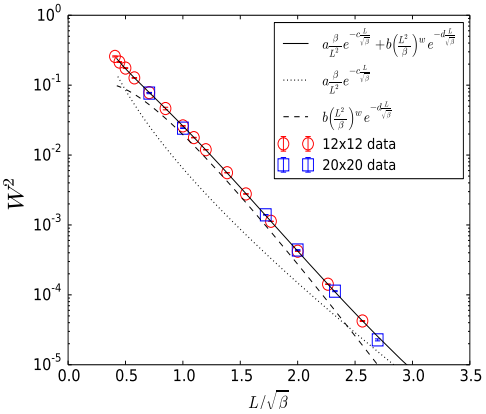

FIG. 4. (Color online) $\beta\rho$ as a function of $L/\sqrt{\beta}$ for the QR model. Results are shown for $L = 12, 20$. The solid black line indicates a fit to the $L = 12$ data of the form $a\frac{\beta}{L^2}e^{-c\frac{L^2}{\beta}} + b\left(\frac{L^2}{\beta}\right)^w e^{-d\frac{L}{\sqrt{\beta}}}$ yielding $w = 0.92(7)$. The dotted line indicates the first part of this fit while the dashed line shows the second part.

[1] A. Priyadarshee, S. Chandrasekharan, J.-W. Lee, and H. U. Baranger, Phys. Rev. Lett. **97**, 115703 (2006).
[2] W. Witczak-Krempa, E. S. Sørensen, and S. Sachdev, Nature Physics **10**, 361 (2014).

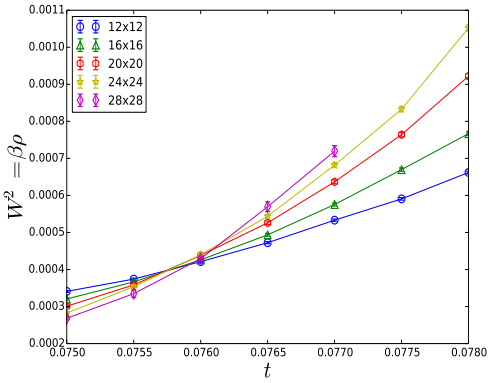

FIG. 5. (Color online) $\beta\rho$ as a function of t for the QR model. All simulations are performed using the fixed aspect ratio $\beta = L^z/4$ with $z = 2$. Lines cross at the critical point $t_c = 0.0760(5)$.

APPENDIX

Appendix 5.A Other models

The BH model can be mapped onto a quantum rotor (QR) model, which has a natural physical realization in Josephson junction (JJ) arrays (Bruder et al., 2005). It is described by the Hamiltonian:

$$H_{JJ} = -\tilde{t}\sum_{\langle i,j\rangle}\cos(\hat{\theta}_i - \hat{\theta}_j) - \sum_i \tilde{\mu}\delta\hat{n}_i + \frac{1}{2}\tilde{U}\sum_i \delta n_i^2, \tag{5.A.1}$$

where the phase and number fluctuations given by: $\hat{\theta}_i$ and $\delta\hat{n}_i$ form conjugate variables satisfying the commutation relations: $\left[\hat{\theta}_i, \delta\hat{n}_i\right] = i\delta_{ij}$. Eq. 5.A.1 can be easily derived by invoking the transformations

$$\hat{b}^\dagger = \sqrt{n_o + \delta\hat{n}_i}e^{i\hat{\theta}_i} \tag{5.A.2}$$

$$\hat{b} = e^{-i\hat{\theta}_i}\sqrt{n_o + \delta\hat{n}_i}, \tag{5.A.3}$$

in eq. 4.2.1. Together with the asymptomatic limit of large occupancies, i.e. $n_o \gg \langle\delta\hat{n}_i\rangle$, quantitative agreement is reached between the BH and quantum rotor (QR) model. Note however that $\delta\hat{n}_i$ represent fluctuations that can take both positive and negative integer values, unlike, n_i in eq. 4.2.1 which is confined to only positive integer values. The parameters of the QR model are related to but not identical to the BH parameters. Following (Weichman and Mukhopadhyay, 2007), their equivalence is given by:

$$\{\tilde{t}, \tilde{U}, \tilde{\mu}\} = \left\{n_o t, U, \mu - n_o U + \frac{U}{2}\right\} \tag{5.A.4}$$

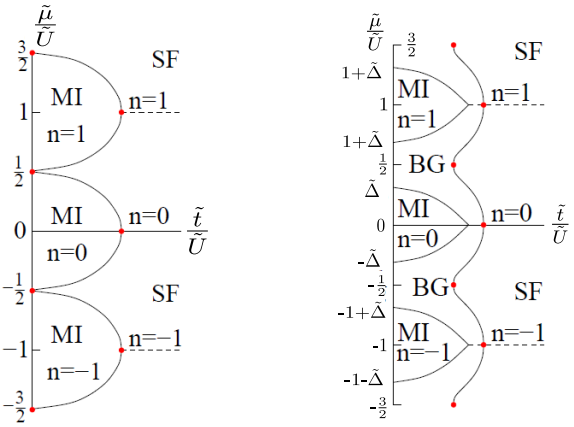

(a) Phase diagram of the clean JJ model

(b) Phase diagram of the JJ model with disorder

Figure 5.6: Phase diagrams of the JJ model adapted from (Weichman, 2008) with and without disorder. The multicritical point is indicated by the red dots. The transition through the latter at fixed $\tilde{\mu}/\tilde{U}$ lies in the (d+1) XY universality class. Note the translational symmetry in the $\tilde{\mu}/\tilde{U}$ direction.

Phase diagram

The phase diagram in Fig. 5.6 exhibits the same qualitative features of the BH model, most notably the existence of the MI and SF phases as in the clean BH model and the characteristic Mott Lobes. However, two symmetries are now explicitly present in the Hamiltonian of eq. 5.A.1. For instance, a translational symmetry defined by: $\delta n_i \to \delta n_i + n_o$, transforms the free energy as: $f_J(\tilde{\mu}) = f_J(\tilde{\mu} - n_o\tilde{U}) + \epsilon_o$, where ϵ_o is a constant, and is reflected in the periodic structure of the phase diagram along the $\tilde{\mu}/\tilde{U}$ axis and the symmetry of the Mott lobes. The extra constant has no effect on the phase diagram.

In addition, the "hidden" particle-hole symmetry of the BH model is now explicitly present in the phase diagram at the tips of their corresponding Mott lobes. Defining this symmetry by the transformation: $\delta n_i \to -\delta n_i, \theta_i \to -\theta_i$, we see that *at the special multicritical points* $\tilde{\mu}_i = kn_i/2$ (red dots in fig. 5.6), where k is any integer, and together with the translational symmetry, the free energy remains invariant such that $f_J(\tilde{\mu}) = f_J(-\tilde{\mu})$.

These symmetries are identical to those present in the classical XY-model defined by the Hamiltonian

$$H = -J \sum_{\langle i,j \rangle} \cos(\theta_i - \theta_j), \tag{5.A.5}$$

where $\{\theta_i\}$ represent the orientation of the spins in spin space. Note that the transformations: $\theta_i \to \theta_i + \theta_o$ and $\theta_i \to -\theta_i$ leave the Hamiltonian invariant. This translational and inversion symmetry in the classical XY model corresponds to the translational and particle-hole symmetry present at the multicritical points in the quantum rotor model. Using the Villain transformation (Villain, J., 1975, José et al., 1977), the QR model can also be mapped on to a link-current model (Sørensen et al., 1992) which is amenable to numerical simulations.

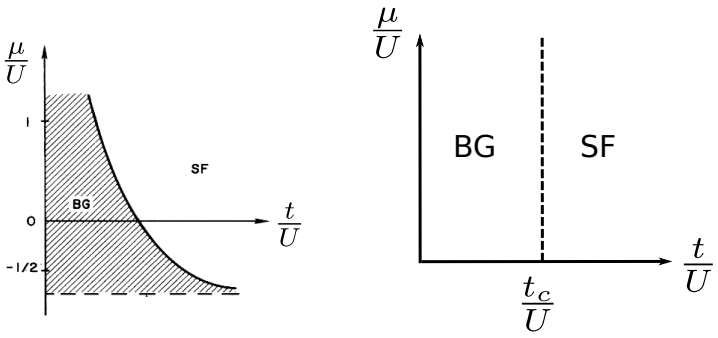

(a) Schematic phase diagram for the BH model in the presence of strong disorder: $\Delta/U > 1/2$. Adapted from (Fisher et al., 1989)

(b) Schematic phase diagram for the QR model in the presence of strong disorder: $\tilde{\Delta}/\tilde{U} > 1/2$.

Figure 5.7: The schematic phase diagrams of the BH and QR model. Note the disappearance of the Mott Phase altogether.

Disorder effects

Just as in the BH model, we model uniform disorder by making the substitution:

$$\tilde{\mu} \to \tilde{\mu} + \delta\tilde{\mu}_i, \tag{5.A.6}$$

where $\delta\tilde{\mu}_i \in [-\tilde{\Delta}, \tilde{\Delta}]$ in eq. 5.A.1. Both the shrinking of the Mott lobes by Δ and the appearance of a surrounding BG phase appears as well. The invariance of the free energy under particle-hole combined with translational symmetry now implies $f_J(\tilde{\mu}, \{\delta\tilde{\mu}_i\}) = f_J(-\tilde{\mu}, \{-\delta\tilde{\mu}_i\})$. Note that for both the disordered BH and QR model, we can classify them in terms of strong ($\Delta/U \geq 1/2$) and weak ($\Delta/U < 1/2$) disorder. As one would expect, in the strong disorder scenario, the Mott lobes completely vanish and we are only left with the SF and BG phase. Due to the translational symmetry of the QR model, the phase boundary is a vertical line at $\tilde{t}_c/\tilde{U}$, while for the BH model, the phase boundary decreases monotonically as μ/U increases. Their phase diagrams are schematically shown in fig. 5.7.

5.A.1 Hardcore-boson model

An even simpler model that is also capable of recapturing the generic BH physics is that of the uniform hardcore boson model governed by the Hamiltonian:

$$H = -\frac{t}{2}\sum_{\langle i,j\rangle}\left(\hat{a}_i^\dagger\hat{a}_j + \hat{a}_j^\dagger\hat{a}_i\right) + \sum_i \mu(n_i - \frac{1}{2}), \tag{5.A.7}$$

where $\hat{a}_i, \hat{a}_i^\dagger$ are hardcore bosonic operators that forbid multiple occupancies for each site, i.e. $\hat{a}_i^2 = \hat{a}^{\dagger 2} = 0$, in addition to abiding the the same commutation relations as their softcore counterpart.

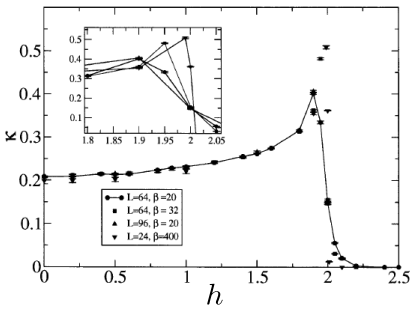

(a) (main) Path Integral Monte-Carlo (PIMC) results for the compressibility: κ for a series of system sizes, L and temperatures: $\beta = 1/T$ (see legend). (inset) A closer view of the κ close to the transition $\mu_c/t = 2$

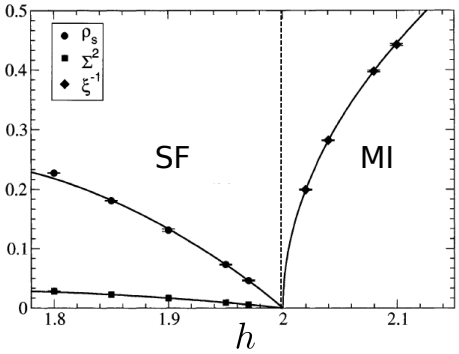

(b) PIMC results for the Superfluid density: ρ_s (circles), inverse spatial correlation length ξ^{-1} (diamonds) and superfluid susceptibility: Σ^2 (squares) as a function of transverse field, h. Results shown are derived using a combination of system sizes.

Figure 5.8: PIMC (QMC) results adapted (Priyadarshee et al., 2006) that clearly locate the critical point that demarcates the SF-MI transition of eq. 5.A.8 in 2d.

They can therefore be equivalently represented by the transverse-field quantum XY model:

$$H = -\frac{t}{2}\sum_{\langle i,j\rangle}\left[\hat{S}_i^+\hat{S}_j^- + \hat{S}_j^+\hat{S}_i^-\right] + \sum_i hS_i^z, \tag{5.A.8}$$

where $\hat{S}_i^-$ and $\hat{S}_i^+$ are the spin-1/2 ladder operators satisfying the commutation relation: $\left[\hat{S}_i^-, \hat{S}_i^+\right] = 2\delta_{ij}\hat{S}_i^z$ and $\hat{S}^z$ measures the transverse spin component, coupled to an external field, h. Clearly, the equivalence between hardcore bosons and quantum spins is obtained via the mapping: $\left\{\hat{b}_i^+, \hat{b}_i, \hat{n}_i - \frac{1}{2}, \mu\right\} = \left\{\hat{S}_i^+, \hat{S}_i^-, \hat{S}_i^z, h\right\}$.

Phase diagram

With only a single parameter to tune, the zero temperature phase diagram can be represented on a straight line that manifests two phases at known critical points: $h_c/t = 2$ (Priyadarshee et al., 2006) with in-plane XY order when $h/t < h_c/t$ and when $h/t > h_c/t$, an S_z polarized phase. These phases can be identified by keeping track of κ and ρ_s as a function of h/t as in fig 5.8 and mimic the SF and MI phases respectively. The insulator-conductor transition yields mean-field critical exponents (Priyadarshee et al., 2006).

CHAPTER 6

QMC-SDE TECHNIQUE: A HYBRID

6.1 Motivation

We have thus far discussed two distinct numerical methods, the SSE and the PPR, both of which have their advantages and disadvantages. The SSE along with most QMC variants are primarily used for simulating imaginary time dynamics but is limited by the sign problem when applied to real time simulations. Generally speaking, this amounts to the appearance of negative weights, which are unphysical. On the other hand, while the PPR is in principle able to compute imaginary time dynamics, it requires the use of drift gauges which then necessitates the introduction of a weight term: Ω, in the formalism (cf. section 2.6.1). More often than not, the distribution of the weight is far from Gaussian and systematic errors arise (Dowling et al., 2007). The PPR has therefore primarily been used for simulating real time dynamics. Interestingly despite its extensive use and with the exception of a few cases (Olsen and Bradley, 2009), initializing the density operator within the PP formalism, beyond a pure state, remains a challenging issue that has not been thoroughly addressed. For instance, how does one initialize the density operator to reflect the quantum correlations of a strongly correlated system in its ground state.

For the TIM simulated in chapters 2 and 3, the initial state was taken to be either polarized up or down, corresponding to the ground state of the system with vanishing transverse field, h. In this limit, the distribution of the stochastic variables are trivial delta functions. How one should initialize the stochastic variables when $h \neq 0$ however, is unclear. To this end, we propose a hybrid formalism that allows us to take advantage of the best features of both algorithms. We are currently in the development stages of this novel formalism which we will document in this chapter.

6.2 Sampling the density operator

The standard SSE formalism only samples the diagonal elements of the density operator via the partition function, in a given orthogonal basis $\{|\alpha\rangle\}$, i.e.

$$Z = \sum_{\alpha} \langle \alpha | \rho | \alpha \rangle, \tag{6.2.1}$$

and non-zero configurations that are sampled are indicative of the diagonal elements of the density operator: $|\alpha\rangle\langle\alpha|$. A full description of the density operator however requires calculation of its off-diagonal elements as well. To this end, we construct an analogous albeit *unphysical* quantity:

$$Z' = \sum_{\alpha} \sum_{\beta} \langle \alpha | \rho | \beta \rangle, \tag{6.2.2}$$

where the states $|\beta\rangle$ and $\langle\alpha|$ are unconstrained to be equal to each other. In this case, contributing configurations allow us to sample off-diagonal density operators: $|\alpha\rangle\langle\beta|$. Strictly speaking, this quantity will also sample the diagonal elements as well. However for an N-site, m-state system, there is an overwhelming number of off-diagonal elements compared to the diagonal elements, i.e. a ratio of $m^{2N} - 1 : 1$. It is therefore preferable to split up the sampling into diagonal and off-diagonal components of the density operator. These initial diagonal and off-diagonal density operators can then be easily initialized in the SU(2) coherent state basis, and subsequently propagated in time using stochastic equations. A schematic description of algorithm is illustrated in fig. 6.1, where the imaginary time evolution is depicted on a hyper-plane, while the real time evolution occurs on the surface of the Bloch sphere. The exact quantum mechanical evolution of the average of the system can then be calculated from a simple stochastic average over all Bloch spheres trajectories.

6.3 SSE sampling of configurations

With periodic boundary conditions in the trace relaxed, both insertion of single diagonal and single off-diagonal operators are now allowed. This gives rise to increased flexibility of possible local updates, unlike the conventional SSE formalism. For instance, one may consider updates of the form:

- $\hat{I}_b \longleftrightarrow \hat{H}_{\text{diagonal},b}$
- $\hat{I}_b \longleftrightarrow \hat{H}_{\text{off-diagonal},b}$
- $\hat{H}_{\text{off-diagonal},b} \longleftrightarrow \hat{H}_{\text{diagonal},b}$,

where the subscript b indicates bond index, $\hat{I}_b$ is the identity operator, $\hat{H}_{\text{diagonal}}$ is a diagonal operator in the chosen basis and $\hat{H}_{\text{off-diagonal}}$ is off-diagonal. The last two updates are specific to the samplings of Z'. The directed loop updates still hold in this formalism as they depend only on the vertex weights and their respective probability tables, which are unaltered when calculating Z'. Since the directed loop is a much more efficient way of sampling off-diagonal operators, one can just rely on the same procedure as the original SSE, namely a combination of diagonal and directed loop

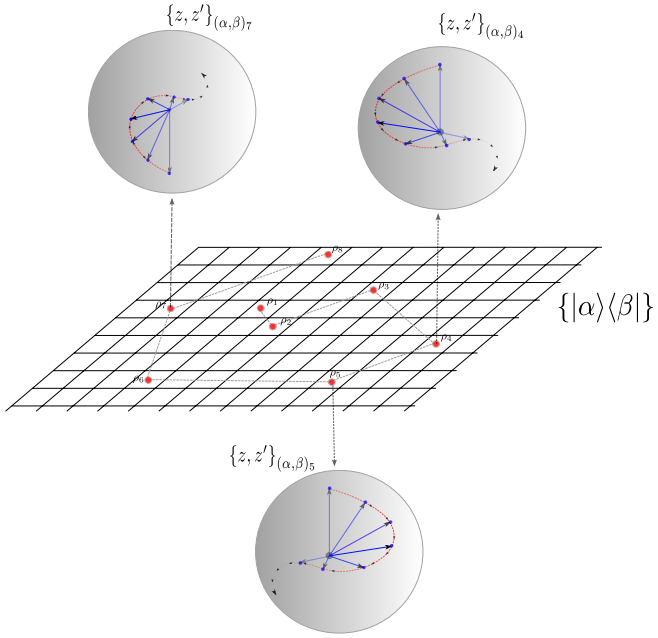

Figure 6.1: Schematic representation of the sse-sde algorithm. The horizontal plane represents the discrete operator basis which will be sampled according to the Boltzmann weight using the modified SSE. This is represented by the gray path with the red dots representing independent samples. Each point on the discrete basis: $\{|\alpha\rangle\langle\beta|\}$ can be mapped on to an equivalent point on the Bloch sphere (for spin-1/2 systems), which is subsequently evolved using the stochastic differential equations derived from the PPR. We have drawn three example Bloch spheres and a possible evolution of the stochastic variables, which can be represented by a path on the surface. The blue arrows demarcates the Bloch spin.

updates. However unlike the original SSE, we now have to keep track of two unique spin states at the boundaries: $|\beta\rangle(=\alpha_0\rangle)$ and $|\alpha\rangle(=|\alpha_L)\rangle$ in eq. 6.2.2. Another crucial modification to the formalism is that the directed loops terminate right away should they hit the propagation boundaries.

6.4 Stochastic evolution.

To reiterate, Z' does not allow us to calculate anything meaningful unlike Z, it only provides us the means to sample the off-diagonal matrix elements of the density operator, to be subsequently used to seed the SDEs. There are however some intricacies that need to be carefully dealt with when initializing the density operator in an off-diagonal kernel, which we will discuss in this section.

First, let us consider the explicit form of the normalized kernel: $\Lambda = \frac{|z\rangle\langle z'^*|}{|z'^*\rangle\langle z|}$ in the S^z-basis:

$$\Lambda = \begin{bmatrix} e^R & e^Q \\ e^{-Q} & e^{-R} \end{bmatrix} \frac{1}{2\cosh(R)} \tag{6.4.1}$$

where $R = \frac{1}{2}(z+z')$ and $Q = \frac{1}{2}(z-z')$. With this representation, initializing the density operator in a pure state is a fairly straightforward procedure. This corresponds to the limit: $(z,z') \to (\pm\infty,\pm\infty) \equiv$

$(R,Q) \to (\pm\infty,0)$ and is well defined because of the normalization of $\cosh(R)$, i.e.:

$$\lim_{(R,Q)\to(+\infty,0)} \Lambda = \begin{bmatrix} 1 & 0 \\ 0 & 0 \end{bmatrix} \tag{6.4.2}$$

and

$$\lim_{(R,Q)\to(-\infty,0)} \Lambda = \begin{bmatrix} 0 & 0 \\ 0 & 1 \end{bmatrix}. \tag{6.4.3}$$

Off-diagonal states, corresponding to the limits: $(z,z') \to (\pm\infty,\mp\infty) \equiv (R,Q) \to (0,\pm\infty)$ however cannot be properly controlled with the normalization: $1/\cosh(R)$ and instead we get:

$$\lim_{(R,Q)\to(0,+\infty)} \Lambda = \begin{bmatrix} 0 & +\infty \\ 0 & 0 \end{bmatrix} \tag{6.4.4}$$

and

$$\lim_{(R,Q)\to(0,-\infty)} \Lambda = \begin{bmatrix} 0 & 0 \\ +\infty & 0 \end{bmatrix}. \tag{6.4.5}$$

This is further demonstrated if one considers the estimator of $\langle S^x \rangle = \frac{1}{2}(\cosh(R+Q) - \sinh(R+Q)\tanh(R))$. One immediately realises that $\lim_{(R,Q)\to(0,\pm\infty)} \langle S^x \rangle \to \infty$. This unphysical result is simply a pathological effect of the normalized kernel chosen.

6.5 Specialised kernel for off-diagonal elements.

To circumvent the issue with off-diagonal elements, we instead introduce the unnormalized kernel.

$$\Lambda' = \frac{|z\rangle\langle z'^*|}{\cosh(z)+\cosh(z')}, \tag{6.5.1}$$

such that:

$$\mathrm{Tr}(\Lambda') = \frac{2\cosh(R)}{\cosh(z)+\cosh(z')}. \tag{6.5.2}$$

One can easily show that evaluating Λ' at the relevant limits now allow both diagonal and off-diagonal elements to be initialized in a well-defined fashion. With the new kernel choice, it is now necessary to rederive new correspondence relations, SDEs and observable estimates which we will detail in the remaining in this chapter.

6.6 Correspondence relations

Before we begin, let us highlight the use of the following abbreviation for notational convenience: $(c,s,c',s') = (\cosh(z),\sinh(z),\cosh(z'),\sinh(z'))$. Their upper case equivalents correspond to functions of $R = (z+z')/2$ instead so that $(C,S) = (\cosh(R),\sinh(R))$. Note that the latter functions have no primed counter parts because it is symmetric under the transformation: c.c.$'$ (recall section 3.3, where we introduced the operation $c.c'$ which implies the transformation $z \leftrightarrow z'$ and complex

numbers are complex conjugated).

Correspondence relations generally require the explicit calculation of the following identity:

$$\frac{\partial \Lambda}{\partial z} = \frac{1}{N}\frac{\partial \Lambda_o}{\partial z} - \frac{1}{N^2}\frac{\partial N}{\partial z}\Lambda_o \tag{6.6.1}$$

$$= \frac{1}{N}\frac{\partial \Lambda_o}{\partial z} - \frac{1}{N}\frac{\partial N}{\partial z}\Lambda, \tag{6.6.2}$$

which upon rearranging gives:

$$\frac{1}{N}\frac{\partial \Lambda_o}{\partial z} = \frac{\partial \Lambda}{\partial z} + \frac{1}{N}\frac{\partial N}{\partial z}\Lambda \tag{6.6.3}$$

where N is an arbitrary function of z, z'. In the generic PPR formalism, it is chosen to be the trace of Λ_o. For the new kernel, Λ', we make the choice $N = \cosh(z) + \cosh(z')$ instead in addition to the usual base kernel: $\Lambda_o = |z\rangle\langle z'^*|$

$$\frac{1}{N}\frac{\partial \Lambda_o}{\partial z} = \frac{\partial \Lambda}{\partial z} + \frac{\sinh(z)}{\cosh(z) + \cosh(z')}\Lambda \tag{6.6.4}$$

$$= \frac{\partial \Lambda}{\partial z} + \frac{s}{c + c'}\Lambda, \tag{6.6.5}$$

The key identities that we will use to derive correspondence relations are the identities for the basis vectors:

$$\begin{bmatrix} 1 \\ 0 \end{bmatrix} = e^{-z/2}\left(\frac{\partial}{\partial z} + \frac{1}{2}\right)|z\rangle \tag{6.6.6}$$

$$\begin{bmatrix} 0 \\ 1 \end{bmatrix} = e^{z/2}\left(-\frac{\partial}{\partial z} + \frac{1}{2}\right)|z\rangle \tag{6.6.7}$$

as well as the correspondence relations for an unnormalized off-diagonal kernel:

$$S^x\Lambda_o = \left(\frac{1}{2}c - s\frac{\partial}{\partial z}\right)\Lambda_o \tag{6.6.8}$$

$$S^y\Lambda_o = -i\left(\frac{1}{2}s + c\frac{\partial}{\partial z}\right)\Lambda_o \tag{6.6.9}$$

$$S^z\Lambda_o = \frac{\partial}{\partial z}\Lambda_o. \tag{6.6.10}$$

A sample derivation for $S^x\Lambda'$ is shown below. First, noting that: $S^x|z\rangle = \begin{bmatrix} e^{-z/2} \\ e^{z/2} \end{bmatrix}$, we can use

eq. 6.6.6 and eq. 6.6.7 to rewrite this as:

$$S^x|z\rangle = \frac{1}{2}\left[e^{-z/2}\left[e^{-z/2}\left(\frac{\partial}{\partial z}+\frac{1}{2}\right)|z\rangle\right]+e^{z/2}\left[e^{z/2}\left(-\frac{\partial}{\partial z}+\frac{1}{2}\right)|z\rangle\right]\right] \tag{6.6.11}$$

$$= \frac{1}{2}\left[(e^{-z}-e^{z})\frac{\partial}{\partial z}+\frac{1}{2}(e^{-z}+e^{z})\right]|z\rangle \tag{6.6.12}$$

$$= \left(-s\frac{\partial}{\partial z}+\frac{1}{2}c\right)|z\rangle. \tag{6.6.13}$$

To obtain the correspondence relation for the desired kernel Λ', we multiply the equation from the left by the bra: $\frac{\langle z'|}{N}$ to get

$$S^x\Lambda = \left(-s\frac{1}{N}\frac{\partial}{\partial z}\Lambda_o+\frac{1}{2}c\Lambda\right). \tag{6.6.14}$$

Putting eq. 6.6.5 to use gives us the desired result:

$$S^x\Lambda = -s\left(\frac{\partial\Lambda}{\partial z}+\frac{s}{c+c'}\right)\Lambda+\frac{1}{2}c\Lambda \tag{6.6.15}$$

$$= \left(-s\frac{\partial}{\partial z}-\frac{s^2}{c+c'}+\frac{c}{2}\right)\Lambda \tag{6.6.16}$$

The left correspondence relations are easily derived by taking $z\to z'$ and the complex conjugate of any complex variables, which we will denote as the operation: c.c.$'$. The remaining identities can be obtained in a similar fashion:

$$\hat{S}^z\Lambda = \left(\frac{\partial}{\partial z}+\frac{s}{c+c'}\right)\Lambda \tag{6.6.17}$$

$$\hat{S}^x\Lambda = \left(-s\frac{\partial}{\partial z}-\frac{s^2}{c+c'}+\frac{1}{2}c\right)\Lambda \tag{6.6.18}$$

$$\hat{S}^y\Lambda = -i\left(c\frac{\partial}{\partial z}+\frac{sc}{c+c'}-\frac{1}{2}s\right)\Lambda. \tag{6.6.19}$$

and under the operation c.c.$'$, we immediately obtain the complementary ordering:

$$\Lambda\hat{S}^z = \left(\frac{\partial}{\partial z'}+\frac{s'}{c+c'}\right)\Lambda \tag{6.6.20}$$

$$\Lambda\hat{S}^x = \left(-s'\frac{\partial}{\partial z'}-\frac{s'^2}{c+c'}+\frac{1}{2}c'\right)\Lambda \tag{6.6.21}$$

$$\Lambda\hat{S}^y = i\left(c'\frac{\partial}{\partial z'}+\frac{s'c'}{c+c'}-\frac{1}{2}s'\right)\Lambda. \tag{6.6.22}$$

6.7 Gauge-P representation and stochastic evolution equations

A point of concern when using an unnormalized kernel is that a direct implementation of the usual steps to derive the FPE will generate constant terms, thereby requiring the use of the gauge-P representation (Deuar and Drummond, 2002) (see section 2.6.1). As an example of how this arises, we consider the TIM again and the contribution of the transverse field term to the FPE:

$$S^x\Lambda - \Lambda S^x = -s\frac{\partial}{\partial z} - \frac{s^2}{c+c'} + \frac{c}{2} + s'\frac{\partial}{\partial z'} + \frac{s'^2}{c+c'} + \frac{c'}{2}. \tag{6.7.1}$$

Paying attention to the constant terms and after some algebraic manipulation, we see that

$$-\frac{s^2}{c+c'} + \frac{c}{2} + \frac{s'^2}{c+c'} - \frac{c'}{2} = \frac{-s^2 - s^2 + c^2 + cc' + s'^2 + s'^2 - c'^2 - cc'}{2(c+c')} \tag{6.7.2}$$

$$= \frac{(s'^2 - s^2) + (cc' - c'c) + (c^2 - s^2) - (c'^2 - s'^2)}{2(c+c')} \tag{6.7.3}$$

$$= \frac{1 - c^2 - 1 + c'^2}{2(c+c')} \tag{6.7.4}$$

$$= \frac{(c'-c)(c'+c)}{2(c+c')} \tag{6.7.5}$$

$$= \frac{c-c'}{2}. \tag{6.7.6}$$

Constant terms as discussed in section 2.6.1, do contribute to the evolution of Ω and therefore cannot simply be discarded. Carrying on, if we map the Ising term in the TIM onto an FPE, we get the following expression:

$$S_i^z S_j^z \Lambda - \Lambda S_i^z S_j^z = \left[\left(\frac{\partial}{\partial z_j} + \frac{s_j}{c_j + c_j'}\right)\left(\frac{\partial}{\partial z_i} + \frac{s_i}{c_i + c_i'}\right) - \text{c.c.}'\right]\Lambda' \tag{6.7.7}$$

$$= \left[\left(\frac{\partial^2}{\partial z_i \partial z_j} + \frac{s_i}{c_i + c_i'}\frac{\partial}{\partial z_j} + \frac{s_j}{c_j + c_j'}\frac{\partial}{\partial z_i} + \frac{s_i s_j}{(c_i + c_i')(c_j + c_j')}\right) - c.c.\right]\Lambda' \tag{6.7.8}$$

This implies a diffusion matrix that can segmented according to the range of the interactions (nearest neighbor for the TIM):

$$\underline{D}_{\langle ij\rangle} = i\begin{bmatrix} 0 & 1 \\ 1 & 0 \end{bmatrix} \tag{6.7.9}$$

to yield the noise matrix:

$$\underline{B}_{\langle ij\rangle} = \sqrt{\frac{i}{2}}\begin{bmatrix} 1 & -i \\ 1 & i \end{bmatrix} \tag{6.7.10}$$

which is in fact the same noise terms obtained when using a normalized kernel. The only change takes place in the ising drift terms of the final SDEs:

$$\frac{dz_i}{dt} = i\left(\frac{s_{i+1}}{c_{i+1}+c'_{i+1}} + \frac{s_{i-1}}{c_{i-1}+c'_{i-1}}\right) - ihs_i + \eta_i + i\eta^*_{i-1} \tag{6.7.11}$$

$$\frac{dz'_i}{dt} = -i\left(\frac{s'_{i+1}}{c_{i+1}+c'_{i+1}} + \frac{s'_{i-1}}{c_{i-1}+c'_{i-1}}\right) + ihs'_i + \eta'_i - i\eta'^*_{i-1} \tag{6.7.12}$$

$$\frac{d\omega}{dt} = i\left[\sum_{\langle i,j\rangle}\frac{s_is_j - s'_is'_j}{(c_i+c'_i)(c_j+c'_j)} + \frac{1}{2}\sum_i h\left(c_i - c'_i\right)\right] \tag{6.7.13}$$

where $\langle\langle \eta_i(t)\eta^*_j(t')\rangle\rangle = \delta(t-t')\delta_{ij}$ are complex Wiener increments and we have introduced the new logarithmic weight variable: $\omega = \ln\Omega$.

6.7.1 Switching to y-variables

In order to circumvent the ill-defined mapping at the poles of the Bloch sphere, we will implement the same transformation and define y-variables such that:

$$y = \begin{cases} e^{-z} \text{ if } z_r > 0 \\ \\ e^{z} \text{ if } z_r < 0 \end{cases} \implies z = \begin{cases} -\ln(y) \text{ if } z_r > 0 : S = +1 \\ \\ \ln(y) \text{ if } z_r < 0 : S = -1 \end{cases} \tag{6.7.14}$$

Table 6.2 and table 6.3 below summarizes the transformation of several important complex functions of the variables y and y' depending on the sector, S which they belong to.

6.7.2 Calculating observables

Observables will now have to be modified because Λ' is unnormalized. We will need to evaluate the following the derivative of the trace, using eq. 6.5.2

$$\frac{\partial \mathrm{Tr}(\Lambda')}{\partial z} = \frac{S}{c+c'} - \frac{2sC}{(c+c')^2} = \frac{Sc + Sc' - 2sC}{(c+c')^2}. \tag{6.7.15}$$

To compute the expectation value for the y spin component for example, we evaluate:

$$\langle S^y\rangle = \frac{\Re\langle\langle \mathrm{Tr}(\Omega S^y\Lambda)\rangle\rangle}{\Re\langle\langle \mathrm{Tr}(\Lambda\Omega)\rangle\rangle}, \tag{6.7.16}$$

$(z,z') \rightarrow$	(+,+)	(+,-)	(-,+)	(-,-)
R	$-\frac{1}{2}\ln(yy')$	$\frac{1}{2}\ln(\frac{y}{y'})$	$\frac{1}{2}\ln(\frac{y'}{y})$	$\frac{1}{2}\ln(yy')$
$\sinh(R)$	$\frac{1}{2}\frac{1-yy'}{\sqrt{yy'}}$	$\frac{1}{2}\frac{y'-y}{\sqrt{yy'}}$	$\frac{1}{2}\frac{y-y'}{\sqrt{yy'}}$	$\frac{1}{2}\frac{yy'-1}{\sqrt{yy'}}$
$\cosh(R)$	$\frac{1}{2}\frac{1+yy'}{\sqrt{yy'}}$	$\frac{1}{2}\frac{y'+y}{\sqrt{yy'}}$	$\frac{1}{2}\frac{y+y'}{\sqrt{yy'}}$	$\frac{1}{2}\frac{yy'+1}{\sqrt{yy'}}$
$\tanh(R)$	$\frac{1-yy'}{1+yy'}$	$\frac{y'-y}{y'+y}$	$\frac{y-y'}{y'+y}$	$\frac{yy'-1}{yy'+1}$

Figure 6.2: Transformation table between z and y variables for multivariate complex functions, depending on the sector, S.

$(z \text{ or } z') \rightarrow$	+	-
$\cosh(z) =$	$\frac{1}{2}\frac{1+y^2}{y}$	$\frac{1}{2}\frac{1+y^2}{y}$
$\sinh(z)$	$\frac{1}{2}\frac{1-y^2}{y}$	$\frac{1}{2}\frac{y^2-1}{y}$

Figure 6.3: Transformation table between z and y variables of univariate complex functions depending on the sector, S.

where $\Re$ denotes the real part of the complex function. Using eq. 6.6.22 the numerator yields:

$$\begin{aligned}
\Omega \mathrm{Tr}(S^y \Lambda') &= -i\left(c\frac{\partial}{\partial z}\mathrm{Tr}\Lambda' + \frac{sc}{c+c'}\mathrm{Tr}(\Lambda') - \frac{s}{2}\mathrm{Tr}(\Lambda')\right) && (6.7.17)\\
&= -i\Omega\left(\frac{Sc^2 + Scc' - 2scC}{(c+c')^2} + \frac{2scC}{(c+c')^2} - \frac{2sC}{2(c+c')}\right) && (6.7.18)\\
&= i\frac{sC - cS}{c+c'} && (6.7.19)
\end{aligned}$$

and so:

$$\langle S^y \rangle = \Re\langle\langle i\frac{\Omega(sC - cS)}{c+c'}\rangle\rangle \Big/ \Re\langle\langle i\frac{2\Omega C}{c+c'}\rangle\rangle \quad (6.7.20)$$

The estimators for the other components can be derived in a similar fashion:

$$\langle S^z \rangle = \Re\langle i\frac{\Omega S}{c+c'}\rangle \Big/ \Re\langle\frac{2\Omega C}{c+c'}\rangle \quad (6.7.21)$$

$$\langle S^x \rangle = \Re\langle\frac{\Omega(cC - sS)}{c+c'}\rangle \Big/ \Re\langle\frac{2\Omega C}{c+c'}\rangle. \quad (6.7.22)$$

It is important to note that the expectation value is given by the independent stochastic averaging of the real parts of the numerator and denominator and not of the whole fraction.

6.8 Status

Unfortunately, we have not been able to produce any concrete simulations for the hybrid scheme. This chapter was written with the purpose of laying the foundation and blueprint for future numerical implementation. A preliminary investigation however does seem to suggest that additional optimization may be necessary to preserve the normalization of the stochastic average of the weight term and prevent it from decaying exponentially.

CHAPTER 7

CONCLUSION

In the first half of this thesis, we performed a detailed investigation of the quantum phase-space method called the positive-P representation and its effectiveness at simulating the real time dynamics of quantum spin systems. In this formalism, the quantum degrees of freedom are mapped on to stochastic variables that evolve according to Ito stochastic differential equations. The positive-P representation was originally designed to handle few mode problems and has only recently been extended to multi-mode systems, particularly for use in the simulation of colliding weakly interacting BECs. However, an application to strongly correlated spin systems had not been explored. Furthermore, in light of the recent advances in optical lattices, the study of non-equilibrium dynamics using different quenching protocols can now be experimentally realized and is fast becoming an increasingly fashionable avenue of research. This strongly motivated our first publication where we used the Schwinger boson representation of quantum spins in order to apply the positive-P, and successfully simulated the ensuing dynamics of the anisotropic quantum XXZ spin-1/2 model (and its derivatives) in a transverse field, after an instantaneous quench of a parameter of the system. While exact results can indeed be obtained, they were only available for relatively short simulation lifetimes of up to $0.5 - 1.0J/\hbar$, where J is the strength of the exchange interactions. Beyond this time scale, spiking occurs which results in either systematic errors or numerical overflow. This spiking behaviour is a notorious feature of the positive-P technique and can be essentially attributed to ill-defined regions of phase space where the kernel is unnormalizable but where trajectories unfortunately tend to gravitate towards to compensate for this.

Our attempt to significantly improve simulation lifetimes formed the premise of our second publication. In this work, we focused our efforts on the quench dynamics of the transverse-field Ising model. Instead, we switched the underlying basis of the positive-P representation to that of SU(2) coherent states, which seemed more aligned with the physical nature of the system. The phase space can now be mapped onto the surface of the unit Bloch sphere with the exception of a single ill-defined point at either of its poles (depending on the definition chosen). Using an elaborate change of variables

toggling mechanism, we were able to carefully avoid these poles, which when combined with a novel extrapolation scheme culminated in a significant improvement of simulation life times. Depending on the observable calculated, we were able to achieve an extension of a two to three-fold improvement in simulation lifetime $\sim 2.-3.J/\hbar$, versus a bare application of the positive-P (in our first publication).

In our third publication that constitutes the second half of the thesis, we present our results on the universality class of the superfluid-Bose glass transition in a 2d dirty-boson system. To this end, we performed large scale quantum Monte-Carlo simulations on two independent quantum models, i.e. a 2d quantum rotor model and the 2d hardcore boson model with on-site disorder introduced through a random chemical potential. Most importantly, we obtain a highly accurate estimate for the elusive dynamic critical exponent, z, using up to $5\times10^4-10^5$ disorder realizations for each data point. Unlike a majority of prior simulations in the literature, we make no biasing assumptions on z in determining the critical exponents of the transition. Our final independent estimates of the exponents: $\{\nu,\eta,z\}$ are $\{0.99(3),-0.16(8),1.88(8)\}_{\mathrm{HC}}$ for the hardcore boson model and $\{1.00(2),-0.3(1),1.99(5)\}_{\mathrm{QR}}$ for the quantum rotor model, both agreeing within error bars. This presents compelling evidence that Fisher's long-standing result: $z=d$ for the dirty-boson Superfluid-Bose glass transition still holds in 2d, contrary to the plethora of recent numerical and analytical contradictory results. Additionally we verify that the quantum Harris criterion is satisfied as an equality while the bound on the anomalous dimensions: $\eta\leq 2-d$ is met.

The natural future direction of this work is outlined in Chapter 6. We present a novel algorithm that is in principle able to hybridize the strongest features of quantum Monte-Carlo and the positive-P representation. The general idea is to sample the initial states from the Monte-Carlo algorithm and subsequently evolve it using the stochastic equations of the positive-P. Of course, it may seem more intuitive to obtain the ground state by using the gauge-P representation to evolve the system in imaginary time and subsequently carrying out the evolution using the positive-P. However, the inherent barrier to this strategy is the typically short simulation life times of the formalism (especially in the regime of strong correlations), which would preclude reaching the ground state at large imaginary time (or inverse temperature) values. The best demonstration to-date of such ground state simulations using a phase space technique, is the post- and pre-projected Gaussian basis Monte-Carlo technique for Fermionic systems (Corney and Drummond, 2004), although extra care has to be taken to deal with potential sign problems (Rombouts, 2006) and to preserve the symmetry of the system (Aimi and Imada, 2007, Assaad et al., 2005). Curiously, its real time evolution has not been explored, presumably due to unfavorable simulation life times (especially in strongly correlated systems). What differentiates our approach from the latter is that we now wish to generate strongly correlated initial states using a stable algorithm (QMC) which can then be evolved via the positive-P built from the SU(2) basis with a potentially simpler Hamiltonian, so as to obtain as long as possible simulation lifetimes. Currently, we have only outlined the theoretical framework for this approach and have yet to produce any concrete numerical results. Interestingly, an algorithm with the same premise but using the Wigner representation has recently been proposed as well (Schachenmayer et al., 2015).

A different avenue of research that I would be most interested in exploring is the application of the positive-P to large spin systems, which was brought to my attention through a recent work on a Dicke Network (Mandt et al., 2014) in the presence of dissipation and pumping. It is my opinion that the positive-P might be better suited for large spin systems as opposed to the pure quantum

case. For sufficiently large spins, it is my conjecture that the effects of quantum fluctuations may be linearized as in a Bogoliubov approximation (Deuar et al., 2011), potentially resulting in well-behaved stochastic differential equations and a significant extension of simulation lifetimes.

We are highly optimistic of the future direction of our research and it is our opinion that phase space methods such as the positive-P representation still has room for further optimization and can one day be developed into a state-of-the-art numerical tool for condensed matter system simulations, particular in real time.

BIBLIOGRAPHY

Aimi, T. and Imada, M. (2007). Gaussian-basis monte carlo method for numerical study on ground states of itinerant and strongly correlated electron systems. Journal of the Physical Society of Japan, 76(8):084709.

Albuquerque, A. F., Alet, F., Sire, C., and Capponi, S. (2010). Quantum critical scaling of fidelity susceptibility. Phys. Rev. B, 81:064418.

Alet, F., Wessel, S., and Troyer, M. (2005). Generalized directed loop method for quantum monte carlo simulations. Phys. Rev. E, 71:036706.

Álvarez Zúñiga, J. P., Luitz, D. J., Lemarié, G., and Laflorencie, N. (2014). Critical Properties of the Superfluid - Bose Glass Transition in Two Dimensions. ArXiv e-prints.

Anderson, P. (1959). Theory of dirty superconductors. Journal of Physics and Chemistry of Solids, 11(1âĂŞ2):26 – 30.

Arnold, L. (1974). Stochastic Differential Equations. New York: Wiley.

Assaad, F. F., Werner, P., Corboz, P., Gull, E., and Troyer, M. (2005). Symmetry projection schemes for gaussian monte carlo methods. Phys. Rev. B, 72:224518.

Ballesteros, H. G., Fernández, L. A., Martín-Mayor, V., Muñoz Sudupe, A., Parisi, G., and Ruiz-Lorenzo, J. J. (1998). Critical exponents of the three-dimensional diluted ising model. Phys. Rev. B, 58:2740–2747.

Barry, D. W. and Drummond, P. D. (2008). Qubit phase space: $\mathsf{SU}(n)$ coherent-state p representations. Phys. Rev. A, 78:052108.

Berry, M. and Keating, J. (1999). H=xp and the riemann zeros. In Lerner, I., Keating, J., and Khmelnitskii, D., editors, Supersymmetry and Trace Formulae, volume 370 of NATO ASI Series, pages 355–367. Springer US.

Bissbort, U. and Hofstetter, W. (2009). Stochastic mean-field theory for the disordered bose-hubbard model. EPL (Europhysics Letters), 86(5):50007.

Bloch, I. (2010). Ultracold quantum gases in optical lattices. Nat Phys, 1(1).

Boninsegni, M., Prokof'ev, N. V., and Svistunov, B. V. (2006). Worm algorithm and diagrammatic monte carlo: A new approach to continuous-space path integral monte carlo simulations. Phys. Rev. E, 74:036701.

Britton, J. W., Sawyer, B. C., Keith, A. C., Wang, C.-C. J., Freericks, J. K., Uys, H., Biercuk, M. J., and Bollinger, J. J. (2012). Engineered two-dimensional ising interactions in a trapped-ion quantum simulator with hundreds of spins. Nature, 484(7395):489–492.

Bruder, C., Fazio, R., and SchÃűn, G. (2005). The bose-hubbard model: from josephson junction arrays to optical lattices. Annalen der Physik, 14(9-10):566–577.

Bruus, H. and Flensberg, K. (2004). Many-body quantum theory in condensed matter physics - an introduction. Oxford University Press.

Caffarel, M. and Krauth, W. (1994). Exact diagonalization approach to correlated fermions in infinite dimensions: Mott transition and superconductivity. Phys. Rev. Lett., 72:1545–1548.

Calabrese, P., Essler, F. H. L., and Fagotti, M. (2011). Quantum quench in the transverse-field ising chain. Phys. Rev. Lett., 106:227203.

Calabrese, P., Essler, F. H. L., and Fagotti, M. (2012a). Quantum quench in the transverse field ising chain: I. time evolution of order parameter correlators. Journal of Statistical Mechanics: Theory and Experiment, 2012(07):P07016.

Calabrese, P., Essler, F. H. L., and Fagotti, M. (2012b). Quantum quenches in the transverse field ising chain: Ii. stationary state properties. Journal of Statistical Mechanics: Theory and Experiment, 2012(07):P07022.

Campostrini, M., Hasenbusch, M., Pelissetto, A., Rossi, P., and Vicari, E. (2001). Critical behavior of the three-dimensional XY universality class. Phys. Rev. B, 63:214503.

Caneva, T., Canovi, E., Rossini, D., Santoro, G. E., and Silva, A. (2011). Applicability of the generalized gibbs ensemble after a quench in the quantum ising chain. Journal of Statistical Mechanics: Theory and Experiment, 2011(07):P07015.

Caneva, T., Fazio, R., and Santoro, G. E. (2007). Adiabatic quantum dynamics of a random ising chain across its quantum critical point. Phys. Rev. B, 76:144427.

Carmichael, H. J. (2002). Statistical Methods in Quantum Optics 1: Master Equations and Fokker-Planck Equations. Springer.

Cassidy, A. C., Clark, C. W., and Rigol, M. (2011). Generalized thermalization in an integrable lattice system. Phys. Rev. Lett., 106:140405.

Chae, S. C., Lee, N., Horibe, Y., Tanimura, M., Mori, S., Gao, B., Carr, S., and Cheong, S.-W. (2012). Direct observation of the proliferation of ferroelectric loop domains and vortex-antivortex pairs. Phys. Rev. Lett., 108:167603.

Chayes, J. T., Chayes, L., Fisher, D. S., and Spencer, T. (1986). Finite-size scaling and correlation lengths for disordered systems. Phys. Rev. Lett., 57:2999–3002.

Chen, D., White, M., Borries, C., and DeMarco, B. (2011). Quantum quench of an atomic mott insulator. Phys. Rev. Lett., 106:235304.

Chib, S. and Greenberg, E. (1995). Understanding the metropolis-hastings algorithm. The american statistician, 49(4):327–335.

Cho, S. and Fisher, M. P. A. (1997). Criticality in the two-dimensional random-bond ising model. Phys. Rev. B, 55:1025–1031.

Cohen, E. G. D. (1985). Fundamental problems in statistical mechanics VI. North-Holland.

Continentino, M. A. (2011). Quantum scaling in Many-Body Systems. World Scientific, first ed. edition.

Cormick, C. and Morigi, G. (2012). Structural transitions of ion strings in quantum potentials. Phys. Rev. Lett., 109:053003.

Corney, J. and Drummond, P. (2006). Gaussian phase-space representations for fermions. Physical Review B, 73(12):125112.

Corney, J. F. and Drummond, P. D. (2003). Gaussian quantum operator representation for bosons. Physical Review A, 68(6):063822.

Corney, J. F. and Drummond, P. D. (2004). Gaussian quantum monte carlo methods for fermions and bosons. Physical review letters, 93(26):260401.

Crowell, P. A., Van Keuls, F. W., and Reppy, J. D. (1997). Onset of superfluidity in ^{4}He films adsorbed on disordered substrates. Phys. Rev. B, 55:12620–12634.

Daley, A. J., Kollath, C., SchollwÃűck, U., and Vidal, G. (2004). Time-dependent density-matrix renormalization-group using adaptive effective hilbert spaces. Journal of Statistical Mechanics: Theory and Experiment, 2004(04):P04005.

Dalfovo, F., Giorgini, S., Pitaevskii, L. P., and Stringari, S. (1999). Theory of bose-einstein condensation in trapped gases. Rev. Mod. Phys., 71:463–512.

Damski, B. (2005). The simplest quantum model supporting the kibble-zurek mechanism of topological defect production: Landau-zener transitions from a new perspective. Phys. Rev. Lett., 95:035701.

Damski, B., Zakrzewski, J., Santos, L., Zoller, P., and Lewenstein, M. (2003). Atomic bose and anderson glasses in optical lattices. Phys. Rev. Lett., 91:080403.

Damski, B. and Zurek, W. H. (2010). Soliton creation during a bose-einstein condensation. Phys. Rev. Lett., 104:160404.

De Grandi, C., Gritsev, V., and Polkovnikov, A. (2010). Quench dynamics near a quantum critical point. Phys. Rev. B, 81:012303.

del Campo, A., De Chiara, G., Morigi, G., Plenio, M. B., and Retzker, A. (2010). Structural defects in ion chains by quenching the external potential: The inhomogeneous kibble-zurek mechanism. Phys. Rev. Lett., 105:075701.

del Campo, A., Kibble, T. W. B., and Zurek, W. H. (2013). Causality and non-equilibrium second-order phase transitions in inhomogeneous systems. Journal of Physics: Condensed Matter, 25(40):404210.

del Campo, A., Retzker, A., and Plenio, M. B. (2011). The inhomogeneous kibbleâĂŞzurek mechanism: vortex nucleation during boseâĂŞeinstein condensation. New Journal of Physics, 13(8):083022.

del Campo, A. and Zurek, W. H. (2014). Universality of phase transition dynamics: Topological defects from symmetry breaking. International Journal of Modern Physics A, 29(08):1430018.

D'Errico, C., Lucioni, E., Tanzi, L., Gori, L., Roux, G., McCulloch, I. P., Giamarchi, T., Inguscio, M., and Modugno, G. (2014). Observation of a disordered bosonic insulator from weak to strong interactions. Phys. Rev. Lett., 113:095301.

Deuar, P. (2005). First-principles quantum simulations of many-mode open interacting Bose gases using stochastic gauge methods. PhD thesis, PhD Thesis, 2005.

Deuar, P. (2015). private communication.

Deuar, P., Chwedeńczuk, J., Trippenbach, M., and Ziń, P. (2011). Bogoliubov dynamics of condensate collisions using the positive-p representation. Phys. Rev. A, 83:063625.

Deuar, P. and Drummond, P. D. (2002). Gauge p representations for quantum-dynamical problems: Removal of boundary terms. Phys. Rev. A, 66:033812.

Deuar, P. and Drummond, P. D. (2006). First-principles quantum dynamics in interacting bose gases: I. the positive p representation. Journal of Physics A: Mathematical and General, 39(5):1163.

Deuar, P. and Drummond, P. D. (2007). Correlations in a bec collision: First-principles quantum dynamics with 150 000 atoms. Phys. Rev. Lett., 98(12):120402.

Deuar, P., Sykes, A. G., Gangardt, D. M., Davis, M. J., Drummond, P. D., and Kheruntsyan, K. V. (2009). Nonlocal pair correlations in the one-dimensional bose gas at finite temperature. Phys. Rev. A, 79:043619.

Deutsch, J. M. (1991). Quantum statistical mechanics in a closed system. Phys. Rev. A, 43:2046–2049.

Dorneich, A. and Troyer, M. (2001). Accessing the dynamics of large many-particle systems using the stochastic series expansion. Phys. Rev. E, 64:066701.

Dowling, M. R., Davis, M. J., Drummond, P. D., and Corney, J. F. (2007). Monte carlo techniques for real-time quantum dynamics. Journal of Computational Physics, 220(2):549 – 567.

Drummond, P. D. (2013). Quantum Dynamics on Extended Phase Space:. The Positive-P Representation. In Proukakis, N. and et al., editors, Quantum Gases: Finite Temperature and Non-Equilibrium Dynamics. Edited by Proukakis Nick et al. Published by World Scientific Publishing Co. Pte. Ltd., 2013. ISBN #9781848168121, pp. 229-240, pages 229–240.

Drummond, P. D. and Gardiner, C. W. (1980). Generalised p-representations in quantum optics. Journal of Physics A: Mathematical and General, 13(7):2353.

Drummond, P. D. and Mortimer, I. K. (1991). Computer simulations of multiplicative stochastic differential equations. Journal of Computational Physics, 93(1):144 – 170.

Dubin, D. H. E. and O'Neil, T. M. (1999). Trapped nonneutral plasmas, liquids, and crystals (the thermal equilibrium states). Rev. Mod. Phys., 71:87–172.

Dziarmaga, J. (2006). Dynamics of a quantum phase transition in the random ising model: Logarithmic dependence of the defect density on the transition rate. Phys. Rev. B, 74:064416.

Dziarmaga, J. (2010). Dynamics of a quantum phase transition and relaxation to a steady state. Advances in Physics, 59(6):1063–1189.

Ejtemaee, S. and Haljan, P. C. (2013). Spontaneous nucleation and dynamics of kink defects in zigzag arrays of trapped ions. Phys. Rev. A, 87:051401.

Elstner, N. and Monien, H. (1999). Dynamics and thermodynamics of the bose-hubbard model. Phys. Rev. B, 59:12184–12187.

Finotello, D., Gillis, K. A., Wong, A., and Chan, M. H. W. (1988). Sharp heat-capacity signature at the superfluid transition of helium films in porous glasses. Phys. Rev. Lett., 61:1954–1957.

Fisher, D. S. (1992). Random transverse field ising spin chains. Phys. Rev. Lett., 69:534–537.

Fisher, M. E., Barber, M. N., and Jasnow, D. (1973). Helicity modulus, superfluidity, and scaling in isotropic systems. Phys. Rev. A, 8:1111–1124.

Fisher, M. P. A., Weichman, P. B., Grinstein, G., and Fisher, D. S. (1989). Boson localization and the superfluid-insulator transition. Phys. Rev. B, 40:546–570.

Flesch, A., Cramer, M., McCulloch, I. P., Schollwöck, U., and Eisert, J. (2008). Probing local relaxation of cold atoms in optical superlattices. Phys. Rev. A, 78:033608.

Friedenauer, A., Schmitz, H., Glueckert, J. T., Porras, D., and Schätz, T. (2008). Simulating a quantum magnet with trapped ions. Nature Physics, 4(10):757–761.

Ghanbari, S., Corney, J. F., and Kieu, T. D. (2010). Finite temperature correlations in the Bose-Hubbard model: application of the Gauge P representation. ArXiv e-prints.

Gilchrist, A., Gardiner, C. W., and Drummond, P. D. (1997). Positive p representation: Application and validity. Phys. Rev. A, 55:3014–3032.

Glauber, R. J. (1963). The quantum theory of optical coherence. Phys. Rev., 130(6):2529–2539.

Goldstein, G. and Andrei, N. (2014). Failure of the local generalized gibbs ensemble for integrable models with bound states. Phys. Rev. A, 90:043625.

Harris, A. B. (1974). Effect of random defects on the critical behaviour of ising models. Journal of Physics C: Solid State Physics, 7(9):1671.

Hastings, M. B., González, I., Kallin, A. B., and Melko, R. G. (2010). Measuring renyi entanglement entropy in quantum monte carlo simulations. Phys. Rev. Lett., 104:157201.

Henelius, P. and Sandvik, A. W. (2000). Sign problem in monte carlo simulations of frustrated quantum spin systems. Phys. Rev. B, 62:1102–1113.

Heyl, M., Polkovnikov, A., and Kehrein, S. (2013). Dynamical quantum phase transitions in the transverse-field ising model. Phys. Rev. Lett., 110:135704.

Humeniuk, S. and Roscilde, T. (2012). Quantum monte carlo calculation of entanglement rényi entropies for generic quantum systems. Phys. Rev. B, 86:235116.

José, J. V., Kadanoff, L. P., Kirkpatrick, S., and Nelson, D. R. (1977). Renormalization, vortices, and symmetry-breaking perturbations in the two-dimensional planar model. Phys. Rev. B, 16:1217–1241.

Kardar, M. (2007). Statistical Physics of Fields. Cambridge University Press. Cambridge Books Online.

Kibble, T. (2007). Phase transition dynamics in the lab and the universe. Physics Today, 60:47–53.

Kibble, T. W. B. (1976). Topology of cosmic domains and strings. Journal of Physics A: Mathematical and General, 9(8):1387.

Kim, K. and Stroud, D. (2008). Quantum monte carlo study of a magnetic-field-driven two-dimensional superconductor-insulator transition. Phys. Rev. B, 78:174517.

Kinoshita, T., Wenger, T., and Weiss, D. S. (2006). A quantum newton's cradle. Nature, 440:900–903.

Krauth, W., Trivedi, N., and Ceperley, D. (1991). Superfluid-insulator transition in disordered boson systems. Physical review letters, 67(17):2307.

Lamporesi, G., Donadello, S., Serafini, S., Dalfovo, F., and Ferrari, G. (2013). Spontaneous creation of kibble-zurek solitons in a bose-einstein condensate. Nature Physics, 9(10):656–660.

Lee, H.-W. (1995). Theory and application of the quantum phase-space distribution functions. Physics Reports, 259(3):147–211.

Lee, J.-W., Cha, M.-C., and Kim, D. (2001). Phase diagram of a disordered boson hubbard model in two dimensions. Phys. Rev. Lett., 87:247006.

Lin, F., Sørensen, E. S., and Ceperley, D. M. (2011). Superfluid-insulator transition in the disordered two-dimensional bose-hubbard model. Phys. Rev. B, 84:094507.

Lin, H. Q. (1990). Exact diagonalization of quantum-spin models. Phys. Rev. B, 42:6561–6567.

Majorana, E. (1932). Atomi orientati in campo magnetico variabile. Il Nuovo Cimento, 9(2):43–50.

Makivić, M., Trivedi, N., and Ullah, S. (1993). Disordered bosons: Critical phenomena and evidence for new low energy excitations. Physical review letters, 71(14):2307.

Mandt, S., Sadri, D., Houck, A. A., and Türeci, H. E. (2014). Stochastic Differential Equations for Quantum Dynamics of Spin-Boson Networks. ArXiv e-prints.

Marković, N., Christiansen, C., Mack, A. M., Huber, W. H., and Goldman, A. M. (1999). Superconductor-insulator transition in two dimensions. Phys. Rev. B, 60:4320–4328.

Marsaglia, G. and Tsang, W. W. (2000). A simple method for generating gamma variables. ACM Trans. Math. Softw., 26(3):363–372.

McCoy, B. M. and Wu, T. T. (1968). Theory of a two-dimensional ising model with random impurities. i. thermodynamics. Phys. Rev., 176:631–643.

McNeil, K. J. and Craig, I. J. D. (1990). Positive-p representation for second-harmonic generation: Analytic and computational results. Phys. Rev. A, 41(7):4009–4018.

Meier, H. and Wallin, M. (2012). Quantum critical dynamics simulation of dirty boson systems. Phys. Rev. Lett., 108:055701.

Meldgin, C., Ray, U., Russ, P., Ceperley, D., and DeMarco, B. (2015). Probing the Bose-Glass–Superfluid Transition using Quantum Quenches of Disorder. ArXiv e-prints.

Midgley, S. L. W., Wüster, S., Olsen, M. K., Davis, M. J., and Kheruntsyan, K. V. (2009). Comparative study of dynamical simulation methods for the dissociation of molecular bose-einstein condensates. Phys. Rev. A, 79:053632.

Mierzejewski, M., Prelovšek, P., and Prosen, T. c. v. (2014). Breakdown of the generalized gibbs ensemble for current-generating quenches. Phys. Rev. Lett., 113:020602.

Moyal, J. E. (1949). Quantum mechanics as a statistical theory. Proc. Cambridge Phil. Sock, 45(99):99–124.

Navon, N., Gaunt, A. L., Smith, R. P., and Hadzibabic, Z. (2015). Critical dynamics of spontaneous symmetry breaking in a homogeneous bose gas. Science, 347(6218):167–170.

Ng, R. (2010). Exact quantum dynamics of spin systems using the positve-P representation. Master's thesis, MSc Thesis, 2010.

Ng, R., Sørensen, E. S., and Deuar, P. (2013). Simulation of the dynamics of many-body quantum spin systems using phase-space techniques. Phys. Rev. B, 88:144304.

Niemeyer, M., Freericks, J. K., and Monien, H. (1999). Strong-coupling perturbation theory for the two-dimensional bose-hubbard model in a magnetic field. Phys. Rev. B, 60:2357–2362.

Norrie, A. A., Ballagh, R. J., and Gardiner, C. W. (2005). Quantum turbulence in condensate collisions: An application of the classical field method. Phys. Rev. Lett., 94:040401.

Olsen, M. and Bradley, A. (2009). Numerical representation of quantum states in the positive-p and wigner representations. Optics Communications, 282(19):3924 – 3929.

Ospelkaus, S., Ospelkaus, C., Wille, O., Succo, M., Ernst, P., Sengstock, K., and Bongs, K. (2006). Localization of bosonic atoms by fermionic impurities in a three-dimensional optical lattice. Phys. Rev. Lett., 96:180403.

Pázmándi, F. and Zimányi, G. T. (1998). Direct mott insulator-to-superfluid transition in the presence of disorder. Phys. Rev. B, 57:5044–5047.

Perret, C. and Petersen, W. P. (2011). Stabilizing simulations of complex stochastic representations for quantum dynamical systems. Journal of Physics A: Mathematical and Theoretical, 44(9):095004.

Pfeuty, P. (1970). The one-dimensional ising model with a transverse field. Annals of Physics, 57(1):79 – 90.

Pippan, P., Evertz, H. G., and Hohenadler, M. (2009). Excitation spectra of strongly correlated lattice bosons and polaritons. Phys. Rev. A, 80:033612.

Plimak, L. I., Olsen, M. K., and Collett, M. J. (2001). Optimization of the positive-p representation for the anharmonic oscillator. Phys. Rev. A, 64(2):025801.

Polkovnikov, A. (2005). Universal adiabatic dynamics in the vicinity of a quantum critical point. Phys. Rev. B, 72:161201.

Polkovnikov, A., Sengupta, K., Silva, A., and Vengalattore, M. (2011). *Colloquium* : Nonequilibrium dynamics of closed interacting quantum systems. Rev. Mod. Phys., 83:863–883.

Pollet, L., Prokof'ev, N. V., Svistunov, B. V., and Troyer, M. (2009). Absence of a direct superfluid to mott insulator transition in disordered bose systems. Phys. Rev. Lett., 103:140402.

Porras, D. and Cirac, J. I. (2004). Effective quantum spin systems with trapped ions. Physical review letters, 92(20):207901.

Pozsgay, B. (2014). Failure of the generalized eigenstate thermalization hypothesis in integrable models with multiple particle species. Journal of Statistical Mechanics: Theory and Experiment, 2014(9):P09026.

Pozsgay, B., Mestyán, M., Werner, M. A., Kormos, M., Zaránd, G., and Takács, G. (2014). Correlations after quantum quenches in the xxz spin chain: Failure of the generalized gibbs ensemble. Phys. Rev. Lett., 113:117203.

Press, W. H., Teukolsky, S. A., Vetterling, W. T., and Flannery, B. P. (2007). Numerical Recipes 3rd Edition: The Art of Scientific Computing. Cambridge University Press, New York, NY, USA, 3 edition.

Priyadarshee, A., Chandrasekharan, S., Lee, J.-W., and Baranger, H. U. (2006). Quantum phase transitions of hard-core bosons in background potentials. Phys. Rev. Lett., 97:115703.

Pyka, K., Keller, J., Partner, H. L., Nigmatullin, R., Burgermeister, T., Meier, D. M., Kuhlmann, K., Retzker, A., Plenio, M. B., Zurek, W. H., Del Campo, A., and Mehlstäubler, T. E. (2013). Topological defect formation and spontaneous symmetry breaking in ion Coulomb crystals. Nature Communications, 4:2291.

Rabson, D. A., Narozhny, B. N., and Millis, A. J. (2004). Crossover from poisson to wigner-dyson level statistics in spin chains with integrability breaking. Phys. Rev. B, 69:054403.

Radcliffe, J. M. (1971). Some properties of coherent spin states. Journal of Physics A: General Physics, 4(3):313.

Rigol, M. (2009a). Breakdown of thermalization in finite one-dimensional systems. Phys. Rev. Lett., 103:100403.

Rigol, M. (2009b). Quantum quenches and thermalization in one-dimensional fermionic systems. Phys. Rev. A, 80:053607.

Rigol, M. (2014). Quantum quenches in the thermodynamic limit. Phys. Rev. Lett., 112:170601.

Rigol, M., Dunjko, V., and Olshanii, M. (2008). Thermalization and its mechanism for generic isolated quantum systems. Nature, 452:854–858.

Rigol, M., Dunjko, V., Yurovsky, V., and Olshanii, M. (2007a). Relaxation in a completely integrable many-body quantum system: An *Ab Initio* study of the dynamics of the highly excited states of 1d lattice hard-core bosons. Phys. Rev. Lett., 98:050405.

Rigol, M., Dunjko, V., Yurovsky, V., and Olshanii, M. (2007b). Relaxation in a completely integrable many-body quantum system: An *Ab Initio* study of the dynamics of the highly excited states of 1d lattice hard-core bosons. Phys. Rev. Lett., 98:050405.

Rigol, M. and Srednicki, M. (2012). Alternatives to eigenstate thermalization. Phys. Rev. Lett., 108:110601.

Risken, H. (1989). The Fokker-Planck Equation. Berlin: Springer.

Rombouts, S. M. A. (2006). Comment on "gaussian quantum monte carlo methods for fermions and bosons". Phys. Rev. Lett., 96:188901.

Rossini, D., Silva, A., Mussardo, G., and Santoro, G. E. (2009). Effective thermal dynamics following a quantum quench in a spin chain. Phys. Rev. Lett., 102:127204.

Roux, G., Barthel, T., McCulloch, I. P., Kollath, C., Schollwöck, U., and Giamarchi, T. (2008). Quasiperiodic bose-hubbard model and localization in one-dimensional cold atomic gases. Phys. Rev. A, 78:023628.

Runge, K. J. (1992). Numerical study of the onset of superfluidity in two-dimensional, disordered, hard-core bosons. Phys. Rev. B, 45:13136–13139.

Sachdev, S. (2011). Quantum phase transitions. Cambridge University Press, Cambridge, second ed. edition.

Sakurai, J. J. (1993). Modern Quantum Mechanics (Revised Edition). Addison Wesley, 1 edition.

Sanchez-Palencia, L. and Lewenstein, M. (2010). Disordered quantum gases under control. Nat Phys, 6.

Sandvik, A. W. (1992). A generalization of handscomb's quantum monte carlo scheme-application to the 1d hubbard model. Journal of Physics A: Mathematical and General, 25(13):3667.

Sandvik, A. W. (2002). Classical percolation transition in the diluted two-dimensional $s = \frac{1}{2}$ heisenberg antiferromagnet. Phys. Rev. B, 66:024418.

Sandvik, A. W. (2010). Computational Studies of Quantum Spin Systems. In Avella, A. and Mancini, F., editors, American Institute of Physics Conference Series, volume 1297 of American Institute of Physics Conference Series, pages 135–338.

Sandvik, A. W. and Kurkijärvi, J. (1991). Quantum monte carlo simulation method for spin systems. Phys. Rev. B, 43:5950–5961.

Santos, L. F. and Rigol, M. (2010a). Localization and the effects of symmetries in the thermalization properties of one-dimensional quantum systems. Phys. Rev. E, 82:031130.

Santos, L. F. and Rigol, M. (2010b). Onset of quantum chaos in one-dimensional bosonic and fermionic systems and its relation to thermalization. Phys. Rev. E, 81:036206.

Schachenmayer, J., Pikovski, A., and Rey, A. M. (2015). Many-body quantum spin dynamics with monte carlo trajectories on a discrete phase space. Phys. Rev. X, 5:011022.

Schollwöck, U. (2005). The density-matrix renormalization group. Rev. Mod. Phys., 77:259–315.

Schwandt, D., Alet, F., and Capponi, S. (2009). Quantum monte carlo simulations of fidelity at magnetic quantum phase transitions. Phys. Rev. Lett., 103:170501.

Silva, A. (2008). Statistics of the work done on a quantum critical system by quenching a control parameter. Phys. Rev. Lett., 101:120603.

Simon, J., Bakr, W. S., Ma, R., Tai, M. E., Preiss, P. M., and Greiner, M. (2011). Quantum simulation of antiferromagnetic spin chains in an optical lattice. Nature, 472(7343):307–312.

Sinatra, A., Lobo, C., and Castin, Y. (2002). The truncated wigner method for bose-condensed gases: limits of validity and applications. Journal of Physics B: Atomic, Molecular and Optical Physics, 35(17):3599.

Smith, A. M. and Gardiner, C. W. (1989). Simulations of nonlinear quantum damping using the positive p representation. Phys. Rev. A, 39(7):3511–3524.

Sørensen, E. S., Wallin, M., Girvin, S. M., and Young, A. P. (1992). Universal conductivity of dirty bosons at the superconductor-insulator transition. Phys. Rev. Lett., 69:828–831.

Söyler, i. m. c. G., Kiselev, M., Prokof'ev, N. V., and Svistunov, B. V. (2011). Phase diagram of the commensurate two-dimensional disordered bose-hubbard model. Phys. Rev. Lett., 107:185301.

Srednicki, M. (1994). Chaos and quantum thermalization. Phys. Rev. E, 50:888–901.

Stanley, H. E. (1987). Introduction to Phase Transitions and Critical Phenomena (International Series of Monographs on Physics). Oxford University Press, USA.

Stanley, H. E. (1999). Scaling, universality, and renormalization: Three pillars of modern critical phenomena. Rev. Mod. Phys., 71:S358–S366.

Steinigeweg, R., Herbrych, J., and Prelovšek, P. (2013). Eigenstate thermalization within isolated spin-chain systems. Phys. Rev. E, 87:012118.

Sudarshan, E. C. G. (1963). Equivalence of semiclassical and quantum mechanical descriptions of statistical light beams. Phys. Rev. Lett., 10(7):277–279.

Syljuåsen, O. F. and Sandvik, A. W. (2002). Quantum monte carlo with directed loops. Phys. Rev. E, 66:046701.

Trotzky, S., Chen, Y.-A., Flesch, A., McCulloch, I. P., Schollwöck, U., Eisert, J., and Bloch, I. (2012). Probing the relaxation towards equilibrium in an isolated strongly correlated one-dimensional Bose gas. Nature Physics, 8:325–330.

Ulm, S., Roßnagel, J., Jacob, G., Degünther, C., Dawkins, S., Poschinger, U., Nigmatullin, R., Retzker, A., Plenio, M., Schmidt-Kaler, F., et al. (2013). Observation of the kibble–zurek scaling law for defect formation in ion crystals. Nature communications, 4.

Vestergren, A., Wallin, M., Teitel, S., and Weber, H. (2004). Effect of columnar disorder on the superconducting transition of a type-ii superconductor in zero applied magnetic field. Phys. Rev. B, 70:054508.

Vidal, G. (2003). Efficient classical simulation of slightly entangled quantum computations. Phys. Rev. Lett., 91:147902.

Vidal, G. (2004). Efficient simulation of one-dimensional quantum many-body systems. Phys. Rev. Lett., 93:040502.

Villain, J. (1975). Theory of one- and two-dimensional magnets with an easy magnetization plane. ii. the planar, classical, two-dimensional magnet. J. Phys. France, 36(6):581–590.

Vogels, J. M., Xu, K., and Ketterle, W. (2002). Generation of macroscopic pair-correlated atomic beams by four-wave mixing in bose-einstein condensates. Phys. Rev. Lett., 89:020401.

Vojta, T. (2006). Rare region effects at classical, quantum and nonequilibrium phase transitions. Journal of Physics A: Mathematical and General, 39(22):R143.

Vojta, T. (2010). Quantum griffiths effects and smeared phase transitions in metals: Theory and experiment. Journal of Low Temperature Physics, 161(1-2):299–323.

Wallin, M., So/rensen, E. S., Girvin, S. M., and Young, A. P. (1994). Superconductor-insulator transition in two-dimensional dirty boson systems. Phys. Rev. B, 49:12115–12139.

Weichman, P. B. (2008). Dirty bosons: Twenty years later. Modern Physics Letters B, 22(27):2623–2647.

Weichman, P. B. and Mukhopadhyay, R. (2007). Critical dynamics of the dirty boson problem: Revisiting the equality $z = d$. Phys. Rev. Lett., 98:245701.

White, M., Pasienski, M., McKay, D., Zhou, S. Q., Ceperley, D., and DeMarco, B. (2009). Strongly interacting bosons in a disordered optical lattice. Phys. Rev. Lett., 102:055301.

White, S. R. (1992). Density matrix formulation for quantum renormalization groups. Phys. Rev. Lett., 69:2863–2866.

Wigner, E. (1932). On the quantum correction for thermodynamic equilibrium. Phys. Rev., 40(5):749–759.

Witkowska, E., Deuar, P., Gajda, M., and Rzążewski, K. (2011). Solitons as the early stage of quasicondensate formation during evaporative cooling. Phys. Rev. Lett., 106:135301.

Wouters, B., De Nardis, J., Brockmann, M., Fioretto, D., Rigol, M., and Caux, J.-S. (2014). Quenching the anisotropic heisenberg chain: Exact solution and generalized gibbs ensemble predictions. Phys. Rev. Lett., 113:117202.

Wu, J. and Phillips, P. (2008). Minimal model for disorder-induced missing moment of inertia in solid h 4 e. Physical Review B, 78(1):014515.

Yu, R., Haas, S., and Roscilde, T. (2010). Universal phase diagram of disordered bosons from a doped quantum magnet. EPL (Europhysics Letters), 89(1):10009.

Yu, R., Miclea, C. F., Weickert, F., Movshovich, R., Paduan-Filho, A., Zapf, V. S., and Roscilde, T. (2012a). Quantum critical scaling at a bose-glass/superfluid transition: Theory and experiment for a model quantum magnet. Phys. Rev. B, 86:134421.

Yu, R., Roscilde, T., and Haas, S. (2008). Field induced disordered-local-moment phase in site-diluted spin-gap antiferromagnets. New Journal of Physics, 10(1):013034.

Yu, R., Yin, L., Sullivan, N. S., Xia, J. S., Huan, C., Paduan-Filho, A., Oliveira Jr, N. F., Haas, S., Steppke, A., Miclea, C. F., Weickert, F., Movshovich, R., Mun, E.-D., Scott, B. L., Zapf, V. S., and Roscilde, T. (2012b). Bose glass and mott glass of quasiparticles in a doped quantum magnet. Nature, 489:379–384.

Zener, C. (1932). Non-Adiabatic Crossing of Energy Levels. Royal Society of London Proceedings Series A, 137:696–702.

Zhang, L. and Ma, M. (1992). Real-space renormalization-group study of hard-core dirty bosons. Physical Review B, 45(9):4855.

Zhang, S., Kawashima, N., Carlson, J., and Gubernatis, J. E. (1995). Quantum simulations of the superfluid-insulator transition for two-dimensional, disordered, hard-core bosons. Phys. Rev. Lett., 74:1500–1503.

Zheludev, A. and Roscilde, T. (2013). Dirty-boson physics with magnetic insulators. Comptes Rendus Physique, 14(8):740 – 756. Disordered systems / SystÃĺmes dÃľsordonnÃľs.

Zimanyi, G. T., Crowell, P. A., Scalettar, R. T., and Batrouni, G. G. (1994). Bose-hubbard model and superfluid staircases in ^{4}He films. Phys. Rev. B, 50:6515–6518.

Zurek, W. H. (1985). Cosmological experiments in superfluid helium? Nature, 317:505–508.

Zurek, W. H. (2009). Causality in condensates: Gray solitons as relics of bec formation. Phys. Rev. Lett., 102:105702.

Zurek, W. H., Dorner, U., and Zoller, P. (2005). Dynamics of a quantum phase transition. Phys. Rev. Lett., 95:105701.

Zwolak, M. and Vidal, G. (2004). Mixed-state dynamics in one-dimensional quantum lattice systems: A time-dependent superoperator renormalization algorithm. Phys. Rev. Lett., 93:207205.